

This item was submitted to Loughborough University as a PhD thesis by the author and is made available in the Institutional Repository (<https://dspace.lboro.ac.uk/>) under the following Creative Commons Licence conditions.



For the full text of this licence, please go to:  
<http://creativecommons.org/licenses/by-nc-nd/2.5/>

**Pilkington Library**

Author/Filing Title ..... SMITH, K.S .....

Accession/Copy No. ....

Vol. No. ....

Class Mark .....

Loan copy

0401990540





# MULTIVARIABLE CONTROL OF DYNAMIC STRUCTURAL TEST SYSTEMS

by

Keith James Smith


A Doctoral Thesis

Submitted in partial fulfilment of the requirements  
for the award of

PhD of the Loughborough University of Technology

1st December 1997

© by Keith James Smith 1997

 Loughborough University P. 1      0000	
Date	Jan 99
Class	
Acc. No.	660199054

~~06~~ K0631290

## **Acknowledgements**

I dedicate this thesis to my family and friends for their constant encouragement and understanding. I would also like to express my sincere gratitude to my supervisor Roger W. Pratt for his support and patience throughout the course of this work.

# Contents

	page
NOMENCLATURE	vi
ABSTRACT .....	1
1. INTRODUCTION .....	2
2. DYNAMIC STRUCTURAL TESTING	
2.1 Introduction .....	5
2.2 A historical perspective .....	6
2.3 A dynamic structural test .....	7
2.4 The need for dynamic structural testing .....	10
2.5 Load types .....	10
2.6 Single actuator tests .....	16
2.6.1 Control system objectives .....	16
2.6.2 Principles of feedback design .....	19
2.7 Multiple actuator tests .....	23
2.7.1 Interaction .....	24
2.7.2 Control system objectives .....	25
2.7.3 Principles of feedback design .....	29
2.8 Current control schemes .....	34
2.8.1 Sequential loop closure .....	34
2.8.2 Remote Parameter Control .....	35
2.9 Conclusions .....	37

### 3. TEST RIGS

3.1	Introduction .....	38
3.2	Beam and Vibrator rig .....	39
3.2.1	Test frame .....	40
3.2.2	Vibrators .....	40
3.2.3	Beam .....	40
3.3	Torsion rig .....	41
3.3.1	Torsion bar assembly .....	42
3.3.2	Hydraulic system .....	45
3.3.3	Control system .....	47
3.3.4	Digital Transfer Function Analyser (DTFA) .....	50
3.4	Conclusions .....	51

### 4. MODELLING

4.1	Introduction .....	52
4.2	Servo-valve .....	53
4.2.1	Flow-pressure characteristic .....	55
4.3	Hydraulic Actuator .....	58
4.4	Dynamic representation of the test specimen .....	61
4.4.1	Introducing damping .....	62
4.4.2	Transfer function matrix .....	62
4.4.3	State space model .....	62
4.4.4	Torsion rig .....	63
4.5	Linear SISO model .....	68
4.5.1	Displacement output .....	70
4.5.2	Load output .....	73
4.6	Linear MIMO model .....	74
4.6.1	Displacement output .....	75
4.6.2	Force output .....	78
4.7	Hydraulic natural frequency and damping ratio .....	81
4.8	Confidence in the linear model .....	83
4.8.1	Simulation study .....	83
4.8.2	'Hydraulic' natural frequency and damping ratio .....	86
4.9	Conclusions .....	87



---

**5. CONTROL SCHEMES**

5.1	Introduction .....	88
5.2	Sequential Loop Closure .....	89
5.3	The Characteristic Locus (CL) method .....	90
5.3.1	Generalised Nyquist stability criterion .....	91
5.3.2	Control philosophy .....	93
5.3.3	Design method .....	95
5.4	Direct digital design of the Characteristic Locus controller .....	96
5.5	Conclusions .....	100

**6. STABILITY ISSUES AND THE RELEVANCE OF  
MULTIVARIABLE CONTROL IN MULTI-CHANNEL  
DYNAMIC STRUCTURAL TESTING**

6.1	Introduction .....	101
6.2	SISO and multivariable approaches to controlling multi-channel tests .....	101
6.3	Stability analysis for SISO tests .....	105
6.3.1	SISO Displacement control .....	105
6.3.2	SISO Load control .....	110
6.4	Stability analysis for MIMO tests .....	114
6.4.1	Multivariable displacement control .....	115
6.4.2	Multivariable load control .....	121
6.5	Guidelines for identifying test conditions best suited to Multivariable control .....	127

**7. CLOSED-LOOP FREQUENCY RESPONSE IDENTIFICATION**

7.1	Introduction .....	128
7.2	system identification .....	129
7.3	Frequency analysis by the correlation method .....	129
7.3.1	Application to a SISO closed-loop experiment .....	134

7.4	Multivariable closed-loop identification . . . . .	137
7.5	Examples	
7.5.1	Simulated identification of a multivariable plant . . . . .	139
7.5.2	Experimental identification of the Torsion rig . . . . .	145
7.6	Conclusions . . . . .	148
8.	<b>CONTROLLER DESIGN AND IMPLEMENTATION</b>	
8.1	Introduction . . . . .	149
8.2	Beam and Vibrator test rig . . . . .	149
8.2.1	Sequential Loop Closure . . . . .	150
8.2.2	Characteristic Locus . . . . .	156
8.2.3	Discrete Characteristic Locus Design. . . . .	164
8.3	Torsion rig . . . . .	169
8.3.1	Sequential Loop Closure . . . . .	170
8.3.2	Characteristic Locus design . . . . .	175
8.4	Conclusions . . . . .	183
9.	<b>CONCLUSIONS</b> . . . . .	184
	<b>REFERENCES</b> . . . . .	187
	<b>APPENDIX 1</b> . . . . .	193
	<b>APPENDIX 2</b> . . . . .	197
	<b>APPENDIX 3</b> . . . . .	201
	<b>APPENDIX 4</b> . . . . .	212
	<b>APPENDIX 5</b> . . . . .	214

## Nomenclature

$x(t)$	Time varying signal
$x(s)$	Laplace transform of $x(t)$
$x(j\omega)$	Frequency response of $x(t)$
$X(\omega)$	Fourier transform of $x(t)$
$G(s)$	Transfer function
$G(j\omega)$	Frequency response of $G(s)$
$\mathbf{x}(t)$	Vector of time varying signals
$\mathbf{x}(s)$	Laplace transform of $\mathbf{x}(t)$
$\mathbf{x}(j\omega)$	Frequency response of $\mathbf{x}(t)$
$\mathbf{X}(\omega)$	Fourier transform of $\mathbf{x}(t)$
$\mathbf{G}(s)$	Matrix of transfer functions, or Transfer Function Matrix (TFM)
$g_{ij}(s)$	Transfer function at the $i^{\text{th}}$ row and $j^{\text{th}}$ column of $\mathbf{G}(s)$
$\mathbf{G}(j\omega)$	Frequency response of $\mathbf{G}(s)$
$\mathbf{G}(\omega)$	Fourier transform of $\mathbf{G}(s)$
$\mathbf{u}$	Vector
$\mathbf{G}$	Matrix
$\ \mathbf{u}\ $	Norm of a vector
$ \mathbf{G} $	Determinant of a matrix
$\underline{\sigma}(\mathbf{G})$	Minimum singular value of $\mathbf{G}$

$\bar{\sigma}(G)$	Maximum singular value of $G$
$\underline{\sigma}(G(j\omega))$	Minimum principal gain of $G(j\omega)$
$\bar{\sigma}(G(j\omega))$	Maximum principal gain of $G(j\omega)$
$\det[G]$	Determinant of $G$

## Abstract

Multi-actuator structural testing has traditionally been regarded, from a control point of view, as a multi-loop, single-input, single-output problem. This approach does not take into account the interaction between different actuators, due to the dynamics of the structure under test, which can be considerable. The result of this is often poor laboratory reproduction of the actual service data.

This project shows that the mass of the structure under test has a considerable impact upon the stability of the traditional multi-loop, single-input, single-output control system. Where stability is prejudiced, the loop gains have to be reduced to maintain stability and this can degrade the performance of the test. In these circumstances multivariable control offers the potential for a significant improvement in performance.

Two experimental rigs are used in this project, both exhibit major interaction and pose a significant control problem. The first rig consists of a laboratory scale cantilever beam excited by two electro-dynamic vibrators with displacements measured by Linear Variable Differential Transformers (LVDTs). The second, industrial-scale, rig consists of a large steel frame excited by two hydraulic actuators with applied force measured by load cells. Multivariable controllers are designed and implemented on these rigs based on the frequency-domain Characteristic Locus method. The multivariable controllers are shown to demonstrate superior performance to traditional multi-loop controllers.

Mathematical models of the rigs are not required for controller design, instead experimental frequency responses are all that are needed. This is a major attraction of the Characteristic Locus method since the task of modelling the dynamics of a multi-channel structural test system is not trivial. However, obtaining the frequency response of the second rig is made difficult by the imposition of closed-loop control during the identification experiment. A technique is presented to overcome this problem using an existing correlation method.

# Chapter 1

## Introduction

All mechanical structures when introduced into their service environments will be subjected to a variety of different conditions and loading forces. The diversity of the service loadings and the complexity of the dynamics of the structure make it impractical, if not impossible to determine the strength of the structure by analytical methods alone. Laboratory dynamic structural tests (fatigue tests) are used to overcome this problem. These tests are intended to reproduce the service conditions of the structure in a controlled environment and frequently involve the application of multiple forces and the measurement of multiple signals; commonly load, acceleration and displacement. Such tests are termed 'multichannel' and give rise, by definition, to multivariable control problems.

Dynamic testing is performed by applying known excitations to the structure in order to reproduce known service conditions of a controlled variable, such as displacement, force, velocity or acceleration, while stress and strain distributions are monitored for subsequent analysis and evaluation. Multi-channel dynamic structural tests are frequently used in the aerospace and automotive industries to investigate the fatigue and vibration properties of structures. Aerospace applications vary in scale from tests involving perhaps 100 actuators on complete aircraft, down to two-input, two-output tests on sub-structures. The input signals for these tests are usually sinusoidal or involve a sinusoidal signal to invoke a transition from one static load level to another. Automotive tests also range from the involvement of complete vehicles down to sub-components. Tests on complete vehicles have advanced from four-input, four-output ("four poster") rigs to twelve or sixteen channel tests with input signals which are often random in nature. The structure is loaded or forced either by servo-hydraulic actuators or electro-magnetic vibrators, with the former method being more common in aerospace and automotive applications.

The fundamental problem encountered in controlling multi-channel tests is the interaction between different actuator inputs and outputs due to the dynamics of the test structure. Often the multivariable nature of the problem is ignored and individual

servo-controllers are used to control each actuator. Naturally this approach does not take into account the interaction and can lead to performance problems when the interaction is severe. Even when optimal inputs to the actuators, in multi-actuator tests, are calculated in order to maximise a displacement severity measure [2], the suggested test will run open loop. In the most sophisticated method [3] of multi-actuator dynamic testing, iterative numerical methods are used to determine the excitations by deconvolution of the measured output, thus producing the required response. Input-output cross-talk, in this case is taken into account, but the calculation of the control input is done off-line, and again the test runs open-loop.

The aims of this project are to address the fundamental issue of the relevance of multivariable control systems applied to dynamic structural test systems and to apply the frequency domain control theory of multivariable systems to the design and implementation of controllers for dynamic structural test systems. The dynamics of the test structure, actuators and transducers are combined into a multiple-input, multiple-output plant. Structural interaction and effective decoupling of different inputs and outputs are central to the design process. The result is a tighter control scheme, with better compliance to performance specifications. The control is based on feedback of directly measurable outputs. Mathematical modelling of the structural dynamics of the test object (often not a trivial job) is not necessary. Simple frequency response tests will provide all the necessary data for the design process.

The importance of the proposed control strategy is that a systematic approach is followed to provide the required system performance and accuracy. Multivariable controllers are designed in the frequency domain from frequency response data, thus mathematical modelling of the structural dynamics of the test object is not necessary. This is a major advantage since mathematical modelling of a structural test system can be a very complex task. The necessary frequency response model of the test system is obtained experimentally, although this is not always straightforward. In some situations, the identification experiment must be performed on the closed-loop system. A proven technique for identifying the open-loop frequency response of a multivariable plant is extended to be used in a closed-loop test.

In order to investigate the use of multivariable control systems, two test rigs were used. The first was developed in a previous project [4] and consists of a laboratory-scale cantilever beam excited by two electro-dynamic vibrators. Multivariable controllers have been designed for the rig using both the Characteristic Locus method and the Inverse Nyquist Array methods [5, 6] and simulations of closed-loop performance were favourable. That work has been extended with digital implementation and a recent extension to the Characteristic Locus method has been

---

implemented for the first time. The second rig is an industrial scale test rig in which a steel frame is excited by two hydraulic actuators. Two control systems were designed and implemented on this latter rig for comparative purposes - two single-loop controllers and a multivariable Characteristic Locus controller.

Results of the work described in this thesis has been presented at several international conferences [7-15, 45, 46] and collaboration with British Aerospace has proven to be an invaluable insight into the dynamic structural testing industry.



## **Chapter 2**

# **Dynamic Structural Testing**

### **2.1 Introduction**

In rare circumstances does the single application of a static load result in the failure of a mechanical structure. Conversely, the repeated application of a lower magnitude load - perhaps a 'safe' load from static considerations, may ultimately cause failure, usually sudden and catastrophic. This is known as fatigue failure and is a phenomenon associated with localised high stress levels [1]. The complexity of many engineering structures make it impractical, if not impossible, to determine the necessary stress distributions for assessing the dynamic strength of the structure through computational means. Consequently, spatially distributed dynamic loads are applied to the structure in order to assess its response to dynamic stresses, this is a Dynamic Structural Test. Static tests can also be carried out on the structure to check static stress calculations but are no substitute for a dynamic test in the determination of fatigue performance.

A brief historical perspective of dynamic structural testing is given in section 2.2, reporting on the development of dynamic structural testing up to the present day, a typical test is described in section 2.3 and the need for dynamic structural testing is established in section 2.4. A characteristic of dynamic structural testing is the well defined loading that will be applied to the structure during the test. This is closely associated with the test application, section 2.5, and leads to the control system objectives developed in section 2.6 for single actuator tests and section 2.7 for multiple actuator tests. In section 2.8 current control schemes are discussed and finally the chapter is summarised in section 2.9.

## 2.2 A historical perspective

Metal fatigue has been studied for many years, the earliest publications on the subject appearing over one hundred years ago. In the 1956 *International Conference on Fatigue* there was an increasing emphasis on fatigue testing of components and structures, although constant amplitude loading was still used in all the reported tests. The major transportation industries, aircraft, automobile and railway, were the noticeable contributors in these two categories, although the only published tests on structures were from the aircraft industry. Until this period, the 1950s, the generally adopted method of dynamic structural testing had been the application of constant amplitude load cycles to the specimen, component or structure. The so called *Palmgren-Miner* rule, resulting from papers published in 1924 [19] and 1945 [20], which hypothesized a linear accumulation of fatigue damage, was widely accepted and predicted, in principal, fatigue cracking due to any combination of differing load amplitude cycles. Gassner [21], who had been advocating the need for variable amplitude testing for many years, performed a dynamic structural test on a vehicle component using a load history with eight discrete levels of magnitude, stepped from low load cycles to high load cycles and back to low load cycles, e.t.c. This load history was determined from proposed stress probability distributions and Gassner's results were two-fold. Firstly, good agreement was found between the dynamic structural test performance and the actual service life of the component. Secondly, and importantly, Gassner found inaccurate and unsafe predictions from the *Palmgren-Miner* rule. Although since the 1940s the technology for recording and quantifying service load histories began to be generally available, it was not until later that the necessity for structural testing with a realistic load history was discussed. Moreau and Peterson in 1955 [22], reporting on the testing of diesel locomotives, comment:

‘It is now possible to predict, with reasonable accuracy, what stresses will be induced in a specific axle design by a certain load and the relationship between the stress and the number of applications which will cause failure is also fairly well established... There is, however, very little information available about the loads an axle is actually exposed to in service.’

However, up until the mid 1960s the fatigue testing machinery available was not advanced or versatile enough to allow application of realistic load histories to large components or structures. The most common system, known as the *Resonance system* [23], excited a natural frequency of the test structure, the load amplitude was controlled via the frequency or amplitude of the exciting force. The disadvantages were

- (i) that the problem of providing the vibration mode required for the correct loading conditions was considerable, and
- (ii) the unsuitability of the system for simultaneous loading in several directions, a common requirement in tests on large components and structures.

Consequently, load histories were limited to constant amplitude cycles or block programmes such as Gassner's. The mid 1960s saw a major breakthrough in dynamic structural testing technology, the introduction of the servo controlled electro-hydraulic actuator. Electronic feedback control combined with the superior load capacity and load deflection capabilities of the electro-hydraulic actuator opened the way to applying service recorded load histories. Sophisticated computer generated load histories could be produced and displacement, load or strain could be controlled. Another important advantage was the suitability of electro-hydraulic actuation to the loading a structure in more than one axis.

## **2.3 A dynamic structural test**

The scale and complexity of dynamic structural testing is diverse, ranging from single-actuator, constant-amplitude tests on material specimens through to 16-actuator, multiple-axis tests on car suspension systems and 100-actuator tests on whole aircraft airframes with quasi-static loading (see section 2.5). Figure 2.1 gives an indication of this diversity. Possibly one of the most complex tests ever carried out in the UK was that on the Concorde at RAE Farnborough [24]; from construction of the test frame to the end of testing took some twenty two years with ninety-five hydraulic actuators loading the airframe.

Figure 2.2 shows a typical loading system for a hypothetical wing fatigue test. The hydraulic actuators are controlled by servo-valves which convert electrical current to fluid flow through the actuator ports, the resulting pressure difference across the piston causes a force to be applied to the test structure and a corresponding displacement of the actuator ram. Displacement and force are measured by suitable transducers and the controller executes an algorithm on the command signals and feedback signals to derive the control signals to the servo-amplifiers, which then drive the servo-valves to maintain control of the loading on the structure. The hydraulic supply is represented simply by the oil reservoir, pump and accumulator, safety features such as pressure release valves are commonly used but not indicated in the figure.

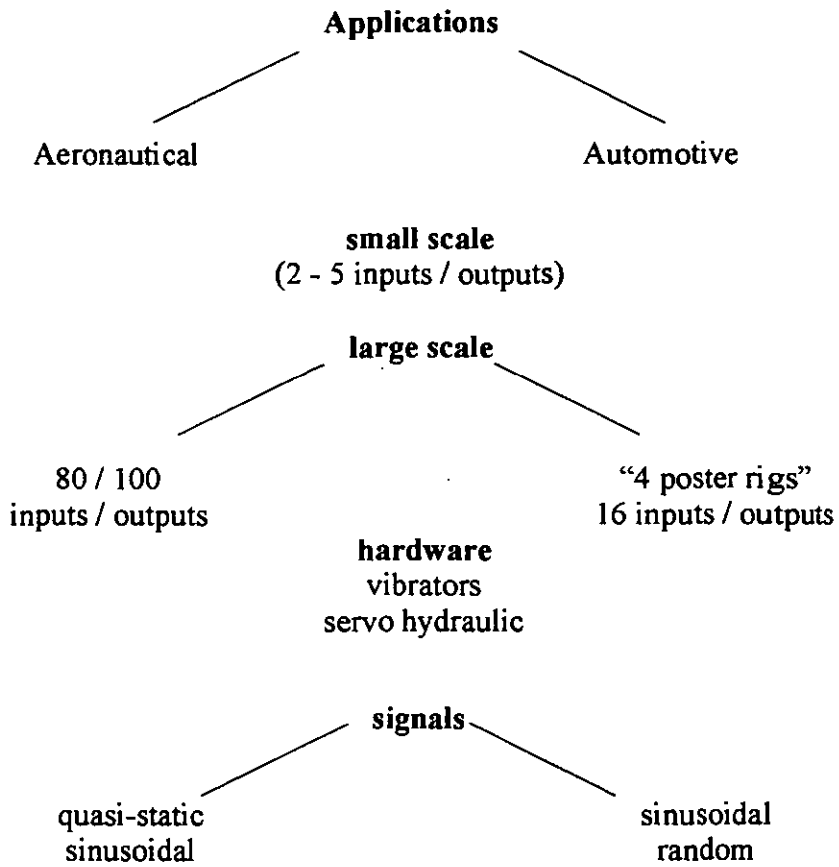


**Figure 2.1 Multichannel structural tests**

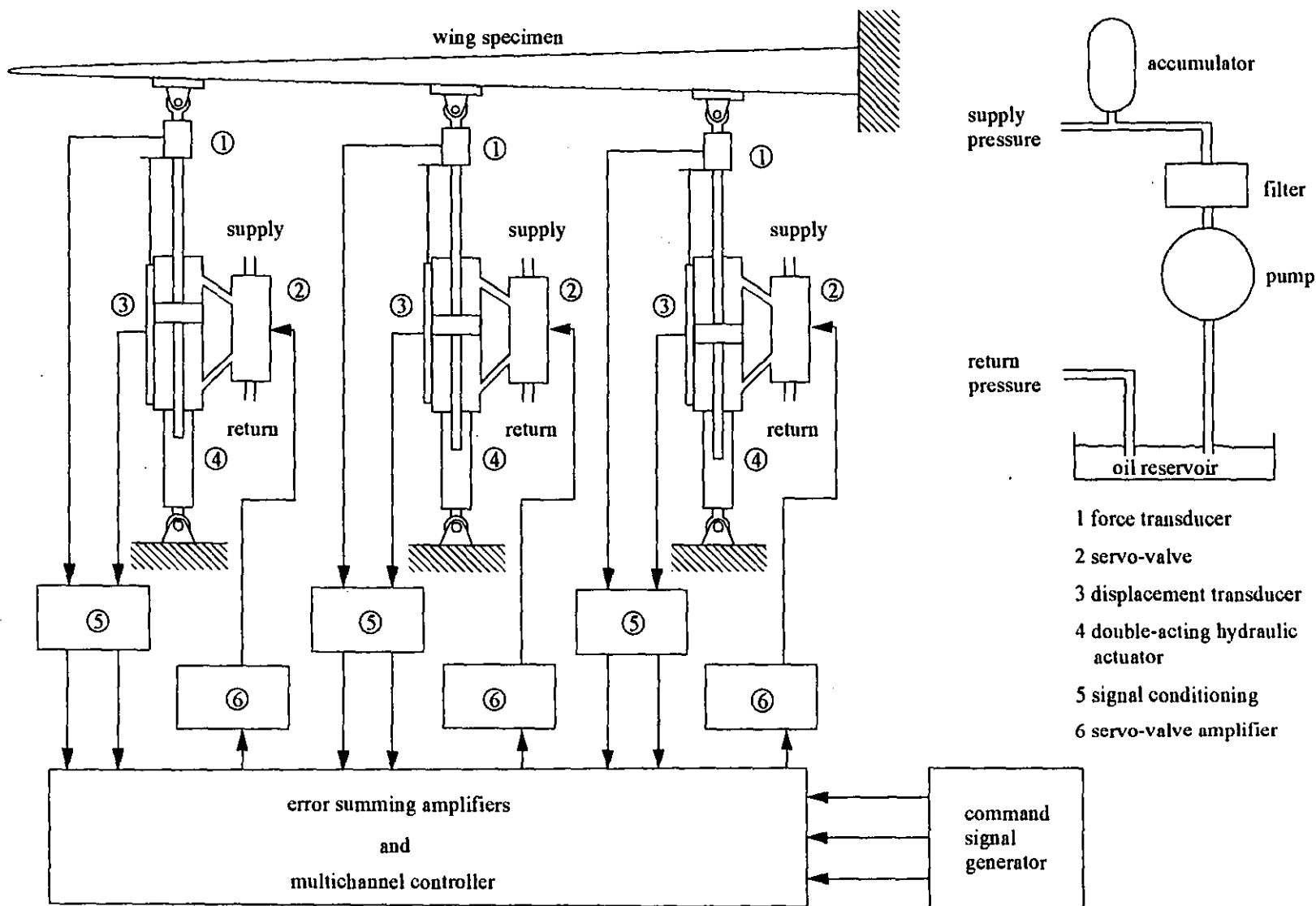


Figure 2.2 A typical structural test

## 2.4 The need for dynamic structural testing

The building blocks of fatigue design are material fatigue data obtained from specimen tests. From this data, component fatigue performance and, ultimately structural fatigue performance, can be accounted for in design. However, the fatigue performance of some component types, typically those possessing complex geometries or having undergone complex manufacturing processes, bear little resemblance to their basic material fatigue data and thus a fatigue test is required, even at the design stage.

Before a product can be introduced into service, confidence in its performance under fatigue loading, for instance time to fatigue failure, is necessary if not mandatory (e.g., civil aircraft worthiness). At the design stage, the probable load history to which the product will be subjected may be imprecisely known and design assumptions, trade-offs and optimisations (e.g., strength for weight) will have been used. All of these factors make a dynamic structural test the only accurate prediction of fatigue performance. Subsequent redesigns and developments can be compared sensibly under the repeatable and controlled conditions of a dynamic structural test.

Areas prone to fatigue and the onset and sequence of fatigue failures can all be monitored during the dynamic structural test of the prototype, enabling the establishment of realistic inspection and repair schedules. It is not uncommon for an engineering structure to undergo a major change in operating conditions or a desired extension of its original service life. Edwards [1] reports on extensive fatigue tests carried out on DH112 Venom aircraft for the Swiss Federal Aircraft Factory resulting in an extension of service life of up to three times the original life and a reduction in cost per flying hour of one half.

## 2.5 Load types

### *Quasi-static*

Some tests involve the measurement of structural response to changing loads where the rate of change of load is not rapid enough to excite dynamic effects such as resonance within the structure. This is known as quasi-static loading and is commonly found in the testing of aircraft structures. The excursion between static loads sometimes follows a low frequency half-sine trajectory as indicated in Figure 2.3.

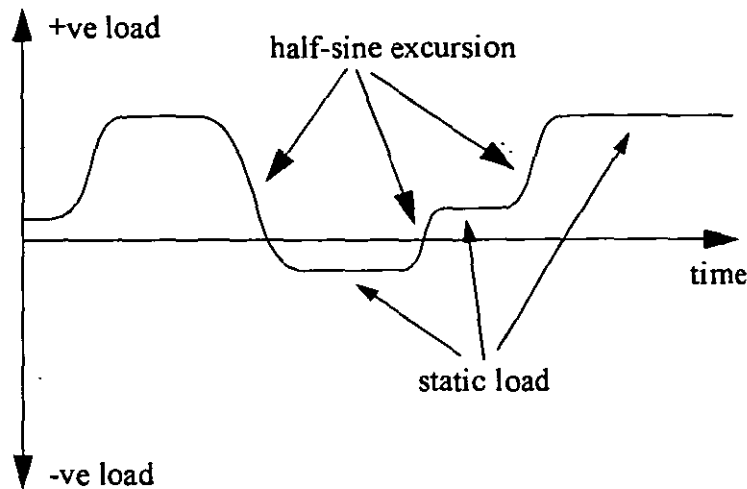


**Figure 2.3** Quasi-static loading

### *Constant amplitude and block programmes*

Engineering components and structures are rarely subjected to constant amplitude load cycles for their entire service life. However, such loading is, for historical reasons, used on specimens in single actuator tests to provide basic material fatigue data in the form of  $S/N$  curves. Figure 2.4 shows a constant amplitude load history whose stress amplitude ( $S$ ) and the resulting number of cycles to failure ( $N$ ) are the ordinates on the  $S/N$  curve. Constant amplitude loading is, however, a gross approximation of service conditions and variable amplitude tests are a step towards ensuring a realistic fatigue test. Block programmes are the most commonly found variable amplitude tests, typically applied to structural components, where the service data are analysed and broken down into blocks of load levels. These blocks of load levels are then applied to the structural component in a stepped manner to form a programme which is then repeated until failure occurs. Introduced in the 1950s, with Gassner [21] being a major proponent of this loading scheme, block programme tests are still in use today, and are commonly found in acceptance tests of automotive components [1]. Figure 2.5 shows a four-level block programme.

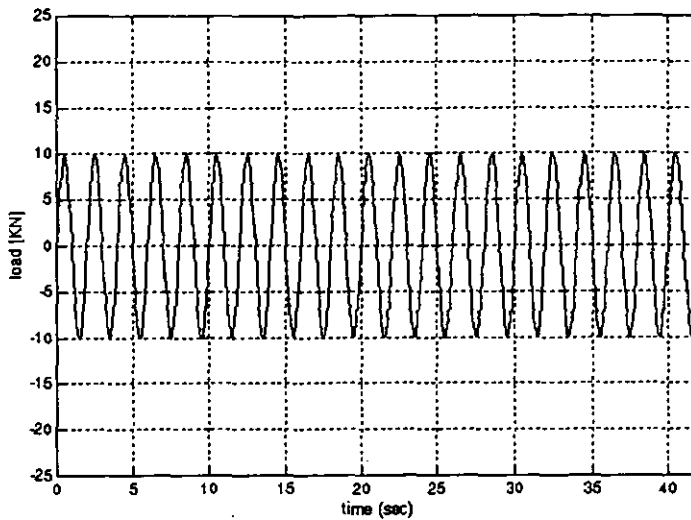


**Figure 2.4 Constant amplitude loading**

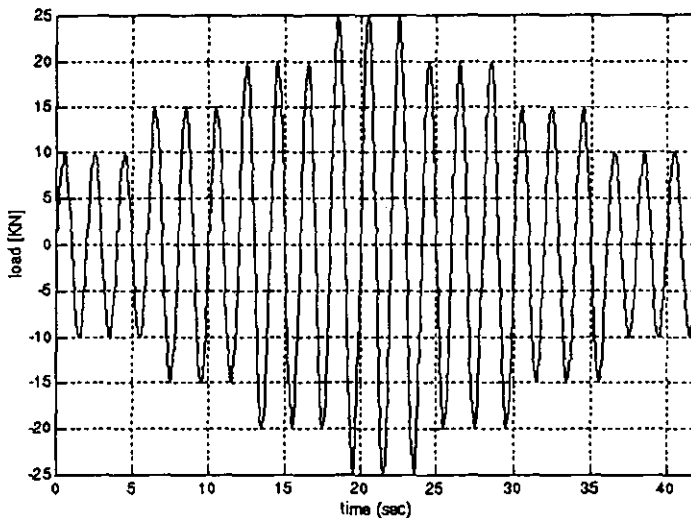


**Figure 2.5 Block-programme loading**

***Random and service-recorded loading***

The block programme test, although being variable in amplitude, may not be representative of service loading since it is generally considered [25] that amplitude, number of occurrences and sequencing of load cycles have a major effect on fatigue performance. Certain operating environments produce a random service loading which can be defined by a probability or stochastic process, from which a temporal signal can be synthesized to excite the structure in the dynamic structural test. This is the case for



automotive vehicles where the vertical profile of the road surface, which excites the vehicular structure through the tyres, may be described by a single-sided power spectral density (PSD) [26]. Such sophisticated loading finds application in tests on automotive suspension, steering and engine mount assemblies, where commonly up to 16 actuators are used in multi-axis configurations. Synthesis of the random test signal is principally an inverse Discrete Fourier Transform applied to the PSD, the process is described below.

Consider that the service loading is described by a stationary stochastic process with an  $N$ -point discrete-time realisation

$$x_n = x(nh) \quad n = 0, 1 \dots N-1 \quad (2.1)$$

where  $h$  is the sampling period of the sequence, in seconds. A Discrete Fourier Transform (DFT) of the sequence yields complex spectra,  $X_k$ , thus

$$X_k = \sum_{n=0}^{N-1} x_n e^{-j \frac{2\pi nk}{N}} \quad k = 0, 1 \dots N-1 \quad (2.2)$$

The stochastic process is conveniently described its power spectral density (PSD)  $S_{xx}(k)$  defined as the power per frequency interval

$$S_{xx}(k) = \frac{|X_k|^2}{N} \quad k = 0, 1 \dots N-1 \quad (2.3)$$

and by direct analogy to the Fourier transform of a continuous-time signal, is defined over negative and positive frequencies. It can be shown that only the first  $N/2 + 1$  spectra  $X_k$  are unique and correspond to the frequencies below (in Hz) where  $f_{N/2}$  is known as the Nyquist frequency.

$$f_k = \frac{k}{hN} \quad k = 0, 1 \dots N/2 \quad (2.4)$$

The remaining  $N/2 - 1$  spectra are complex conjugates of the first  $1, 2 \dots N/2 - 1$  spectra, according to equation (2.5),

$$X_{N-r} = X_r^* \quad 0 < r < N/2 \quad (2.5)$$

and can be ascribed to negative frequencies. However, since negative frequencies do not exist in practice, the PSD can be re-defined over positive frequency by suitably adjusting the positive frequency contribution. The result is a single-sided

PSD,  $G_{xx}(k)$ , and it is  $G_{xx}(k)$  that is used to describe the stochastic properties of the random load. Assuming that  $X_0 = 0$ , i.e. the mean of the sequence  $x_n$  is zero, and that  $X_{N/2} = 0$ , i.e. the signal is band limited to a frequency below the Nyquist frequency, then

$$G_{xx}(k) = 2 \frac{|X_k|^2}{N} \quad k = 0, 1 \dots N/2 \quad (2.6)$$

Now since the excitation  $x_n$  is a stochastic process, the computed spectrum from a single time record, equation (2.2), will itself be stochastic and is referred to as a spectral *estimate*. The PSD of a stochastic process is therefore determined from averaged spectral estimates

$$G_{xx}(k) = 2E \left\{ \frac{|X_k|^2}{N} \right\} \quad k = 0, 1 \dots N/2 \quad (2.7)$$

where  $E$  is the mathematical expectation operator. The averaging technique used (e.g. Bartlett's or Welch's method) does not concern this analysis since the PSD is already known and the task is to determine suitable spectra from which a time domain sequence can be synthesized. The obvious choice of  $|X_k|$  from equation (2.7) is

$$|X_k| = \left[ \frac{G_{xx}(k) N}{2} \right]^{\frac{1}{2}} \quad k = 0, 1 \dots N/2 \quad (2.8)$$

and gives a signal whose spectra have completely defined magnitudes. This is desirable for dynamic structural testing as it will produce a repeatable test signal. Note that the spectra for  $k = N/2 + 1 \dots N - 1$  are obtained from equation (2.5).

However, in general a real-valued discrete sequence yields complex spectra, and since the PSD conveys no phase information, random phases,  $\alpha_k$ , can be assigned to the spectra in equation (2.8) from a uniform distribution over the range  $0, 2\pi$ . This gives equation (2.9) where, again, the spectra for  $k = N/2 + 1 \dots N - 1$  are obtained from equation (2.5).

$$|X_k| = \left[ \frac{G_{xx}(k) N}{2} \right]^{\frac{1}{2}} e^{j\alpha_k} \quad k = 0, 1 \dots N/2 \quad (2.9)$$

The discrete-time sequence  $x_n$  can now be synthesized from an inverse DFT, equation (2.10)

$$x_n = \frac{1}{N} \sum_{k=0}^{N-1} X_k e^{j \frac{2\pi nk}{N}} \quad n = 0, 1 \dots N-1 \quad (2.10)$$

For example, suppose that a loading environment is characterised by a single-sided PSD with a bandwidth of 10 Hz. Following the analysis described above, a discrete time sequence is synthesized in Figure 2.6 with  $N = 1024$  data points at a sampling frequency of 20Hz.

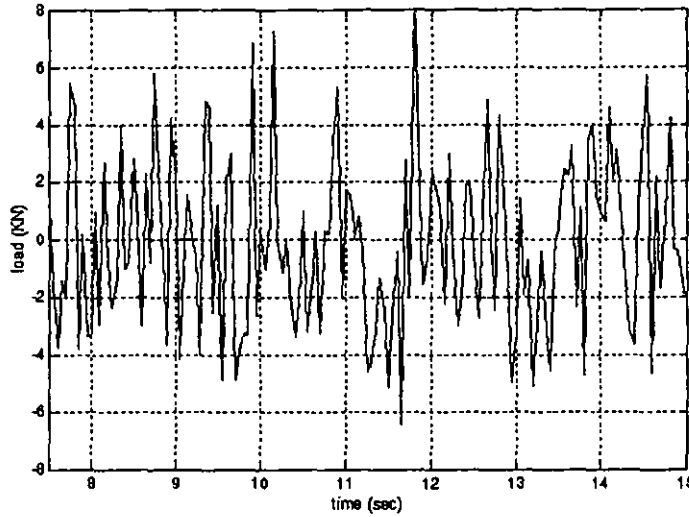


**Figure 2.6 Synthesized random load signal**

Using actual service recorded load histories in the fatigue test will give the most accurate prediction of fatigue performance. Acknowledged for some time, this has only become feasible with electrohydraulic actuation, electronic control and sophisticated computer data processing. The use of service recorded load histories is found in a wide variety of engineering structural tests such as those on artillery guns, portable bridges used by the military and automotive vehicles. The latter is a considerable application area using almost exclusively the Remote Parameter Control technique (see section 2.8).

### ***Standardised load histories***

By standardising load histories for a particular structural form, it becomes possible to compare and sensibly exchange fatigue performance data for various structures with that form. Obviously, if a sufficient similarity of load histories cannot

be established from a considerable number of structures then standardisation is irrelevant. Fortunately for transport aircraft, tactical aircraft and helicopters this has, up to the present time, never been the case, mainly due to a clear structural form and a service environment controlled and well defined by operational requirements. However, a load history from a structure such as an aircraft will comprise of a great number of simultaneous load signals over many thousands of flying hours; a colossal amount of data totally unmanageable to process. By performing a counting algorithm on the load history such as peak, level, range, rain-flow or to/from, the characteristics of the load history contributing to fatigue damage can be quantified and the data greatly compacted. The counting algorithms construct tables of exceedences or crossings, or matrices of To/From load peaks, termed the *load spectrum*. Suitable analysis of many spectra yields an 'average' spectrum which becomes the standardised spectrum, from which a load history can be synthesized. In the structural test, loading is commonly quasi-static with half-sine excursions between load cases. Standardised spectra are used virtually exclusively in the full-scale testing of fighter aircraft (FALSTAFF) [27], transport aircraft (TWIST, MiniTWIST), [28, 29] and helicopter rotor blades (Helix, Felix) [30, 31].

## 2.6 Single actuator tests

Representative excitation of the structure under test will require, in all but the simplest of cases, the use of several or more actuators. However, to tackle the MIMO control problem thus presented it is instructive to first consider the SISO control problem from which general objectives can be established.

Fatigue performance was earlier characterised in the time-domain and so naturally the control problem is a time-domain tracking problem, i.e. the output response must follow some desired trajectory. The discussion presented in the next section, however, illustrates that the control problem is better suited to formulation in the frequency domain, in a manner that is equally applicable to quasi-static, sinusoidal, random or service recorded loading. In section 2.6.2 a feedback control structure is presented and general principles of design are discussed.

### 2.6.1 Control system objectives

The combined dynamics of the actuator, test frame and test specimen will be referred to as the dynamics of the test rig, modelled as a transfer function  $G(s)$ . The combination of the controller and the test rig will be referred to as the controlled test

rig which may be modelled by a transfer function  $F(s)$ . Tracking performance is illustrated schematically in Figure 2.7 where the desired output response is defined as  $r(t)$  and the actual output response is defined as  $y(t)$ .

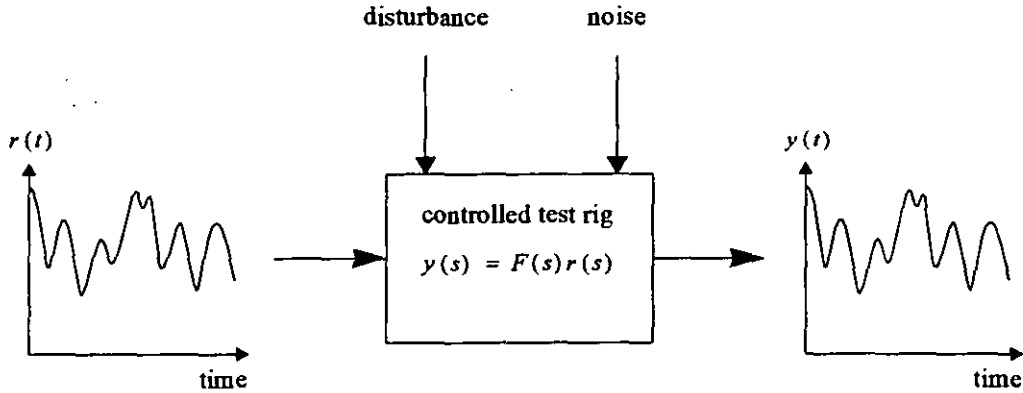


**Figure 2.7 Tracking in a SISO system**

Exogenous noise and disturbance signals are also indicated and their effect on controller design is discussed in section 2.6.2. The performance objective for steady-state and forced response is stated in equation (2.11) where  $\varepsilon$  is a bound on the allowable tracking error.

$$r(t) - y(t) \leq \varepsilon \quad (2.11)$$

Although succinct, this statement does not lend itself well to control system design with a possibly infinite number of desired trajectories. Consider, however, the fact that the all desired trajectories will be well defined by their frequency content and will be known in advance of the test. The input-output relationship for the controlled test rig is

$$y(s) = F(s)r(s) \quad (2.12)$$

and in the frequency-domain this becomes:

$$y(j\omega) = F(j\omega)r(j\omega) \quad (2.13)$$

### *Quasi-static loading*

For accurate tracking of a quasi-static signal, comprising of steady-state levels linked by half-sine excursions at a radian frequency  $\omega_o$ , it is obvious that the following is required

$$\left. \begin{array}{l} y(0) = r(0) \\ y(j\omega_o) = r(j\omega_o) \end{array} \right\} \Rightarrow \begin{array}{l} |F(j\omega)| = 1 \\ \angle F(j\omega) \approx 0 \end{array} \quad \omega = 0, \omega_o \quad (2.14)$$

regardless of the sequence and magnitude of the steady-state load levels.

### *Sinusoidal loading*

Consider that the sinusoidal loading occurs over a bandwidth from 0 to  $\omega_{max}$ , then the above requirement can be extended to equation (2.15) below, which applies equally well to purely sinusoidal tests.

$$\begin{array}{l} |F(j\omega)| = 1 \\ \angle F(j\omega) \approx 0 \end{array} \quad 0 \leq \omega \leq \omega_{max}$$

(2.15)

### *Random loading*

Consider the now the case of random loading as described in section 2.5 where the desired output response  $r(t)$  is characterised by a double-sided power spectral density (PSD)  $\Phi_{rr}(\omega)$ . The objective of the test is to reproduce the PSD on the structure, the relationship between the input and output PSDs is given by

$$\Phi_{yy}(\omega) = \frac{1}{\gamma_{ry}^2(\omega)} |F(j\omega)|^2 \Phi_{rr}(\omega) \quad (2.16)$$

where  $\gamma_{ry}(\omega)$  is the coherence function. Throughout this thesis attention is restricted to linear systems, in which case it can be shown that  $\gamma_{ry}(\omega)$  is unity. Consequently, the resulting control system requirement is given in equation (2.17) where the PSDs are bandwidth limited to  $\omega_{max}$ . This is a relaxed requirement to that obtained for sinusoidal testing, equation (2.15), as it places no restriction on the phase of the transfer function of the controlled test rig. This stems from the fact that tracking has been interpreted in terms of PSDs which themselves convey no phase information.

$$|F(j\omega)| = 1 \quad 0 < \omega \leq \omega_{max} \quad (2.17)$$

### *Service-recorded loading*

Such an approach is not suitable for reproduction of service recorded load histories and the following analysis is required.

Let the Fourier transform of the service recorded load history be  $R(\omega)$ , then the load history can be obtained from an inverse Fourier transform thus

$$r(t) = \frac{1}{2\pi} \int_{-\infty}^{\infty} R(\omega) e^{j\omega t} d\omega \quad (2.18)$$

and for accurate tracking it is required that  $y(t) \approx r(t)$ . Let the Fourier transform of the controlled output be  $Y(\omega)$ , then it is clear that equality of input and output Fourier transforms is required, i.e.

$$Y(\omega) = R(\omega) \quad (2.19)$$

However, the input transform  $R(\omega)$  will be modified by the frequency response of the controlled test rig according to equation (2.20)

$$Y(\omega) = R(\omega)F(j\omega) \quad (2.20)$$

Therefore, from comparison of equation (2.19) and equation (2.20), the control system requirement is identical to that for sinusoidal testing, equation (2.15), the recorded load history is assumed to have a negligible frequency content beyond  $\omega_{max}$ .

Clearly from the analysis in this section, a simple tracking performance objective expressed in the frequency domain is applicable to quasi-static, sinusoidal, random and service recorded load excitation; this is stated in equation (2.15). In the next section a feedback control scheme is introduced and general principles of frequency domain design are discussed.

## **2.6.2 Principles of feedback design**

First of all consider the open-loop system  $G(s)$  with a disturbance  $d(s)$  acting on the input and measurement noise  $n(s)$  present at the output of the system, this is illustrated in Figure 2.8.

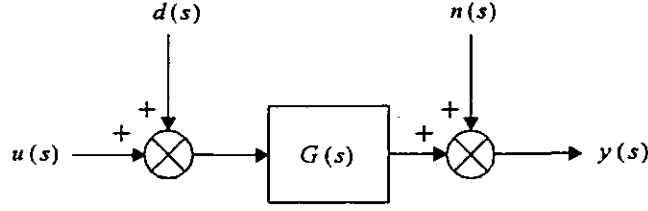


**Figure 2.8 Open-loop system with disturbance and noise signals**

The noise appears immediately in the plant output and the disturbance has a direct effect on the plant output, equation (2.21). This situation is undesirable as the disturbance and noise terms are unwanted.

$$y(s) = G(s)u(s) + G(s)d(s) + n(s) \quad (2.21)$$

Consider now the feedback scheme illustrated in Figure 2.9, where the measured plant output is compared with the reference signal and the resulting error is modified by the controller gain  $K(s)$  to excite the plant. The output response  $y(s)$  is now given by equation (2.22).

$$y(s) = \frac{G(s)K(s)}{1 + G(s)K(s)}r(s) + \frac{G(s)}{1 + G(s)K(s)}d(s) + \frac{1}{1 + G(s)K(s)}n(s) \quad (2.22)$$

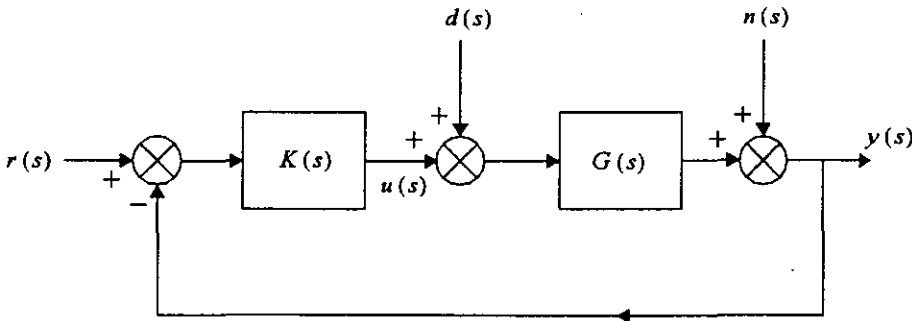


**Figure 2.9 Closed-loop block diagram of SISO system**

### Tracking

Ignoring for the present time the noise and disturbance signals, it can be seen from equations (2.12) and (2.22) that the transfer function of the controlled test rig is

$$F(s) = \frac{G(s)K(s)}{1 + G(s)K(s)} \quad (2.23)$$



Consequently, the performance objective of equation (2.15) requires that  $G(s)K(s) [1 + G(s)K(s)]^{-1}$  has unity magnitude with approximately zero phase over the bandwidth  $0 \leq \omega \leq \omega_{max}$ .

### *Disturbance attenuation and noise insensitivity*

The introduction of feedback has attenuated the disturbance that appears in the plant output by a factor of  $G(s) [1 + G(s)K(s)]^{-1}$  and has attenuated the noise that appears in the plant output by a factor of  $[1 + G(s)K(s)]^{-1}$ . This is an improvement over the open-loop system since both of these factors are usually made to be less than unity by suitable design of  $K(s)$ .

### *Controller design*

From equation (2.23) the following is obtained, which suggests the obvious design approach of specifying  $F(s)$ ,  $G(s)$  is assumed to be known, and then obtaining  $K(s)$ .

$$K(s) = F(s) G^{-1}(s) [1 - F(s)]^{-1} \quad (2.24)$$

However, the choice of  $F(s)$  is essentially arbitrary and if  $G(s)$  has poles or zeros in the right half plane then unstable modes will be built into the controller. Additionally, care must be taken to ensure that the resulting controller is realisable in practice (i.e. gain of the controller asymptotically approaches zero at infinite frequency).

A more acceptable approach to feedback design, and indeed the most common, is to inject gain into the return ratio,  $G(j\omega)K(j\omega)$  such that  $|G(j\omega)K(j\omega)| \gg 1$  and  $|K(j\omega)| \gg 1$ . This gives desirable tracking of the reference signal whilst attenuating the effects of the input disturbance and the noise, as shown below:

(1) Tracking of reference signal, equation (2.23),

$$|G(j\omega)K(j\omega)| \gg 1 \Rightarrow |F(j\omega)| = \left| \frac{G(j\omega)K(j\omega)}{1 + G(j\omega)K(j\omega)} \right| \approx 1 \quad (2.25)$$

(2) Disturbance attenuation, equation (2.22),

$$\begin{matrix} |G(j\omega)K(j\omega)| \gg 1 \\ |K(j\omega)| \gg 1 \end{matrix} \Rightarrow \left| \frac{G(j\omega)}{1 + G(j\omega)K(j\omega)} \right| \approx 0 \quad (2.26)$$

(3) Noise insensitivity, equation (2.22),

$$|G(j\omega)K(j\omega)| \gg 1 \Rightarrow \left| \frac{1}{1 + G(j\omega)K(j\omega)} \right| \approx 0 \quad (2.27)$$

The attractions of working with the return ratio, as opposed to the closed-loop transfer function  $F(s)$ , are that the arbitrary selection of  $F(s)$  is removed from the design procedure and the design of the controller  $K(s)$  is directly based on knowledge of the plant dynamics  $G(s)$ .

### *Stability and shaping near the critical point*

In the discussion thus far the solution to the feedback problem appears to be simply 'use a high gain return ratio'. However, stability of the closed-loop must be ensured and the phase of the return ratio must be taken into account, this requirement is embodied in Nyquist's Stability Theorem, stated below

**Nyquist's Stability Theorem:** The closed-loop system is stable if and only if the number of anticlockwise encirclements of the  $-1 + j0$  point made by the locus of  $G(s)K(s)$ , as  $s$  traverses the Nyquist contour, is equal to the number of poles of  $G(s)K(s)$  with positive real parts.

Most commonly  $G(s)K(s)$  has no unstable poles which means that there should be no encirclements of the  $-1 + j0$  point (also known as the critical point) for stability of the closed-loop system. Exact shaping of  $G(j\omega)K(j\omega)$  near the critical point can be related to desired closed-loop frequency response characteristics and step response characteristics. Many so-called 'classical' design techniques exist for this purpose.

### *Plant uncertainty and stability margins*

In reality, processes and plants are rarely absolutely linear and time invariant, hence there will inevitably be some error in the plant model  $G(s)$ . Denote the actual plant by  $G_{act}(s)$ , then the actual plant may be described by

$$G_{act}(s) = G(s) + \Delta_G(s) \quad (2.28)$$

where  $\Delta_G(s)$  represents the error or uncertainty in the model. With a high gain return ratio, the approximation in equation (2.25) will, in general, still hold for the actual plant, i.e.

$$|(G + \Delta_G)K| \gg 1 \Rightarrow |F| = \left| \frac{(G + \Delta_G)K}{1 + (G + \Delta_G)K} \right| \approx 1 \quad (2.29)$$

where the  $(j\omega)$  has been dropped for brevity. Thus, the feedback loop reduces the effect of the plant uncertainty on tracking performance. Similarly, the disturbance and noise rejection properties of the closed-loop system will be preserved in the presence of the uncertainty. The uncertainty may have some bearing upon the stability of the closed-loop system, for this reason it is usual practice to specify gain and phase margins on the return ratio to allow for the presence of uncertainty.

## 2.7 Multiple actuator tests

Consider the fatigue testing of a four-wheeled road vehicle; at least four actuators are required to provide the road excitation through the vehicle tyres or axle hubs, and often more actuators are used to additionally simulate braking and sideways motion of the vehicle. Another major area of application is the fatigue testing of aeronautical structures where spatially distributed aerodynamic loads constitute a significant part of service loading; by definition, multiple actuators are required to reproduce this loading. Often, several adhesive pads bonded to the aircraft skin are connected to each actuator to distribute tensile load more accurately. In all cases a control system is required to ensure that the applied excitation follows some pre-defined trajectory.

To a lesser or greater degree, there will be interaction or cross-coupling between non corresponding inputs and outputs in a multiple actuator test, this coupling has an impact on the difficulty of the control problem and is described in section 2.7.1. Not surprisingly, just as for single actuator tests, control system objectives are well suited to formulation in the frequency domain as discussed in section 2.7.2. Finally, the control problem presented by a multiple actuator test can be tackled using similar principles to those already established for single actuator tests, these principles are discussed in section 2.7.3.

### 2.7.1 Interaction

In a multiple actuator test, the signals driving the actuators and the resulting output responses measured on the test specimen will be cross-coupled through the dynamics of the test structure. The combined dynamics of the actuators, test frame and the test structure itself are described by a matrix of transfer functions, known as a Transfer Function Matrix (TFM), denoted through the remainder of this section by  $G(s)$  and referred to as the dynamics of the test rig. Let the test rig have  $l$  actuators and  $n$  output responses, e.g. load or displacement, measured at spatially distributed points throughout the structure. The actuator driving signals form a vector of  $l$  inputs  $u(s)$  and the output responses form a vector of  $n$  outputs  $y(s)$  as below,

$$\begin{aligned} u(s) &= \begin{bmatrix} u_1(s) & \dots & u_l(s) \end{bmatrix}^T \\ y(s) &= \begin{bmatrix} y_1(s) & \dots & y_n(s) \end{bmatrix}^T \end{aligned} \quad (2.30)$$

the input-output relationship is given in equation (2.31)

$$y(s) = G(s) u(s) \quad (2.31)$$

The coupling between non corresponding inputs and outputs can be viewed explicitly by writing equation (2.31) in terms of the elements of the input and output vectors and the elements of the TFM, this gives equation (2.32) below

$$\begin{bmatrix} y_1(s) \\ \vdots \\ y_n(s) \end{bmatrix} = \begin{bmatrix} g_{11}(s) & \dots & g_{1l}(s) \\ \vdots & \ddots & \vdots \\ g_{n1}(s) & \dots & g_{nl}(s) \end{bmatrix} \begin{bmatrix} u_1(s) \\ \vdots \\ u_l(s) \end{bmatrix} \quad (2.32)$$

and the general expression for the  $i^{th}$  output is

$$y_i(s) = g_{ii}(s) u_i(s) + \sum_{\substack{j=1 \\ j \neq i}}^l g_{ij}(s) u_j(s) \quad i = 1 \dots n \quad (2.33)$$

The summation term in equation (2.33) represents the contribution to the  $i^{th}$  output from all other non-corresponding inputs. This is the coupling or interaction that gives rise to the multivariable nature of the MIMO test and is clearly undesirable. The extent to which this unwanted interaction is present complicates the control system design. In fact, if there was no interaction present the test could be viewed as a set of independent single actuator tests for which a set of SISO controllers could be designed

using well established classical control techniques. It is, therefore, the very presence of interaction that provides the motivation for pursuing multivariable control techniques.

### 2.7.2 Control system objectives

The controlled test rig has multiple inputs and multiple outputs and so is represented by a TFM  $F(s)$ . The tracking objective of the test is illustrated in Figure 2.10, where there are  $n$  reference inputs and  $n$  output responses, e.g. load or displacement, forming the vectors  $r(t) = [r_1(t) \dots r_n(t)]^T$  and  $y(t) = [y_1(t) \dots y_n(t)]^T$  respectively. The structure of the control system has not been specified, only that  $r(t)$  is the reference vector and  $y(t)$  is the controlled variable, the tracking objective may be formally stated in equation (2.34) where  $\varepsilon$  is a bound on the tracking error

$$r_i(t) - y_i(t) \leq \varepsilon \quad i = 1 \dots n \quad (2.34)$$

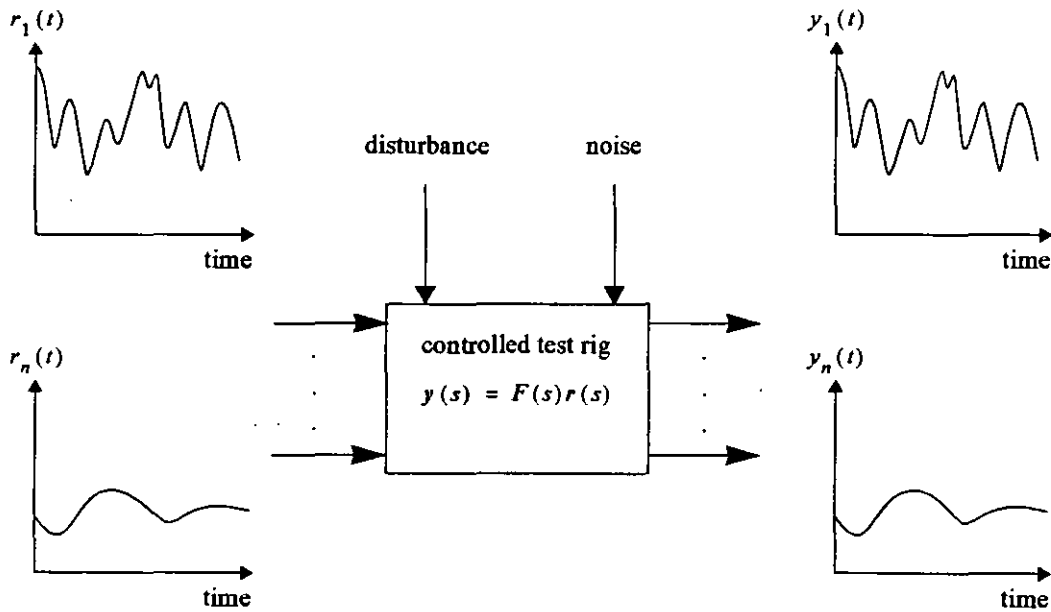


Figure 2.10 Tracking in a MIMO system

Implicit in this statement is the necessary objective of minimal interaction between non-corresponding inputs and outputs. This objective will be developed following the frequency-domain approach adopted in section 2.6.1.

The input - output relationship of the controlled test rig in the frequency domain is given in equation (2.35)

$$y(j\omega) = F(j\omega)r(j\omega) \quad (2.35)$$

and the general expression for the  $i^{th}$  output is given in equation (2.36) where  $f_{ij}$  is the transfer function at the  $i^{th}$  row and  $j^{th}$  column of  $F$ .

$$y_i(j\omega) = f_{ii}(j\omega)r_i(j\omega) + \sum_{\substack{j=1 \\ j \neq i}}^I f_{ij}(j\omega)r_j(j\omega) \quad i = 1 \dots n \quad (2.36)$$

### *Quasi-static loading*

Consider the tracking of a quasi-static signal  $r(t)$  comprising of steady state levels linked by half sine excursions at a radian frequency  $\omega_0$ , then the following is required

$$\begin{aligned} y_i(0) &\equiv r_i(0) \\ y_i(j\omega_0) &\equiv r_i(j\omega_0) \end{aligned} \quad (2.37)$$

and so the summation term in equation (2.36), which represents interaction in the controlled test rig, must be reduced to zero. The TFM  $F(j\omega)$  then becomes diagonal at  $\omega = 0$  and  $\omega = \omega_0$ , the magnitude and phase of the diagonal elements are specified in the tracking objective of equation (2.38).

$$\begin{aligned} |F(j\omega)| &\equiv I \\ \angle f_{ii}(j\omega) &\equiv 0 \end{aligned} \quad i = 1 \dots n \quad \omega = 0, \omega_0 \quad (2.38)$$

### *Sinusoidal loading*

If the sinusoidal excursions occur over a range of frequencies from  $\omega = 0$  to  $\omega = \omega_{max}$ , then the previous requirement can be extended to that of equation (2.39) which applies equally well to purely sinusoidal tests.

$$\boxed{\begin{aligned} |F(j\omega)| &\equiv I \\ \angle f_{ii}(j\omega) &\equiv 0 \end{aligned} \quad i = 1 \dots n \quad 0 \leq \omega \leq \omega_{max}} \quad (2.39)$$

### *Random loading*

When a random load is applied to the structure, the objective of the test is usually to ensure that the power spectral density (PSD) of the measured output is approximately equal to the PSD of the reference input. Suppose the reference inputs

are stochastic processes, then the PSD of the reference vector will be a matrix  $\Phi_{rr}(\omega)$  given below

$$\Phi_{rr}(\omega) = \begin{bmatrix} \phi_{r_{11}}(\omega) & \phi_{r_{12}}(\omega) & \dots & \phi_{r_{1n}}(\omega) \\ \phi_{r_{21}}(\omega) & \phi_{r_{22}}(\omega) & \dots & \phi_{r_{2n}}(\omega) \\ \vdots & \vdots & \ddots & \vdots \\ \phi_{r_{n1}}(\omega) & \phi_{r_{n2}}(\omega) & \dots & \phi_{r_{nn}}(\omega) \end{bmatrix} \quad (2.40)$$

where  $\phi_{r_{ii}}$  is the autospectral density function of  $r_i(t)$  and  $\phi_{r_{ij}}$  is the cross-spectral density function of  $r_i(t)$  and  $r_j(t)$ . The PSD matrix of the output vector is then given in equation (2.41)

$$\begin{aligned} \Phi_{yy}(\omega) &= E[y(j\omega)y^*(j\omega)] \\ \Phi_{yy}(\omega) &= E[F(j\omega)r(j\omega)r^*(j\omega)F^*(j\omega)] \end{aligned} \quad (2.41)$$

and assuming that  $F(j\omega)$  is constant at each frequency point  $\omega$  (which is the case for a linear system) then

$$\begin{aligned} \Phi_{yy}(\omega) &= F(j\omega)E[r(j\omega)r^*(j\omega)]F^*(j\omega) \\ \Phi_{yy}(\omega) &= F(j\omega)\Phi_{rr}(\omega)F^*(j\omega) \end{aligned} \quad (2.42)$$

Writing  $\Phi_{yy}(\omega)$  explicitly in terms of the elements of  $F(j\omega)$ ,  $F^*(j\omega)$  and  $\Phi_{rr}(\omega)$  is extremely unwieldy. However, if interaction is removed from the controlled test rig, i.e.  $F(j\omega)$  is made diagonal, then the following is obtained where for brevity  $f_{ij}$  is written for  $F^{[i,j]}(j\omega)$  and  $\phi_{ij}$  is written for  $\Phi_{rr}^{[i,j]}(\omega)$

$$\Phi_{yy}(\omega) = \begin{bmatrix} f_{11}\phi_{11}f_{11}^* & f_{11}\phi_{12}f_{22}^* & \dots & f_{11}\phi_{1n}f_{nn}^* \\ f_{22}\phi_{21}f_{11}^* & f_{22}\phi_{22}f_{22}^* & \dots & f_{22}\phi_{2n}f_{nn}^* \\ \vdots & \vdots & \ddots & \vdots \\ f_{nn}\phi_{n1}f_{11}^* & f_{nn}\phi_{n2}f_{22}^* & \dots & f_{nn}\phi_{nn}f_{nn}^* \end{bmatrix} \quad (2.43)$$

For the  $(i,j)$  th element of  $\Phi_{yy}(\omega)$  we have

$$\Phi_{yy}^{[i,j]}(\omega) = \Phi_{rr}^{[i,j]}(\omega)F^{[i,i]}(j\omega)F^{[j,j]*}(j\omega) \quad (2.44)$$

Expressing the elements of the TFM  $F(j\omega)$  in polar form thus

$$F^{[p,q]}(j\omega) = |F^{[p,q]}(j\omega)|e^{j\theta_{pq}(\omega)} \quad (2.45)$$

where  $\theta_{pq}(\omega)$  is the phase of the transfer function  $F^{[p,q]}(j\omega)$ , allows  $\Phi_{yy}^{[i,j]}(\omega)$  to be written as

$$\Phi_{yy}^{[i,j]}(\omega) = \Phi_{rr}^{[i,j]}(\omega) |F^{[i,i]}(j\omega)| |F^{[j,j]}(j\omega)| e^{j\{\theta_{ii}(\omega) - \theta_{jj}(\omega)\}} \quad (2.46)$$

and so for approximate equality of the PSDs of the input and output vectors it is required that

$$\begin{aligned} |F^{[i,i]}(j\omega)| &\cong 1 & i &= 1 \dots n \\ \theta_{ii}(\omega) &\cong \theta_{jj}(\omega) & i &\neq j \end{aligned} \quad (2.47)$$

Therefore,  $F(j\omega)$  must be a diagonal matrix whose diagonal elements have a magnitude of approximately unity, the phase of the elements must be identical although not necessarily equal to zero. Thus the requirement for  $F(j\omega)$  is a relaxed version of that derived for quasi-static and sinusoidal tests (where the phases must be made approximately equal to zero).

### *Service-recorded loading*

Consider now the reproduction of a service-recorded load history and let the Fourier transform be  $R(\omega)$ , then the load history can be obtained from an inverse Fourier transform thus

$$r(t) = \frac{1}{2\pi} \int_{-\infty}^{\infty} R(\omega) e^{j\omega t} d\omega \quad (2.48)$$

and for accurate tracking it is required that  $y(t) \cong r(t)$ . Let the Fourier transform of the controlled output be  $Y(\omega)$ , then it is clear that approximate equality of input and output Fourier transforms is required, i.e.

$$Y(\omega) \cong R(\omega) \quad (2.49)$$

However, the input transform  $R(\omega)$  will be modified by the frequency response of the controlled test rig according to equation (2.50)

$$Y(\omega) = F(j\omega) R(\omega) \quad (2.50)$$

Therefore, from comparison of equations (2.49) and (2.50), the requirement placed upon the controlled test rig is identical to that for sinusoidal testing, equation (2.39). The bandwidth of the recorded load history is assumed to be  $\omega_{max}$ .



Clearly, from this analysis, a simple objective for tracking performance objective is expressed in the frequency domain and is applicable to quasi-static, sinusoidal, random and service recorded load excitation, this is stated in equation (2.39). In the next section a feedback control scheme is introduced and the general principles of frequency domain design are discussed.

### 2.7.3 Principles of feedback design

In the discussion of a SISO system in section 2.6.2, the performance of the controlled test rig was determined by the variation of the gain of the return ratio with frequency. Tracking, disturbance rejection and noise attenuation could be achieved with a large gain, whilst paying due attention to stability. In attempting to extend this principle to a multivariable feedback system a significant obstacle is encountered. The gain of the return ratio does not have a single value, but rather is bounded between upper and lower limits. Consequently, the designer has to be satisfied with shaping the upper and lower bounds on the gain of the return ratio in a corresponding manner to the principles discussed in section 2.6.2.

#### *Principal gains*

Consider a matrix  $G$  with complex elements and the input - output relationship  $y = Gu$ , then the 'magnitude' of the input is defined by the vector norm  $\|u\|$  and the 'magnitude' of the output is defined by the vector norm  $\|y\|$ , the 'gain' of the matrix is then

$$\frac{\|y\|}{\|u\|} = \frac{\|Gu\|}{\|u\|} \quad (2.51)$$

However, this 'gain' is not unique and depends upon the direction of the input vector  $u$ , thus the notion of a single gain is replaced by the idea of a range of gains. If the Euclidean vector norm is used, the upper and lower bounds on this range are the known as the maximum and minimum singular values respectively of  $G$ , i.e.

$$\underline{\sigma} \leq \frac{\|Gu\|}{\|u\|} \leq \bar{\sigma} \quad (2.52)$$

The singular values,  $\sigma_i$ , are the positive square roots of the eigenvalues of  $G$  (or if  $G$  is not a square matrix, then  $G^{*T}G$  or  $GG^{*T}$ ).

If  $G$  is now replaced by the frequency response of a TFM  $G(j\omega)$ , the singular values become functions of frequency and are known as *principal gains* and equation (2.52) becomes

$$\underline{\sigma}(j\omega) \leq \frac{\|G(j\omega)u(j\omega)\|}{\|u(j\omega)\|} \leq \bar{\sigma}(j\omega) \quad (2.53)$$

### Feedback structure

The feedback structure is the same as that used in the single actuator analysis and is shown in Figure 2.11, the output is given by

$$y(s) = T(s)r(s) + S(s)G(s)d(s) + S(s)n(s) \quad (2.54)$$

where, as in the SISO discussion,  $S(s)$  is the sensitivity function and  $T(s)$  is the closed-loop transfer function, these are given in equation (2.55) below

$$\begin{aligned} S(s) &= (I + G(s)K(s))^{-1} \\ T(s) &= (I + G(s)K(s))^{-1}G(s)K(s) \end{aligned} \quad (2.55)$$

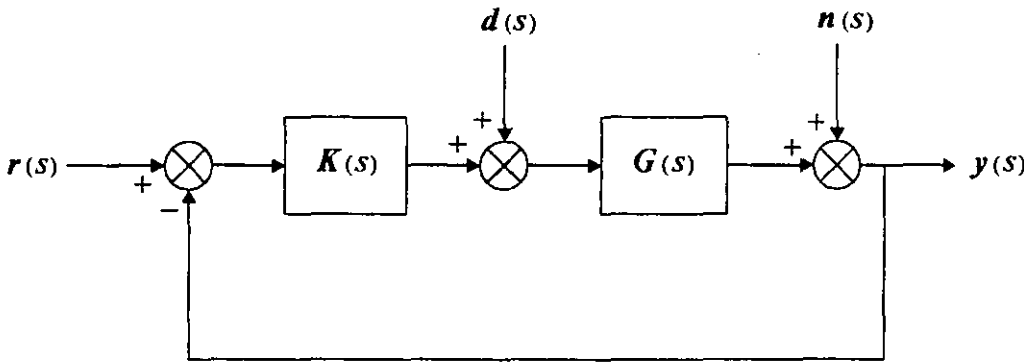


Figure 2.11 Block diagram of a closed-loop MIMO system

For accurate tracking of the desired output response, the principle gains of  $T(j\omega)$  need to be close to unity to ensure that the output  $y(j\omega)$  follows the input  $r(j\omega)$  and is largely unaffected by the direction of  $r(j\omega)$ . For rejecting disturbances and minimising the effect of noise, the principle gains of  $S(j\omega)$  need to be near zero. In the remainder of this section, the following notation will be used:  $\bar{\sigma}(S)$  denotes the maximum principal gain of  $S(j\omega)$ ,  $\underline{\sigma}(S)$  denotes the minimum principal gain of

$S(j\omega)$ ,  $\bar{\sigma}(T)$  denotes the maximum principal gain of  $T(j\omega)$  and  $\underline{\sigma}(T)$  denotes the minimum principal gain of  $T(j\omega)$

### *Shaping the return ratio*

For SISO feedback control, closed-loop performance specifications were easily converted into requirements placed on the magnitude of the open-loop return ratio. The following discussion expresses closed-loop specifications for multivariable systems in terms of the principle gains of the open-loop return ratio. Firstly, the following closed-loop specifications are summarised:

- (1) **Tracking of reference signal:** keep  $\bar{\sigma}(T) \approx 1$  and  $\underline{\sigma}(T) \approx 1$ .

The closed-loop transfer function in equation (2.55) can be written

$$T(s) = I - [I + G(s)K(s)]^{-1} \quad (2.56)$$

and we require that  $T(s) \approx I$  or  $[I + G(s)K(s)]^{-1} \approx 0$ . In other words, we require that

$$\frac{\| [I + G(s)K(s)]^{-1} r(s) \|}{\| r(s) \|} \ll 1 \text{ for all } r(s) \quad (2.57)$$

The maximum principal gain of  $[I + G(s)K(s)]^{-1}$  is of interest since the objective is to minimise the gain of the matrix  $[I + G(s)K(s)]^{-1}$ . Equation (2.57) can also be expressed as

$$\bar{\sigma}\left(\frac{1}{I + G(s)K(s)}\right) \ll 1 \quad (2.58)$$

To proceed at this point it is convenient to express equation (2.58) alternatively in terms of the the minimum principal gain of the matrix argument. To do this, we make use of the following Lemma [32]:

$$\text{Lemma 1: } \bar{\sigma}(Q) = \frac{1}{\underline{\sigma}(Q^{-1})} \quad (2.59)$$

Applying Lemma 1 to equation (2.58) gives

$$\frac{1}{\underline{\sigma}(I + G(s)K(s))} \ll 1 \Rightarrow \underline{\sigma}(I + G(s)K(s)) \gg 1 \quad (2.60)$$

The following triangle inequality (Lemma 2) is required in order to extract from equation (2.60) a requirement on the return ratio  $G(s)K(s)$ .

$$\text{Lemma 2: } \overline{\sigma}(I + Q) \leq 1 + \overline{\sigma}(Q) \quad \underline{\sigma}(I + Q) \leq 1 + \underline{\sigma}(Q) \quad (2.61)$$

Thus,

$$1 \ll \underline{\sigma}(I + G(s)K(s)) \leq 1 + \underline{\sigma}(G(s)K(s)) \quad (2.62)$$

$$\underline{\sigma}(G(s)K(s)) \gg 1$$

Hence, for tracking of the reference signal, the minimum principal gain of the return ratio should be made large.

**(2) Disturbance rejection: keep  $\overline{\sigma}(SG)$  and  $\underline{\sigma}(SG)$  as small as possible**

From equation (2.55), the sensitivity matrix is  $S(s) = [I + G(s)K(s)]^{-1}$  and the requirement is to keep  $S(s)G(s) \approx 0$ . This requirement can be relaxed to keeping  $S(s) \approx 0$  or  $[I + G(s)K(s)]^{-1} \approx 0$ . This requirement is identical to that derived previously for tracking of the reference signal, i.e.,

$$\underline{\sigma}(G(s)K(s)) \gg 1$$

**(3) Noise attenuation: keep  $\overline{\sigma}(S)$  and  $\underline{\sigma}(S)$  as small as possible.**

From equation (2.55), the sensitivity matrix is  $S(s) = [I + G(s)K(s)]^{-1}$  and the requirement is to keep  $S(s) \approx 0$  or  $[I + G(s)K(s)]^{-1} \approx 0$ . This requirement is identical to that derived previously for tracking of the reference signal, i.e.,

$$\underline{\sigma}(G(s)K(s)) \gg 1$$

### Stability

The discussion is not complete as stability of the closed-loop multivariable system must be guaranteed. Return to Figure 2.10, the objective of the control system

is to ensure that the outputs of the plant track desired reference signals, consequently there will usually be the same number of reference inputs as outputs of the plant. Thus, the return ratio  $G(s)K(s)$  will be a square transfer function matrix and the characteristic polynomial of the closed-loop system is

$$|I + G(s)K(s)| \quad (2.63)$$

Let  $|I + G(s)K(s)|$  have  $P$  poles and  $Z$  zeros in the closed-right-half  $s$  plane. Then, as  $s$  traverses the Nyquist contour, the number of clockwise encirclements of the origin made by the mapping  $|I + G(s)K(s)|$  in the  $|I + G(s)K(s)|$  plane is

$$N = Z - P \quad (2.64)$$

or, the change in argument is

$$\Delta \arg (|I + G(s)K(s)|) = -2\pi (Z - P) \quad (2.65)$$

where  $\Delta \arg (.)$  denotes the change in argument as  $s$  traverses the Nyquist contour. For closed-loop stability  $Z$  must be zero. Let  $\lambda_i(s)$  be an eigenvalue of  $G(s)K(s)$ , then it can be shown that  $1 + \lambda_i(s)$  is an eigenvalue of  $I + G(s)K(s)$ . Consequently, since the determinant of a matrix is equal to the product of its eigenvalues,

$$|I + G(s)K(s)| = \prod_i (1 + \lambda_i(s)) \quad (2.66)$$

and so

$$\Delta \arg (|I + G(s)K(s)|) = \sum_i \Delta \arg (1 + \lambda_i(s)) \quad (2.67)$$

Thus, we can infer closed-loop stability by counting the total number of encirclements of the origin made by the loci of  $1 + \lambda_i(s)$ , or, equivalently, by counting the number of encirclements of the  $-1 + j0$  point made by the loci of  $\lambda_i(s)$ . The frequency dependent eigenvalues  $\lambda_i(s)$  are referred to as *characteristic loci* and can be shaped by suitable controller design to meet stability and performance objectives. This approach to multivariable controller design is known as the Characteristic Locus Method and is discussed in chapter 5.

## 2.8 Current control schemes

The simplest method of controlling a multiple actuator test is to treat each actuator input and corresponding test variable output as a separate single-input, single-output (SISO) system and design a controller for each SISO system. This control method is known as Sequential Loop Closure and is widely used in aerospace fatigue testing, particularly where large scale tests are undertaken employing up to several tens of actuators. The attraction of this method is that well understood classical control techniques can be used, notably techniques that obviate the need for a plant model such as on line PID tuning. Markedly different to this approach is Remote Parameter Control (RPC), a technique which emerged in the late 1970s from MTS corporation [3], which tackles the problem of interaction in multiple actuator tests. RPC is employed almost exclusively in the automotive industry for the fatigue testing of suspension systems. Both of these control methods are discussed briefly below.

### 2.8.1 Sequential loop closure

The multivariable nature of the control problem is ignored and the fatigue test is treated as a set of decoupled single actuator tests. This is illustrated in Figure 2.12 where  $G(s)$  is a matrix of transfer functions representing the linear dynamics of the load actuators, test frame and test specimen,  $k_i(s)$  are the SISO loop controllers and  $h_i(s)$  are the transducer dynamics.

The drawbacks of this method are:

- (i) Since commissioning the control system is an iterative process, it can be very time consuming. The control loops are 'tuned' sequentially with only the necessary reference input excited so as to achieve best performance without regard to interaction from other loops. Consequently, when two or more reference signals are excited, interaction may well destroy the performance of any number of control loops.
- (ii) The only means of reducing interaction is to use high gain controllers; the interaction can be viewed as a disturbance and therefore rejected by employing high gain in the controller. However, high gain settings may conflict with stability requirements and performance may be compromised.

Sequential Loop closure is discussed further in chapter 5.

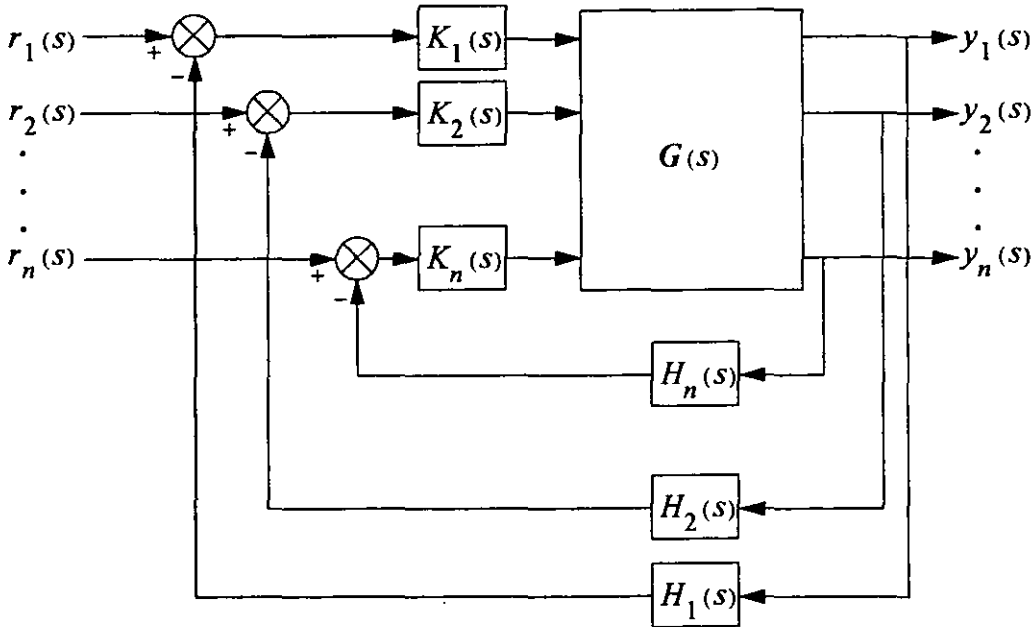
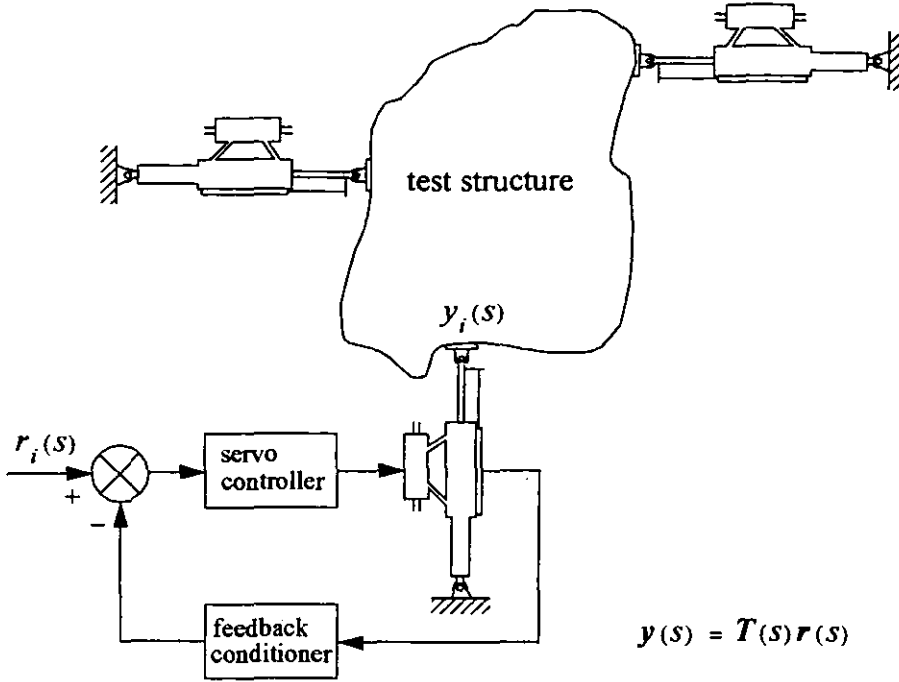


Figure 2.12 Schematic of sequential loop closure control

### 2.8.2 Remote Parameter Control

Multiple actuator tests for producing sophisticated trajectories such as service-recorded load histories require highly accurate tracking and near zero interaction. With sequential loop closure, interaction is a limiting factor which can often render this method unsuitable for such tests. Remote Parameter Control (RPC) tackles the problem of interaction and is a technique commonly used where the output transducers are non-collated with the force inputs. For example, a suspension test where the force excitation is applied at the wheel axles and accelerometers measure acceleration in the chassis. The philosophy of the control scheme is described below.

The test structure is loaded by hydraulic actuators acting under local displacement feedback servo-control. Only one local feedback loop is shown in Figure 2.13 for clarity, the displacement is usually measured by a linear variable differential



**Figure 2.13 Schematic of Remote Parameter Control**

transformer (LVDT). The dynamic response of the complete system from the servo-loop drive signals,  $r_i(s)$ , to the transducer output signals,  $y_i(s)$ , can be modelled by a transfer function matrix  $T(s)$ . Field measurements of the transducer outputs are carried out on an identical structure under service loading conditions. The aim of the test is to reproduce these field measurements on the laboratory structure.

First of all, the frequency response matrix of the system,  $T(j\omega)$ , is identified experimentally. The Fourier transform of the drive signal  $R(\omega)$  is then given by

$$R(\omega) = T^{-1}(j\omega) Y(\omega) \quad (2.68)$$

where  $Y(\omega)$  is the Fourier transform of the field measured output signal. The time-domain drive signal is then determined from an inverse Fourier transform of  $R(\omega)$ . Excitation with the drive signal will, however, not in general result in the desired service recorded load reproduction. This will be due to experimental error in the identification of  $T(j\omega)$  and numerical error in the inversion of  $T(j\omega)$ , particularly at high frequencies where  $T(j\omega)$  can become ill conditioned. To minimise these errors the input drive signal is iteratively adjusted until the test output is acceptably close to the service-recorded output.



The strengths of the RPC method are that experimentally identified frequency responses are required, as opposed to a mathematical model, and a high degree of automation is introduced into the test. However, when the drive signal has been finally adjusted, the structural test proper is executed without any feedback from the output signal. However, the process can be 'slow' at times to converge, during which time an expensive test specimen may accrue a significant level of fatigue damage.

## 2.9 Conclusions

A historical perspective of dynamic structural testing has been given and the need for the dynamic testing of engineering structures has been explained. The scale and diversity of testing is very wide ranging. Also, the load pattern produced on a structure can vary from simple sinusoidal excitation to reproduction of service recorded loading, the latter demanding a sophisticated control scheme. Control system objectives for both single actuator and multiple actuator tests have been discussed, with formulation in the frequency domain yielding a simple objective which lends itself to feedback control system design. Principles of feedback design have been discussed for single actuator tests and carried over to the multivariable control problem posed by a multiple actuator test. The gain of a matrix is not unique but bounded between two values, known as the minimum and maximum singular values of the matrix. With this definition of multivariable gain, the principles established for feedback design of single actuator tests have been extended to multiple actuator tests. Finally, current control systems employed in multiple actuator tests have been briefly discussed.

## Chapter 3

### Test Rigs

#### 3.1 Introduction

Two test rigs have been used in the work described in this thesis, both rigs have two inputs and two outputs and suffer from significant interaction. However, the test rigs are very different in terms of their scale and complexity, type of actuation, measured variable and frequency range of excitation. The first test rig described is the Beam and Vibrator rig, located at Loughborough University of Technology. This is a laboratory scale rig employing electro-dynamic actuation to vibrate a cantilevered steel beam up to a frequency of 160 Hz. The controlled variable on the test rig is displacement of the beam, measured at two locations. This rig has been developed to provide a worst case control problem. The rig is described in section 3.2, the reader is referred to [4] for details.

The second test rig is the Torsion rig, located at British Aerospace, Military Aircraft Division, Brough, Hull. This is a large industrial scale test rig in which servo-hydraulic actuators are used to excite the torsional modes of a steel frame, the controlled variable on the test rig is the force applied by the actuators. The rig was modified to promote a significant control problem and is described in section 3.3.

The two test rigs differ significantly in the 'shape' and bandwidth of their open-loop frequency responses. The Beam and Vibrator rig exhibits a constant gain at steady state with three well damped resonant modes; a bandwidth of 160 Hz was sufficient to identify the frequency response of the rig. By contrast, the Torsion rig exhibits integrator action in its dynamic behaviour, i.e. a type '1' system, with four very lightly damped resonant modes; a bandwidth of only 40 Hz was sufficient to identify the frequency response of the rig. The difference between bandwidths is a reflection of the very different dynamic characteristics of the two rigs.

### 3.2 Beam and Vibrator rig

The Beam and Vibrator test rig consists of a test frame on which a cantilevered steel beam is mounted. The beam is forced into vibration by two electro-dynamic vibrators, one located mid-way along the beam and the other located at the free end of the beam. The forces applied by the vibrators act in a horizontal plane. The vibrators are rigidly fastened to the test frame, their moving coil armatures are connected to the beam with "push-rods". Each vibrator is driven by a power amplifier. Displacement of the beam is measured at the points where the vibrators are attached, using Linear Variable Differential Transformers (LVDTs). A plan view of the rig is presented in Figure 3.1 and a side view of the test rig is presented in Figure 3.2.

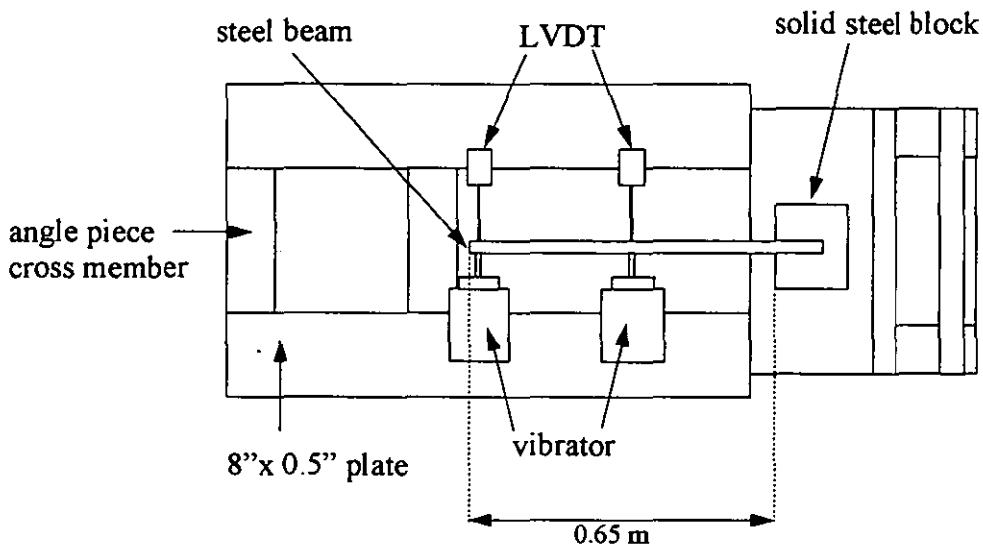


Figure 3.1 Plan view of Beam and Vibrator test rig

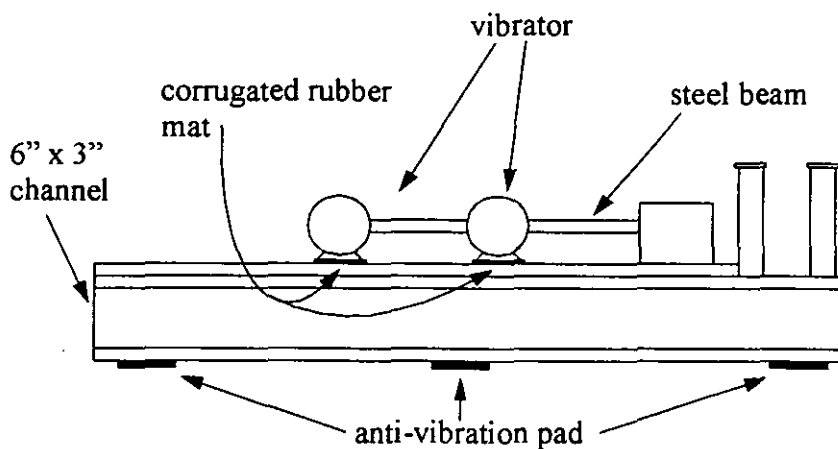


Figure 3.2 Side view of Beam and Vibrator test rig

### 3.2.1 Test frame

The test frame is a mild steel construction weighing approximately 210 Kg, forming a rigid reference upon which to mount the vibrators and clamp the cantilevered beam. However, steel structures have little inherent ability to dissipate energy and so are susceptible to excitation into resonance. In this case, the sources of excitation are vibrations from the body of each vibrator and vibrations transmitted through the floor upon which the frame is located. Consequently, vibration isolators were sought to isolate the vibrators from the test frame and isolate the test frame from the floor. Corrugated rubber mats were used to isolate the vibrators from the test frame and anti-vibration felt pads were used to isolate the test frame from the floor.

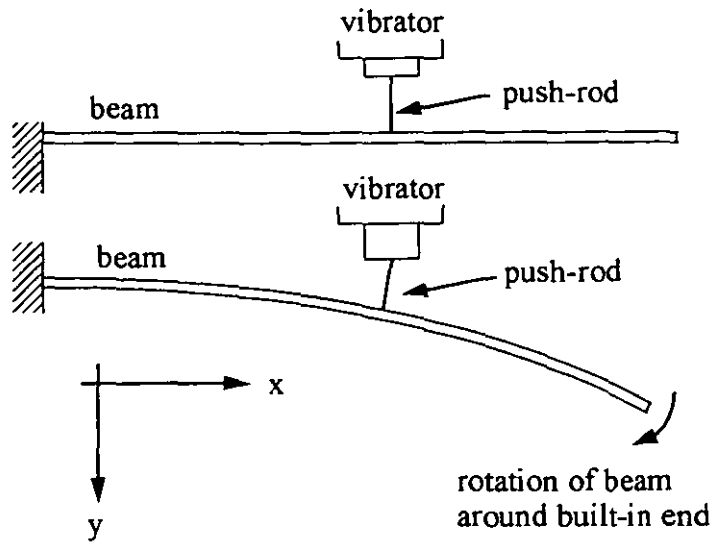
### 3.2.2 Vibrators

The electro-dynamic vibrators used in the test rig are the Ling Dynamic systems 403 series model. The housing of each vibrator contains a permanent magnet, the armature assembly consists of a copper coil located around the central axis of the vibrator, there is a small air gap between the coil and the magnet. The vibrator is excited by an electrical current which is fed to the armature coil. The current in the coil cuts through the magnetic flux in the air gap (provided by the permanent magnet), producing a force which acts along the axis of the vibrator. A flexure arrangement provides axial support for the armature whilst restraining lateral and rotational motion of the armature.

Due to the cantilevered clamping of the beam, the beam will rotate in response to the application of a force, as indicated in Figure 3.3. This causes problems if the vibrator armature is rigidly attached to the beam as it is unlikely that the armature will have the lateral flexibility to permit the necessary movement. The solution adopted with the test rig was to use a special drive rod to connect the armature to the beam. Known as a "push rod", this is a rod which is stiff along its axis (i.e., the direction of excitation), but flexible enough in a lateral direction to accommodate the rotation of the beam.

### 3.2.3 Beam

It was decided to configure the test rig so as to present the worst possible control problem to the engineer. In pursuing this objective, the choice of the stiffness of the beam was investigated by Pratt and Tsavdaras [6] and a value for the stiffness determined which promoted the worst case interaction.



push-rod is stiff along axis of force application (e.i. 'y' axis). Rod is flexible in other directions to permit lateral movement of beam in relation to vibrator

NOTE. Figure is greatly exaggerated

**Figure 3.3 Rotation of beam and "push-rod" solution**

### 3.3 Torsion rig

The torsion rig is essentially a large steel frame structure in which two hollow beams are excited by two hydraulic actuators. The geometry of the frame does not permit rigid body dynamics and the beams undergo angular displacement owing to their finite torsional stiffness. Each actuator is controlled by a force feedback servo-valve, which is driven by an electrical current supplied from the output stage of a PID controller. The force applied by each actuator is measured by a load cell, located at either end of the actuator ram. The signal from the load cell is amplified internally by the PID controller and compared to the external reference or 'command' signal to generate the error signal.

The controller can be used in two modes of operation: (a) 'internal' in which case internal P, P+I or P+I+D action is applied to the error signal, or (b) 'external' in which case the error signal is output to an external controller and the external controller drives the servo-valve through the final output stage of the PID controller. 'Internal' is used in frequency response identification (where P action gives sufficient

performance for the purpose of frequency response identification), 'external' is used when implementing multivariable controllers. A schematic of the rig and control system is given in Figure 3.4

### **3.3.1 Torsion bar assembly**

The steel frame structure will be referred to as the Torsion Bar Assembly or the Torsion Frame, a schematic is given in Figure 3.5. The two long vertical beams, B1 and B2, are pivoted at their bases and connected at their tops by a cross beam, B3; this arrangement allows angular displacement of the vertical beams in response to the torques applied by the hydraulic actuators. The angular displacements are about the polar axis of the beam sections and are due to the finite torsional stiffness of the beams. All beams are constructed of mild steel with hollow cross sections according to BS4848:Part 2, as illustrated in Figure 3.6. The geometrical data are summarised in Table 3.1

The lever arms translate the forces applied by the hydraulic actuators to torques applied to the vertical beams. The vertical beams are welded into the bottom lever arms. The top lever arms, however, are bolted to the vertical beams and can be moved to any desired location along the length of the vertical beams.

At the outset of the work detailed in this thesis, the left hand lever arm was rigidly clamped in a stationary position and the vertical distance between centre lines of the actuators was 1040 mm. However, in this configuration the Torsion rig exhibited natural frequencies beyond the anticipated bandwidth of structural testing (10 Hz). The rig was consequently modified to its current form in an attempt to lower its natural frequencies, thus bringing the undesirable lightly damped resonances of the Torsion rig within the bandwidth of the test signals and promoting a more significant control problem. The left hand lever arm was unclamped, the top lever arms were moved to the positions indicated in Figure 3.5 and a 100 Kg mass was attached to each bottom lever arm. I.e., the stiffness of the rig was reduced and its mass increased, thus reducing the natural frequencies of the Torsion Frame.

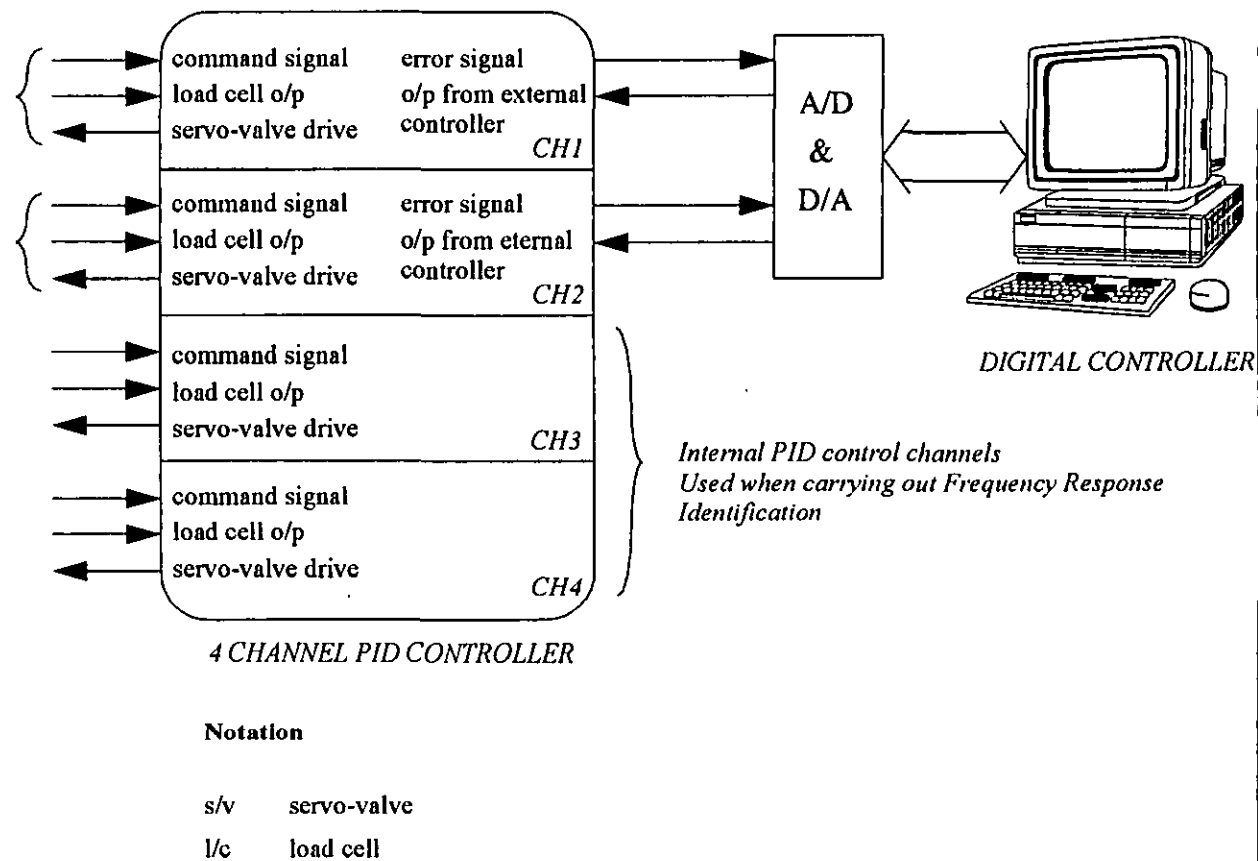
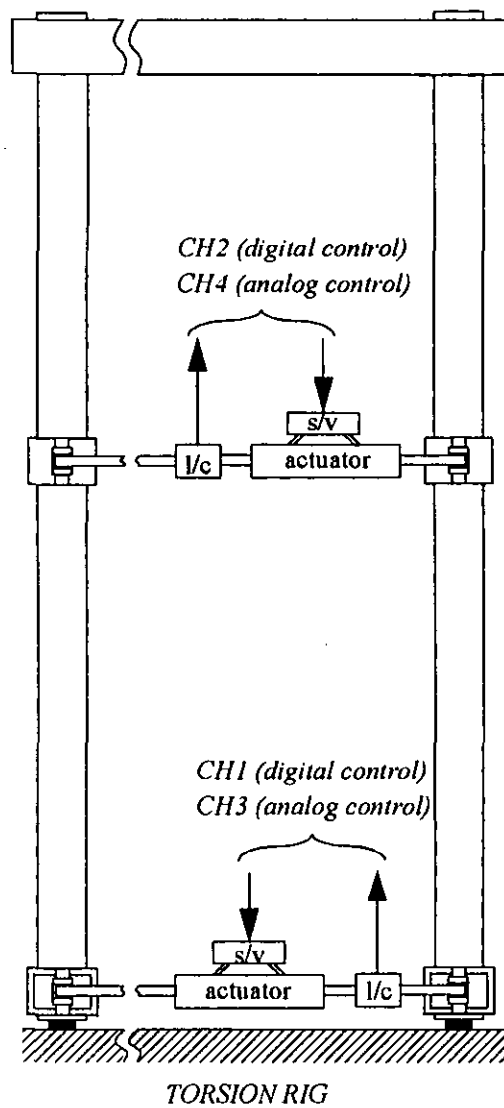


**Figure 3.4** Schematic of the Torsion rig test system

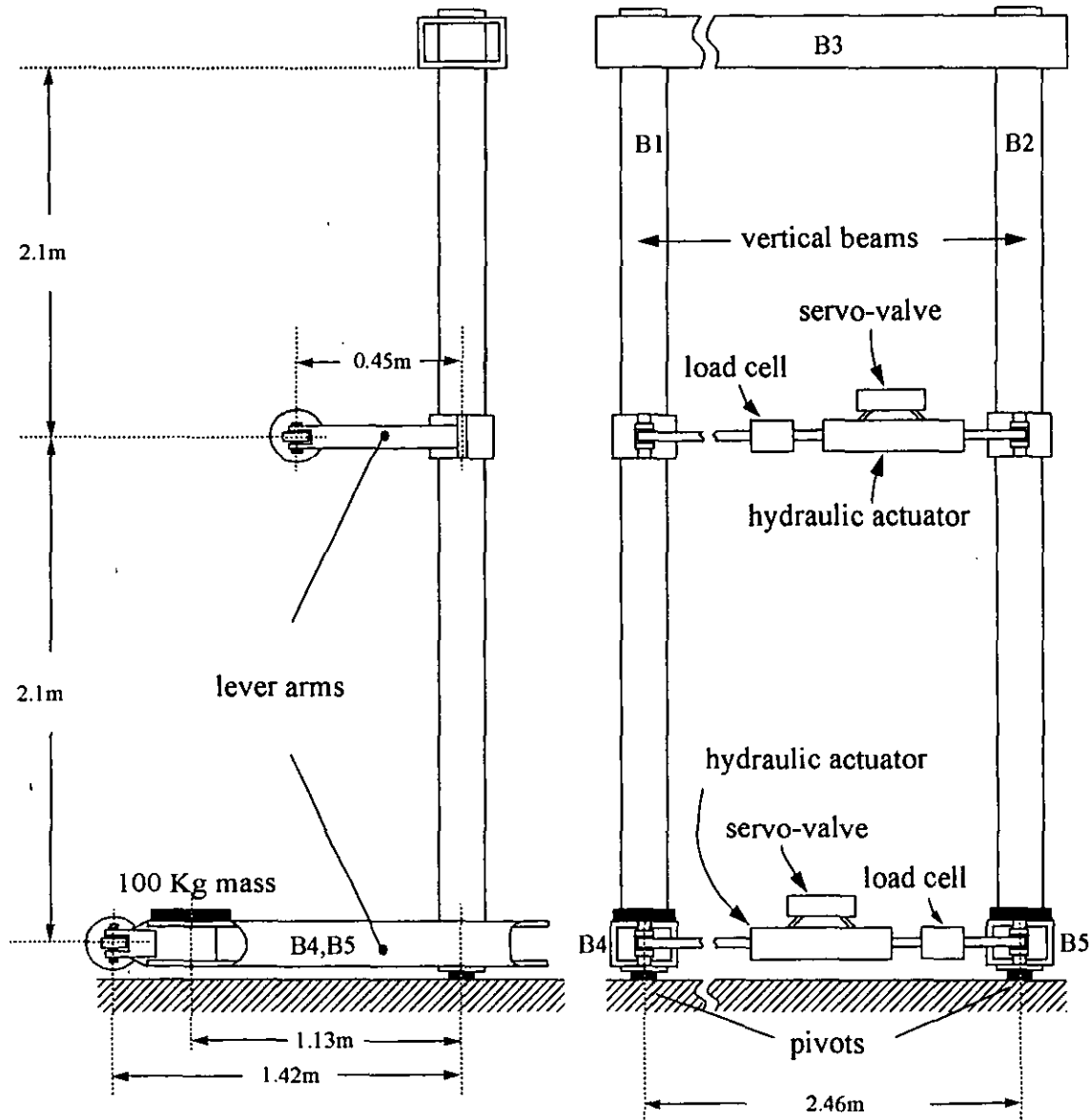


Figure 3.5 Schematic of the Torsion bar assembly (not to scale)



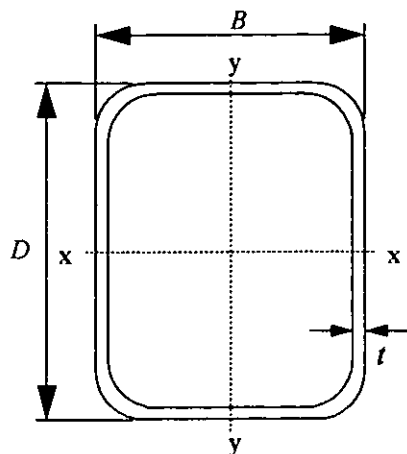


Figure 3.6 Cross-section of Beam

TABLE 3. 1 Beam geometry

Beam ref.	Size $D \times B$ mm	Thickness $t$ mm	Mass per metre Kg/m	Area of section $\text{cm}^2$	Moment of inertia $\text{cm}^4$	Radius of gyration cm	Elastic modulus $\text{cm}^3$	Plastic modulus $\text{cm}^3$	Torsional constant $J$ $\text{cm}^4$	Torsional constant $C$ $\text{cm}^3$
B1, B2	180 x 180	16	81.4	104	4607	6.66	512	634	7339	725
B3	400 x 200	16	142	181	36300 (x-x) 11950 (y-y)	14.2 (x-x) 8.14 (y-y)	1815 (x-x) 1195 (y-y)	2285 (x-x) 1388 (y-y)	28835	2011
B4, B5	300 x 200	16	117	149	17700 (x-x) 9239 (y-y)	10.9 (x-x) 7.89 (y-y)	1180 (x-x) 924 (y-y)	1462 (x-x) 1094 (y-y)	19227	1469

### 3.3.2 Hydraulic system

#### *Servo-valves*

The servo-valves are of the force feedback type and exhibit the square-root flow pressure characteristic of sharp edged orifices, the characteristic is illustrated in Figure 3.7 and described in chapter 4. The load flow axis is normalised against maximum flow through the servo-valve (which occurs with zero load pressure). The servo-valves are specified by the flow rate that occurs with a 1000 psi pressure drop across the valve at 'rated' current, with a supply pressure of 3000 psi - this is the 'rated' flow of the servo-valve. The pressure of the oil supply to the test rig is 3000 psi.

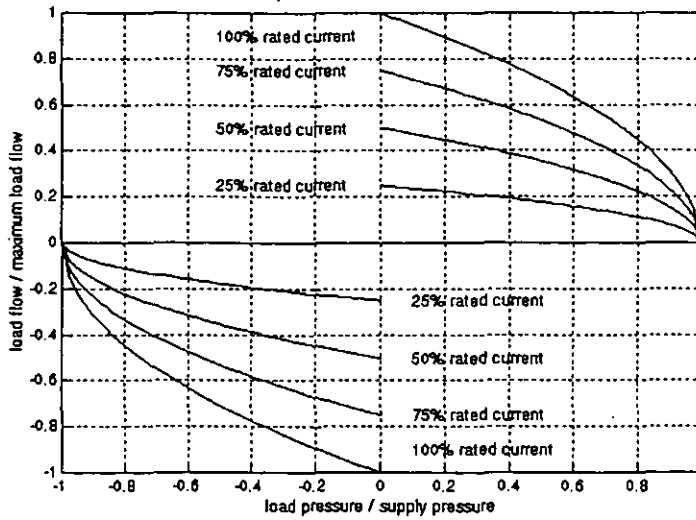


**Figure 3.7 Flow-pressure characteristic of servo-valve**

The frequency response of both servo-valves can be adequately described by a second order transfer function of the form given in equation (3.1) where  $q_L$  is the flow rate and  $i$  is the current.  $K$  is a gain constant which will vary with operating point due to the non linear flow - pressure characteristic of the valve, this is described in chapter 4.

$$\frac{q_L(s)}{i(s)} = \frac{K\omega_T^2}{s^2 + 2\zeta_T\omega_T s + \omega_T^2} \quad (3.1)$$

The relevant data for the servo-valves are summarised in Table 3.2.

**TABLE 3.2 Servo-valve data**

Location on rig	Manufacturer	Type	Serial No.	Rated flow US gpm	Rated current mA	$\omega_T$ rad/s	$\zeta_T$
Bottom	Moog	76-103	GB52	10	15	880	0.9
Top	Moog	73-125	E102	7.5	15	880	0.9

### Actuators

The actuators used on the rig are both double acting, i.e. equal annulus area either side of the piston, the annulus area and stroke length data are summarised in Table 3.3.

TABLE 3.3 Actuator data

Location on rig	Annulus area in <sup>2</sup>	stroke in
Bottom	12.5664	12
Top	9.4248	12

### 3.3.3 Control system

The analog PID controller used in controlling the test rig is manufactured by Kelsey Controllers Ltd. As described in section 3.3, the controller provides voltage to current amplifiers to drive the servo-valves and also provides either analog PID control action, or buffering to an external control system. The controller has four channels which are designated according to Figure 3.4. A schematic of Channels 3 and 4 is presented in Figure 3.8 (note that this Figure is not a circuit diagram), a corresponding block diagram is given in Figure 3.10. The *set point* amplifier provides a DC offset from -10V to +10V, the *input* amplifier applies a gain from 0 to 1 to the reference input or 'Dynamic Command' and the load cell signal is amplified by the *tx span* amplifier. Note that the gain of *tx span* is not calibrated but is adjusted to give a 10V output at maximum load. The *servo gain* amplifier is the error summer (set point + dynamic command - amplified load cell) with a gain from 1 to 20. P, P+I or P+I+D action is then applied to the error signal, which drives the output servo-amplifier. A *balance* input can also be applied to the servo-amplifier input to remove any offset from the control signal. Finally, a high frequency (approx. 200 Hz) and low amplitude sinusoid, known as *dither* can be added to the servo-amplifier input; this will help to overcome stiction in the servo-valve.

The controller can alternatively be used to supply the error signal to an external control system and provide the servo-amplifier drive for an external control system. Channels 1 and 2 are configured in this manner and a schematic is given in Figure 3.9, a corresponding block diagram is given in Figure 3.11

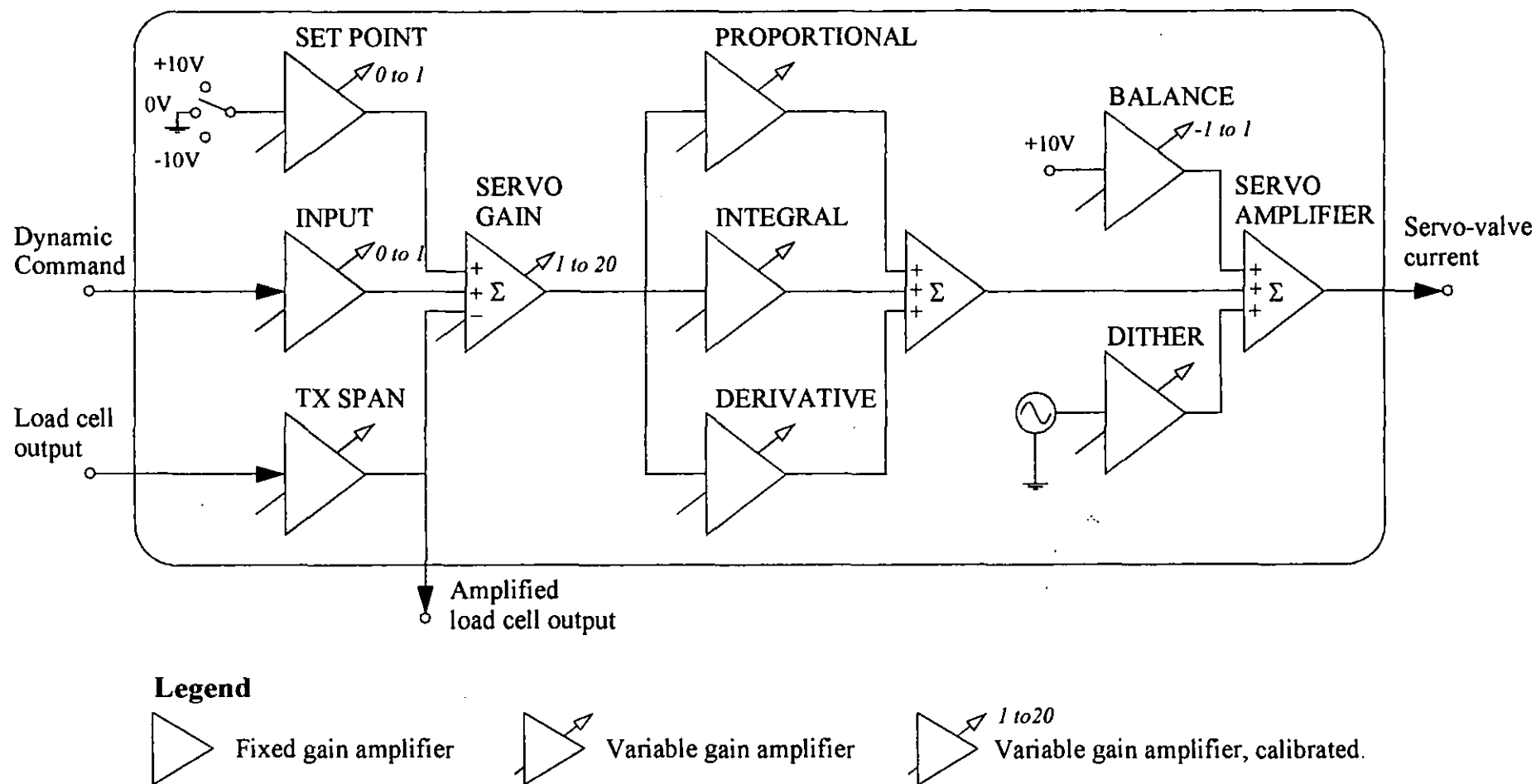


Figure 3.8 Schematic of controller channel with internal PID

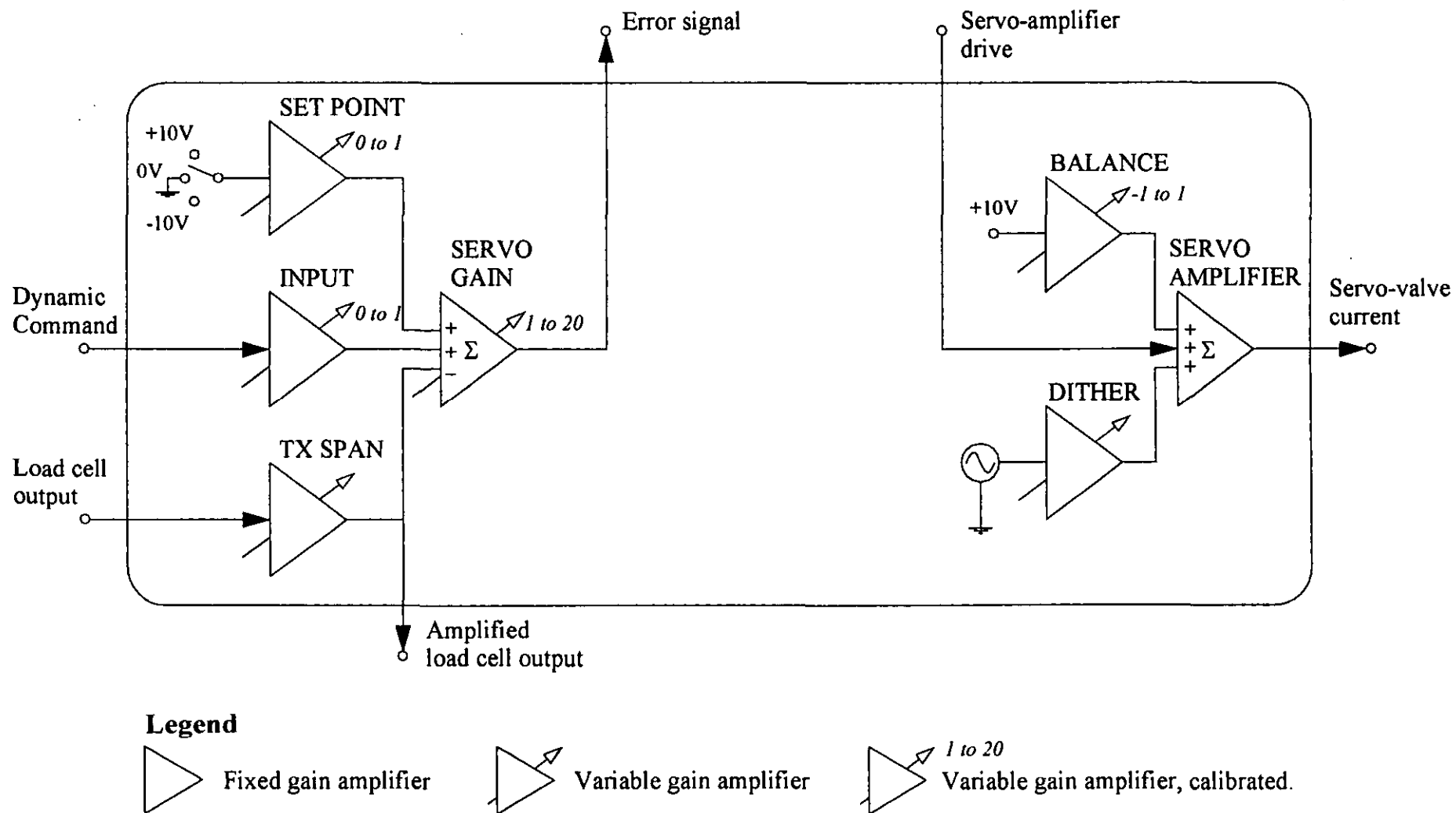
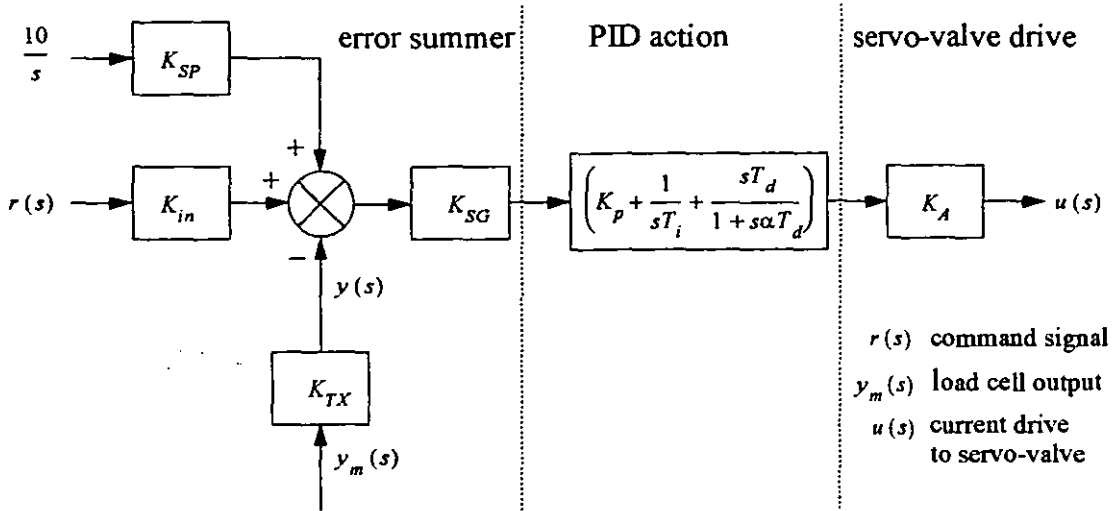
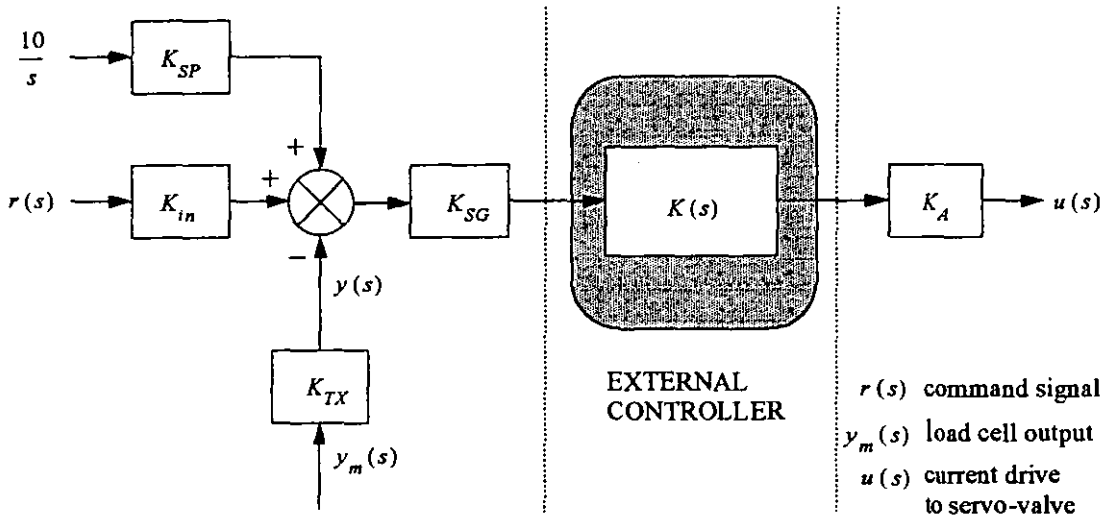


Figure 3.9 Schematic of controller channel configured for external control



**Figure 3.10 Block diagram of controller channel with internal PID action**



**Figure 3.11 Block diagram of controller channel configured for external control**

### 3.3.4 Digital Transfer Function Analyser (DTFA)

This instrument is used to measure the frequency response of a linear system. The analyser excites the system with a sinusoidal signal, the magnitude ratio (or gain) and phase difference between any two voltage signals in the system are measured by the analyser. The frequency and magnitude of the excitation signal are swept over a specified range, the magnitude ratio and phase difference of the measured voltages are measured at each frequency point in the sweep. The measurement itself is a correlation performed over an integer number of cycles of the excitation signal, the measurement is discussed in chapter 7.

The DTFA is shown in Figure 3.12 measuring the frequency response of the command signal to the load applied by the bottom actuator. The command signal to the top actuator is set to zero. The process of frequency response identification using the DTFA is discussed in chapter 7.

The DTFA used in the test system is manufactured by Voltech Ltd., model TF2000, with an accuracy of to within 1%.

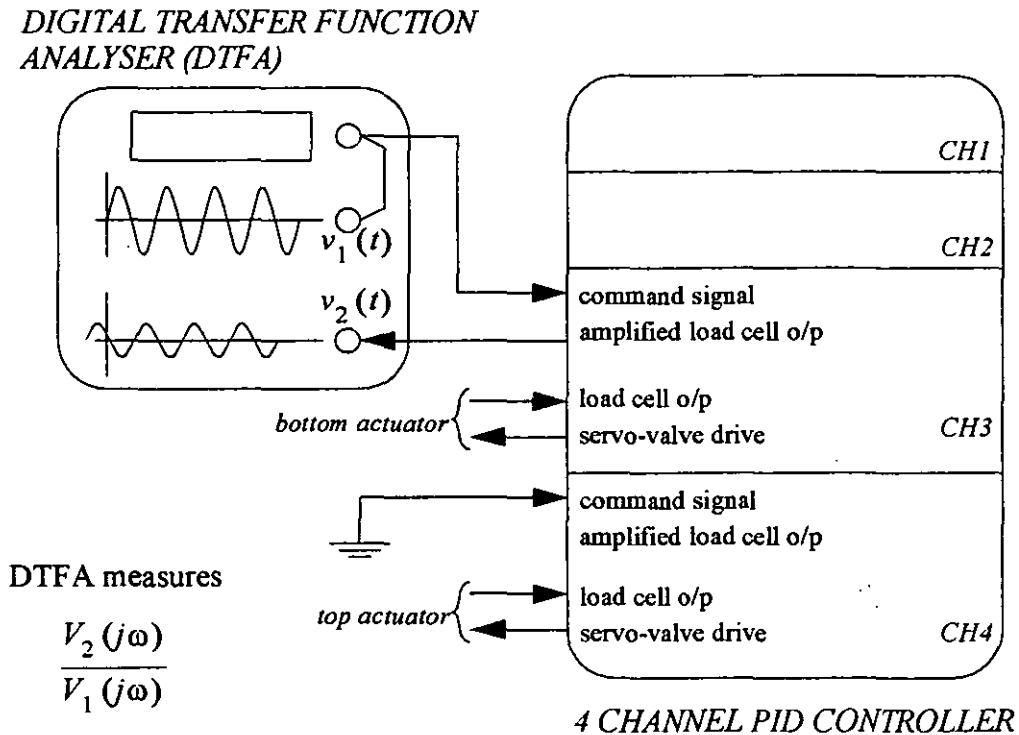


**Figure 3.12 Digital Transfer Function Analyser (DTFA)**

### 3.4 Conclusions

Two test rigs have been used to implement multivariable controllers, these have been described. The test rigs are very different in many ways, notably in terms of their scale and type of actuation. However, both test rigs have been developed to present a genuine multivariable control problem.

## Chapter 4

### Modelling

#### 4.1 Introduction

The purpose of this chapter is to develop an understanding of the dynamic behaviour of a structural test rig (employing servohydraulic actuation) through modelling. Although not required for control system design, models will be developed for SISO and MIMO systems and will be used in the stability analysis detailed in chapter 6. Also, an approximate model of the Torsion rig will be developed for comparison against the experimentally obtained frequency response presented later.

The modelling in this chapter is approached by combining three distinct elements that form the complete model. These are the servo-valve, the hydraulic actuator and the test specimen, described in sections 4.2, 4.3 and 4.4 respectively. Attention is restricted to developing linear models and so the non linear flow-pressure characteristic of the servo-valve is linearised in section 4.2. In section 4.4, a transfer function matrix and a state space model are derived for a test specimen, including a simple formula to calculate the required damping matrix for a desired modal damping ratio.

SISO models for displacement and force (or 'load') output are presented in section 4.5 and evaluated for the case of a test specimen with a single degree of freedom. MIMO models are presented in section 4.6 for displacement and load output and are evaluated for the case of a test specimen with two degrees of freedom. An approximate model of the Torsion rig is given in section 4.6.2.

'Hydraulic' natural frequency and 'hydraulic' damping ratio are commonly referred to in the study of hydraulic systems, these terms are explained in section 4.7 and their variation with operating point is discussed. The validity of the linear modelling approach taken in this chapter is considered in section 4.8, with the aid of a comparative study between an accurate non-linear model and a corresponding linear



approximation. Finally, the pertinent issues in the chapter are summarised in section 4.9.

## 4.2 Servo-valve

The servo-valve is a crucial element in any servo-hydraulic system, converting a low power electrical signal into the motion of a valve, which in turn controls flow and/or pressure of a fluid to a high power hydraulic ram.

Servo-valves can be broadly classified as single stage or two-stage. Single-stage servo-valves consist of a torque motor which directly positions a spool valve. However, torque motors have limited power capability which limits the flow capacity of this type of servo-valve and stability of the servo-valve itself depends on the dynamics of the load [33]. Two-stage servo-valves have a hydraulic pre-amplifier which greatly amplifies the force output of the torque motor to a level sufficient to overcome, to a great extent, flow forces and stiction forces. Also, the two-stage servo-valve exhibits more dependable stability. Two-stage servo-valves employ internal feedback of the output stage and may be classified according to the type of feedback used (spool position, load pressure, load flow). The spool position type of feedback is the most common and can be further sub-classified depending on how the position of the spool is sensed: direct feedback, force feedback and spring centred spool. The force feedback servo-valve was used in the Torsion test rig.

A schematic of a two-stage force feedback servo-valve is shown in Figure 4.1, the servo-valve is shown in it's null position. A positive differential current

$$i(t) = i_1(t) - i_2(t)$$

causes a torque on the armature, moving the flapper to the left, increasing pressure  $P_{1_p}(t)$  and decreasing pressure  $P_{2_p}(t)$  on the spool. The spool then moves to the right until the torque on the armature due to the feedback spring balances the torque on the armature due to the differential current. In this new steady-state condition the flapper has returned to it's initial central position but the spool has taken a new position directly proportional to the differential current.

The relationship between the current and the position of the spool can be described by a transfer function relating differential current to spool position, defined as  $g_{sv}(s)$ , i.e.

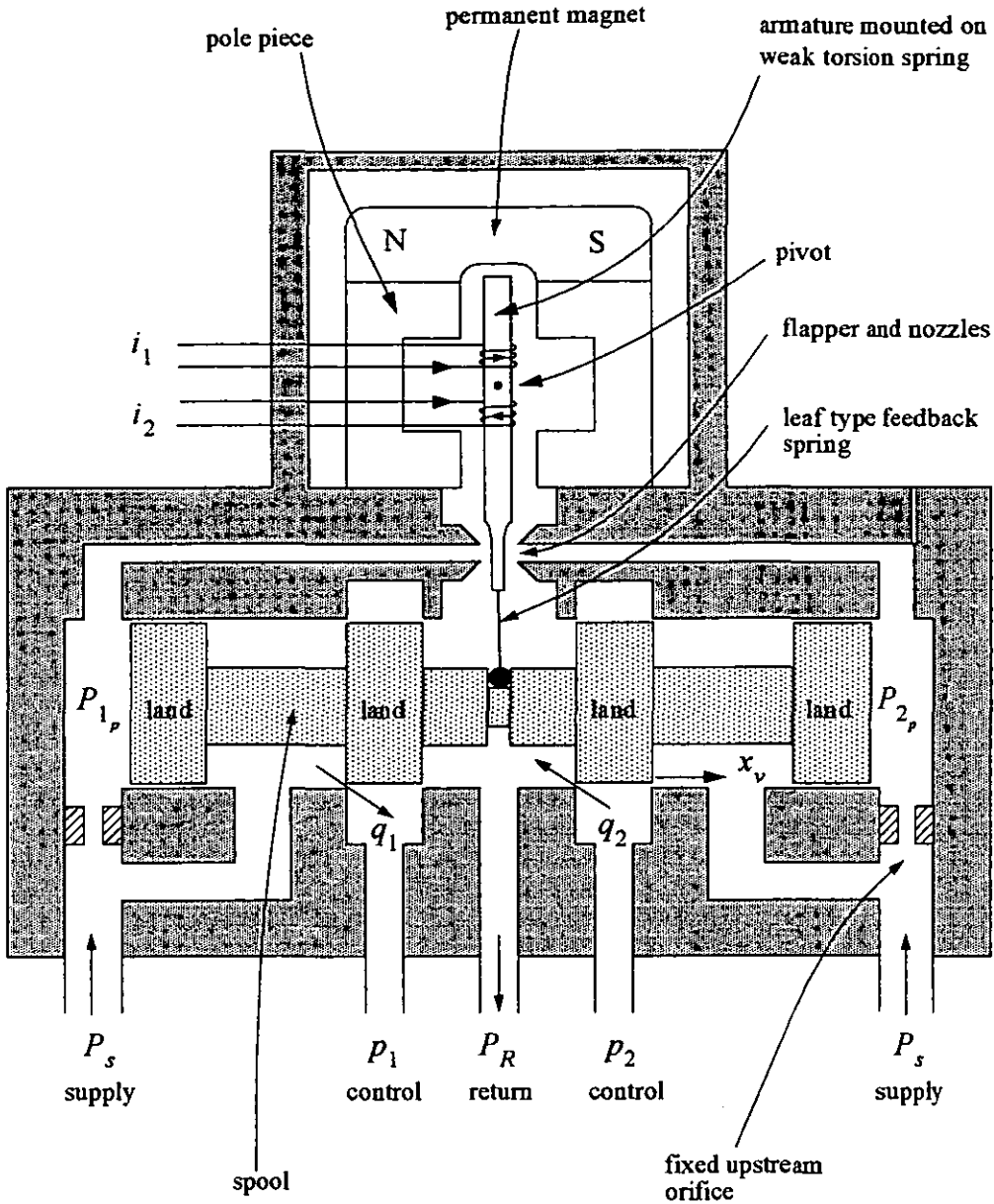


**Figure 4.1 Schematic of a two-stage force feedback servo-valve**

$$x_v(s) = g_{sv}(s) i(s) \quad (4.1)$$

Typically  $g_{sv}(s)$  is a heavily damped quadratic lag as given in equation (4.2).  $K_i$  is the gain,  $\zeta_T$  is the damping ratio and  $\omega_T$  is the natural frequency of the response.

$$g_{sv}(s) = \frac{K_i \omega_T^2}{s^2 + 2\zeta_T \omega_T s + \omega_T^2} \quad (4.2)$$

### 4.2.1 Flow-pressure characteristic

Throughout this chapter, the following assumptions are made with regard to the servo-valve:

- (a) supply pressure  $P_s$  is constant,
- (b) return pressure  $P_R$  is zero,
- (c) the servo-valve has rectangular, symmetrical ports with a width identical to the width of the spool lands (known as 'critically lapped'),
- (d) the oil is incompressible
- (e) there is no leakage across the pistons

The effects of oil compressibility and leakage can be ignored since they have a greater effect in the hydraulic actuator (where they are taken into account in section 4.3). The spool valve with related ports (supply, return,  $p_1$  and  $p_2$  - Figure 4.1) is simply a four-way valve. In appendix 1, the flow-pressure characteristic of the spool valve is derived and is shown to be non linear. Fortunately, this characteristic is easily linearised, as described below.

The pressure drop across the load,  $p_L$ , is defined in equation (4.3). For the remainder of this analysis  $p_L$  will be referred to as the load pressure.

$$p_L = p_1 - p_2 \quad (4.3)$$

Analysis of the pressure drops across the ports of the spool valve gives the following result, detail can be found in appendix 1.

$$P_s = p_1 + p_2 \quad (4.4)$$

Equation (4.3) and equation (4.4) are a simultaneous pair which describe the pressure at each load port as a function of the supply pressure and the load pressure, thus

$$\begin{aligned} p_1 &= \frac{P_s + p_L}{2} \\ p_2 &= \frac{P_s - p_L}{2} \end{aligned} \quad (4.5)$$

Hence, at zero load pressure, the pressure at each load port is exactly one half of the supply pressure.

Define  $q_L$  as the average flow-rate through the valve, given by

$$q_L = \frac{q_1 + q_2}{2} \quad (4.6)$$

Then the flow-pressure characteristic of the servo-valve is derived in appendix 1 and is given in equation (4.7).  $C_d$  is the discharge coefficient of each port orifice (all orifices are identical),  $w$  is the width of the orifice and  $\rho$  is the density of the hydraulic fluid.

$$q_L = x_v (C_d w \sqrt{P_s / \rho}) \sqrt{1 - \text{sgn}(x_v) \frac{p_L}{P_s}} \quad (4.7)$$

By defining  $x_{vm}$  as the maximum displacement of the spool valve from the null position,  $x = x_v / x_{vm}$  as the normalised displacement of the spool valve,  $p = p_L / P_s$  as the normalised load pressure and  $q = q_L / (C_d w x_{vm} \sqrt{P_s / \rho})$  as the normalised load flow rate, the flow-pressure characteristic can be plotted as in Figure 4.2. It can be seen that the flow-rate is linearly related to the position of the spool valve. However, the flow rate is a non-linear function of load pressure.

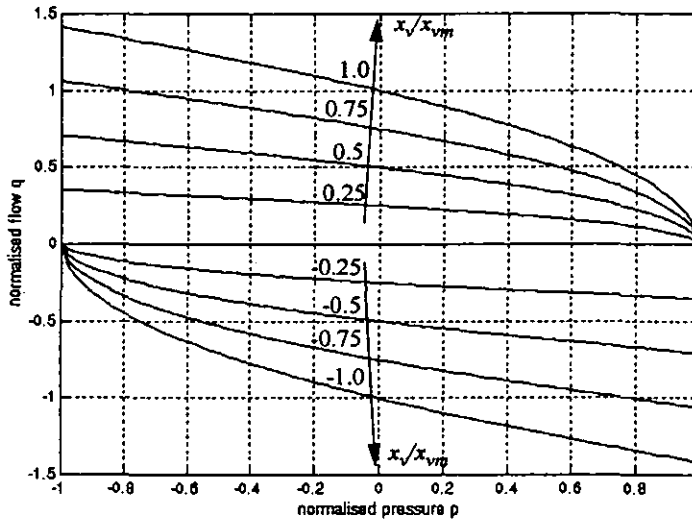


**Figure 4.2 Normalised flow-pressure characteristic of two-stage force feedback servo-valve**

A linear approximation of equation (4.7) can be made by expressing the load flow rate as a Taylor series about an operating point and considering first order derivatives only. Thus

$$\Delta q_L \cong \left. \frac{\partial q_L}{\partial x_v} \right|_O \Delta x_v + \left. \frac{\partial q_L}{\partial p_L} \right|_O \Delta p_L \quad (4.8)$$

where  $O$  denotes the operating point  $\{q_{Lo}, x_{vo}, p_{Lo}\}$  and  $\Delta q_L, \Delta x_v, \Delta p_L$  are excursions around the operating point. The partial derivatives are referred to as the flow gain  $K_q$  and the flow-pressure coefficient  $K_c$  respectively, and are evaluated in equations (4.9) and (4.10).

$$K_q \equiv \left. \frac{\partial}{\partial x_v} (q_L) \right|_O = \frac{C_d w}{\sqrt{\rho}} (P_s - \text{sgn}(x_{vo}) p_{Lo})^{\frac{1}{2}} \quad (4.9)$$

$$K_c \equiv \left. \frac{\partial}{\partial p_L} (q_L) \right|_O = \frac{C_d w |x_{vo}|}{2\sqrt{\rho}} (P_s - \text{sgn}(x_{vo}) p_{Lo})^{-\frac{1}{2}} \quad (4.10)$$

Equation (4.8) is more commonly written

$$\Delta q_L \cong K_q \Delta x_v - K_c \Delta p_L \quad (4.11)$$

From equation (4.9) it can be seen that the flow gain has a maximum value at the null operating point (zero load pressure, zero flow rate and zero displacement of the spool), decreasing as the magnitude of the load pressure increases (at a steady-state operating point,  $x_{vo}$  and  $p_{Lo}$  have the same sign). This reduction in gain will degrade servo-control performance if the servo-valve is operated far from its null position. Conversely, the flow-pressure coefficient is zero at the null operating point and increases with both the displacement of the spool and an increasing magnitude in load pressure. This tends to increase damping in the system (see section 4.7).

It is convenient to relate the linearised flow-pressure characteristic directly to input current and load pressure, combining equations (4.1) and (4.11) gives

$$\Delta q_L \cong K_q g_{sv}(s) \Delta i - K_c \Delta p_L \quad (4.12)$$

The servo-valves used in the Torsion rig are modelled by the quadratic lag given in equation (4.2), the manufacturer's details are referenced in chapter 3 and the transfer function data are summarised in Table 4.1.

**TABLE 4.1 Servo-valve data at 1000 psi drop across valve with 3000 psi supply pressure**

Actuator location on Torsion rig	$K_i K_q \text{ (m}^3 \text{ s}^{-1} \text{ A}^{-1}\text{)}$	$\omega_T \text{ (rad/s)}$	$\zeta_T$
Bottom	0.042	880	0.9
Top	0.0315	880	0.9

The frequency response model of the servo-valve located at the bottom of the Torsion rig is illustrated in Figure 4.3

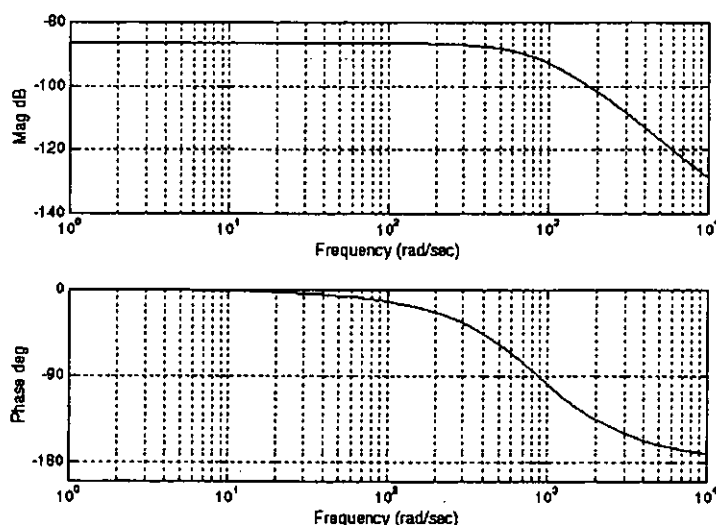


**Figure 4.3 Frequency response of servo-valve**

### 4.3 Hydraulic actuator

A hydraulic actuator converts the flow and pressure of a hydraulic fluid into the linear displacement of a piston. Hydraulic actuators are manufactured in a wide range of sizes and are capable of applying large forces, up to several million newtons of force. Principally, hydraulic actuators are either 'single-acting' or 'double-acting'; the distinction being that in the single-acting type, the ram is connected to only one side of the piston, whilst in the double-acting type, the ram is connected to both sides of the piston. Double-acting actuators were used in the Torsion test rig, a double-acting actuator is illustrated schematically in Figure 4.4.

The volume of oil contained in the body of actuator is far greater than that contained in the body of the servo-valve. Therefore, compressibility of the oil will be taken into account in the following analysis, as will leakage effects across the piston. Denote the volume of the left chamber as  $v_1(t)$  with an initial value of  $V_1$ . Similarly, the volume of the right chamber is  $v_2(t)$  with an initial value of  $V_2$ . Then

$$\begin{aligned} v_1(t) &= V_1 + Ax(t) \\ v_2(t) &= V_2 - Ax(t) \end{aligned} \quad (4.13)$$

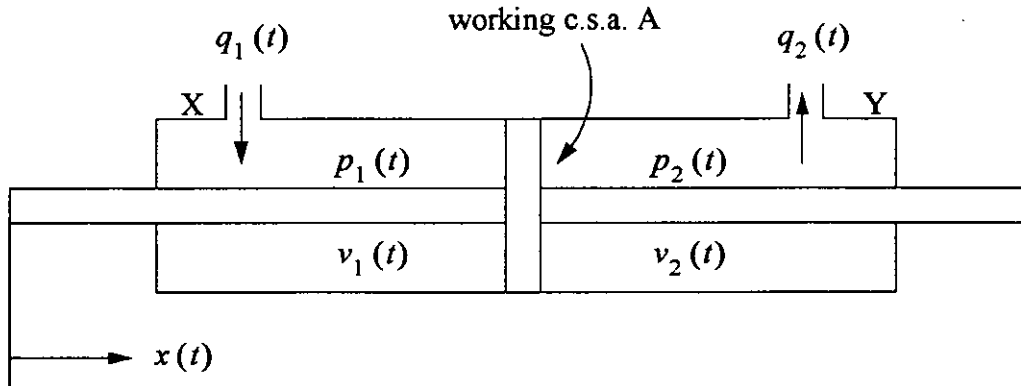


**Figure 4.4 Schematic of double-acting hydraulic actuator**

Denote the flow-rate of oil entering into port  $X$  of the actuator, at a pressure  $p_1(t)$ , by  $q_1(t)$ . Including the effects of compressibility of the oil and leakage across the piston, then  $q_1(t)$  is given below

$$q_1(t) = \frac{d}{dt}v_1(t) + \frac{v_1(t)}{\beta_e} \frac{d}{dt}p_1(t) + K_l(p_1(t) - p_2(t)) \quad (4.14)$$

The first term in equation (4.14) is due to the volumetric displacement of the piston and the second term is due to compressibility of the oil,  $\beta_e$  is the bulk modulus of the oil. The final term in equation (4.14) is leakage flow across the piston and is a linearised approximation of the fundamental orifice flow equation;  $K_l$  is referred to as the leakage coefficient. In quality actuators, the leakage flow is very small and a linear approximation is valid. Similarly, the flow-rate of oil exiting from port  $Y$  of the actuator, denoted by  $q_2(t)$ , at a pressure  $p_2(t)$  is given by

$$q_2(t) = -\frac{d}{dt}v_2(t) - \frac{v_2(t)}{\beta_e} \frac{d}{dt}p_2(t) + K_l(p_1(t) - p_2(t)) \quad (4.15)$$

Defining the average flow-rate as

$$q_l(t) = \frac{q_1(t) + q_2(t)}{2} \quad (4.16)$$

and substituting equations (4.14) and (4.15) into equation (4.16) gives

$$q_l(t) = \frac{1}{2} \left( \frac{d}{dt}v_1(t) - \frac{d}{dt}v_2(t) \right) + \frac{1}{2\beta_e} \left( v_1(t) \frac{d}{dt}p_1(t) - v_2(t) \frac{d}{dt}p_2(t) \right) + K_l p_L(t) \quad (4.17)$$

Now, from equation (4.13)

$$\frac{d}{dt}v_1(t) - \frac{d}{dt}v_2(t) = 2A \frac{d}{dt}x(t) \quad (4.18)$$

and also

$$\begin{aligned} v_1(t) \frac{d}{dt}p_1(t) - v_2(t) \frac{d}{dt}p_2(t) &= V_1 \frac{d}{dt}p_1(t) - V_2 \frac{d}{dt}p_2(t) \\ &+ Ax(t) \left( \frac{d}{dt}p_1(t) + \frac{d}{dt}p_2(t) \right) \end{aligned} \quad (4.19)$$

With a critically lapped and symmetrical four-way servo-valve controlling the actuator, the pressures at ports  $X$  and  $Y$  will be as given by equation (4.5). Substituting for  $p_1(t)$  and  $p_2(t)$  from equation (4.5) into equation (4.19) yields

$$v_1(t) \frac{d}{dt}p_1(t) - v_2(t) \frac{d}{dt}p_2(t) = \frac{V_1 + V_2}{2} \frac{d}{dt}p_l(t) \quad (4.20)$$

Now,  $V_1 + V_2$  is the total volume of oil in the actuator, which will be denoted by  $V_o$ . Substituting equations (4.18) and (4.20) into equation (4.17) gives

$$q_l(t) = A \frac{d}{dt}x(t) + \frac{V_o}{4\beta_e} \frac{d}{dt}p_L(t) + K_l p_L(t) \quad (4.21)$$



#### 4.4 Dynamic representation of the test specimen

The dynamics of the test specimen can be modelled by a lumped parameter system or a finite element system, the former is illustrated in Figure 4.5 where the  $f_i$  are applied forces, the  $x_i$  are displacements, the  $M_i$  are lumped masses and the  $K_i$  are lumped stiffnesses. Both approaches produce a set of linear differential equations and lend themselves well to development of a transfer function matrix or a state space model.

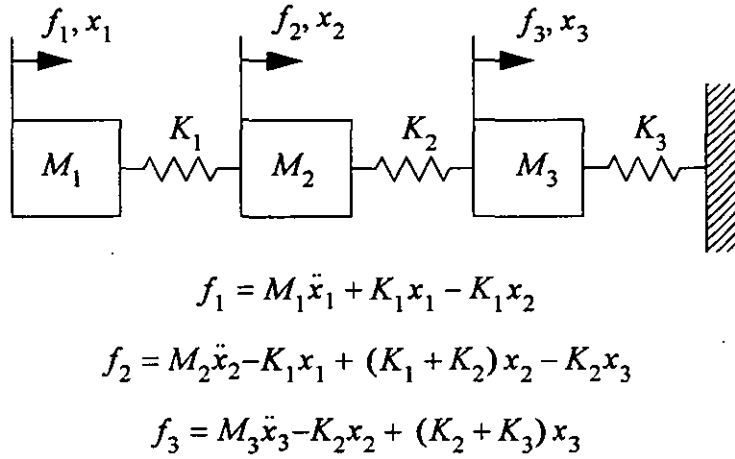


**Figure 4.5** A lumped parameter model of a test specimen

The differential equations can be expressed in matrix form as below where  $f(t)$  is a vector of applied forces and  $x(t)$  is a vector of displacements.

$$f(t) = M\ddot{x}(t) + Kx(t) \quad (4.22)$$

The matrices  $M$  and  $K$  contain the mass and stiffness elements of the distributed system and thus far, it has been assumed that the vibration of the test specimen is undamped. However, in practice there will be some damping present, which can be caused by internal molecular friction or sliding friction. Generally, the mathematical description of these forms of friction is quite complicated and not suitable for vibrational analysis. Therefore, simple viscous damping will be used to model the damping forces acting on the structure of the test specimen. It is also desirable to introduce the damping in such a way as not to alter the natural frequencies of the structure. This is described in section 4.4.1.

In section 4.4.2 a means of deriving a transfer function model of the test specimen is described, the corresponding state space model is determined in section 4.4.3. The state space model has the added attraction of readily providing the velocity

of the structure, this proves useful later in the chapter when building the complete model. Finally, mass, stiffness and damping matrices are determined for the frame of the Torsion rig (or Torsion Bar assembly) in section 4.4.4.

#### 4.4.1 Introducing damping

Viscous damping is easily introduced into the system of differential equations governing the dynamic behaviour of the test structure by adding an additional term  $C\dot{x}(t)$  to equation (4.22), giving equation (4.23) below.

$$f(t) = M\ddot{x}(t) + C\dot{x}(t) + Kx(t) \quad (4.23)$$

Given the mass and stiffness matrices of the test specimen, the objective is to construct a suitable damping matrix  $C$ . Throughout this chapter it is assumed that the vibrational modes of the structure have the same damping ratio  $\zeta$ , in which case the damping matrix can be obtained from the following result (proven in appendix 2).

$$C = 2\zeta M (M^{-1}K)^{\frac{1}{2}} \quad (4.24)$$

#### 4.4.2 Transfer function matrix

A transfer function matrix modelling the dynamics of the structure is obtained very simply. Taking a Laplace transform of equation (4.23) gives

$$f(s) = (s^2M + sC + K)x(s) \quad (4.25)$$

and defining the required transfer function matrix as  $G(s)$ , where  $x(s) = G(s)f(s)$ , then

$$G(s) = (s^2M + sC + K)^{-1} \quad (4.26)$$

#### 4.4.3 State space model

With knowledge of the mass, stiffness and damping matrices of the test specimen, deriving a state space model is straightforward. Define  $z_1(t) = \dot{x}(t)$  and  $z_2(t) = x(t)$ , then equation (4.23) can be written

$$\dot{z}_1(t) = -M^{-1}Cz_1(t) - M^{-1}Kz_2(t) + M^{-1}f(t) \quad (4.27)$$

This allows the following state space model to be written

$$\begin{bmatrix} \dot{z}_1 \\ \dot{z}_2 \end{bmatrix} = \begin{bmatrix} -M^{-1}C & -M^{-1}K \\ I & 0 \end{bmatrix} \begin{bmatrix} z_1 \\ z_2 \end{bmatrix} + \begin{bmatrix} M^{-1} \\ 0 \end{bmatrix} f \quad (4.28)$$

$$x = \begin{bmatrix} 0 & I \end{bmatrix} \begin{bmatrix} z_1 \\ z_2 \end{bmatrix}$$

An attractive feature of the state space model is that the velocity of the structure is readily obtained as it is the state vector  $z_1$ , equation (4.29). This proves to be useful when evaluating the block diagrams in sections 4.5 and 4.6.

$$\dot{x} = \begin{bmatrix} I & 0 \end{bmatrix} \begin{bmatrix} z_1 \\ z_2 \end{bmatrix} \quad (4.29)$$

#### 4.4.4 Torsion rig

A schematic of the Torsion rig was given in Figure 3.5. The frame or 'Torsion Bar Assembly' essentially consists of two steel beams (B1 and B2 in Figure 3.5) which behave as stiff torsional springs under the excitation of the hydraulic actuators. The lever arms and hydraulic actuators can be regarded as discrete masses attached to the beams. A simple lumped parameter representation of the Torsion Bar Assembly was felt to be sufficient to capture its principle dynamic behaviour.

A two-degree-of-freedom lumped parameter model of a single upright beam is shown below in Figure 4.6, the Reaction Beam is assumed to be infinitely stiff. The stiffness elements  $K_1$  and  $K_2$  represent the torsional stiffness of the beam sections above and below the top lever arm respectively. The inertia element  $I_1$  represents the inertia of the beam section above the top lever arm and the inertia of the top lever arm itself. Similarly, the bottom inertia element  $I_2$  represents the inertia of the beam section below the top lever arm and the inertia of the bottom lever arm.

The torsional stiffness of a beam is given by

$$K = \frac{GJ}{l} \quad \text{Nm/rad} \quad (4.30)$$

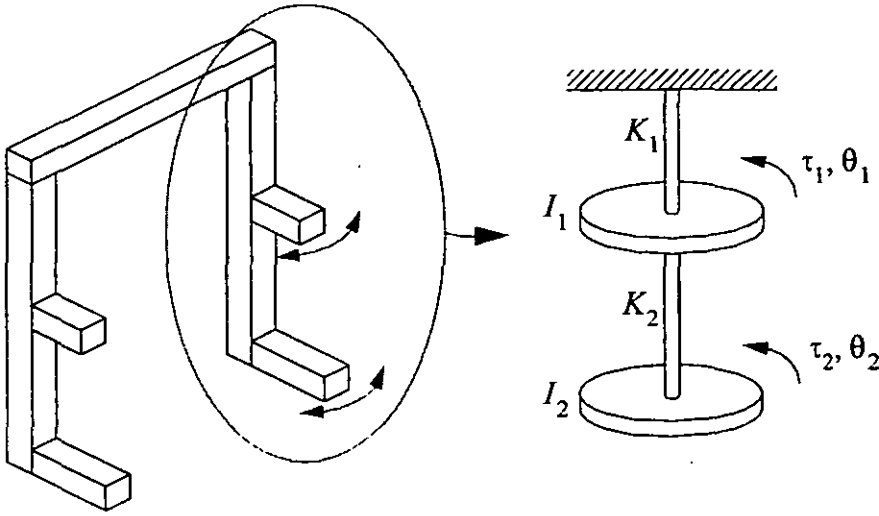


**Figure 4.6 Lumped parameter model of upright beam, Torsion Bar Assembly**

where, for mild steel  $G = 80 \text{ GN/m}^2$  and from Table 3.1, the second moment of area of the beam cross section is  $J = 7339 \times 10^{-8} \text{ m}^4$ . From Figure 3.5,  $I_1 = 2.013 \text{ m}$  and  $I_2 = 1.994 \text{ m}$ . Thus, from equation (4.30),

$$\begin{aligned} K_1 &= 2.92 \quad \text{MNm/rad} \\ K_2 &= 2.94 \quad \text{MNm/rad} \end{aligned} \quad (4.31)$$

Denote the inertia of the section of upright beam above the top lever arm as  $I_{B_1}$  and the inertia of the top lever arm as  $I_{L_1}$ . Similarly, denote the inertia of the section of upright beam below the top lever arm as  $I_{B_2}$  and denote the inertia of the bottom lever arm as  $I_{L_2}$ . Then

$$\begin{aligned} I_1 &= I_{B_1} + I_{L_1} \\ I_2 &= I_{B_2} + I_{L_2} \end{aligned} \quad (4.32)$$

Calculation of  $I_{B_1}$  and  $I_{B_2}$  is straightforward using the following formula

$$I = \rho l J \quad (4.33)$$

where  $\rho$  is the density of the material,  $\rho = 7826.9 \text{ Kg/m}^3$  for mild steel,  $l$  is the length of the beam section along the polar axis and  $J$  is the second moment of area of the cross section about the polar axis. Hence,

$$\begin{aligned} I_{B_1} &= 1.15 \quad \text{Kgm}^2 \\ I_{B_2} &= 1.14 \quad \text{Kgm}^2 \end{aligned} \quad (4.34)$$

Calculation of  $I_{L_1}$  and  $I_{L_2}$  is laborious and is given in appendix 3, the resulting values are given below

$$\begin{aligned} I_{L_1} &= 2.54 \quad \text{Kgm}^2 \\ I_{L_2} &= 212.6 \quad \text{Kgm}^2 \end{aligned} \quad (4.35)$$

It can be seen immediately that the inertia of the bottom lever arm (with an additional 100 Kg mass) is far greater than that of the beam section above it. Consequently, we can reasonably expect the lumped parameter representation to be accurate for the bottom section of the Torsion rig. However, the inertia of the top lever arm is not much greater than that of the related section of beam. Therefore, we can only expect the lumped parameter representation to be an approximation for the top section of the Torsion rig.

Since we have assumed that the reaction beam is infinitely stiff, we can make use of the symmetry of the Torsion Bar Assembly - The whole assembly can be modelled by simply doubling the inertia elements and halving the stiffness elements that have been obtained for an upright beam. From Figure 4.6 and equations (4.31), (4.32), (4.34) and (4.35), the equations of motion of this system then become

$$\tau = I_T \ddot{\theta} + K_T \theta \quad (4.36)$$

where the inertia matrix and stiffness matrix are

$$I_T = \begin{bmatrix} 7.38 & 0 \\ 0 & 427.62 \end{bmatrix} \quad K_T = \begin{bmatrix} 2.93 & -1.47 \\ -1.47 & 1.47 \end{bmatrix} \times 10^6 \quad (4.37)$$

The coordinate system needs to be changed from rotational to translational in order to comply with the work detailed in previous sections. The length of arc  $s$  described by each lever arm is given by the relationship  $s = r\theta$  where  $r$  is the radius of the lever arm from the axis of the upright beam to the attachment point of the hydraulic actuator. For small angular displacements, this relationship can be approximated by  $x = r\theta$  where  $x$  is the displacement of the actuator piston. By defining a matrix of radii

$$R = \begin{bmatrix} r_1 & 0 \\ 0 & r_2 \end{bmatrix} \quad (4.38)$$

where  $r_1 = 0.45$  and  $r_2 = 1.42$  are taken from Figure 3.5, equation (4.36) can be transformed thus

$$f = M\ddot{x} + Kx \quad (4.39)$$

where

$$M = R^{-1} I_T R^{-1} = \begin{bmatrix} 36.94 & 0 \\ 0 & 212.97 \end{bmatrix} \quad (4.40)$$

$$K = R^{-1} K_T R^{-1} = \begin{bmatrix} 14.67 & -2.32 \\ -2.32 & 0.73 \end{bmatrix} \times 10^6$$

The Torsion Bar Assembly is intrinsically lightly damped, a global damping ratio of 0.01 was assumed and a corresponding damping matrix  $C$  generated using equation (4.24):

$$C = \begin{bmatrix} 464.63 & -69.09 \\ -69.09 & 186.91 \end{bmatrix} \quad (4.41)$$

A transfer function matrix was determined using equation (4.26) and is given below

$$G(s) = \begin{bmatrix} g_{11}(s) & g_{12}(s) \\ g_{21}(s) & g_{22}(s) \end{bmatrix}$$

$$g_{11}(s) = \frac{212.97s^2 + 186.91s + 730000}{d(s)}$$

$$g_{22}(s) = \frac{36.94s^2 + 464.63s + 14670000}{d(s)} \quad (4.42)$$

$$g_{12}(s) = g_{21}(s) = \frac{69.09s + 2320000}{d(s)}$$

$$d(s) = 7.8669 \times 10^3 s^4 + 1.0586 \times 10^5 s^3 + 3.1508 \times 10^9 s^2 + 2.7609 \times 10^9 s + 5.3499 \times 10^{12}$$

All transfer functions within the matrix have the same denominator polynomial,  $d(s)$ , and also note that the off-diagonal transfer functions  $g_{12}(s)$  and

$g_{21}(s)$  are identical. The poles and zeros of the transfer function elements are summarised in Table 4.2. The model represents a structure with two lightly damped vibrational modes, at approximately 41.3 rad/s and 631.5 rad/s, the complex zeros in the diagonal transfer functions represent anti-resonances in these responses. Thus,  $g_{11}(s)$  exhibits an anti-resonance at approximately 59 rad/s; however, in the case of  $g_{22}(s)$  there is a virtual pole-zero cancellation and the higher frequency resonance at

TABLE 4.2 Poles and zeros of the model of Torsion bar assembly

Transfer function	Poles	Zeros
$g_{11}(s)$	$-0.413 \pm j41.293$ , $-6.315 \pm j631.5$	$-0.439 \pm j58.67$
$g_{12}(s)$	$-0.413 \pm j41.293$ , $-6.315 \pm j631.5$	$-33640$
$g_{21}(s)$	$-0.413 \pm j41.293$ , $-6.315 \pm j631.5$	$-33640$
$g_{22}(s)$	$-0.413 \pm j41.293$ , $-6.315 \pm j631.5$	$-6.2891 \pm j630.1$

approximately 631.5 rad/s will be virtually cancelled by the anti-resonance at 630.1 rad/s. The resonant and anti-resonant behaviour of the model is illustrated in the frequency responses presented in Figures 4.7 to 4.9.

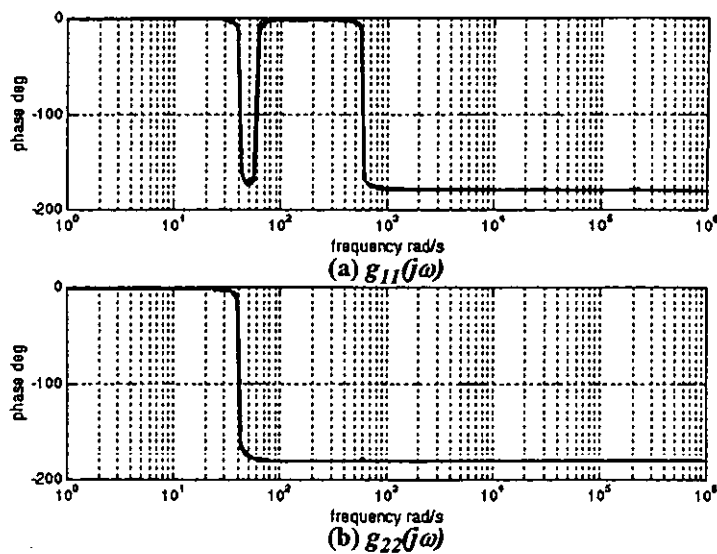
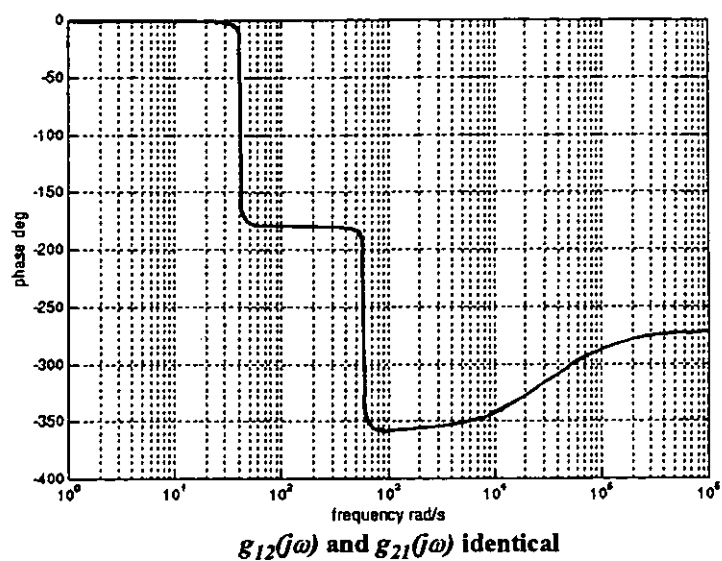
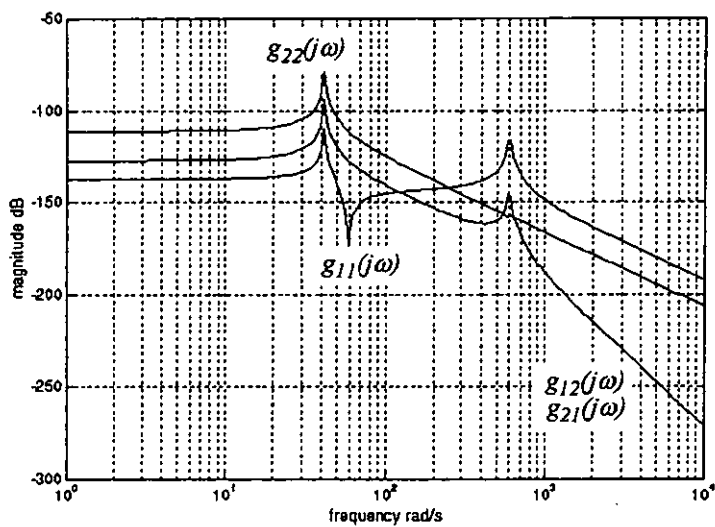


Figure 4.7 Frequency response of the phase of the Torsion bar assembly ( $g_{11}(j\omega)$  and  $g_{22}(j\omega)$ )



**Figure 4.8** Frequency response of the phase of the Torsion bar assembly ( $g_{12}(j\omega)$  and  $g_{21}(j\omega)$ )



**Figure 4.9** Frequency response of the magnitude of the Torsion bar assembly model

4.5 Linear SISO model

A schematic of a SISO system is given below in Figure 4.10, where the test specimen is represented by a single degree-of-freedom mass-spring-damper



arrangement. This simple system serves to illustrate the fundamental characteristics of a hydraulically actuated structural test system. Based on this schematic, block diagrams and transfer functions are derived for both displacement output and force (or load) output. The block diagrams, however, are equally applicable to a test specimen with multiple degrees of freedom.

Note that since the flow-pressure characteristic of the servo-valve is linearised about an operating point  $\{q_{Lo}, x_{vo}, p_{Lo}\}$ , the transfer functions derived in this section relate to excursions around the chosen operating point. The notation ' $\Delta$ ' is used throughout to emphasize this point.

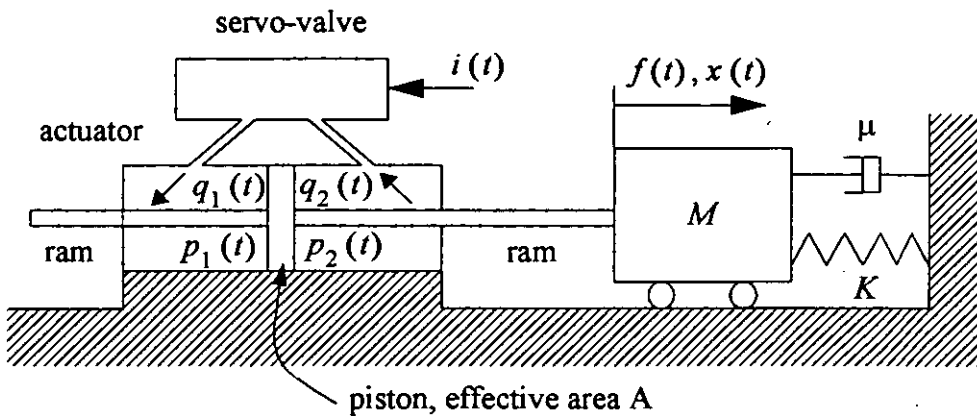


**Figure 4.10 Schematic of SISO system**

Transfer function models are built by combining the relationships described in the previous sections regarding the displacement of the spool, the linearised flow-pressure characteristic of the servo-valve, the flow of fluid through the hydraulic actuator and the dynamics of the test specimen. The transfer functions are written explicitly for the specific case of a single degree-of-freedom test specimen, shown in Figure 4.10.

In developing the models, transfer functions are used throughout and a block diagram is presented below from which the model can be built, using a suitable software tool such as MATLAB. The transfer function  $g_p(s)$  relates the displacement of the test specimen to the force applied by the actuator, the transfer function  $sg_p(s)$  relates the velocity of the test specimen to the force applied by the actuator. The block diagram is presented in Figure 4.11 and is used for both displacement and force output - the final  $g_p(s)$  block is omitted in the force output system. Also, the transfer functions  $g_p(s)$  and  $sg_p(s)$  may be replaced by their state space equivalents if so desired, equations (4.28) and (4.29).

Assuming that the ram is infinitely stiff, then

$$\Delta x(s) = g_p(s) \Delta f(s) \quad (4.43)$$

Taking Laplace transforms of the actuator dynamics, equation (4.21), gives

$$\Delta q_L(s) = sA\Delta x(s) + \frac{1}{K_B} (sV_o + K_B K_I) \Delta p_L(s) \quad (4.44)$$

where  $K_B = 4\beta_e$ . Similarly, the linearised flow-pressure characteristic of the servo-valve can be written

$$\Delta q_L(s) = K_q \Delta x_v(s) - K_c \Delta p_L(s) \quad (4.45)$$

From equations (4.43), (4.44), (4.45) and including the transfer function relating servo-valve current to displacement of the spool valve, the block diagram in Figure 4.11 is derived. Note that the state space equivalent of  $g_p(s)$  is given in equation (4.28) and that the state space equivalent of  $sg_p(s)$  given in equations (4.28) and (4.29).

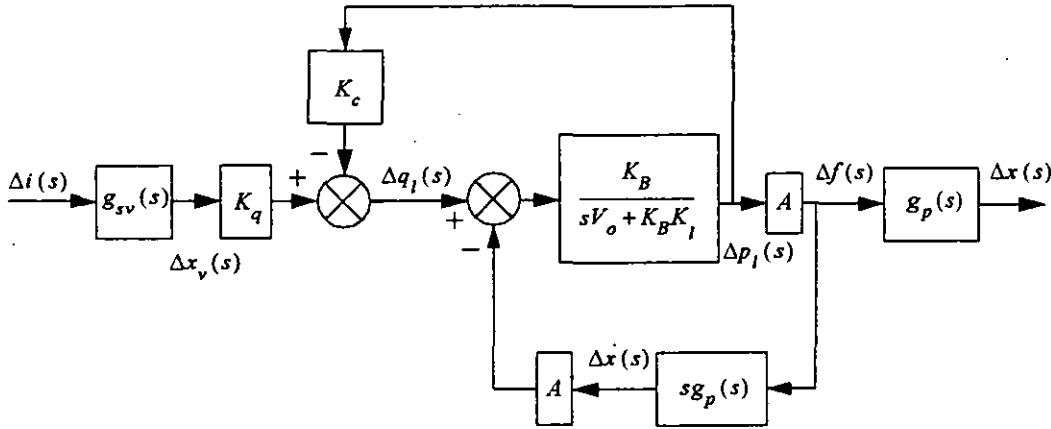


Figure 4.11 Block diagram for SISO plant

#### 4.5.1 Displacement output

From Figure 4.11 the following transfer function can be derived

$$\frac{\Delta x}{\Delta i} = K_q K_B A \frac{g_{sv}(s)}{sA^2 K_B + \frac{\alpha(s)}{g_p(s)}} \quad (4.46)$$

where the leakage coefficient and the flow-pressure coefficient are combined into a single coefficient  $K_{ce}$ , i.e.

$$K_{ce} = K_l + K_c \quad (4.47)$$

and

$$\alpha(s) = sV_o + K_B K_{ce} \quad (4.48)$$

For the specific case of a single degree-of-freedom test specimen, Figure 4.10, the equation of motion can be written by inspection and a Laplace transform taken, giving

$$g_p(s) = \frac{1}{s^2 M + s\mu + K_s} \quad (4.49)$$

Substituting equations (4.2), (4.48) and (4.49) into equation (4.46) gives

$$\frac{\Delta x(s)}{\Delta i(s)} = \frac{\frac{K_l K_q K_B A \omega_T^2}{MV_o}}{(s^2 + 2\zeta_T \omega_T s + \omega_T^2) \left( s^3 + s^2 \left( \frac{\mu}{M} + \frac{K_{ce} K_B}{V_o} \right) + s \left( \frac{K_s}{M} + \frac{K_B A^2}{MV_o} + \frac{\mu K_{ce} K_B}{MV_o} \right) + \frac{K_{ce} K_s K_B}{MV_o} \right)} \quad (4.50)$$

The poles of this transfer function are listed below in Table 4.3 with the model data taken from Table 4.4, the hydraulic data are taken from the Torsion rig and the test specimen characterises a structure with a natural frequency below 10 Hz (i.e. within the bandwidth of some structural tests). The servo-valve contributes a pair of under damped poles (although with a damping ratio close to unity) as prescribed whilst the combination of the actuator and the test specimen gives rise to a pair of very lightly damped poles, the latter is described in section 4.7. A simple pole close to the origin of the complex plane is also obtained, arising from the integrating relationship between the displacement of the piston and the flow rate through of the actuator (i.e. the first term in equation (4.21) expressed in integral form).

**TABLE 4.3 Poles of transfer function model of SISO displacement system**

Poles	Description
$-792 \pm j383.5$	poles of servo-valve
$-1.05 \pm j716.5$	second order dynamics due to the combination of hydraulic actuator and specimen
$-0.005$	simple pole due to the integrator like action of the hydraulic actuator

The frequency response of this transfer function is plotted in Figure 4.12 with the data listed in Table 4. 4.

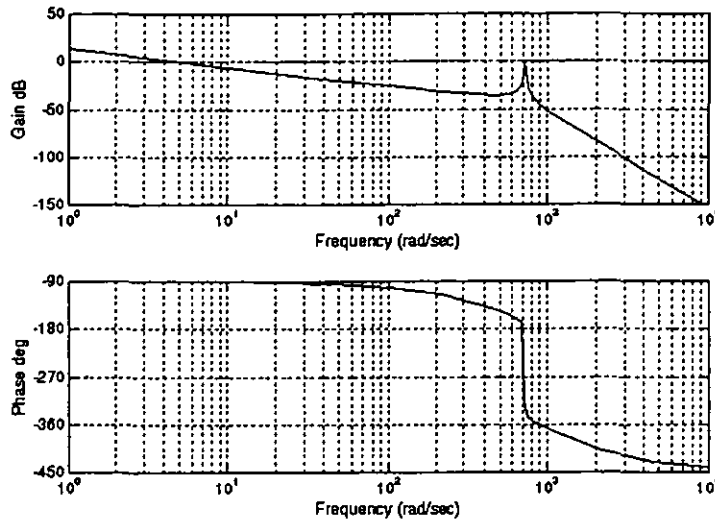


**Figure 4.12** Frequency response of a SISO displacement system

**TABLE 4. 4** Model data for SISO system

$K_{ce}$	$1 \times 10^{-13} \text{ m}^5/\text{Ns}$
$K_B$	$4 \times 1.86 \times 10^9 \text{ N/m}^2$
$K_i K_q$	$0.042 \text{ m}^3/\text{sA}$
$A$	$0.008107 \text{ m}^2$
$V_o$	$0.002469 \text{ m}^3$
$\omega_T$	$880 \text{ rad/s}$
$\zeta_T$	$0.9$
$M$	$392.34 \text{ Kg}$
$K_s$	$3.19 \times 10^6 \text{ N/m}$
$\mu$	$706.22 \text{ Kg/s}$

### 4.5.2 Load output

From Figure 4.11 the following transfer function is obtained

$$\frac{\Delta f(s)}{\Delta i(s)} = K_q K_B A \frac{g_{sv}(s)}{\alpha(s) + s A^2 K_B g_p(s)} \quad (4.51)$$

As in the displacement-control system, equations (4.2), (4.48) and (4.49) can be substituted into equation (4.51) to evaluate the transfer function for the single degree-of-freedom test specimen illustrated in Figure 4.10. This gives

$$\frac{\Delta f(s)}{\Delta i(s)} = \frac{\frac{K_i K_q K_B A \omega_T^2}{V_o} \left( s^2 + s \frac{\mu}{M} + \frac{K_s}{M} \right)}{(s^2 + 2\zeta_T \omega_T s + \omega_T^2) \left( s^3 + s^2 \left( \frac{\mu}{M} + \frac{K_{ce} K_B}{V_o} \right) + s \left( \frac{K_s}{M} + \frac{K_B A^2}{MV_o} + \frac{\mu K_{ce} K_B}{MV_o} \right) + \frac{K_{ce} K_s K_B}{MV_o} \right)} \quad (4.52)$$

The poles of this transfer function are identical to those of the displacement output system, Table 4.3, since both transfer functions have the same denominator. In addition, the poles of the transfer function describing the test specimen, equation (4.49), appear as zeros in equation (4.52). With the model data taken from Table 4. 4, the zeros are located at  $-0.9 \pm j90$  and the frequency response of equation (4.52) is plotted in Figure 4.13.

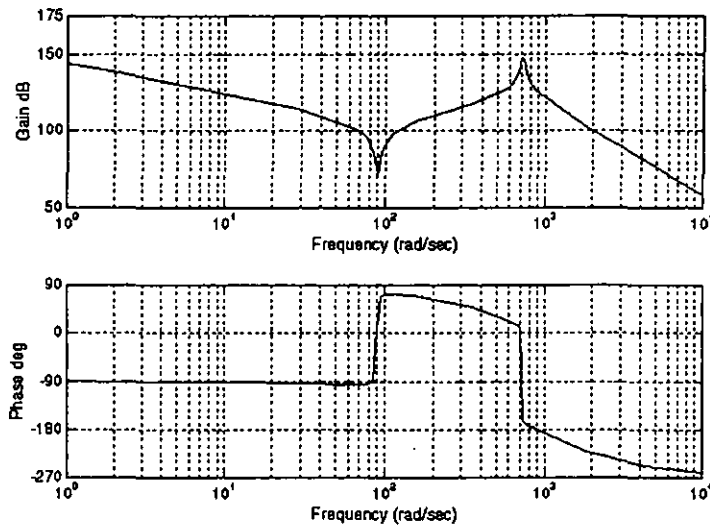


Figure 4.13 Frequency response of a SISO load system

## 4.6 Linear MIMO model

Building a linear model of a MIMO structural test system is straightforward; the basic equations governing operation of the servo-valves and the hydraulic actuators are unchanged and now form diagonal matrices, the test specimen is described by a transfer function matrix (or a state space model). The coupling in the dynamics of the test specimen gives rise to the interaction present in the completed model.

Consider the general multi-channel test with  $n_v$  hydraulic actuators exciting the test specimen, the fluid flow to each actuator being controlled by a servo-valve. Then the transfer functions for all the servo-valves can be combined into a diagonal Transfer Function Matrix  $G_{sv}(s)$  where

$$G_{sv}(s) = \text{diag}(g_{sv_1}(s), g_{sv_2}(s) \dots g_{sv_{nv}}(s)) \quad (4.53)$$

Similarly, the flow-pressure coefficients  $K_{c_i}$  and the flow gains  $K_{q_i}$  of the servo-valves may also be combined to form diagonal matrices  $K_c$  and  $K_q$  where

$$\begin{aligned} K_c &= \text{diag}(K_{c_1}, K_{c_2}, \dots, K_{c_{nv}}) \\ K_q &= \text{diag}(K_{q_1}, K_{q_2}, \dots, K_{q_{nv}}) \end{aligned} \quad (4.54)$$

The cross sectional areas of the pistons of the  $n_v$  actuators may be also combined to form a diagonal matrix  $A$  where

$$A = \text{diag}(A_1, A_2, \dots, A_{nv}) \quad (4.55)$$

Finally, define  $G_p(s)$  as the transfer function matrix representing the dynamic behaviour of the test specimen, i.e.  $\Delta x(s) = G_p(s) \Delta f(s)$ .

The block diagram is the same as that developed for the SISO system except that now the blocks contain transfer function matrices and is shown in Figure 4.14. Again, the block diagram is applicable to displacement and force output systems, in the latter case the final  $G_p(s)$  block is omitted.

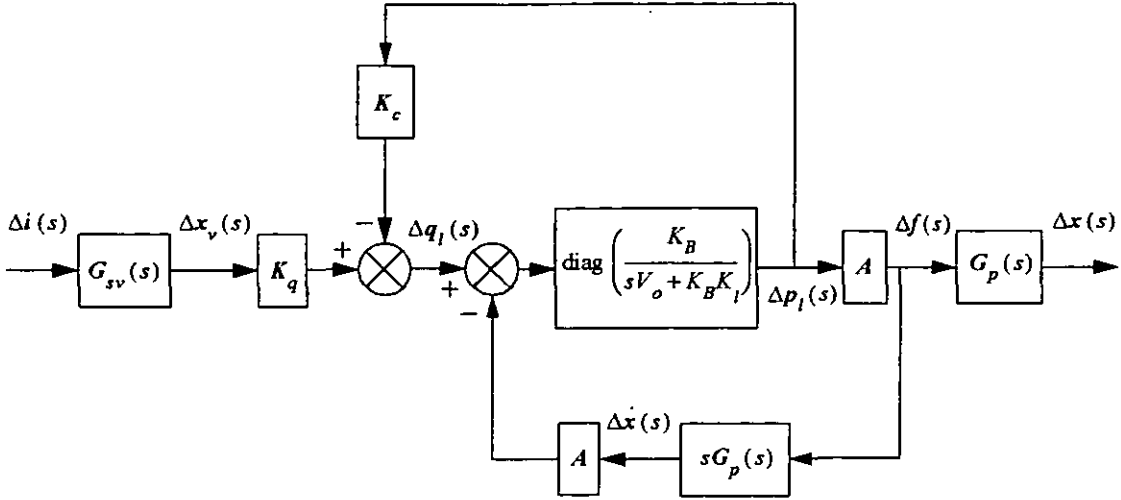


Figure 4.14 Block diagram for MIMO plant

#### 4.6.1 Displacement output

From Figure 4.14, the transfer function matrix relating servo-valve current to displacement of the test specimen is

$$\Delta \mathbf{x}(s) = \mathbf{G}_p(s) \left[ \mathbf{I} + s \mathbf{A} \text{diag} \left( \frac{K_B}{\alpha(s)} \right) \mathbf{G}_p(s) \mathbf{A} \right]^{-1} \mathbf{A} \text{diag} \left( \frac{K_B}{\alpha(s)} \right) \mathbf{K}_q \mathbf{G}_{sv}(s) \Delta \mathbf{i}(s) \quad (4.56)$$

where  $\alpha(s)$  is given by equation (4.48). The hydraulic data and the data for the Torsion bar assembly (equations (4.40) and (4.41)) are summarised in Table 4.5. With this data, equation (4.56) is evaluated and the state space model in equation (4.57) is obtained. The eigenvalues of the state space model are presented in Table 4.6 and the frequency response of the state space model is presented in Figures 4.15(a) and 4.15(b).

TABLE 4.5 Model data for MIMO system

$K_{ce}$	$1 \times 10^{-13} \quad \text{m}^5/\text{Ns}$
$K_B$	$4 \times 1.86 \times 10^9 \quad \text{N/m}^2$
$K_{i_1} K_{q_1}$	$0.0545 \quad \text{m}^3/\text{sA}$
$K_{i_2} K_{q_2}$	$0.0727 \quad \text{m}^3/\text{sA}$
$A_1$	$0.0061 \quad \text{m}^2$
$A_2$	$0.0081 \quad \text{m}^2$
$V_{o_1}$	$0.00186 \quad \text{m}^3$
$V_{o_2}$	$0.00247 \quad \text{m}^3$
$\omega_T$	$880 \quad \text{rad/s}$
$\zeta_T$	$0.9$
$M$	equation (4.40)
$K$	equation (4.40)
$C$	equation (4.41)

TABLE 4.6 Eigenvalues of Torsion rig displacement model

Eigenvalues
$-2.94 \pm j2030$
$-0.55 \pm j971$
$-792 \pm j384$
$-792 \pm j384$
$-7.39 \times 10^{-3}$
$-4.98 \times 10^{-4}$
$-2.74 \pm j275$
$-0.396 \pm j39.6$



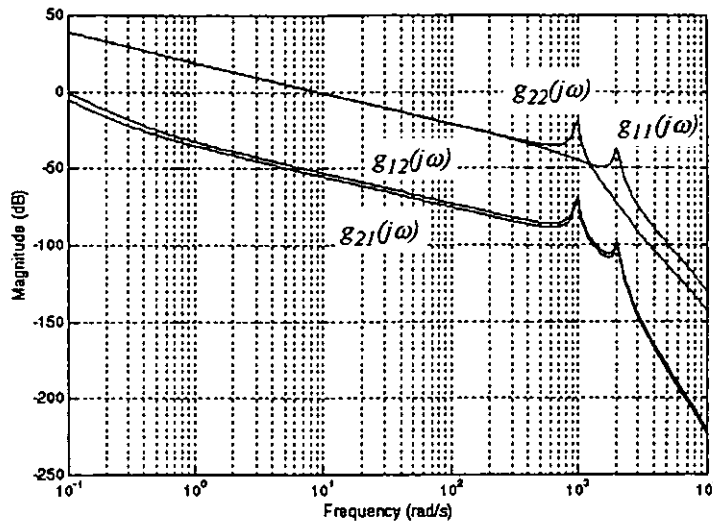


**Figure 4.15(a) Frequency response of the magnitude of the Torsion rig model, displacement output**

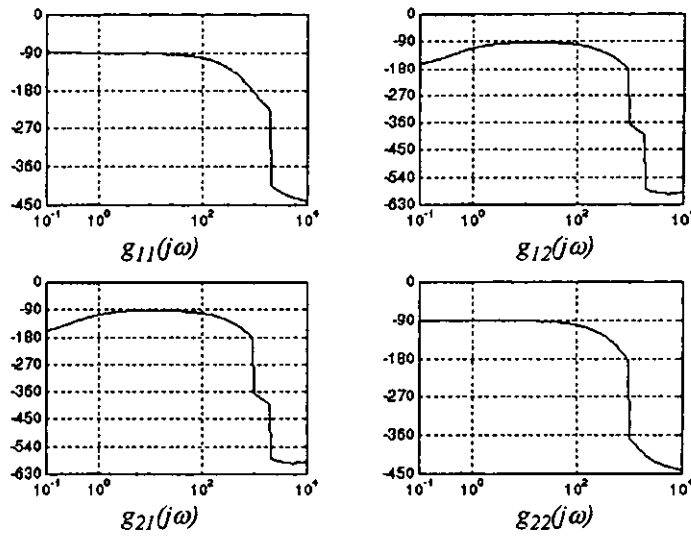


**Figure 4.15(b) Frequency response of the phase of the Torsion rig model, displacement output**

[illegible]

#### 4.6.2 Force output

From Figure 4.14, the transfer function matrix relating servo-valve current to the force applied to the test specimen is

$$\Delta f(s) = \left[ I + sA \operatorname{diag} \left( \frac{K_B}{\alpha(s)} \right) G_p(s) A \right]^{-1} A \operatorname{diag} \left( \frac{K_B}{\alpha(s)} \right) K_q G_{sv}(s) \Delta i(s) \quad (4.58)$$

On the Torsion rig, the servo-valves were electrically driven by amplifiers excited with an input voltage signal  $u(s)$ . The forces applied by the actuators were measured by load cells, the load cell outputs were amplified to give the measured signal  $y(s)$ . Define the gain of the servo-valve amplifiers as  $K_{in}$  and the combined

gain of the load cells with amplifiers as  $K_{out}$ . Then

$$\begin{aligned} i(s) &= K_{in} u(s) \\ y(s) &= K_{out} f(s) \end{aligned} \quad (4.59)$$

$$K_{in} = \begin{bmatrix} 1.56 & 0 \\ 0 & 5.4 \end{bmatrix} \times 10^{-3} \quad K_{out} = \begin{bmatrix} 1.4927 & 0 \\ 0 & 0.9997 \end{bmatrix} \times 10^{-4} \quad (4.60)$$

Then the model of the force output response of the Torsion rig is given by equations (4.58) and (4.59). With the data given in Table 4.5 and equation (4.60), equation (4.58) is evaluated and the state space model of the force output response is given in equation (4.61). The eigenvalues of the state space model are presented in Table 4.7 and the frequency response of the state space model is shown in Figures 4.16(a) and 4.16(b).

**TABLE 4.7 Eigenvalues of Torsion rig force model**

Eigenvalues
$-2.94 \pm j2030$
$-0.55 \pm j971$
$-792 \pm j384$
$-792 \pm j384$
$-7.39 \times 10^{-3}$
$-4.98 \times 10^{-4}$

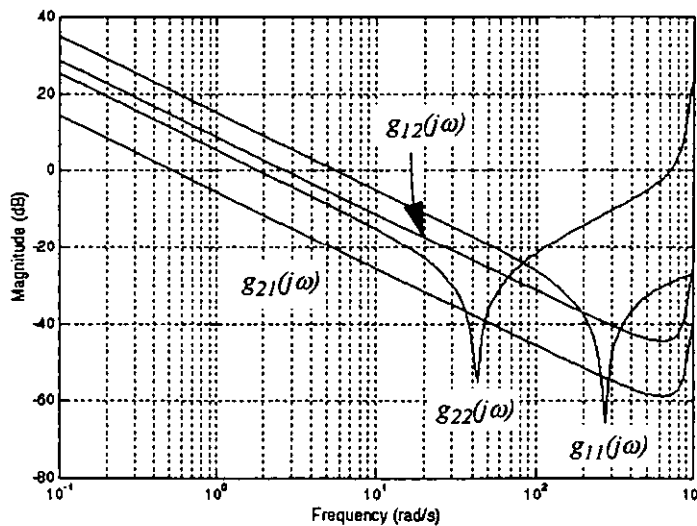


**Figure 4.16(a) Frequency response of the magnitude of the Torsion rig model, force output**

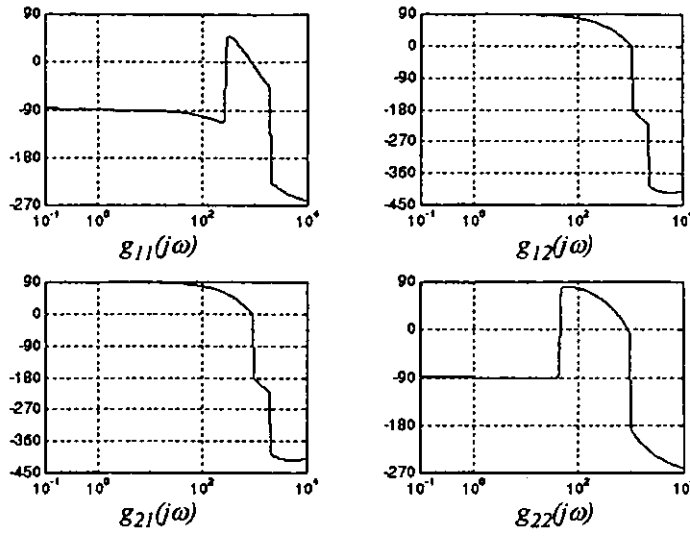


**Figure 4.16(b) Frequency response of the phase of the Torsion rig model, force output**

$$\begin{aligned}
 A = & \begin{bmatrix} -1.58 \times 10^3, 0, -7.74 \times 10^5, 0, 0, 0, 0, 0, 0 \\ 0, -1.58 \times 10^3, 0, -7.74 \times 10^5, 0, 0, 0, 0, 0 \\ 1, 0, 0, 0, 0, 0, 0, 0 \\ 0, 1, 0, 0, 0, 0, 0, 0 \\ 0, 0, 0, 5.23 \times 10^4, -3.01 \times 10^{-1}, 0, 0, -7.52 \times 10^{-3}, 0, 0 \\ 0, 0, 4.04 \times 10^4, 0, 0, -4.00 \times 10^{-1}, -5.84 \times 10^{-3}, 0, 0, 0 \\ 0, 0, 0, 0, 6.93 \times 10^8, -5.48, 6.64 \times 10^{-1}, -7.53 \times 10^4, 1.04 \times 10^4 \\ 0, 0, 0, 0, 1.25 \times 10^8, 0, 1.16 \times 10^{-1}, -8.09 \times 10^{-1}, 1.83 \times 10^3, -1.83 \times 10^3 \\ 0, 0, 0, 0, 0, 0, 1, 0, 0, 0 \\ 0, 0, 0, 0, 0, 0, 0, 1, 0, 0 \end{bmatrix} \\
 B = & \begin{bmatrix} 1.56 \times 10^{-3}, 0 \\ 0, 5.4 \times 10^{-3} \\ 0, 0 \\ 0, 0 \\ 0, 0 \\ 0, 0 \\ 0, 0 \\ 0, 0 \\ 0, 0 \end{bmatrix} \\
 C = & \begin{bmatrix} 0, 0, 0, 0, 0, 3.81 \times 10^6, 0, 0, 0, 0 \\ 0, 0, 0, 0, 2.63 \times 10^6, 0, 0, 0, 0, 0 \end{bmatrix} \\
 D = & \begin{bmatrix} 0 & 0 \\ 0 & 0 \end{bmatrix}
 \end{aligned} \tag{4.61}$$

## 4.7 Hydraulic natural frequency and damping ratio

Most hydraulic fluids, although very stiff, are to some extent compressible. The change in volume of the fluid due to a change in pressure is given by equation (4.62) [33] where  $V$  is the initial volume of the fluid,  $\Delta V$  is the change in the volume of the fluid,  $\Delta P$  is the change in the pressure of the fluid and  $\beta_e$  is the bulk modulus of the oil.

$$\Delta V = \frac{V}{\beta_e} \Delta P \quad (4.62)$$

For example, taking  $V$  and  $\beta_e$  from Table 4.4, the percentage change in volume due to a 100 psi change in pressure is 0.037%. Consequently, the volume of oil contained in a hydraulic actuator will behave as a very stiff spring. When the actuator is exciting a mass, the result is a lightly damped mass-spring system whose natural frequency is known as the 'hydraulic' natural frequency  $\omega_h$ , the damping ratio is known as the 'hydraulic' damping ratio  $\zeta_h$ . This behaviour is observable as a sharp resonant peak in the open-loop frequency response of a structural test system at the hydraulic natural frequency. In the following analysis, approximate relationships are derived for  $\omega_h$  and  $\zeta_h$  for the SISO system illustrated in Figure 4.10.

The transfer functions for SISO displacement and force output, equations (4.48) and (4.50) respectively, have the same cubic denominator, which may be factorised thus

$$(s + \omega_l) (s^2 + 2\zeta_h \omega_h s + \omega_h^2) \quad (4.63)$$

Direct algebraic determination of  $\omega_l$ ,  $\omega_h$  and  $\zeta_h$  is extremely unwieldy. However, the following approximations can be made [33], providing that the inequalities in equation (4.65) are met. Fortunately, the inequalities are usually satisfied as  $K_{ce} \approx 0$  and typically  $K_B \gg K_s V_o / A^2$

$$\begin{aligned} \omega_l &\approx \frac{K_{ce} K_s}{A^2} \\ \omega_h &\approx \sqrt{\frac{K_B A^2}{M V_o}} \\ \zeta_h &\approx \frac{1}{2\omega_h} \left( \frac{K_{ce} K_B}{V_o} + \frac{\mu}{M} \right) \end{aligned} \quad (4.64)$$

From the above approximations, the following observations are made:

1. Typically  $K_{ce} \approx 0$  and so the pole at  $s = -\omega_l$  is virtually at the origin of the complex plane. This gives rise to the integrator like behaviour of the open-loop system.

$$\begin{aligned} \frac{K_{ce}K_s}{A^2} &\ll \frac{\mu}{M} + \frac{K_{ce}K_B}{V_o} \\ \frac{K_{ce}^2K_sK_B}{A^2V_o} + \frac{\mu K_{ce}K_s}{A^2M} &\ll \frac{K_B A^2}{MV_o} \\ \frac{K_s}{M} + \frac{\mu K_{ce}K_B}{MV_o} &\ll \frac{K_B A^2}{MV_o} \end{aligned} \quad (4.65)$$

2. Typically  $K_B \gg K_s V_o / A^2$  and so the 'hydraulic' natural frequency  $\omega_h$  is greater than the natural frequency of the test specimen,  $\omega = \sqrt{K_s/M}$ .
3. The hydraulic damping is a function of the position of the spool in the servo-valve: from equations (4.10), (4.47) and (4.64) the hydraulic damping ratio can be written explicitly in terms of the position of the spool valve at it's operating point,  $x_{vo}$ , as below

$$\zeta_h \approx \frac{1}{2\omega_h} \left\{ \frac{K_B}{V_o} \left( K_l + \frac{C_d w}{2\sqrt{\rho}} |x_{vo}| \sqrt{P_s - \text{sgn}(x_{vo}) P_{Lo}} \right) + \frac{\mu}{M} \right\} \quad (4.66)$$

At the null position ( $x_{vo} = 0$ ) the hydraulic damping ratio is at a minimum, the damping ratio then increases with the magnitude of the displacement of the spool from the null position. The extent to which  $\zeta_h$  can vary is illustrated in section 4.8.

## 4.8 Confidence in the linear model

For the transfer functions and transfer function matrices previously developed to be of use, they must be a good approximation to the actual non-linear system over a reasonable operating range. The following study shows that this is the case and the following analysis also alerts the reader to the sensitivity of the hydraulic damping ratio with position of the spool in the servo-valve.

### 4.8.1 Simulation study

A comparative simulation study is undertaken below based on the SISO force output system described in section 4.5.2. To simplify the study, consider that the system is excited at a frequency well below  $\omega_T$  in which case the position of the spool valve is proportional to the servo-valve current, i.e. from equation (4.2)  $g_{sv}(s) = K_i$ . Then, from equations (4.1) and (4.7)

$$q_L(t) = K_i C i(t) \sqrt{1 - \operatorname{sgn}(i(t)) \frac{p_L(t)}{P_s}} \quad (4.67)$$

where

$$C = C_d w \sqrt{\frac{P_s}{\rho}} \quad (4.68)$$

and from equation (4.9),  $K_q = C$  at the null position ( $i(t) = 0$ ,  $x_v(t) = 0$  and  $p_L(t) = 0$ ). Note also that at the null position  $K_c = 0$ , equation (4.10).

The block diagram of the linear system is taken from Figure 4.11 and is repeated below in Figure 4.17 with all transfer functions written explicitly. The corresponding non-linear system is derived from Figure 4.17 by replacing the blocks grouped as 'linearised dynamics' with equation (4.67). The schematic of the non-linear system is shown in Figure 4.18. The model data are given in Table 4.8.

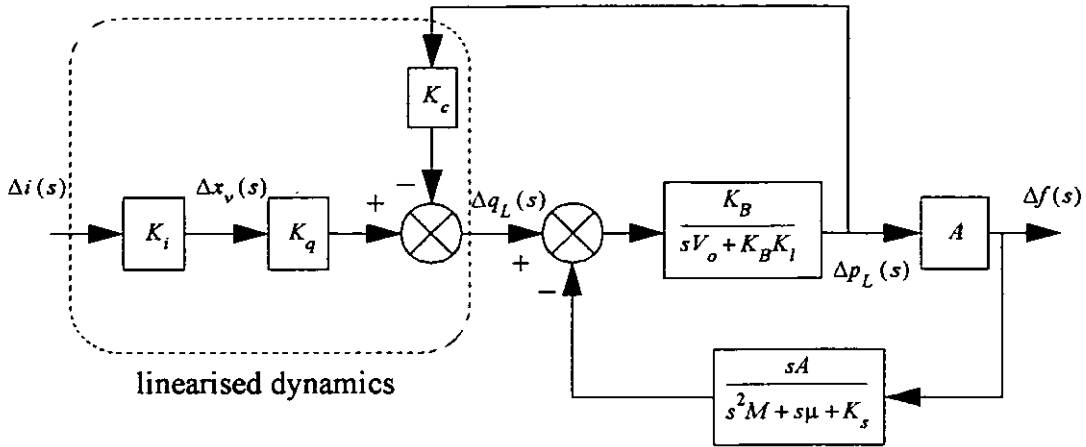


**Figure 4.17** Block diagram of SISO system, linear simulation

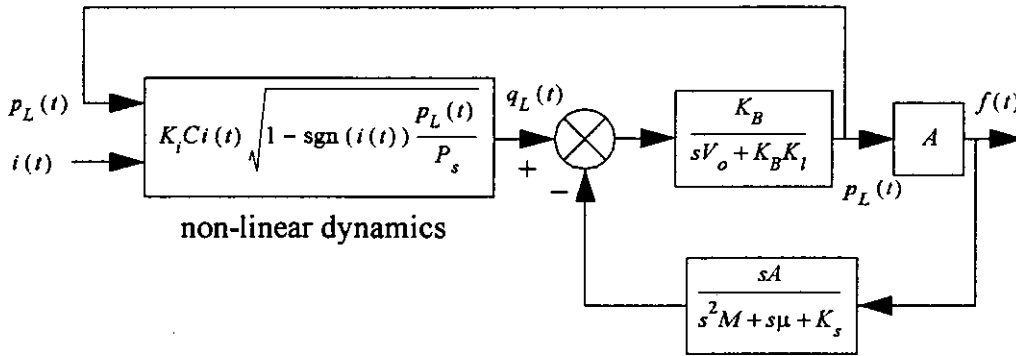


**Figure 4.18** Schematic of SISO system, non-linear simulation

Sinusoidal excitation and corresponding force output was determined at the null operating point with four different excitation magnitudes, the excitation magnitudes are shown in Figure 4.19 in relation to the flow-pressure characteristic of the servo-valve. It can be seen that the excitation magnitudes cover a wide operating region. The resulting time responses are plotted in Figure 4.20. There is a steady state off-set between the linear and non-linear responses. However, the responses are in phase with each other and the peak to peak magnitudes are very close; (a) 0.36% error, (b) 0.58% error, (c) 0.65% and (d) 1.2% error. The agreement between the non-linear and linear response gives confidence in the validity of the linear model over a wide operating region



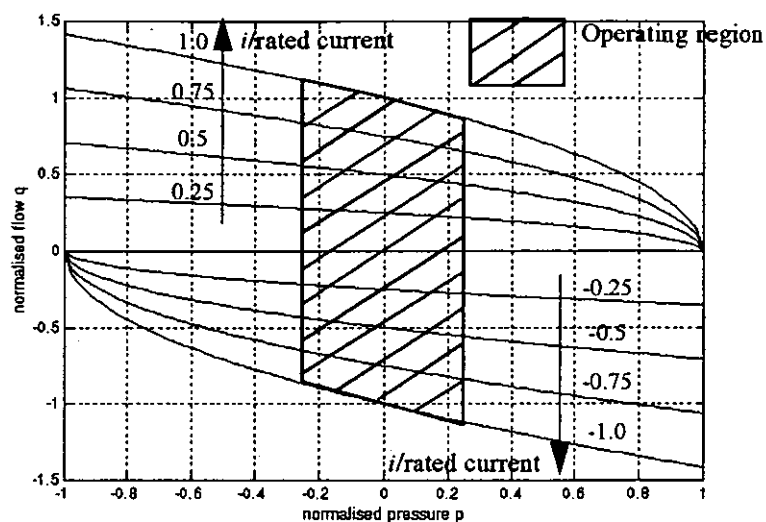
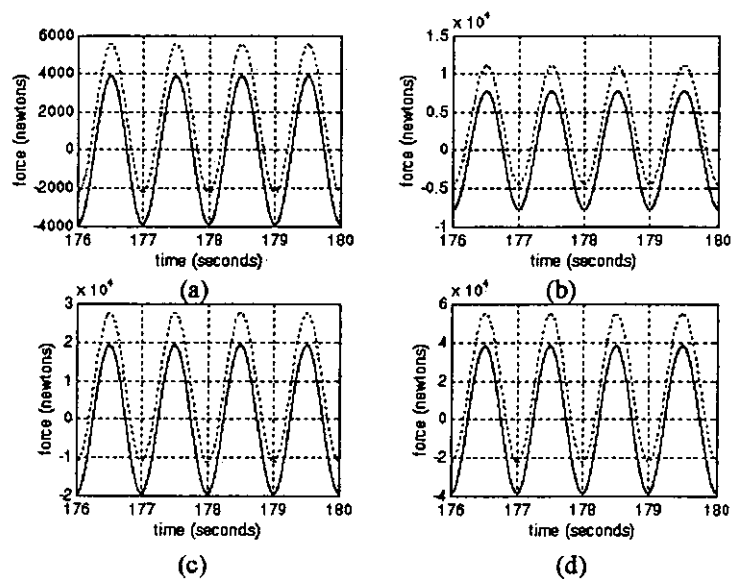


**Figure 4.19** Operating region of the servo-valve flow-pressure characteristic covered by the simulation study



(a) peak servo-valve current = 1.5 mA    (b) peak servo-valve current = 3 mA  
(c) peak servo-valve current = 7.5 mA    (d) peak servo-valve current = 15 mA

**Figure 4.20** Time response of linear model and non-linear model  
(solid line - nonlinear, dashed line - linear)

**TABLE 4.8 Model data for SISO simulation**

$K_I$	$1 \times 10^{-13} \quad \text{m}^5/\text{Ns}$
$K_B$	$4 \times 1.86 \times 10^9 \quad \text{N/m}^2$
$K_i K_q$	$0.042 \quad \text{m}^3/\text{sA}$
$K_i C$	$0.042 \quad \text{m}^3/\text{sA}$
$K_c$	$0 \quad \text{m}^5/\text{Ns}$
$A$	$0.008107 \quad \text{m}^2$
$V_o$	$0.002469 \quad \text{m}^3$
$M$	$392.35 \quad \text{Kg}$
$K_s$	$3.19 \times 10^6 \quad \text{N/m}$
$\mu$	$706.22 \quad \text{Kg/s}$
$P_S$	$3000 \quad \text{psi}$
Maximum or rated current of servo-valve	$15 \quad \text{mA}$

NOTE:  $1 \text{ psi} = 6894.8 \text{ Nm}^{-2}$ 

#### 4.8.2 'Hydraulic' natural frequency and damping ratio

The variation in the hydraulic natural frequency with operating point for the linearised system studied in section 4.8.1 is illustrated in Figure 4.21(a), the corresponding approximation from equation (4.64) is shown in Figure 4.21(b). It can be seen that the hydraulic natural frequency varies to a slight extent with the operating point of the servo-valve current (and hence spool position) whilst it remains virtually constant with load pressure. The approximation is accurate to within 1% at all times. By contrast, the variation in damping ratio with operating point, plotted in Figure 4.22(a), is far greater and it is clear that the damping ratio increases as the spool moves away from its null position (i.e. as the current increases). The approximation to the damping ratio is determined from equations (4.10), (4.47) and (4.64) and is illustrated in Figure 4.22(b). The approximation closely matches the actual damping ratio.

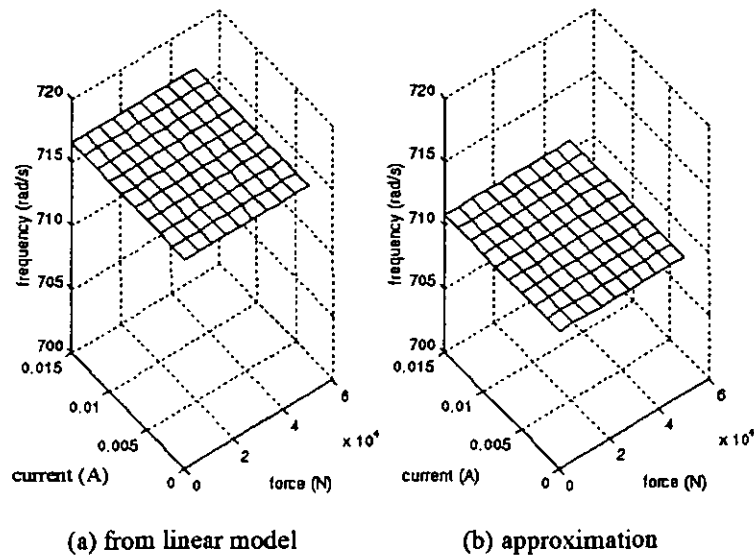


**Figure 4.21** Variation in hydraulic natural frequency with operating point

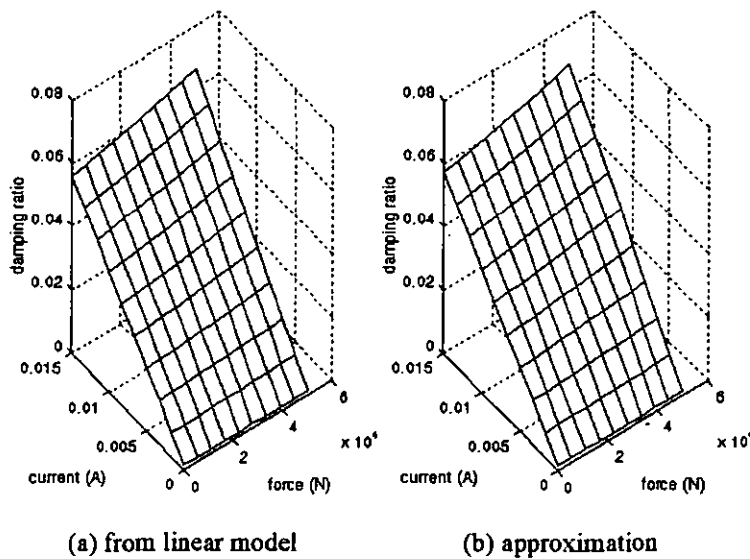


**Figure 4.22** Variation in hydraulic damping ratio with operating point

## 4.9 Conclusions

Linear models have been derived for both SISO and MIMO dynamic structural tests employing servo-hydraulic actuation. Furthermore, models have been derived for both displacement and force output, based on block diagrams that can be used to build models with any number of hydraulic actuators and measured outputs. The question of the validity of linear modelling has been considered in light of the non-linear flow-pressure characteristic of the servo-valve, analysis and simulation have both shown that the linear approach gives a good approximation to the non-linear system.

## **Chapter 5**

### **Control Schemes**

#### **5.1 Introduction**

In this chapter two techniques of MIMO control system design are discussed: Sequential Loop Closure (SLC) and the Characteristic locus (CL) method. There are of course many design methods available for tackling multivariable control problems, the motivation for using these techniques in this thesis is described below.

SLC is by far the most widespread technique in industrial application, with PID action commonly used in the individual loop controllers. It is therefore necessary to use SLC to provide a bench-mark against which other MIMO control system implementations can be judged. The CL method has been used successfully in previous research [5 - 7] in simulated control of a small structural test rig. The larger scale Torsion test rig described in chapter 3 poses a more challenging control problem. However, although a model of the Torsion rig has been developed in chapter 4, it is not uncommon in practice to find that no model of the structure and test rig exists. In such cases, a suitable model must be obtained by analytical or experimental means. Analytical modelling can prove too complex to be a viable option, whereas experimental identification, by contrast, is relatively straightforward. The CL method lends itself well in this respect since the only requirement is a frequency response of the plant. Also, the CL method has the added attraction to the practitioner of its similarity with widely understood SISO frequency domain design methods.

A brief description of SLC is given in section 5.2, where the problem of tuning loop controllers and the associated problem of input-output pairing is discussed. In section 5.3, the CL method is discussed and three important aspects are described:

- (1) The generalised Nyquist Stability criterion, which leads to the conclusion that closed-loop stability can be directly affected by compensating the characteristic loci.
- (2) CL control system philosophy.
- (3) Controller design.

Discretisation of the CL method provides scope for dynamically decoupling the plant over its entire frequency range, the inability to do this is the principal limitation in the original CL method. Section 5.4 describes recent advances in this area.

## 5.2 Sequential Loop Closure

This is the simplest approach to controlling a multiple-input, multiple-output plant. An array of single-loop controllers are designed and each single-loop controller is considered as a SISO system, see Figure 5.1. For a system with  $n$  inputs,  $n$  SISO control loops are installed. Tuning of the loop controllers proceeds with the closing of each feedback loop, in turn - hence the term 'Sequential Loop Closure'. If the plant is unstable in the open-loop, then all of the feedback loops are closed before the sequential tuning procedure is carried out.

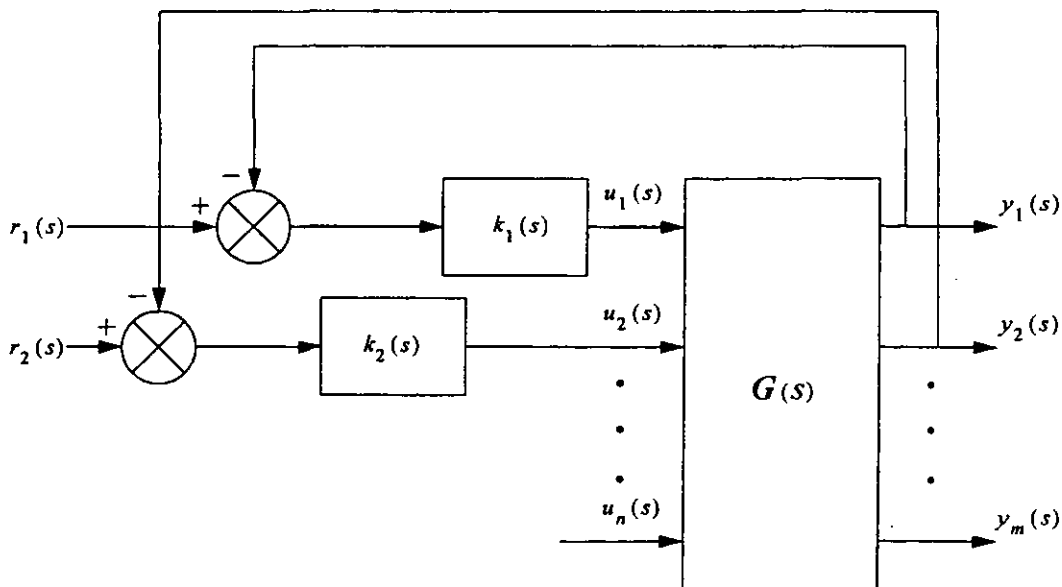


Figure 5.1 Sequential Loop Closure

This method has three major advantages for the practitioner:

- (1) A model of the plant is not necessarily required, although a model may be desirable in determining suitable input and output pairing.
- (2) Widely understood SISO design techniques can be used (e.g. PID, frequency response shaping).
- (3) The approach is very pragmatic.

The method does, however, suffer, from a number of drawbacks. Principally, the only way to combat interaction is to use high loop gains in the controllers - this, however, will be limited by stability requirements. During the tuning phase, successive closing of individual loops may well lead to deterioration in the performance achieved with previous loops. The design procedure often turns out to be very *ad hoc* in practice and the whole process of tuning loop controllers becomes iterative and time consuming.

Control loops are usually formed from corresponding input and output pairs, although this is not a requirement of the SLC method. Consideration of the choice of the most appropriate input-output pairing has been considered [34 - 36] but still remains under-developed in the literature.

### 5.3 The Characteristic Locus (CL) method

The Characteristic Locus method was first introduced in the late 1970s by MacFarlane and Kouvaritakis [37] and has proven itself to be an effective approach to multivariable controller design. The CL method attempts to decouple the plant and compensate the characteristic loci of the plant. The great attraction of the method is that the compensation of the characteristic loci is very akin to traditional SISO frequency domain controller design. Furthermore, the method requires only a frequency response for a plant model (as opposed to a parametric model) and good controllers can be designed relatively easily with a suitable CAD package (i.e., MATLAB [38]). Owens [Owens, D.H., 'Feedback and multivariable systems', Peter Peregrinus, Stevenage, 1978] also contributed significantly to this field at the same time.

Central to the CL method is the stabilisation of the plant by suitable shaping of the characteristic loci of the plant. In fact, the loci are shaped to meet the generalised

Nyquist Stability criterion, described below, which is a generalisation of the Nyquist stability criterion for SISO systems. Hence, the similarity between the CL method and SISO frequency response shaping.

Building upon the generalised Nyquist stability criterion, the philosophy of the CL method is discussed in section 5.3.2 and the design method is summarised in section 5.3.3 for the reader.

### 5.3.1 Generalised Nyquist stability criterion [39]

Consider the closed-loop control scheme illustrated in Figure 5.2 and define

$$Q(s) = G(s)K(s) \quad (5.1)$$

where  $Q(s)$  has  $n$  inputs and  $n$  outputs. The input-output relationship is  $y(s) = T(s)r(s)$ , where  $T(s)$  is the closed-loop transfer function matrix given by

$$T(s) = (I + Q(s))^{-1} Q(s) \quad (5.2)$$

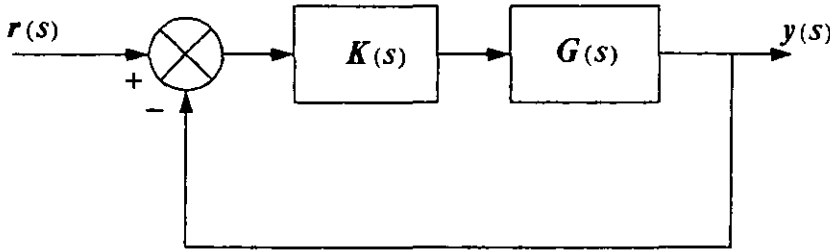


Figure 5.2 Closed-loop block diagram

The poles of the closed-loop system are given by the zeros of  $\det [I + Q(s)]$ , so it is therefore required for stability that  $\det [I + Q(s)]$  does not have any zeros in the right-half s-plane. Define

$$f(s) = \det [I + Q(s)] \quad (5.3)$$

and let  $f(s)$  have  $P$  poles and  $Z$  zeros in the closed right-half s-plane. Now the net change in phase of  $f(s)$  as  $s$  takes on all values along the closed contour illustrated in Figure 5.3, as it traverses in the direction indicated, is

$$\Delta \arg (f(s)) = -2\pi (Z - P) \quad (5.4)$$

where  $\Delta \arg$  denotes the net change in phase. The path illustrated in Figure 5.3 is known as the 'Nyquist' contour and encloses the entire right-half  $s$ -plane, deviating around any poles of  $f(s)$  that fall on the imaginary axis. This result can be expressed in a more familiar form as

$$N = Z - P \quad (5.5)$$

where  $N$  is the number of times the locus of  $f(s)$  encircles the origin in the  $f(s)$  plane as  $s$  follows the 'Nyquist' contour. If  $N$  is positive, travel along the locus of  $f(s)$  is in the same direction as travel along the 'Nyquist' contour; if  $N$  is negative, the directions of travel are opposite. This is the Nyquist stability criterion for SISO systems if  $f(s)$  is the characteristic equation of a SISO system.

Returning to our multivariable system, the poles of  $f(s)$  are the poles of  $Q(s)$ . Hence, since for stability it is required that  $Z = 0$ , the net change in phase of  $f(s)$  must be equal to  $2\pi P$ .

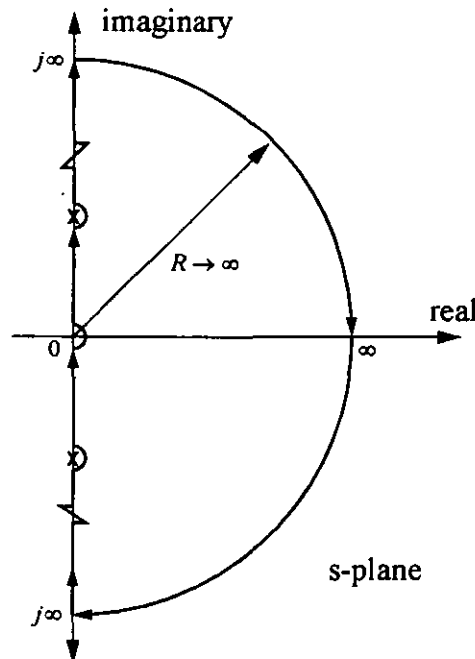


**Figure 5.3** The Nyquist contour



Now since a determinant is the product of its eigenvalues, we have

$$f(s) = \det [I + Q(s)] = \prod \text{eig} (I + Q(s)) \quad (5.6)$$

and denote the eigenvalues of  $I + Q(s)$  as  $\lambda_i(s)$ . It can be shown that  $1 + \lambda_i(s)$  is an eigenvalue of  $I + Q(s)$ . Consequently,

$$\det [I + Q(s)] = \prod_{i=1}^n (1 + \lambda_i(s)) \quad (5.7)$$

Hence, for stability, the total number of encirclements of the origin made by the loci of  $1 + \lambda_i(s)$ , or the total number of encirclements of the  $(-1, 0)$  point made by the loci of  $\lambda_i(s)$ , must be equal to  $-P$ . This is the generalised stability criterion.

The graphs of  $\lambda_i(s)$ , as  $s$  traverses the 'Nyquist' contour, are known as the **characteristic loci** of  $Q(s)$ .

### 5.3.2 Control philosophy

The closed-loop control scheme has been illustrated in Figure 5.2. The spectral decomposition of the plant  $G(s)$  is given below

$$G(s) = W(s) \Lambda(s) W^{-1}(s) \quad (5.8)$$

where  $W(s)$  is a matrix whose columns are the eigenvectors of  $G(s)$ ,  $W^{-1}(s)$  is a matrix whose columns are the dual eigenvectors of  $G(s)$  and

$$\Lambda(s) = \text{diag} \{ \lambda_1(s), \lambda_2(s), \dots, \lambda_n(s) \} \quad (5.9)$$

where the  $\lambda_i(s)$  are the eigenvalues, or characteristic loci, of  $G(s)$ . Consider now that the controller  $K(s)$  has the same eigenvectors as the plant, i.e.

$$K(s) = W(s) M(s) W^{-1}(s) \quad (5.10)$$

where

$$M(s) = \text{diag} \{ \mu_1(s), \mu_2(s), \dots, \mu_n(s) \} \quad (5.11)$$

The return ratio  $G(s)K(s)$  is then given below and  $K(s)$  is known as a commutative controller since its structure gives  $G(s)K(s) = K(s)G(s)$

$$G(s)K(s) = W(s) \text{diag} \{v_1(s), v_2(s), \dots, v_n(s)\} W^{-1}(s) \quad (5.12)$$

where

$$v_i(s) = \lambda_i(s) \mu_i(s) \quad i = 1 \dots n \quad (5.13)$$

Thus, providing that the plant and the controller share the same eigenvectors and dual eigenvectors, then the system obtained by connecting them in series has eigenvalues which are simply the product of the controller and plant characteristic loci. From the generalised Nyquist stability criterion, closed-loop stability requires that, together, the loci of the eigenvalues  $\lambda_i(s) \mu_i(s)$  encircle the  $(-1, 0)$  point  $P$  times anticlockwise, where  $P$  are the number of unstable poles of  $G(s)K(s)$ . Commonly, both the open-loop plant and the controller are stable and  $P = 0$ . Stability can therefore be achieved by designing the characteristic loci of the controller to ensure that  $\lambda_i(s) \mu_i(s)$  meet this requirement. Performance is obtained through shaping the characteristic loci in a very similar fashion to the shaping of the open-loop frequency response of a SISO plant.

Unfortunately, it is quite impractical to build a controller with this structure as the elements of the matrices  $W(s)$  and  $W^{-1}(s)$  are almost always irrational functions with no practical realisations. The alternative is to approximate  $W(s)$  and  $W^{-1}(s)$  with rational matrices. The widely adopted approximation is that developed by Kouvaritakis [40, 41] which yields constant and real valued matrices  $A$  and  $B$  at a fixed frequency,  $s = j\omega_o$ , such that

$$\begin{aligned} A &\approx W(j\omega_o) \\ B &\approx W^{-1}(j\omega_o) \end{aligned} \quad (5.14)$$

This approximation is determined using the ALIGN algorithm and is used in this thesis. Building the controller with the structure  $K(s) = AM(s)B$  will only guarantee the desired shaping of the characteristic loci at the single frequency  $\omega_o$ . This will limit the effectiveness of the method and leads to the standard procedure of designing three compensators at three very different frequencies; high, medium and low frequency. This approach is known as the Characteristic Locus method and is described in section 5.3.3.

In principle, more compensators could be designed, each for a particular frequency of interest. However, this leads to a complicated overall controller and furthermore, the component compensators will interfere with each other. Compensator interference is explained in section 5.3.3

### 5.3.3 Design method

#### High-frequency compensator $K_h$

A fixed gain controller is designed to decouple the plant at a high frequency  $\omega_h$ . A frequency beyond the desired closed-loop bandwidth is usually selected in order that interference between this step of compensation and the next step is kept to a minimum. The controller is a real rational approximation of  $G^{-1}(j\omega_h)$ , obtained using the ALIGN algorithm.

$$K_h \approx G^{-1}(j\omega_h) \quad (5.15)$$

#### Medium-frequency compensator $K_m(s)$

A dynamic controller is designed to shape the characteristic loci of  $G(s)K_h$  for stability and performance near the  $(-1, 0)$  point.  $K_m(s)$  has the commutative structure discussed in section 5.3.2 to facilitate the desired shaping, namely

$$K_m(s) = A_m M(s) B_m \quad (5.16)$$

where  $A_m$  and  $B_m$  are the required real and rational approximations to the eigenvectors and dual eigenvectors, respectively, of  $G(j\omega_m)K_h$  at a medium frequency  $\omega_m$ . The approximation is usually carried out at a frequency when the characteristic loci of  $G(s)K_h$  are in the vicinity of the  $(-1, 0)$  point.  $M(s)$  is a diagonal controller whose elements are chosen to shape the characteristic loci of  $G(s)K_h$  in a similar manner to classical SISO frequency response shaping. Simple lead, lag or PID compensation is effective. Ideally,  $K_m(j\omega)$  should approach  $I$  as  $\omega \rightarrow \omega_h$ , so as not to interfere with the compensation achieved with the high frequency compensator.

#### Low-frequency compensator $K_l(s)$

At low frequencies, the control objectives are to reduce steady-state error and reduce interaction. Often these can be met with simple integral action in the low-frequency commutative controller, the phase lag introduced usually not having a bearing upon stability at low frequencies. If this is the case, the following form can be used

$$K_I(s) = A_I \text{diag} \left( \frac{k_i}{s} \right) B_I + I \quad (5.17)$$

where  $A_I$  and  $B_I$  are the required real and rational approximations to the eigenvectors and dual eigenvectors, respectively, of  $G(s) K_h K_m(s)$  at a suitable low frequency  $\omega_l$ .  $k_i$  is the weighting of each diagonal integral gain. The frequency  $\omega_l$  should be chosen so that the compensator has negligible effect upon the magnitude and phase of the characteristic loci at frequencies approaching  $\omega_m$ . I.e., it is vital to ensure minimal interaction between the different compensators and ideally  $K_I(j\omega)$  should approach  $I$  as  $\omega \rightarrow \omega_m$ . The overall controller is given by

$$K(s) = K_h K_m(s) K_I(s) \quad (5.18)$$

## 5.4 Direct digital design of the Characteristic Locus controller

Although effective, the original CL method does have a limitation. It relies on constant and real approximations to the eigenvectors of the plant at three distinct frequencies - in general, the eigenvectors are neither real or constant, varying with frequency. Also, the method relies on the three component compensators not interfering with each other - in practice this is difficult to achieve. In recent years, an improved characteristic locus approach has been proposed [42, 43] which is formulated in the  $z$ -plane and uses dynamic approximations to the eigenvectors of the plant. This allows the design of a single commutative controller which decouples the system over its entire frequency range and is described below.

In discrete time, the spectral decomposition of the plant can be written as in equation (5.19) where  $W(z)$  is a matrix whose columns are eigenvectors of  $G(z)$  and  $\Lambda_G(z)$  is a matrix of eigenvalues of  $G(z)$ .  $z^{-1}$  is the delay operator.

$$G(z) = W(z) \Lambda_G(z) V(z) \quad W(z) V(z) = I \quad (5.19)$$

The controller is given the structure below

$$K(z) = W(z) \Lambda_K(z) V(z) \quad (5.20)$$

and since the controller shares the same eigenvectors and dual eigenvectors as the plant, the controller is commutative. The return ratio matrix is then given by

$$G(z) K(z) = K(z) G(z) = W(z) \Lambda_{GK}(z) V(z) \quad (5.21)$$

where the diagonal matrix  $\Lambda_{GK}(z)$  is the product of the characteristic loci of the plant and the characteristic loci of the controller. Exactly as in the original method, the characteristic loci of the controller are designed to compensate the characteristic loci of the plant in order to meet stability and performance requirements.

The improvement over the original method lies in finding dynamic approximations to  $W(z)$  and  $V(z)$  over the entire frequency range. The principal idea is to write the matrices of eigenvectors and dual eigenvectors as finite impulse responses in the delay operator, i.e.

$$W(z) = \sum_{i=1}^n W_i z^{-i} \quad V(z) = \sum_{i=1}^n V_i z^{-i} \quad (5.22)$$

In the general case, the plant model  $G(z)$  will have unstable branch points and the above sequences can be viewed as a Laurent series in  $z^{-1}$ . This implies positive powers of  $z$ , giving an unrealisable model for the eigenvectors and dual eigenvectors. However, it can be shown that in many cases an expansion in negative powers alone can give very good approximations, and certainly better than a constant approximation [44]. As infinite sequences are impractical, a mechanism is needed for determining the best finite approximation to the sequence. Many algorithms have been proposed in the literature for this purpose. A time domain algorithm based on the minimisation of a 2-norm measure of error proposed in [43] has been used successfully [9, 45] and is given below.

The plant model can be written as

$$G(z) = \frac{N(z)}{d(z)} \quad (5.23)$$

where  $d(z)$  is a common denominator and the numerator can be written as

$$N(z) = \sum_{i=0}^n N_i z^{-i} \quad (5.24)$$

The approximate spectral decomposition of  $G(z)$  may be written as below, where  $W_a(z)$  and  $V_a(z)$  are the desired dynamic approximations to the actual eigenvectors and dual eigenvectors of the plant model. The matrix  $\Lambda_N(z) = \text{diag}(\lambda_N^{(i)}(z))$  contains the eigenvalues of  $N(z)$ .

$$N(z) \approx W_a(z) \Lambda_N V_a(z) \quad (5.25)$$

The matrices  $W_a(z)$  and  $V_a(z)$  are sequences, with elements of the form

$$c_0 + c_1 z^{-1} + \dots + c_{n_w} z^{-n_w} \quad (5.26)$$

and are written explicitly in terms of their column vectors as below, where  $W_a(z)$  and  $V_a(z)$  have  $m$  rows and  $m$  columns.

$$\begin{aligned} W_a(z) &= [w_a^{(1)}(z), \dots, w_a^{(m)}(z)] \\ V_a(z) &= [v_a^{(1)}(z), \dots, v_a^{(m)}(z)]^T \end{aligned} \quad (5.27)$$

From the basic definition of eigenvalue decomposition,  $Ax_i = \lambda_i x_i$ , the following errors are defined, where  $e_1^{(i)}(z)$  and  $e_2^{(i)}(z)$  are vectors and  $e_3^{(i)}(z)$  is a scalar.

$$\begin{aligned} e_1^{(i)}(z) &= N(z) w_a^{(i)}(z) - w_a^{(i)}(z) \lambda_N^{(i)}(z) \\ e_2^{(i)}(z) &= v_a^{(i)T}(z) N(z) - \lambda_N^{(i)}(z) v_a^{(i)T}(z) \\ e_3^{(i)}(z) &= v_a^{(i)T}(z) w_a^{(i)}(z) - 1 \end{aligned} \quad (5.28)$$

The errors can be written as sequences themselves. The most negative power of  $z$  in both  $e_1^{(i)}(z)$  and  $e_2^{(i)}(z)$  will be  $-(n + n_w)$ , denote this quantity as  $p_1, p_2 = n + n_w$ . In a similar manner, the most negative power of  $z$  in  $e_3^{(i)}(z)$  will be  $p_3 = 2n_w$ . Thus, the errors can be written as

$$\begin{aligned}
e_1^{(i)}(z) &= e_1^{(i)}(0) + e_1^{(i)}(1)z^{-1} + \dots + e_1^{(i)}(p_1)z^{-p_1} \\
e_2^{(i)}(z) &= e_2^{(i)}(0) + e_2^{(i)}(1)z^{-1} + \dots + e_2^{(i)}(p_2)z^{-p_2} \\
e_3^{(i)}(z) &= e_3^{(i)}(0) + e_3^{(i)}(1)z^{-1} + \dots + e_3^{(i)}(p_3)z^{-p_3}
\end{aligned} \tag{5.29}$$

where  $e_j^{(i)}(q)$  is the vector of coefficients of  $z^{-q}$  in  $e_j^{(i)}(z)$ . From this sequence representation, the coefficients of powers of  $z$  are readily extracted to form the following vectors

$$\begin{aligned}
e_1^{(i)} &= [e_1^{(i)T}(0), e_1^{(i)T}(1), \dots, e_1^{(i)T}(p_1)]^T \\
e_2^{(i)} &= [e_2^{(i)}(0), e_2^{(i)}(1), \dots, e_2^{(i)}(p_2)]^T \\
e_3^{(i)} &= [e_3^{(i)}(0), e_3^{(i)}(1), \dots, e_3^{(i)}(p_3)]^T
\end{aligned} \tag{5.30}$$

The following least squares cost function is defined, the objective is to minimise the function for each eigenvalue-eigenvector set

$$J^{(i)} = \|e_1^{(i)}\|_2^2 + \|e_2^{(i)}\|_2^2 + \|e_3^{(i)}\|_2^2 \quad i = 1, \dots, m \tag{5.31}$$

The coefficients of  $w_a^{(i)}(z)$ ,  $v_a^{(i)}(z)$  and  $\lambda_N^{(i)}(z)$  provide the degrees of freedom over which the minimisation is to be carried out. An iterative procedure based on a gradient search is adopted whereby  $w_a^{(i)}(z)$ ,  $v_a^{(i)}(z)$  and  $\lambda_N^{(i)}(z)$  are calculated in turn, while the other two are kept fixed.

Although this method allows for compensation of the characteristic loci across the whole frequency range, it is undesirable to introduce large gains at high frequency to decouple the system. Therefore, the fixed gain controller  $K_h$ , equation (5.15), is retained to reduce interaction at high frequencies. In the previous analysis,  $G(z)$  is replaced by  $G(z)K_h$ .

## 5.5 Conclusions

Two techniques of MIMO control system design have been described: Sequential Loop Closure (SLC) and the Characteristic Locus (CL) method. SLC is perhaps the simplest approach to the control of MIMO system, employing an array of single-loop controllers and relying upon the use of high gain in the control loops to combat interaction. However, this approach is limited when stability requirements dictate that high loop gains cannot be used.

The Characteristic Locus method, by contrast, addresses the true multivariable nature of the control problem. The CL controller decouples the plant and compensates the characteristic loci of the plant in a similar fashion to the frequency response shaping of SISO systems. In practice, there is a high degree of similarity, making the CL design method attractive to the practitioner. Additionally, the design method only requires a frequency response model of the plant, which may be obtained experimentally.

A recent discrete approach to the CL method has been discussed and it has been shown that in a discrete formulation, it is possible to decouple the plant over its entire frequency range, thereby improving upon the closed-loop performance achieved with the original CL method.



## Chapter 6

# Stability Issues and the Relevance of Multivariable Control in Multi-Channel Dynamic Structural Testing

### 6.1 Introduction

The fundamental objective in controlling a multichannel dynamic structural test is to achieve a desired set of output responses. In practice, classical SISO methods are used and the true multivariable nature of the problem is rarely perceived. This is a pragmatic approach which often works well, raising the question: Is there a need for multivariable control? Indeed, since classical SISO methods obviate the need for a mathematical model of the plant and rely upon widely understood design principles, it makes no sense to use multivariable control unnecessarily. This chapter seeks to answer this motivating question, by identifying the conditions under which a SISO approach is flawed.

The success, or otherwise, of the SISO approach can be attributed to the simple principle of disturbance rejection, this is explored in section 6.2. A qualitative comparison is made with multivariable control, leading to the conclusion that the SISO approach is flawed when disturbance rejection is compromised by stability requirements. This rationale is pursued in sections 6.3 and 6.4 with a detailed analysis of the stability of a two-input, two-output test system. From this analysis general guidelines are derived, to recommend test conditions under which multivariable control would be most suitable [10, 15].

### 6.2 SISO and Multivariable approaches to controlling multi-channel tests

Figure 6.1 shows a SISO test under feedback control. It is well understood that good disturbance rejection can be achieved if a high gain controller can be used,

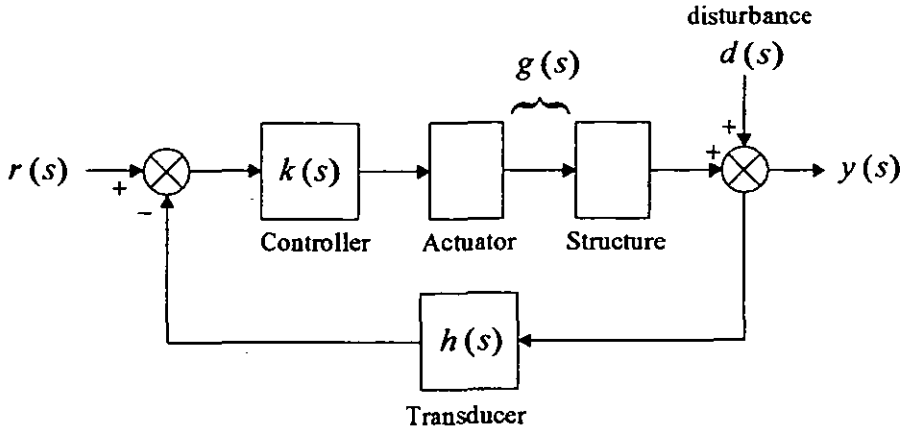


**Figure 6.1** Single-input, Single-output system with a disturbance

providing that the stability of the system is not prejudiced.

Now consider the general case of a test with multiple inputs and outputs. The discussion throughout the remainder of this section applies to the general case and is illustrated by way of a two-input, two-output dynamic structural test. The dynamics of the structure in a two-input, two-output test can be represented by a transfer function matrix (TFM)  $G(s)$  where

$$G(s) = \begin{bmatrix} g_{11}(s) & g_{12}(s) \\ g_{21}(s) & g_{22}(s) \end{bmatrix} \quad (6.1)$$

The off-diagonal elements  $g_{12}(s)$  and  $g_{21}(s)$  describe the cross-coupling present in the specimen. The open-loop block diagram for this test is illustrated in Figure 6.2 and shows explicitly the two inputs and the two outputs. It is clear from the Figure that the dynamic coupling in the specimen is responsible for the interaction in the system.

In principal, the SISO approach to controlling this plant is to design a feedback controller for the first input-output pair, then, when completed successfully, move onto the second input-output pair. In the general case,  $n$  actuators are used to control the force or displacement at  $n$  points on the structure and so  $n$  control loops are installed. This is the Sequential Loop Closure (SLC) approach described in chapter 5. In practice the process becomes iterative, as the successive tuning of each loop controller can destroy the performance achieved in previous loops. A further complication arises with hydraulic actuation in that all loops must be closed simultaneously before tuning, to prevent drift of the actuators. This SLC control scheme is illustrated in Figure 6.3

where the transfer function matrix  $G(s)$  also incorporates the dynamics of the actuators

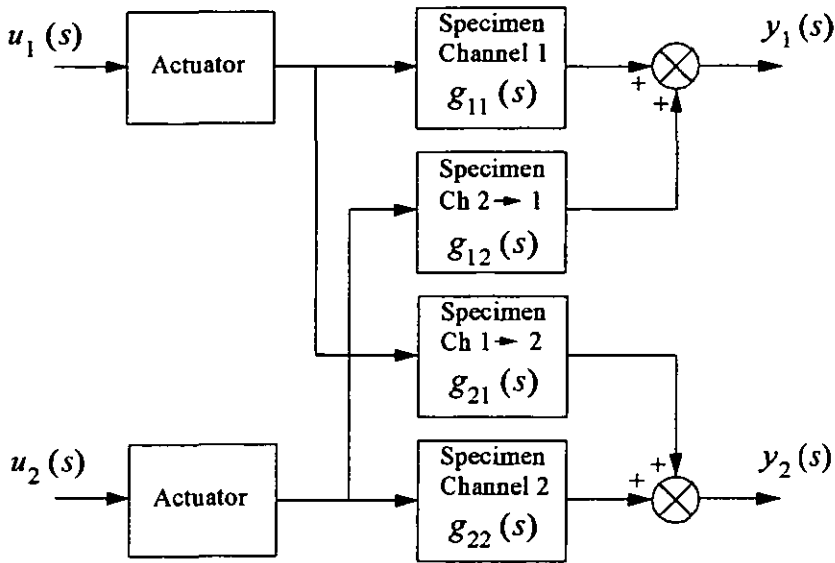


Figure 6.2 Open-loop test with two inputs and two outputs

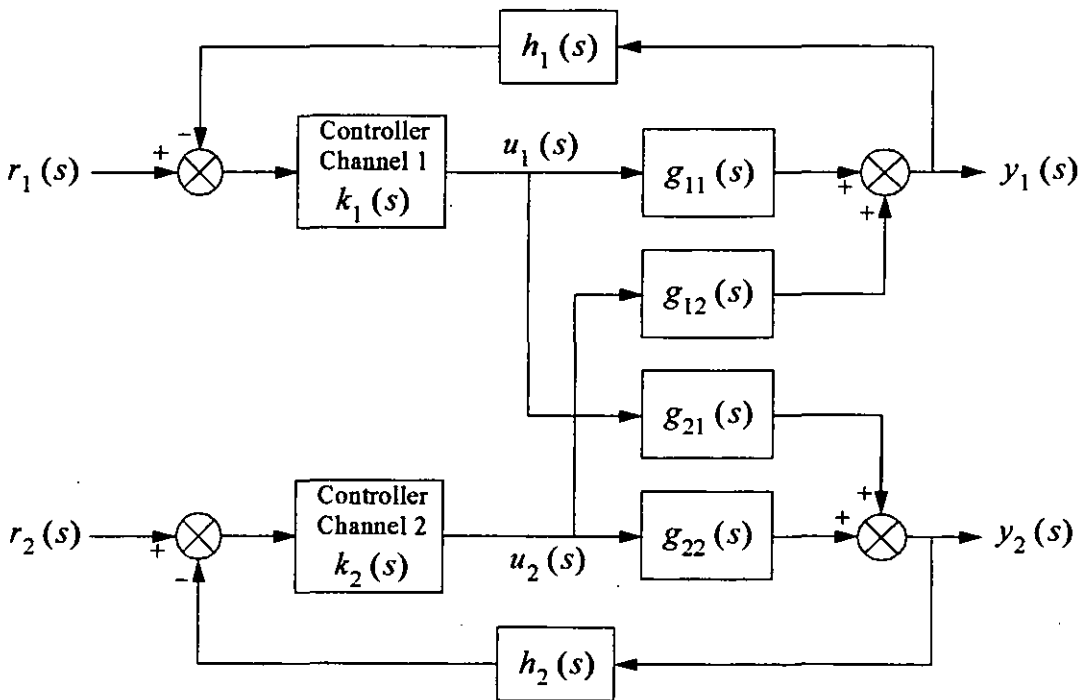


Figure 6.3 Two-channel test seen as two SISO systems

It can be seen in Figure 6.3 that the interaction is viewed as a disturbance by an individual channel. Thus, providing stability margins are maintained, the interaction can be suppressed with high gain controllers. This proviso is crucial to the success of SLC.

Now consider the same test under multivariable control, this is illustrated in Figure 6.4. The controller  $K(s)$  has the structure

$$K(s) = \begin{bmatrix} k_{11}(s) & k_{12}(s) \\ k_{21}(s) & k_{22}(s) \end{bmatrix} \quad (6.2)$$

The gains  $k_{12}(s)$  and  $k_{21}(s)$  provide interaction in the controller itself, which gives the engineer a greater ability to compensate for the interaction in the open-loop plant. Fundamentally, the multivariable nature of the control problem is being tackled in a true multivariable manner.

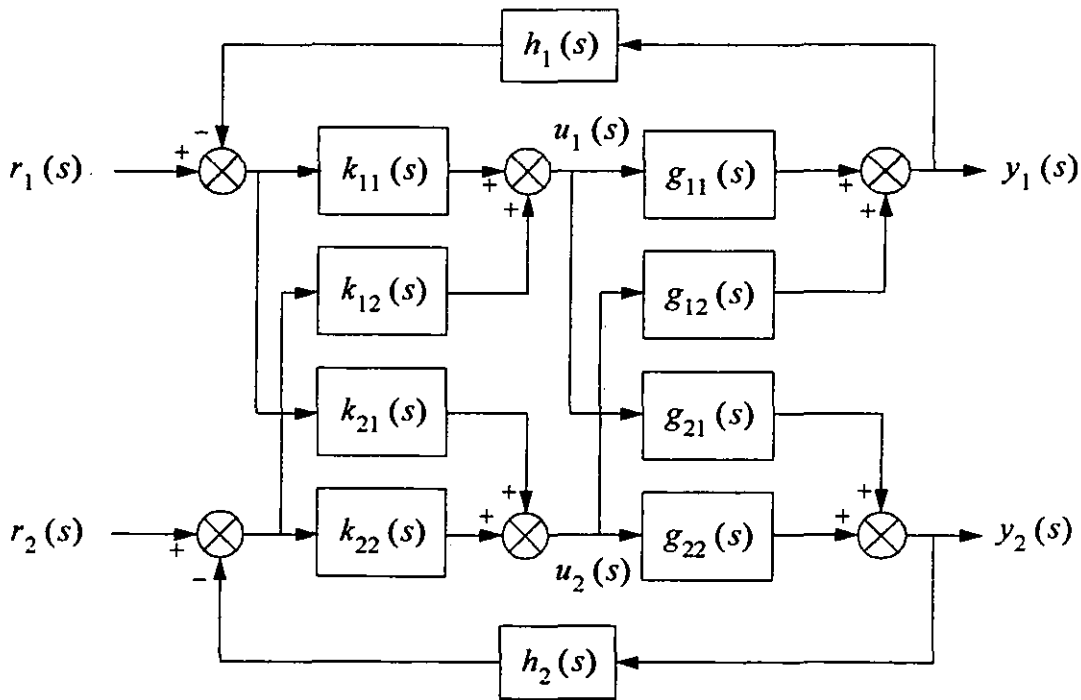


Figure 6.4 Two-channel test with multivariable control

### 6.3 Stability analysis for SISO tests

From the foregoing section it is clear that the performance of a SLC scheme will suffer when disturbance rejection is poor. This situation occurs when controller gains have to be reduced to maintain stability. Consequently, dynamic structural tests likely to suffer from poor performance under SLC control may be identified as those in which the loop gains are necessarily low to maintain stability. This reasoning, however, needs to be extended to be of real use: that is, to relate poor performance under SLC control to the relative mass and stiffness of the structure under test. Guidelines can then be constructed for identifying dynamic structural tests that stand to gain significantly from multivariable control:

It is instructive to first consider the stability characteristics of a SISO test with respect to the mass and stiffness of the specimen. Stability is easily visualised as a function of mass and stiffness, and this provides an insight to the corresponding behaviour to be expected of a MIMO system

#### 6.3.1 Displacement control

The system studied in this section has been modelled in chapter 4, the schematic is repeated below and the nominal model data are given in appendix 4.

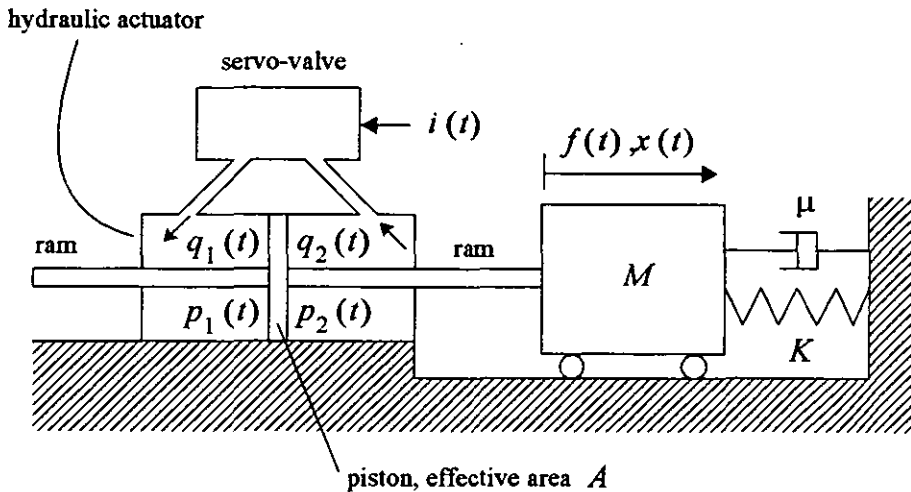


Figure 6.5 Schematic of a SISO system

Likewise, the transfer function has been derived in chapter 4 and is repeated in equation (6.3):

$$\frac{\Delta x(s)}{\Delta i(s)} = \frac{K_x}{(s + \omega_l) (s^2 + 2\zeta_T \omega_T s + \omega_T^2) (s^2 + 2\zeta_h \omega_h s + \omega_h^2)} \quad (6.3)$$

The torque-motor contributes a pair of heavily damped poles to the transfer function (the quadratic factor  $(s^2 + 2\zeta_T \omega_T s + \omega_T^2)$  in the denominator) and the quadratic factor  $(s^2 + 2\zeta_h \omega_h s + \omega_h^2)$  describes a very lightly damped pair of poles, referred to as the 'hydraulic' poles, arising from the mass of the structure oscillating with the very stiff spring formed by the volume of compressible oil in the actuator. The remaining simple pole at  $s = -\omega_l$  can be regarded approximately as an integrator as typically  $\omega_l \approx 0$ .

The SISO system is controlled under the scheme in Figure 6.1 with  $g(s) = \Delta x(s) / \Delta i(s)$ . For the remainder of this chapter the gain  $k(s)h(s)$  is constant, i.e.  $k(s)h(s) = kh$ . The pole locations of  $g(s)$ , with the nominal model data, are shown in Figure 6.6 as 'x'. This Figure shows the loci of the poles of the closed-loop system as the gain  $kh$  is increased. It can be seen that as the gain increases, the hydraulic poles move into the unstable right-half complex plane. The gain at which the hydraulic poles cut the imaginary axis is the 'critical' gain, when the closed-loop system is at the limit of stability.

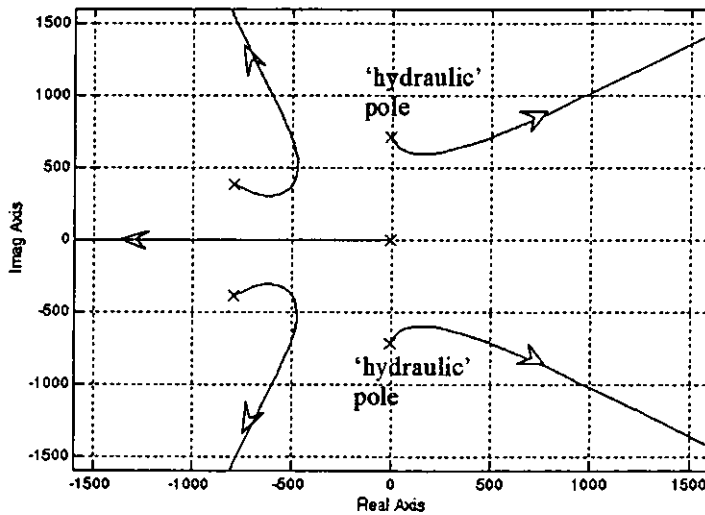


**Figure 6.6** Root-locus plot of nominal SISO displacement system

Recall from chapter 4 that the hydraulic natural frequency  $\omega_h$  strongly depends upon the mass of the specimen, whilst the hydraulic damping ratio  $\zeta_h$  is strongly influenced by the stiffness. These two quantities are plotted in Figure 6.7 for a model

with the hydraulic data given in appendix 4 and a range of mass and stiffness values given in tables A4.3 and A4.4 in appendix 4. Since  $\omega_h$  and  $\zeta_h$  are clearly dependent upon the mass and stiffness of the specimen, and also describe the location of the 'hydraulic poles', it is reasonable to suspect that stability will also be affected by mass and stiffness. The following study will investigate the nature of the relationship between stability and the mass and stiffness of the specimen.

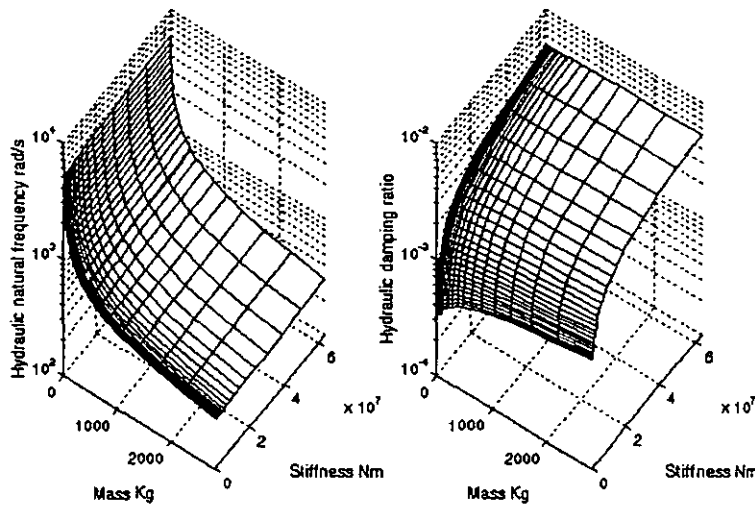


**Figure 6.7** Effect of mass and stiffness variation upon  $\omega_h$  and  $\zeta_h$

Consider the nominal system under closed-loop control with the controller gain  $kh$  at the critical value, i.e. the closed-loop system is at the limit of stability. Now, consider the effect upon stability of changing the mass and stiffness of the specimen whilst the controller gain remains constant. A locus of closed-loop pole positions can be obtained as the mass of the specimen changes whilst the stiffness is held constant. This can be repeated with differing values of stiffness, thus obtaining a family of loci to illustrate the stability of system through the movement of its closed-loop poles. Such a family of loci are presented in Figure 6.8, where the poles of the nominal closed-loop system, with critical gain, are indicated by stars.

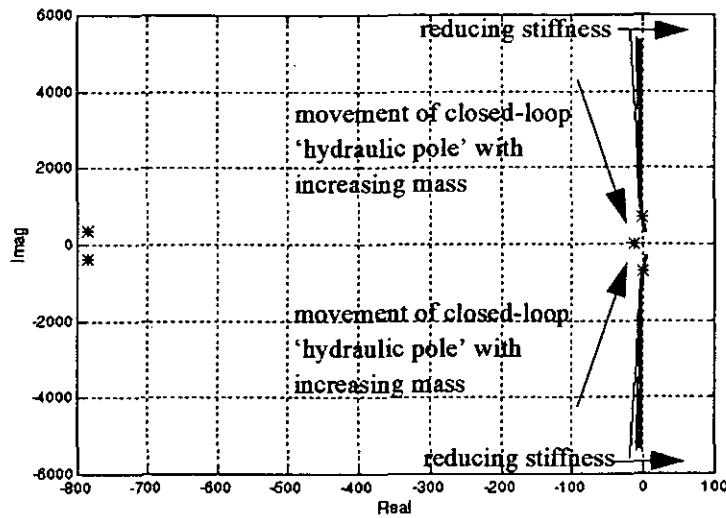


**Figure 6.8 Root loci of SISO displacement system with changing mass and stiffness**

Figure 6.8 shows that the location of the closed-loop 'hydraulic' poles are clearly dependent upon the mass and stiffness of the specimen whilst the other closed-loop poles remain virtually stationary. This dependence is shown in more detail in Figure 6.9, where each curve is the locus of a closed-loop hydraulic pole with varying mass, the family of curves illustrate the effect on the locus of varying the stiffness of the specimen. This figure shows that increasing the mass of the specimen serves to move the 'hydraulic' poles toward, and eventually into, the right half complex plane, thus degrading stability. Conversely, reducing the mass of the specimen moves the hydraulic poles deeper into the left hand complex plane, thus, improving stability. In terms of the stiffness of the specimen, reducing the stiffness serves to move the 'hydraulic' poles closer to the right half complex plane, thereby degrading stability. Conversely, increasing the stiffness of the specimen moves the hydraulic poles away from the left hand complex plane, thus improving stability. In summary, the root loci indicate that the stability of the system will degrade with increasing mass and decreasing stiffness.

Another important observation is that the movement of the pole positions due to changing mass values is far greater than that due to changing stiffness values; note the axes scaling in Figures 6.8 and 6.9. In other words, the mass of the specimen has a greater impact upon stability than does its stiffness.



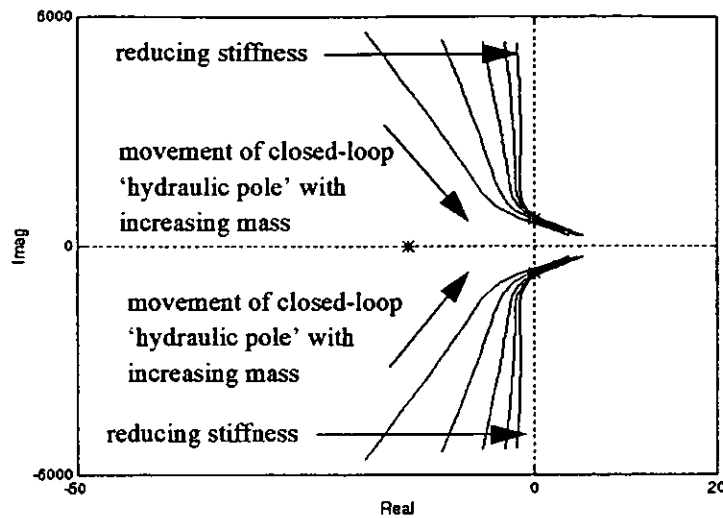


**Figure 6.9 Root loci of SISO displacement system with changing mass and stiffness - detail**

The movement of the closed-loop pole locations certainly indicate the nature of the relationship between stability and the mass and stiffness of the specimen. This relationship is made more apparent when the critical gain of the closed-loop system is determined as a function of mass and stiffness. This will provide a surface of controller gain for which the system becomes unstable and clearly illustrates the relationship, complementing the study of the root loci of the system. The surface for a SISO displacement system with wide mass and stiffness variation is presented in Figure 6.10 (the hydraulic data and mass and stiffness ranges are given in appendix 4, tables A4.1, A4.3 and A4.4 respectively) where, for each pair of mass and stiffness coordinates, the critical gain is determined.

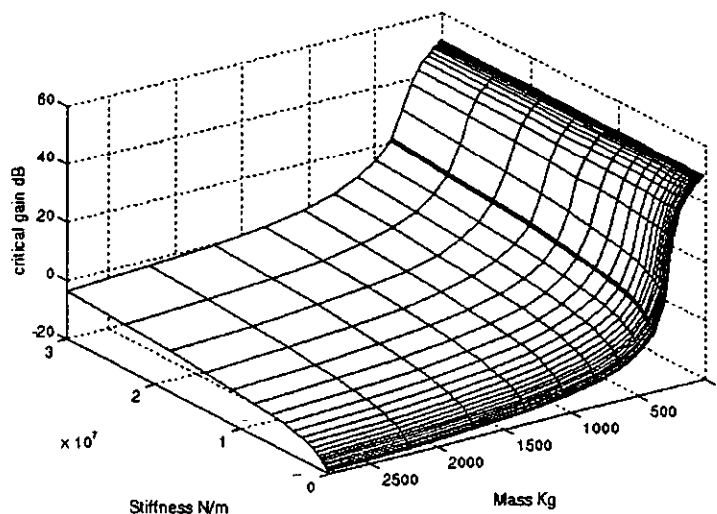


**Figure 6.10 Critical gain surface for SISO displacement system**

It can be clearly seen that low critical gain (and hence poor relative stability) occurs when the specimen has a high mass and that, to a lesser degree, reducing the stiffness further lowers the critical gain. I.e., poor relative stability occurs when the specimen has a low natural frequency. These conclusions concur with those drawn from consideration of the movement of the closed-loop poles of the system.

### 6.3.2 SISO Load Control

The transfer function relating servo-valve current to the force applied by the actuator ram has been derived in chapter 4 and is repeated below in a slightly different form.

$$\frac{\Delta x(s)}{\Delta i(s)} = \frac{K_f(s^2 + 2\zeta_p\omega_p s + \omega_p^2)}{(s + \omega_l)(s^2 + 2\zeta_T\omega_T s + \omega_T^2)(s^2 + 2\zeta_h\omega_h s + \omega_h^2)} \quad (6.4)$$

The denominator is identical to that in the transfer function for the displacement system and the numerator contains a quadratic factor due to the dynamics of the specimen. Again, the system is controlled under the scheme of Figure 6.1, this time with  $G(s) = \Delta f(s) / \Delta i(s)$ . The root locus plot for this system, with the nominal model data in appendix 4 (tables A4.1 and A4.2), is shown in Figure 6.11. The open-loop poles are marked by 'x' and the open-loop zeros are marked by 'o'. It can be seen that as the gain  $kh$  increases, the hydraulic poles again move into the right half complex plane. The critical gain is the value of the controller gain at which point the hydraulic poles cut the imaginary axis, i.e. the limit of stability.

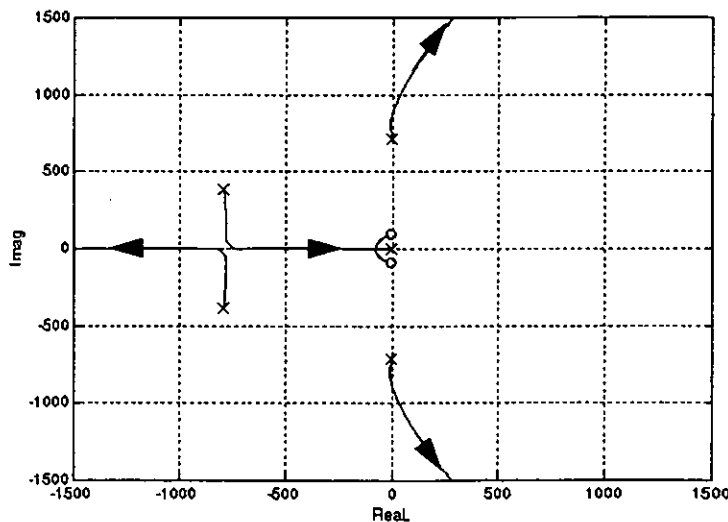
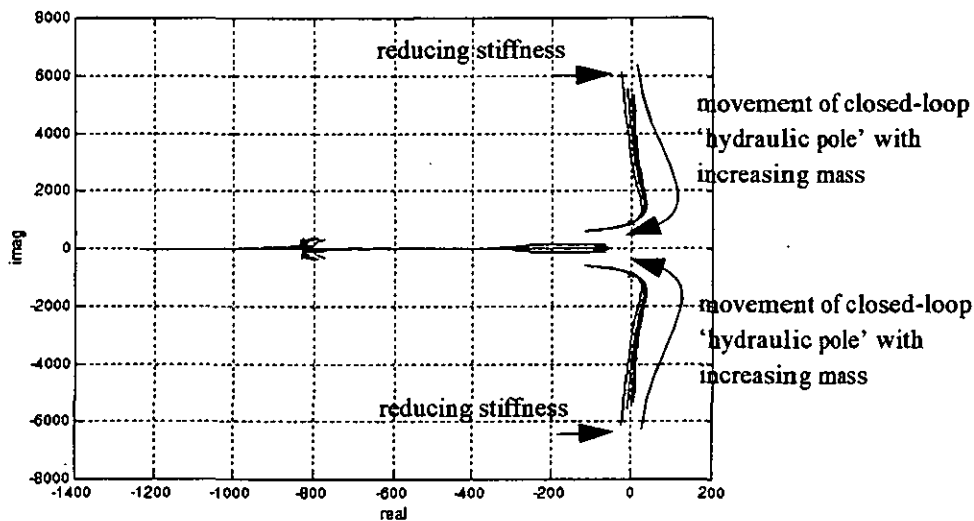


Figure 6.11 Root-locus plot of nominal SISO load system

As with the study of the displacement system, stability is investigated by considering the effect of mass and stiffness variation upon closed-loop pole positions and the effect upon the controller gain required to destabilise the system. Attention is focused on the relationship between relative stability and the mass and stiffness of the specimen, this is explained in the remainder of the section.

Consider the nominal system under closed-loop control with the controller gain  $kh$  at the critical value, i.e. the closed-loop system is at the limit of stability. Now, consider the effect upon stability of changing the mass and stiffness of the specimen whilst the controller gain remains constant. A locus of closed-loop pole positions can be obtained as the mass of the specimen changes whilst the stiffness is held constant. This can be repeated with differing stiffness values, thus obtaining a family of loci to illustrate the stability of the system through the movement of its closed loop poles. Such a family of loci are illustrated in Figure 6.12, where the poles of the nominal closed-loop system, with critical gain, are indicated by stars. The range of mass and stiffness values are given in appendix 4 (tables A4.3 and A4.4).



**Figure 6.12 Root loci of SISO load system with changing mass and stiffness**

Figure 6.12 clearly shows that the location of the closed-loop 'hydraulic' poles are again dependent upon the mass and stiffness of the specimen. The other closed-loop poles, whilst undergoing a degree of movement, are constrained to the left-half complex plane and so can be disregarded from a stability point of view. The movement of the hydraulic poles is shown in more detail in Figure 6.13, where each curve is the locus of a closed-loop hydraulic pole with varying mass, the family of curves illustrate

the effect on the locus of varying the stiffness of the specimen. Consider that the specimen has a low mass, then the closed-loop hydraulic poles will be located at the extremity of the loci as indicated in the Figure. As the mass increases, the closed-loop poles move further to the right in the s-plane, degrading the stability of the system. With the model data in appendix 4 (tables A4.1 and A4.2), worst case stability occurs, for all stiffness values, when the hydraulic natural frequency is in the range  $1.5\omega_T$  to  $1.7\omega_T$ . The corresponding mass values can be determined from the approximation in equation (4.64), as below.

$$1.5\omega_T < \sqrt{\frac{K_B A^2}{MV_0}} < 1.7\omega_T \quad (6.5)$$

Re-arranging equation (6.5) and inserting the hydraulic model data gives the following range of mass that correspond to worst-case stability.

$$89\text{Kg} < M < 113\text{Kg} \quad (6.6)$$

The factors of  $1.5\omega_T$  and  $1.7\omega_T$  in equation (6.5) are valid for the model data used. With values of mass greater than equation (6.6), the family of root loci are tightly bunched - in other words, the stiffness of the specimen has negligible effect upon stability. However, when the mass of the specimen falls into, and below, the range for worst case stability, equation (6.6), the family of root loci spread out and the stiffness of the specimen has some effect; in this region, reducing the stiffness moves the hydraulic poles further to the right in the s-plane and degrades stability.

An important observation to make is that the movement of the pole positions due to changing mass values is far greater than that due to changing stiffness values; note the axes scaling in Figures 12 and 13. Hence, as in the displacement system, the mass of the specimen has a greater impact upon stability than does its stiffness.

In summary, the root loci indicate that the stability of the system will degrade as the mass of the specimen increases from zero to the range given in equation (6.6), which represents worst case stability. Simultaneously, a reduction in stiffness will further degrade stability. However, as the mass increases beyond the worst case range, stability will improve and the effect of stiffness upon stability will be negligible.

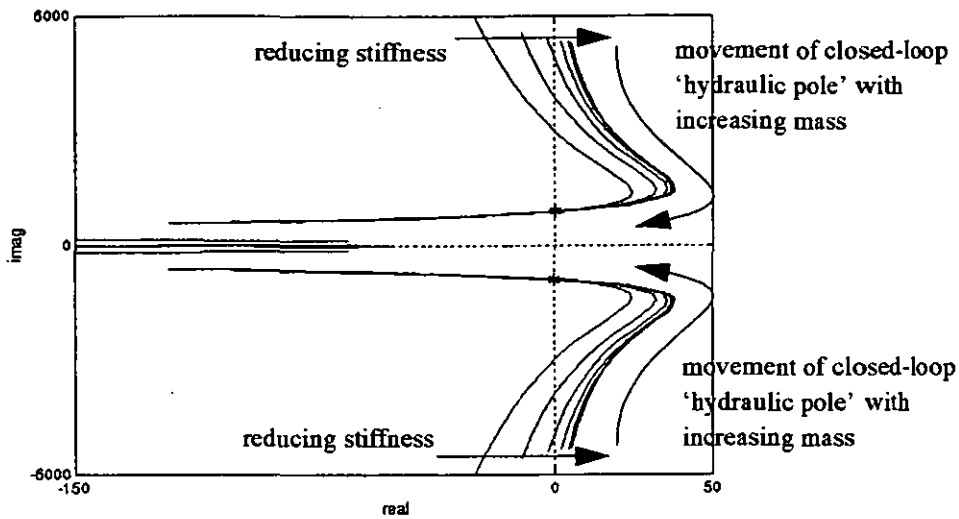


**Figure 6.13 Root loci of SISO load system with changing mass and stiffness - detail**

As in the study of the displacement system, the relationship between stability and the mass and stiffness of the specimen is more apparent when the surface of critical gain is determined for the closed-loop system. With the model data and the range of mass and stiffness values given in appendix 4, the critical gain surface in Figure 6.14 is obtained. Once again, the surface shows controller gains at which the closed-loop system becomes unstable, as a function of mass and stiffness. The surface clearly illustrates the stability characteristics of the system and exhibits a prominent 'valley' at a low value of mass, which occurs in the range given in equation (6.6). The behaviour illustrated by the surface agrees with that deduced from the root loci study: as the mass increases from zero up to the worst case value, stability is degraded whilst at the same time a reduction in stiffness worsens the situation. Beyond the worst case value, increasing the mass improves stability and the stiffness no longer has an observable effect. The surface also shows that at high values of mass, the critical gain is constant and mass now has no effect upon stability.

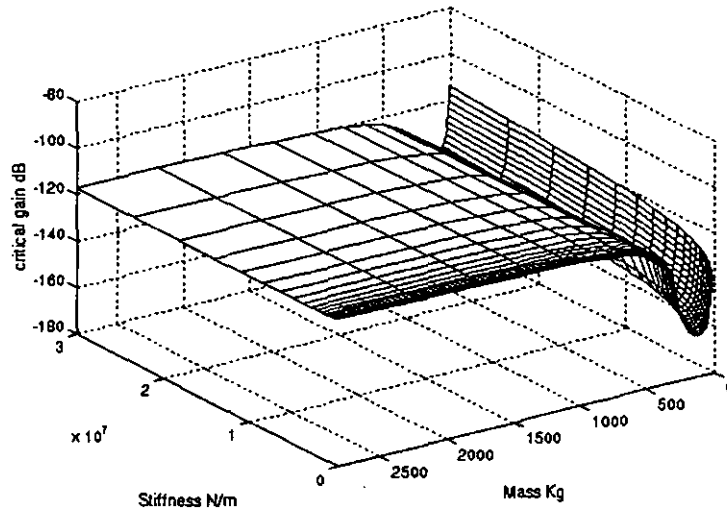


Figure 6.14 Critical gain surface for SISO displacement system

## 6.4 Stability analysis for MIMO tests

A structural test may involve several actuators. To simplify the analysis in this section, a test with two actuators is considered and the specimen is represented by a two degree-of-freedom mass-spring-damper arrangement as shown in Figure 6.15. The damping configuration allows both vibrational modes to have the same damping ratio (see chapter 4).

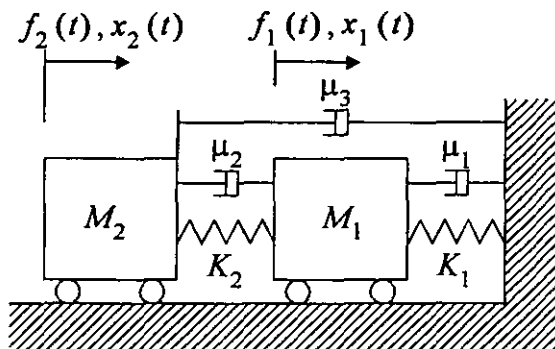


Figure 6.15 Two degree-of-freedom specimen for a MIMO test

The masses are excited by two identical hydraulic actuators, the actuators are described in chapter 4. Using the notation in Figure 6.15, with  $f(s) = \begin{bmatrix} f_1(s) & f_2(s) \end{bmatrix}^T$  and  $x(s) = \begin{bmatrix} x_1(s) & x_2(s) \end{bmatrix}^T$ , the dynamics of the structure are described by equation (6.7).

$$f(s) = (s^2 M + sB + K)x(s) \quad (6.7)$$

where

$$\begin{aligned} M &= \begin{bmatrix} m_1 & 0 \\ 0 & m_2 \end{bmatrix} \\ B &= \begin{bmatrix} (\mu_1 + \mu_2) & -\mu_2 \\ -\mu_2 & (\mu_2 + \mu_3) \end{bmatrix} \\ K &= \begin{bmatrix} (k_1 + k_2) & -k_2 \\ -k_2 & k_2 \end{bmatrix} \end{aligned} \quad (6.8)$$

The specimen now has four parameters that influence stability,  $K_1$ ,  $K_2$ ,  $M_1$  and  $M_2$ , complicating the task of relating their combined effect to stability. To build upon the previous SISO investigation it is desirable to normalise these mass and stiffness elements as shown below.

$$\begin{aligned} M &= m \begin{bmatrix} 1 & 0 \\ 0 & \beta \end{bmatrix} \\ K &= k \begin{bmatrix} (1 + \gamma) & -\gamma \\ -\gamma & \gamma \end{bmatrix} \end{aligned} \quad (6.9)$$

This provides a more useful description of the specimen: homogenous variation in the material constants of the specimen, or the scaling of the specimen, are reflected in variation in  $m$  and  $k$  whilst  $\beta$  and  $\gamma$  are constant; conversely, local variations in the structure of the specimen are reflected in variations in  $\beta$  and  $\gamma$  whilst  $m$  and  $k$  are constant.

#### 6.4.1 Multivariable displacement control

The block diagram of the open-loop system has been presented in chapter 4. A state-space model of the system can be readily obtained by combining state-space representations of the individual blocks. The eigenvalues of the state-space model, using the nominal model data in appendix 5 (Tables A5.1 and A5.2), are given below.

**TABLE 6.1 Eigenvalues of the state-space model of the nominal displacement system**

Eigenvalue	Description
$-792 \pm j383.6$	Complex 'servo-valve' pole pair
$-792 \pm j383.6$	Complex 'servo-valve' pole pair
$-2.58 \pm j1211.7$	Complex 'hydraulic' pole pair
$-1.08 \pm j1190.6$	Complex 'hydraulic' pole pair
$-0.0121$	Real pole close to s-plane origin (i.e. approximate integrator)
$-0.0018$	Real pole close to s-plane origin (i.e. approximate integrator)
$-0.93 \pm j92.9$	Complex pole pair in the response of the specimen, $x(s) = (s^2M + sB + K)^{-1}f(s)$
$-2.43 \pm j243.2$	complex pole pair in the response of the specimen, $x(s) = (s^2M + sB + K)^{-1}f(s)$

The eigenvalues are very similar in nature to the poles of the SISO displacement system; those of the servo-valves, 'hydraulic' poles and 'integrator' poles.

As with the SISO systems, the test is controlled under the scheme in Figure 6.1 with  $\Delta x(s) = G(s)\Delta i(s)$ . The gain  $K(s)H(s)$  is again constant and the individual controller gains are restricted to being identical, thus the gain matrix is written

$$KH = c \begin{bmatrix} 1 & 0 \\ 0 & 1 \end{bmatrix} \quad (6.10)$$

The pole locations of  $G(s)$  with nominal model data are shown in Figure 6.16 as 'x', the model data is found in appendix 5. This figure shows the loci of the poles of the closed-loop system as the gain  $c$  is increased. The behaviour of the pole locations is similar to that in the SISO displacement system and it is the 'hydraulic' poles that move into the right half complex plane, resulting in instability. The critical gain is the limiting value of  $c$  beyond which the closed-loop system becomes unstable, the pole locations at critical gain are shown on Figure 6.16 as 'o'. The figure also shows that the poles due to the response of the specimen are unaffected by the gain of the controller.



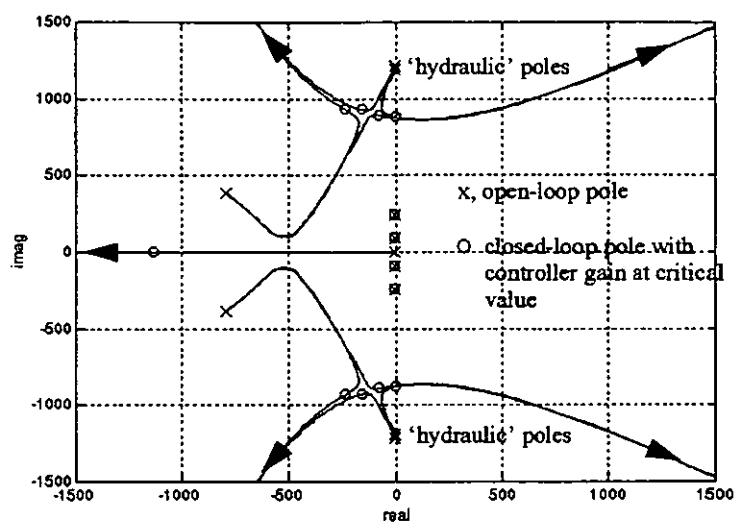


Figure 6.16 Multivariable root locus plot of nominal displacement system

Consider the nominal system under closed-loop control with the controller gain  $KH$  at the critical value, i.e. the closed-loop system is at the limit of stability. Furthermore, consider the effect upon stability of homogenously changing the mass of the specimen whilst the controller gain and the stiffness remain constant, i.e  $m$  varies whilst  $k$ ,  $\beta$  and  $\gamma$  remain constant in equation (6.9). A locus of closed-loop pole positions can be obtained to illustrate the stability of system and is presented in Figure 6.17, where the poles of the nominal closed-loop system, with critical gain, are indicated by 'o'. The model data and range in mass values are given in appendix 5 (tables A5.1 and A5.3).

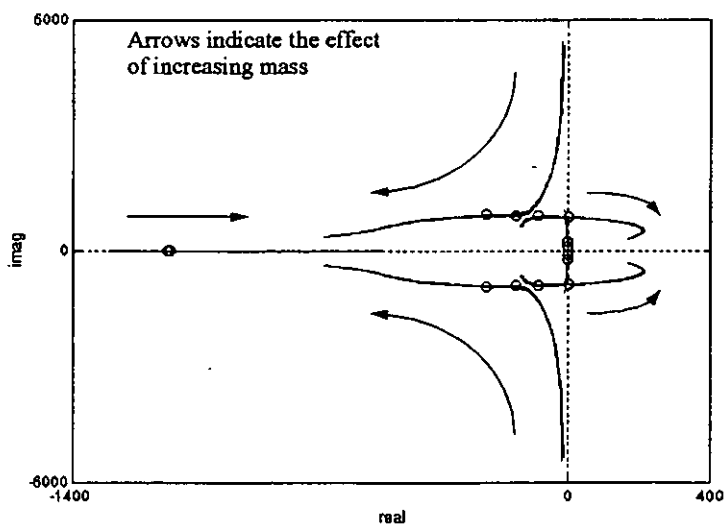
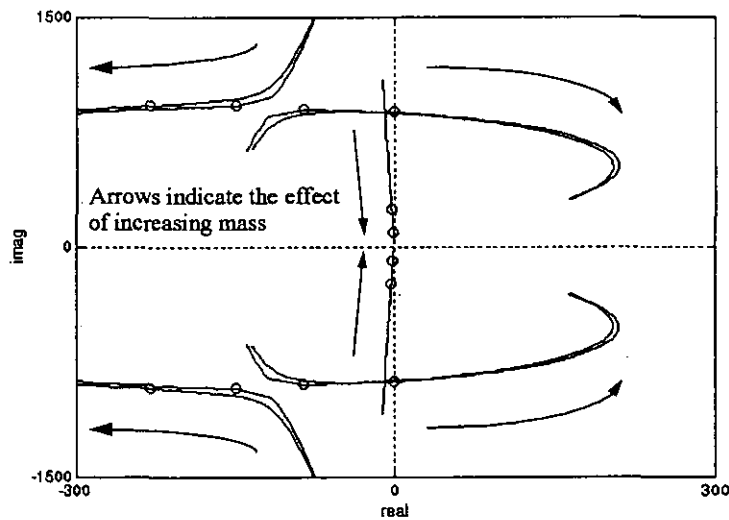


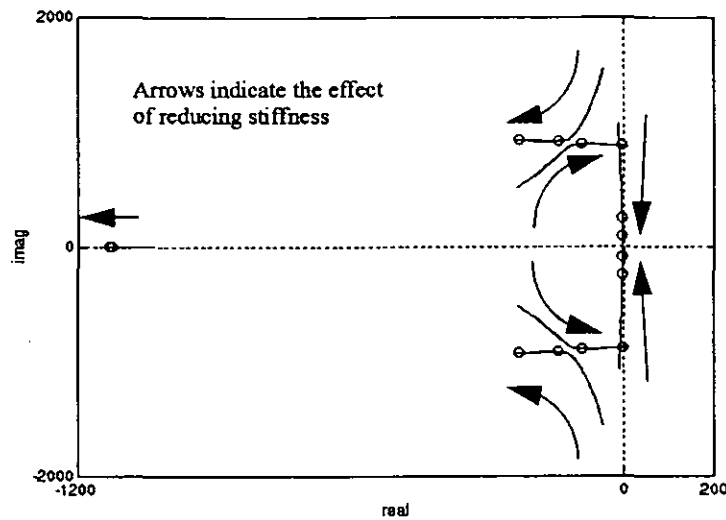
Figure 6.17 Multivariable root loci of displacement system with varying  $m$

Figure 6.17 shows that the poles of the closed-loop system are clearly dependent upon the mass of the system and in particular, two pairs of complex poles move toward, and into, the right half complex plane as the mass increases. The region containing the unstable loci is shown in more detail in Figure 6.18, the closed-loop poles with nominal model data are again marked on the plot with 'o'. As in the previous case when the controller gain was increased, the 'hydraulic' poles are responsible for causing the instability, this time as the mass of the specimen increases. Figure 6.18 also show two pairs of complex poles moving along lines of constant damping toward the origin of the s-plane: these are the poles due to the response of the specimen and will remain stable as the specimen itself is stable.



**Figure 6.18 Multivariable root loci of displacement system with varying  $m$  - detail**

Let us now return to the nominal system under closed-loop control with the controller gain  $KH$  still at the critical value, i.e. the closed-loop system is at the limit of stability. Now, consider the effect upon stability of homogenously changing the stiffness of the specimen whilst the controller gain and the mass remain constant, i.e.  $k$  varies whilst  $m$ ,  $\beta$  and  $\gamma$  remain constant in equation (6.9). The corresponding loci of closed-loop pole positions is illustrated in Figure 6.19, where the poles of the nominal closed-loop system, with critical gain, are indicated by 'o'. The model data and stiffness variation are given in appendix5 (tables A5.1 and A5.4).



**Figure 6.19** Multivariable root loci of displacement system with varying  $k$

Figure 6.19 shows that the poles of the closed-loop system are dependent upon the stiffness of the system. However, the dependency is far less than that observed in the case when the mass of the specimen was varying (Figure 6.17). The region close to the unstable right-half s-plane is shown in more detail in Figure 6.20, the closed-loop poles with nominal model data are again marked on the plot with 'o'. The 'hydraulic' poles move toward, and eventually into, the right-half plane as the stiffness of the specimen reduces. However, the penetration into the unstable right-half s-plane is very limited. Thus, a reduction in stiffness is destabilising but not as great as the destabilising effect of increasing the mass of the specimen. Figure 6.20 also shows two pairs of complex poles moving along lines of constant damping toward the origin of the s-plane: these are, again, the poles due to the response of the specimen and will remain stable as the specimen itself is stable.

The movement of the closed-loop poles certainly indicate the nature of the relationship between stability and the mass and stiffness of the specimen. This relationship is made more apparent when the critical gain of the closed-loop system is determined as a function of mass and stiffness. This will provide a surface of controller gain for which the system becomes unstable and clearly illustrates the relationship, complementing the study of the root loci of the system. The surface for a MIMO displacement system with wide mass and stiffness variation is presented in Figure 6.21 (the hydraulic data and mass and stiffness ranges are given in appendix 5; tables A5.1, A5.3 and A5.4 respectively) where, for each pair of mass and stiffness coordinates, the critical gain is determined. It can be clearly seen that low critical gain (and hence poor relative stability) occurs when the specimen has either a low stiffness, a high mass or

both. I.e., when the specimen has low natural frequencies. These conclusions concur with those drawn from consideration of the movement of the closed-loop poles of the system.

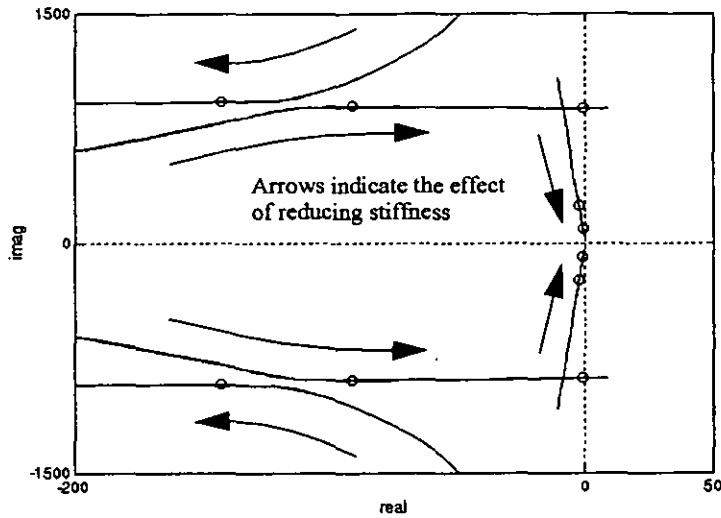


**Figure 6.20** Multivariable root loci of displacement system with varying  $k$  - detail

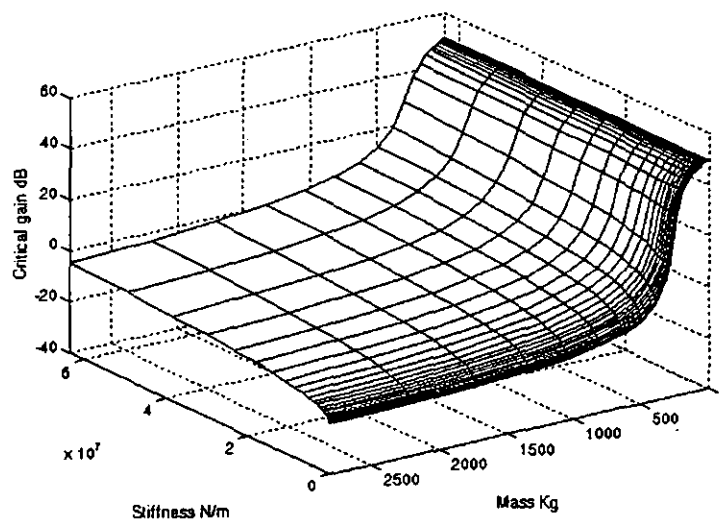


**Figure 6.21** Critical gain surface. Varying  $m$  and  $k$ , fixed  $\beta$  and  $\gamma$

A similar investigation can be conducted into the effect of local structural changes in the specimen, i.e. variation in  $\beta$  or  $\gamma$ . For these cases, the root loci plots are

omitted but the critical gain surface is presented in Figure 6.22, where, for each pair of  $\beta$  and  $\gamma$  coordinates, the critical gain is the gain of the controller at which point the system becomes unstable.

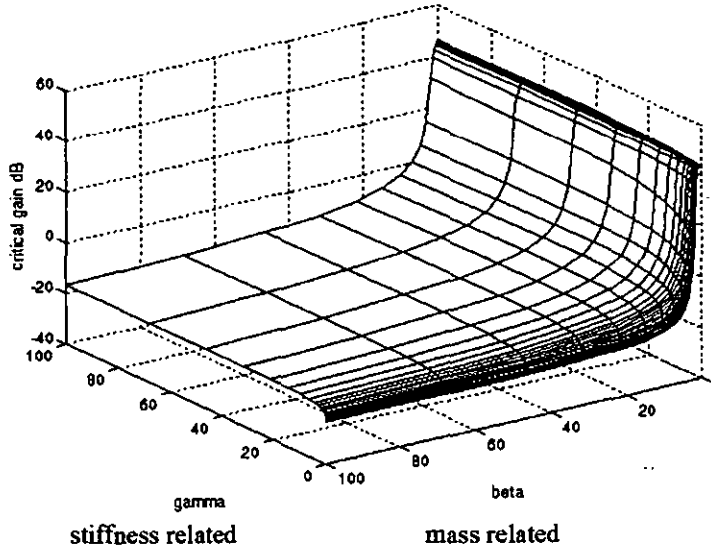


**Figure 6.22** Critical gain surface. Varying  $\beta$  and  $\gamma$ , fixed  $m$  and  $k$

The stability behaviour is very close to that already determined for homogenous variation in mass and stiffness. That is, increasing mass and/or reducing stiffness, i.e. reducing the natural frequencies of the structure, serves to degrade stability.

#### 6.4.2 Multivariable load control

The block diagram of the open-loop system has been presented in chapter 4. A state-space model of the system can be readily obtained by combining state-space representations of the individual blocks. The eigenvalues of the state-space model, using the nominal model data in appendix 5 (tables A5.1 and A5.2), are given below.

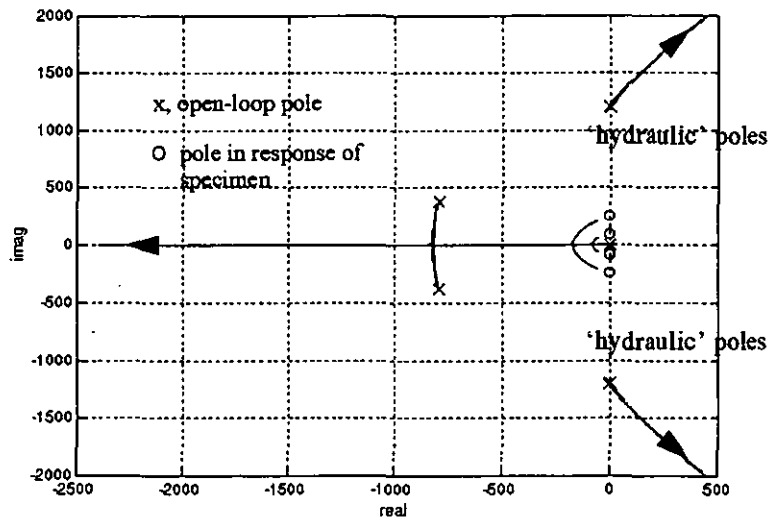
**TABLE 6.2** Eigenvalues of the nominal load system state-space model

eigenvalue	description
$-792 \pm j383.6$	complex 'servo-valve' pole pair
$-792 \pm j383.6$	complex 'servo-valve' pole pair
$-2.58 \pm j1211.7$	complex 'hydraulic' pole pair
$-1.08 \pm j1190.6$	complex 'hydraulic' pole pair
$-0.0121$	real pole close to s-plane origin (i.e. approximate integrator)
$-0.0018$	real pole close to s-plane origin (i.e. approximate integrator)

The eigenvalues are very similar in nature to the poles of the SISO displacement system; those of the servo-valves, 'hydraulic' poles and 'integrator' poles.

As with the SISO systems, the test is controlled under the scheme in Figure 6.1 with  $\Delta f(s) = G(s) \Delta i(s)$ . The gain  $K(s)H(s)$  is again constant and the individual controller gains are restricted to being identical, thus the gain matrix is unchanged from equation (6.10).

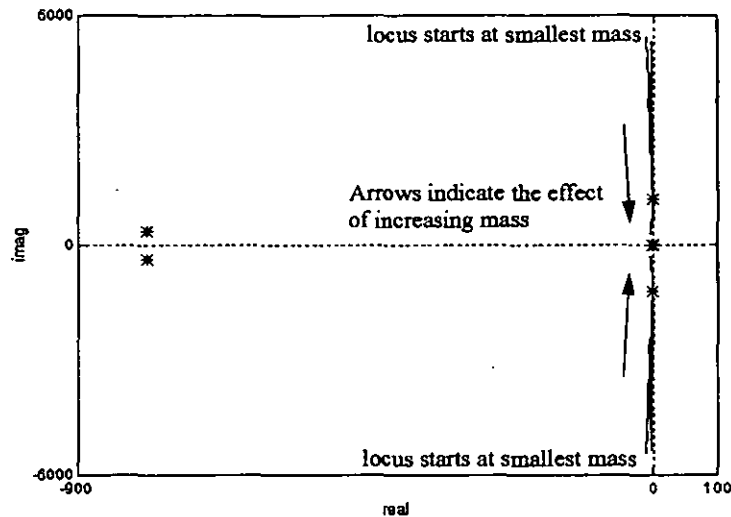
The pole locations of  $G(s)$  with nominal model data are shown in Figure 6.23 as 'x'. The poles in the response of the specimen are also shown on the figure as 'o'. This figure shows the loci of the poles of the closed-loop system as the gain  $c$  is increased. The behaviour of the pole locations is similar to that in the SISO load system and it is the 'hydraulic' poles that move into the right half complex plane, resulting in instability. The critical gain is the limiting value of  $c$  beyond which the closed-loop system becomes unstable.



**Figure 6.23 Multivariable root locus plot of nominal load system**

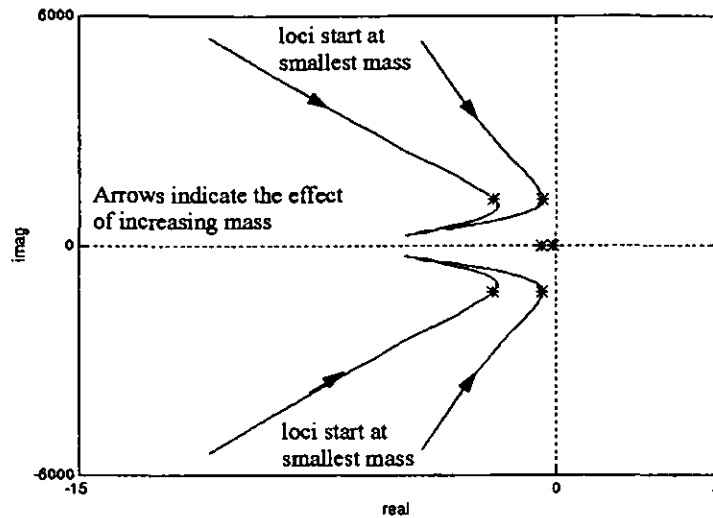
Consider the nominal system under closed-loop control with the controller gain  $KH$  at the critical value, i.e. the closed-loop system is at the limit of stability. Furthermore, consider the effect upon stability of homogeneously changing the mass of the specimen whilst the controller gain and the stiffness remain constant, i.e.  $m$  varies whilst  $k$ ,  $\beta$  and  $\gamma$  remain constant in equation (6.9). A locus of closed-loop pole positions can be obtained to illustrate the stability of system and is presented in Figure 6.24, where the poles of the nominal closed-loop system, with critical gain, are

indicated by '\*'. The model data and range in mass values are given in appendix 5 (tables A5.1 and A5.3).



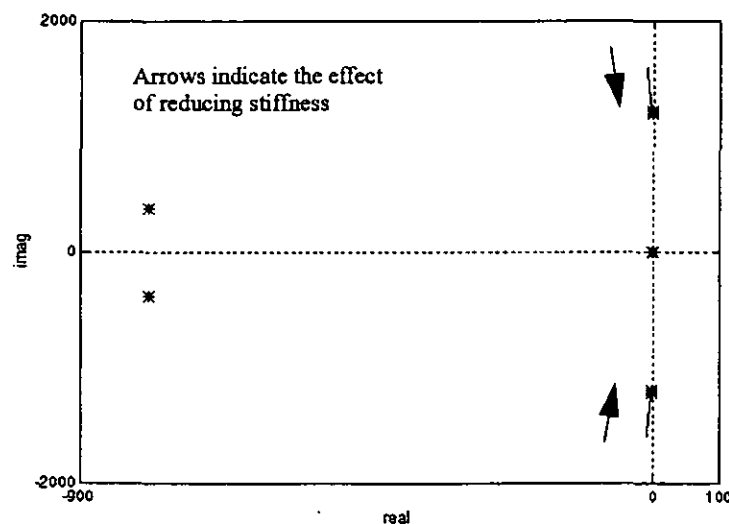
**Figure 6.24** Multivariable root loci of load system as a function of  $m$

Figure 6.24 shows that the poles of the closed-loop system are clearly dependent upon the mass of the system, with significant movement close to the right half-complex plane. This region is shown in more detail in Figure 6.25, the closed-loop poles with nominal model data (and controller gain at the critical value) are again marked on the plot with '\*'. Consider that the specimen has a low mass, then the closed-loop 'hydraulic' poles will be located at the extremity of the loci as indicated in the Figure. As the mass increases, the closed-loop poles decrease in magnitude but move further to the right in the s-plane, degrading the stability of the system until a worst case stability point is reached. With the model data in appendix 5, worst case stability occurs when the mass of the specimen is at the nominal value. As the mass increases beyond this value, the closed-loop poles continue to reduce in magnitude but now move back to the left in the s-plane, thereby recovering from the point of worst case stability.



**Figure 6.25** Multivariable root loci of load system as a function of  $m$  - detail

Let us now return to the nominal system under closed-loop control with the controller gain  $KH$  still at the critical value, i.e. the closed-loop system is at the limit of stability. Now, consider the effect upon stability of homogeneously changing the stiffness of the specimen whilst the controller gain and the mass remain constant, i.e.  $k$  varies whilst  $m$ ,  $\beta$  and  $\gamma$  remain constant in equation (6.9). The corresponding loci of closed-loop pole positions is illustrated in Figure 6.26, where the poles of the nominal closed-loop system, with critical gain, are indicated by '\*'. The model data and stiffness variation are given in appendix 5 (tables A5.1 and A5.4).



**Figure 6.26** Multivariable root loci of load system as a function of  $k$



Figure 6.26 shows that the poles of the closed-loop system are dependent upon the stiffness of the system. However, the dependency is far less than that observed in the case when the mass of the specimen was varying. The region close to the unstable right-half s-plane is shown in more detail in Figure 6.27, the closed-loop poles with nominal model data are again marked on the plot with '\*'. The 'hydraulic' poles move toward, and eventually into, the right-half plane as the stiffness of the specimen reduces. However, the penetration into the unstable right-half s-plane is very limited. Thus, a reduction in stiffness is destabilising but not as great as the destabilising effect of increasing the mass of the specimen.

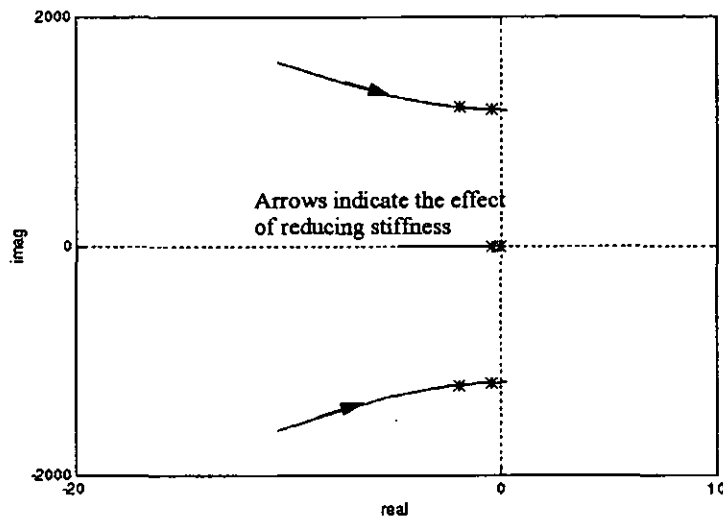


**Figure 6.27 Multivariable root locus of load system as a function of stiffness  $k$  - detail**

The movement of the closed-loop poles certainly indicate the nature of the relationship between stability and the mass and stiffness of the specimen. This relationship is made more apparent when the critical gain of the closed-loop system is determined as a function of mass and stiffness. This will provide a surface of controller gain for which the system becomes unstable and clearly illustrates the relationship, complementing the study of the root loci of the system. The surface for a MIMO load system with wide mass and stiffness variation is presented in Figure 6.28 (the hydraulic data and mass and stiffness ranges are given in appendix 5) where, for each pair of mass and stiffness coordinates, the critical gain is determined. The surface shows a clear 'valley' which represents a region of worst case stability. The 'valley' corresponds directly to the movement of the closed-loop poles in the root loci plots of Figures 6.25 and 6.27. Furthermore, the valley is parallel to the stiffness axis, which

means that worst-case stability is a function of the mass of the specimen only. For the model data in appendix 5, worst case stability occurs when the mass  $m$  is in the range 85 Kg to 181 Kg. This agrees with the root locus study where, with nominal stiffness, worst case stability was found to occur when the mass  $m$  was at it's nominal value of 141 Kg.

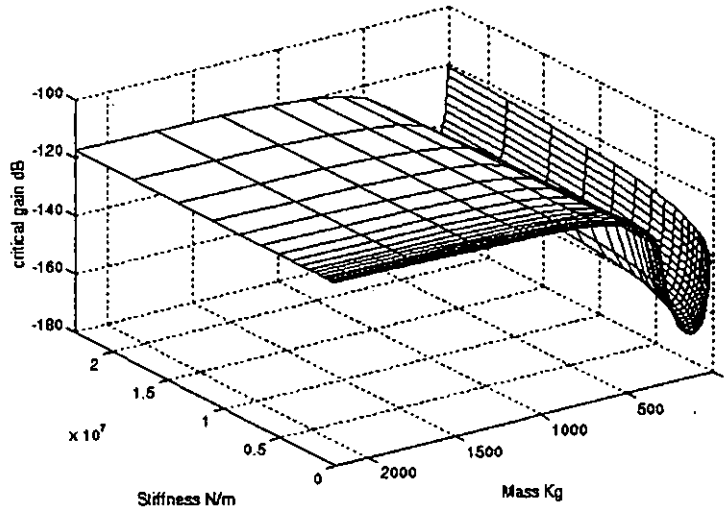


**Figure 6.28 Critical gain surface. Varying  $m$  and  $k$ , fixed  $\beta$  and  $\gamma$**

A similar investigation can be conducted into the effect of local structural changes in the specimen, i.e. variation in  $\beta$  or  $\gamma$ . For these cases, the root locus plots are omitted but the critical gain surface is presented in Figure 6.29, where, for each pair of  $\beta$  and  $\gamma$  coordinates, the critical gain is the gain of the controller at which point the system becomes unstable.

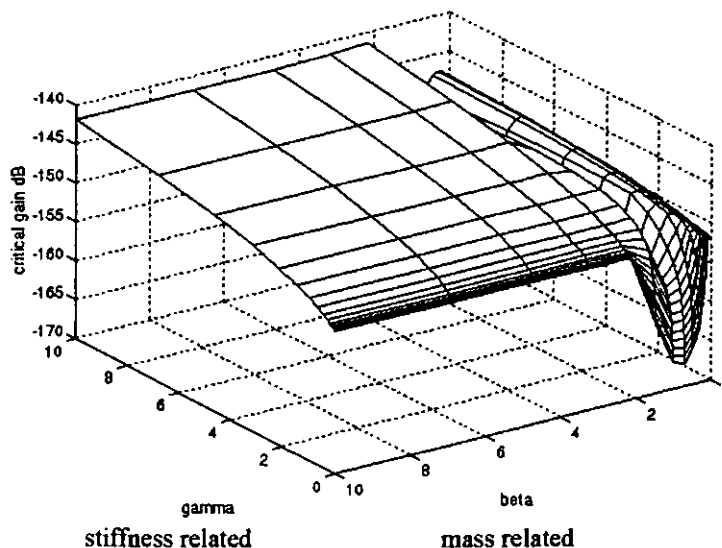


**Figure 6.29 Critical gain surface. Varying  $\beta$  and  $\gamma$ , fixed  $m$  and  $k$**

The stability behaviour is very close to that already determined for homogenous variation in mass and stiffness. That is, the surface shows a clear 'valley' which represents a region of worst case stability. Again, the 'valley' is parallel to the stiffness axis, which means that worst-case stability is a function of the mass of the specimen only. For the model data in appendix 6, worst case stability occurs when  $\beta$  is in the range 0.5 to 1.5.

## **6.5 Guidelines for identifying test conditions best suited to Multivariable control**

From Figures 6.21, 6.22, 6.28 and 6.29 it is clear that a load controlled test suffers from greater stability problems than does a displacement controlled test. In both types, it is also apparent that a change to the mass of the specimen impacts directly upon stability whilst a change to the stiffness of the specimen has relatively little impact upon stability.

In the case of a displacement controlled test, stability worsens as the mass of the specimen increases, and to a much lesser degree, as the stiffness of the specimen reduces. Multivariable control would therefore be most suited to tests where the specimen has a large mass. The stability characteristic of the load controlled test, however, presents a more challenging control problem. Here, the mass of the specimen again causes much more of a problem than does its stiffness. However, the relationship between the critical gain of the system (and hence its relative stability) and the mass of the specimen is not monotonic. The critical gain undergoes a sharp local minimum as the mass increases from zero. In terms of relative stability, the minimum value of the critical gain represents a significant worst-case and it is in this region that the test is best suited to multivariable control methods.

## Chapter 7

# Closed-loop Frequency Response Identification

### 7.1 Introduction

Inherent in multivariable controller design is *a priori* knowledge of a plant model. In the absence of an existing model, one of two approaches must be followed in order to obtain a suitable model (as linear models have been developed thus far, attention will be restricted in this chapter to linear models); either from mathematical modelling of the plant dynamics, or from experimental observations of the plant excitation and resulting response, i.e. system identification. It is not uncommon to find the former method untenable and experimental observation is preferred. For example, although a model of the Torsion rig has been developed in chapter 4, this was not sufficiently accurate for control system design and an experimental frequency response of the rig was required.

Some plants cannot be operated open-loop due to type 1 (integrating) behaviour, economic constraints or safety reasons. In such cases, the identification task is complicated by the imposition of closed-loop control. In a previous paper [46], the identification of the frequency response of a multivariable plant operating under closed-loop control was considered and a correlation technique used. That work is expanded here to demonstrate the suitability of the technique to the closed-loop multivariable experiment and several examples are presented. Furthermore, the correlation technique is simple and robust in the presence of noise, disturbance and harmonics.

A brief discussion of system identification is given in section 7.2, the technique of correlation analysis is discussed in section 7.3 and generalised for the closed-loop multivariable experiment in section 7.4. Applied examples of the technique are presented in section 7.5.

## Chapter 7

# Closed-loop Frequency Response Identification

### 7.1 Introduction

Inherent in multivariable controller design is *a priori* knowledge of a plant model. In the absence of an existing model, one of two approaches must be followed in order to obtain a suitable model (as linear models have been developed thus far, attention will be restricted in this chapter to linear models); either from mathematical modelling of the plant dynamics, or from experimental observations of the plant excitation and resulting response, i.e. system identification. It is not uncommon to find the former method untenable and experimental observation is preferred. For example, although a model of the Torsion rig has been developed in chapter 4, this was not sufficiently accurate for control system design and an experimental frequency response of the rig was required.

Some plants cannot be operated open-loop due to type 1 (integrating) behaviour, economic constraints or safety reasons. In such cases, the identification task is complicated by the imposition of closed-loop control. In a previous paper [46], the identification of the frequency response of a multivariable plant operating under closed-loop control was considered and a correlation technique used. That work is expanded here to demonstrate the suitability of the technique to the closed-loop multivariable experiment and several examples are presented. Furthermore, the correlation technique is simple and robust in the presence of noise, disturbance and harmonics.

A brief discussion of system identification is given in section 7.2, the technique of correlation analysis is discussed in section 7.3 and generalised for the closed-loop multivariable experiment in section 7.4. Applied examples of the technique are presented in section 7.5.

## 7.2 System identification

Extensive work over the past twenty years or so has been conducted in the field of system identification, the interested reader is referred to several established texts, for example Ljung [47] and Soderstrom and Stoica [48], and many review papers, e.g. Godfrey [49], Ljung and Glover [50], Wellstead [51] and Unbehauen and Rao [52]. The main thrust of research activity has been concerned with the identification of plants with some assumed model structure, the objective being to identify the model parameters. Such identification methods are known as 'parametric' and are based on input-output observations of the open-loop plant. 'Non Parametric' methods do not presume a model structure and yield constructions such as frequency responses and impulse responses. Both methods suffer from difficulties when the plant is operated in a closed-loop regime, the introduction of feedback sometimes makes it impossible to identify all of the model parameters [47, pp 365-368]. In such circumstances the validity of a parametric method must obviously be questioned but non-parametric constructions can still be found. Unfortunately, comparatively little attention has been paid to closed-loop identification methods.

Several techniques exist for identifying open-loop non-parametric constructions [49, 51], in this paper only frequency response models are considered for controller design. The simplest technique is to excite the plant with a sinusoid and measure the gain and phase change between input and output. In the presence of noise, disturbance and harmonics this technique is obviously unacceptable. Spectral techniques are superior but are computationally involved and their application to the closed-loop is not straightforward. Correlation analysis is a straightforward technique yielding accurate results, known to give very good immunity to noise [49], and is further acknowledged as a very robust practical method [51], found at the heart of many commercially available frequency-response analysers. Indeed it is for these reasons that the practitioner is drawn to correlation analysis. Surprisingly, there appears to be no mention in the literature of applying this technique to a multivariable plant operating in the closed-loop, although in addressing the same identification problem Melo and Friedly [53] have proposed a technique employing fast Fourier transforms.

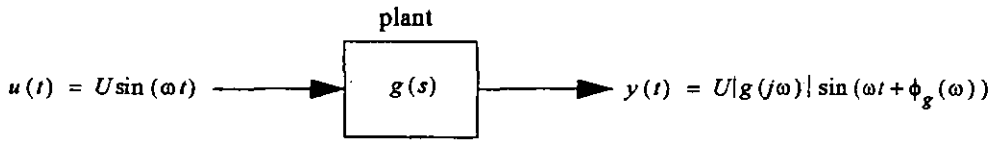
## 7.3 Frequency analysis by the correlation method

Godfrey [49] gives a good account of correlation techniques and discusses their properties, of which the most important is the ability to detect periodic signals in the

presence of noise, disturbance and harmonics. This property will become evident in the following analysis which begins with the autocorrelation function,  $R_{xx}(\tau)$ , defined below, where  $x(t)$  is a stationary stochastic or deterministic signal.

$$R_{xx}(\tau) = \lim_{T \rightarrow \infty} \frac{1}{2T} \int_{-T}^T x(t) x(t + \tau) dt \quad (7.1)$$

Consider a linear time invariant plant,  $g(t)$ , with a transfer function denoted by  $g(s)$ . Under sinusoidal excitation, the plant output is a time-shifted and amplitude-scaled version of the plant input. Consequently, if the plant input is  $u(t) = U \sin(\omega t)$  then the plant output is  $y(t) = U|g(j\omega)| \sin(\omega t + \phi_g(\omega))$ , where  $|g(j\omega)|$  is the magnitude of the plant frequency response and  $\phi_g(\omega)$  is the phase of the plant frequency response. This is illustrated in Figure 7.1



$|g(j\omega)|$  magnitude of plant frequency response

$\phi_g(\omega)$  phase of plant frequency response

**Figure 7.1 Sinusoidal excitation of a plant**

Consider now the product of the plant input and the plant output, i.e.

$$u(t)y(t) = U^2|g(j\omega)| \sin(\omega t) \sin(\omega t + \phi_g(\omega)) \quad (7.2)$$

This bears a strong resemblance to the integrand of the autocorrelation function, equation (7.1), leading to the following result which may be interpreted as a ‘correlation’ between the plant input and the plant output.

$$\lim_{T \rightarrow \infty} \frac{1}{2T} \int_{-T}^T u(t)y(t) dt = |g(j\omega)| R_{uu}(\tau) = \frac{U^2}{2} |g(j\omega)| \cos \phi_g(\omega) \quad (7.3)$$

Furthermore, since the plant frequency response is given by  $|g(j\omega)| (\cos\phi_g(\omega) + j\sin\phi_g(\omega))$ , the correlation of equation (7.3) extracts the real part of the plant frequency response.

In any realistic identification experiment, noise will be present to a lesser or greater extent, this is represented by the noise source  $n(t)$  in Figure 7.2 where the product of the plant input and the measured output is

$$u(t)y_m(t) = U^2|g(j\omega)| \sin(\omega t) \sin(\omega t + \phi_g(\omega)) + u(t)n(t) \quad (7.4)$$

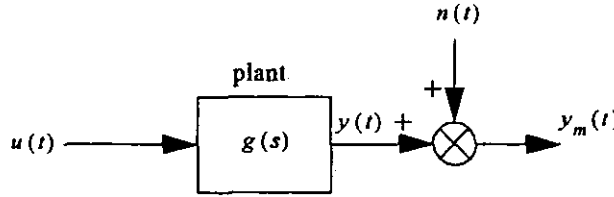


**Figure 7.2 Sinusoidal excitation with measurement noise**

Applying the correlation integral to this product, which now contains a noise term, gives

$$\lim_{T \rightarrow \infty} \frac{1}{2T} \int_{-T}^T u(t)y_m(t) dt = \frac{U^2}{2} |g(j\omega)| \cos\phi_g(\omega) + \lim_{T \rightarrow \infty} \frac{1}{2T} \int_{-T}^T u(t)n(t) dt \quad (7.5)$$

where the extracted real part of the plant frequency response is now contaminated by a noise integral term. However,  $u(t) = U\sin(\omega t)$  and  $n(t)$  are uncorrelated, thus the noise integral will decay as  $T$  increases, which gives rise to the robust noise rejection of the method. If the measured plant output is now multiplied by a cosine wave, the following product is obtained

$$\cos(\omega t)y_m(t) = U|g(j\omega)| \cos(\omega t) \sin(\omega t + \phi_g(\omega)) + \cos(\omega t)n(t) \quad (7.6)$$

and integration gives the following result

$$\lim_{T \rightarrow \infty} \frac{1}{2T} \int_{-T}^T \cos(\omega t)y_m(t) dt = \frac{U}{2} |g(j\omega)| \sin\phi_g(\omega) + \lim_{T \rightarrow \infty} \frac{1}{2T} \int_{-T}^T \cos(\omega t)n(t) dt \quad (7.7)$$



Thus, the imaginary part of the plant frequency response is obtained but as before, a noise integral term is present. However, since  $\cos(\omega t)$  and  $n(t)$  are uncorrelated, the noise integral will again decay as  $T$  increases.

The period of integration in equations (7.5) and (7.7) extends into negative time, which, of course, renders the integrals quite useless in any measuring device. Consequently, the period of integration is modified to be from 0 to  $KT$ , where  $K$  is an integer number of cycles of the exciting sinusoid and  $T$  is the period of the exciting sinusoid. The method retains its noise rejection property with a large number of cycles. A further useful property of the correlation (although not relevant to the linear approach adopted in this thesis) is that harmonics produced by non-linearities in the plant do not affect the measurement. This is shown below for completeness.

Referring to Figure 7.2, suppose that there is a harmonic component present in the plant output,  $V \sin(N\omega t + \phi_h)$ , where  $N$  is a positive integer. The product of the plant input and the measured plant output then becomes

$$\begin{aligned} u(t)y_m(t) &= U^2|g(j\omega)| \sin(\omega t) \sin(\omega t + \phi_g(\omega)) \\ &+ UV \sin(\omega t) \sin(N\omega t + \phi_h) + U \sin(\omega t) n(t) \end{aligned} \quad (7.8)$$

and the correlation integral yields

$$\begin{aligned} \frac{1}{KT} \int_0^{KT} u(t)y_m(t) dt &= \frac{U^2|g(j\omega)|}{2KT} \{KT \cos \phi_g(\omega) - \frac{1}{2\omega} [\sin(4\pi K + \phi_g(\omega)) - \sin(\phi_g(\omega))]\} \\ &+ \frac{UV}{2KT} \left\{ \frac{1}{(N-1)\omega} [\sin([N-1]2\pi K + \phi_h) - \sin(\phi_h)] - \frac{1}{(N+1)\omega} [\sin([N+1]2\pi K + \phi_h) - \sin(\phi_h)] \right\} \\ &+ \frac{U}{KT} \int_0^{KT} \sin(\omega t) n(t) dt \end{aligned} \quad (7.9)$$

Although equation (7.9) appears cumbersome, many terms equate to zero since they are of the form  $\sin(2\pi P + \phi) - \sin(\phi) = 0$ , where  $P$  is a positive integer. Hence, equation (7.9) reduces to

$$\frac{1}{KT} \int_0^{KT} u(t)y_m(t) dt = \frac{U^2|g(j\omega)|}{2} \cos \phi_g(\omega) + \frac{U}{KT} \int_0^{KT} \sin(\omega t) n(t) dt \quad (7.10)$$

which is the same as equation (7.5), with revised integral limits, and the harmonic component has no effect on the correlation. Similarly, the harmonic

component has no effect when obtaining the imaginary component of the frequency response. Equation (7.10), and the corresponding integral used to obtain the imaginary part of the frequency response of the plant, are illustrated diagrammatically in Figure 7.3. Note that both the multiplying sine and cosine functions have unity magnitude.

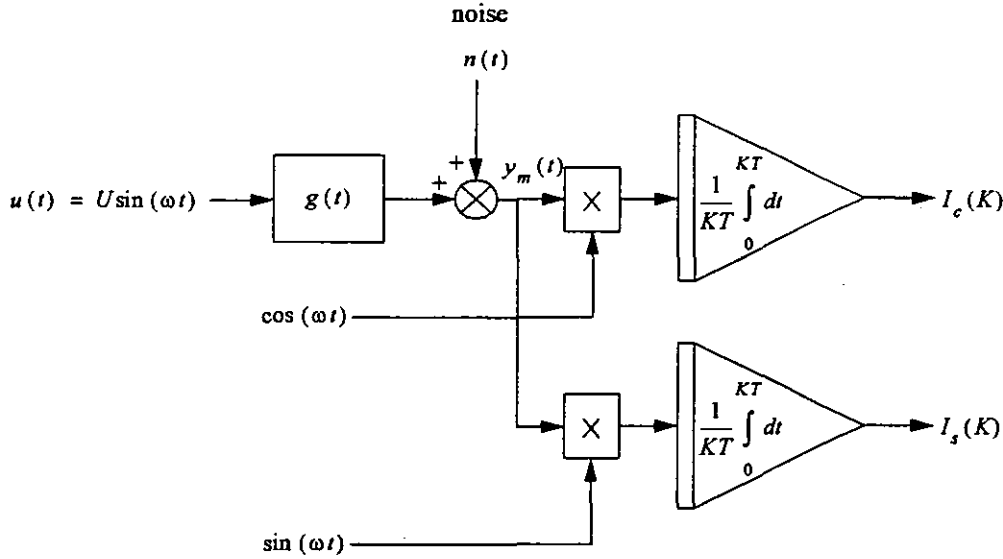


**Figure 7.3 Schematic of correlation method**

Using the notation found in Figure 7.3, the integrals are summarised below in equation (7.11).

$$\begin{aligned}
 I_c(K) &= \frac{U|g(j\omega)| \sin \phi_g(\omega)}{2} + \frac{1}{KT} \int_0^{KT} n(t) \cos(\omega t) dt \\
 I_s(K) &= \frac{U|g(j\omega)| \cos \phi_g(\omega)}{2} + \frac{1}{KT} \int_0^{KT} n(t) \sin(\omega t) dt
 \end{aligned}
 \tag{7.11}$$

The magnitude and phase of the plant frequency response are then obtained from equations (7.11) as follows, paying due regard to the sign of  $I_c(K)$  and  $I_s(K)$  when evaluating the atan function.

$$|g(j\omega)| \cong \frac{2}{U} \sqrt{I_c^2(K) + I_s^2(K)} \quad \phi_g(\omega) \cong \text{atan} \left( \frac{I_c(K)}{I_s(K)} \right)
 \tag{7.12}$$

### 7.3.1 Application to a SISO closed-loop experiment

As discussed earlier, identification from a closed-loop experiment can cause significant problems, this is primarily due to input-output noise correlation as a result of the feedback path. Figure 7.4 is a block diagram of the closed-loop experiment with an input disturbance  $d(s)$  and measurement noise  $n(s)$ ; the measured output is  $y_m(s)$ . An output disturbance could also be incorporated into the block diagram (directly after the plant) and in the following analysis can be accounted for by replacing  $n(s)$  with  $n(s) + d_{out}(s)$

In identifying  $g(j\omega)$  the following two approaches suggest themselves and are discussed below,

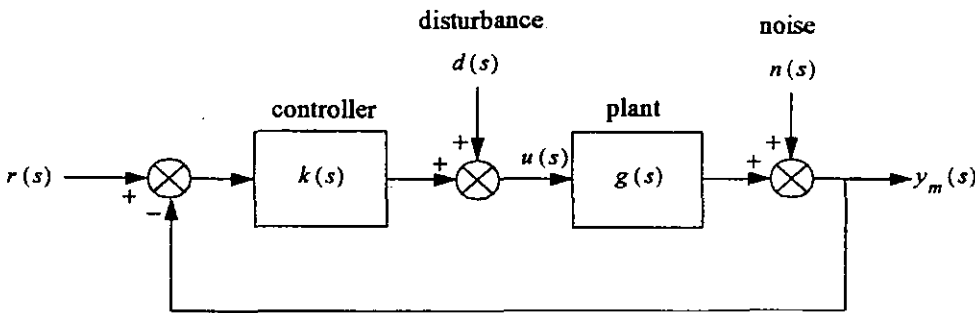


Figure 7.4 Block diagram of closed-loop system

#### (i) identification of $g(j\omega)$ from inside the loop

The frequency analysis is applied to the measured plant input and the measured plant output exactly as in the open-loop case. However, the presence of the feedback loop results in the disturbance and noise sources appearing in both  $u(s)$  and  $y_m(s)$ , equations (7.13).

$$\begin{aligned} u(s) &= \frac{k(s)}{1 + g(s)k(s)} r(s) + \frac{1}{1 + g(s)k(s)} d(s) - \frac{k(s)}{1 + g(s)k(s)} n(s) \\ y_m(s) &= \frac{g(s)k(s)}{1 + g(s)k(s)} r(s) + \frac{g(s)}{1 + g(s)k(s)} d(s) + \frac{1}{1 + g(s)k(s)} n(s) \end{aligned} \quad (7.13)$$

Consequently, the noise measured at the input and the noise measured at the output are correlated, as are the disturbance measured at the input and the disturbance measured at the output. To proceed with the frequency-response analysis, denote the disturbance and noise terms appearing in  $u(s)$  as  $d_i(s)$  and  $n_i(s)$  respectively.

Similarly, denote the disturbance and noise terms in the measured output as  $d_o(s)$  and  $n_o(s)$  respectively. The plant input and the measured output can then be written in the time domain, as below, where  $u'(s) = k(s) [1 + g(s)k(s)]^{-1}r(s)$  and  $*$  denotes convolution.

$$\begin{aligned} u(t) &= u'(t) + d_i(t) - n_i(t) \\ y_m(t) &= g(t) * u'(t) + d_o(t) + n_o(t) \end{aligned} \quad (7.14)$$

The closed-loop is excited by a sinusoid, in which case  $u'(t)$  may be written  $U'(\omega) \sin(\omega t)$  and time domain expressions for the plant input and measured plant output are

$$\begin{aligned} u(t) &= U'(\omega) \sin(\omega t) + d_i(t) - n_i(t) \\ y_m(t) &= U'(\omega) |g(j\omega)| \sin(\omega t + \phi_g(\omega)) + d_o(t) + n_o(t) \end{aligned} \quad (7.15)$$

where  $|g(j\omega)|$  is the magnitude of the plant frequency response and  $\phi_g(\omega)$  is the phase of the plant frequency response. Applying the correlation integral of equation (7.5) to the closed-loop plant input and the measured plant output yields the following result.

$$\begin{aligned} \lim_{T \rightarrow \infty} \frac{1}{2T} \int_{-T}^T u(t) y_m(t) dt &= \frac{U'^2(\omega)}{2} |g(j\omega)| \cos(\phi_g(\omega)) \\ &+ \lim_{T \rightarrow \infty} \frac{1}{2T} \int_{-T}^T U'(\omega) |g(j\omega)| \sin(\omega t + \phi_g(\omega)) [d_i(t) - n_i(t)] dt \\ &+ \lim_{T \rightarrow \infty} \frac{1}{2T} \int_{-T}^T U'(\omega) \sin(\omega t) [d_o(t) + n_o(t)] dt \\ &+ \lim_{T \rightarrow \infty} \frac{1}{2T} \int_{-T}^T [d_o(t) + n_o(t)] [d_i(t) - n_i(t)] dt \end{aligned} \quad (7.16)$$

The first term on the right hand side of equation (7.16) contains the real part of the plant frequency response, however  $U'(\omega)$  cannot be measured directly and so the real part of the frequency response of the plant cannot be accurately determined. The remaining three integrals on the right hand side are unwanted and are due to the noise and disturbance sources; the first two of these integrals will decay to zero as  $T \rightarrow \infty$ . The final integral, however, will not decay to zero as  $T$  increases since the input and

output noise terms are correlated, as are the input and output disturbance terms. Consequently, estimates of  $g(j\omega)$  obtained from inside the loop will suffer from reduced accuracy and bias.

### (ii) Identification of $g(j\omega)$ from outside the loop

The approach yields a frequency-response estimate that is less affected by noise and disturbance than the previous approach from within the loop. The approach consists of two stages: identification of the frequency response of the closed-loop system,  $f(j\omega)$ , followed by calculation of  $g(j\omega)$  from the closed-loop system  $f(j\omega)$  and knowledge of  $k(j\omega)$ . The frequency-response analysis is applied to the product  $r(t)y_m(t)$  and  $r(t)$  does not contain any noise or disturbance signals since it is outside the feedback loop. This is illustrated in Figure 7.5 where the block diagram of Figure 7.4 is suitably redrawn.

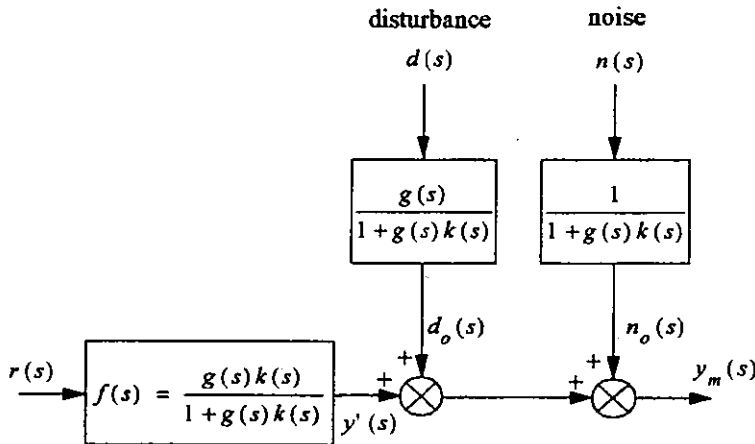


**Figure 7.5 Identification of closed-loop frequency response**

With sinusoidal excitation, and the transient response of the plant having decayed to an insignificant level, the reference input and the measured plant output may be written as in equation (7.17).

$$\begin{aligned} r(t) &= R \sin(\omega t) \\ y_m(t) &= R|f(j\omega)| \sin(\omega t + \phi_f(\omega)) + d_o(t) + n_o(t) \end{aligned} \quad (7.17)$$

where  $|f(j\omega)|$  is the magnitude of the closed-loop frequency response and  $\phi_f(\omega)$  is the phase of the closed-loop frequency response. Applying the correlation integral of equation (7.5) to the product of the reference input and the measured plant output gives

$$\begin{aligned} \lim_{T \rightarrow \infty} \frac{1}{2T} \int_{-T}^T r(t) y_m(t) dt &= \frac{R^2}{2} |f(\omega)| \cos(\phi_f(\omega)) \\ &+ \lim_{T \rightarrow \infty} \frac{1}{2T} \int_{-T}^T R \sin(\omega t) [d_o(t) + n_o(t)] dt \end{aligned} \quad (7.18)$$

Contrasting this result against that obtained from identification of  $g(j\omega)$  from within the loop, equation (7.16), it can be seen that identification of the frequency response of the closed-loop system is less affected by the noise and disturbance terms. Furthermore, since these terms are uncorrelated with the reference input,  $r(t)$ , the noise and disturbance integral will decay to zero as  $T \rightarrow \infty$  leading to an unbiased estimate of  $f(j\omega)$ . Also, the magnitude of the reference input  $R$  is known leading to a more accurate identification of  $f(j\omega)$  than the previous identification of  $g(j\omega)$  from within the loop. Consequently, identification of the closed-loop transfer function  $f(j\omega)$  is preferred and  $g(j\omega)$  is obtained thus

$$g(j\omega) = f(j\omega) [1 - f(j\omega)]^{-1} k^{-1}(j\omega) \quad (7.19)$$

The inversion in equation (7.19) may cause numerical problems if  $f(j\omega)$  is extremely close to unity, this will depend upon the software and computer used to perform the calculation. For example, if the real and imaginary parts of  $1 - f(j\omega)$  have magnitudes less than  $1 \times 10^{-12}$  then the inversion may be inaccurate beyond 3 significant figures using MATLAB version 4.0 running under Windows 3.1 on a 486 personal computer. Such a problem is most likely to occur in the case of a control system designed for a tracking application, where a primary objective is to make  $f(j\omega) \approx 1$ , especially at low frequencies. In the event that difficulties are encountered, de-tuning the controller to introduce some steady-state error should alleviate the problem.

## 7.4 Multivariable closed-loop identification

A two stage approach has been presented for the identification of a SISO plant operating under closed-loop control, the method is easily generalised for any multivariable plant with  $n$  inputs and  $l$  outputs. The block diagram for the multivariable closed-loop system is the same as Figure 7.4 with  $k(s)$  and  $g(s)$  replaced by transfer function matrices  $K(s)$  and  $G(s)$  respectively, and the inputs

$r(s)$ ,  $d(s)$  and  $n(s)$  are now vector valued quantities. The measured output is given by

$$y_m(s) = F(s)r(s) + P(s)d(s) + Q(s)n(s) \quad (7.20)$$

where the transfer function matrices  $F(s)$ ,  $P(s)$  and  $Q(s)$  are

$$\begin{aligned} F(s) &= (I + G(s)K(s))^{-1}G(s)K(s) \\ P(s) &= (I + G(s)K(s))^{-1}G(s) \\ Q(s) &= (I + G(s)K(s))^{-1} \end{aligned} \quad (7.21)$$

Throughout the remainder of this chapter the following notation is used:  $M^{[p,q]}$  refers to the element  $(p,q)$  of the matrix  $M$ ,  $r^{[p]}$  refers to the  $p^{th}$  element of the vector  $r$ .

With sinusoidal excitation  $R\sin(\omega t)$  on the  $i^{th}$  reference input, all other reference inputs zero, the measured output in the time domain is given in equation (7.22), where  $\phi_F(\omega)$  is the phase of the closed-loop frequency response  $F(j\omega)$ .

$$y_m^{[p]}(t) = R|F^{[pi]}(j\omega)|\sin(\omega t + \phi_F^{[pi]}(\omega)) + d_o^{[p]}(t) + n_o^{[p]}(t) \quad p = 1 \dots l \quad (7.22)$$

where

$$\begin{aligned} d_o^{[p]}(s) &= \sum_{q=1}^n P^{[pq]}(s)d^{[q]}(s) \\ n_o^{[p]}(s) &= \sum_{q=1}^l Q^{[pq]}(s)n^{[q]}(s) \end{aligned} \quad (7.23)$$

Equation (7.22) is very similar to the SISO closed-loop measured output, equation (7.17), where now the output noise and disturbance terms are combinations of the multivariable sources, equation (7.23). The reference input and the exogenous inputs  $d_o(s)$ ,  $n_o(s)$  are again uncorrelated and the frequency-response analysis can be applied to identify each element of the closed-loop frequency response matrix  $F(j\omega)$  as follows: The open-loop plant and noise source in Figure 7.3 are replaced with the closed-loop system of Figure 7.4; then, with sinusoidal excitation

$R \sin(\omega t)$  on the  $i^{th}$  reference input, all other reference inputs zero, correlation between the  $i^{th}$  reference input and the  $p^{th}$  measured output yields

$$\begin{aligned} I_c(K) &= \frac{R|F^{[pi]}(j\omega)| \sin \phi_F^{[pi]}(\omega)}{2} + \frac{1}{KT} \int_0^{KT} [d_o^{[p]}(t) + n_o^{[p]}(t)] \cos(\omega t) dt \\ I_s(K) &= \frac{R|F^{[pi]}(j\omega)| \cos \phi_F^{[pi]}(\omega)}{2} + \frac{1}{KT} \int_0^{KT} [d_o^{[p]}(t) + n_o^{[p]}(t)] \sin(\omega t) dt \end{aligned} \quad (7.24)$$

from which

$$|F^{[pi]}(j\omega)| \cong \frac{2}{R} \sqrt{I_c^2(K) + I_s^2(K)} \quad \phi_F^{[pi]}(\omega) \equiv \text{atan} \left( \frac{I_c(K)}{I_s(K)} \right) \quad (7.25)$$

The correlation is repeated for all input-output combinations to construct  $F(j\omega)$ , the desired plant frequency response is then determined from equation (7.26)

$$G(j\omega) = F(j\omega) [I - F(j\omega)]^{-1} K^{-1}(j\omega) \quad (7.26)$$

It is noted that, in a similar fashion to the SISO system, the inversion in equation (7.26) may cause numerical problems if  $F(j\omega)$  is extremely close to the identity matrix; this will depend upon the software and computer used to perform the calculation. For example, if the elements of the matrix  $I - F(j\omega)$  all have real and imaginary parts with magnitudes less than  $1 \times 10^{-12}$  then the inversion may be inaccurate beyond 3 significant figures using MATLAB version 4.0 running under Windows 3.1 on a 486 personal computer. Such a problem is most likely to occur in the case of a control system designed for a tracking application, where a primary objective is to make  $F(j\omega) \approx I$ , especially as low frequencies. In the event that difficulties are encountered, de-tuning the controller to introduce some steady-state error should alleviate the problem.

## 7.5 Examples

### 7.5.1 Simulated identification of a multivariable plant

The following plant model is taken from Wood and Berry [54] and is used here for the purpose of an example only. The plant is controlled with PI action in the



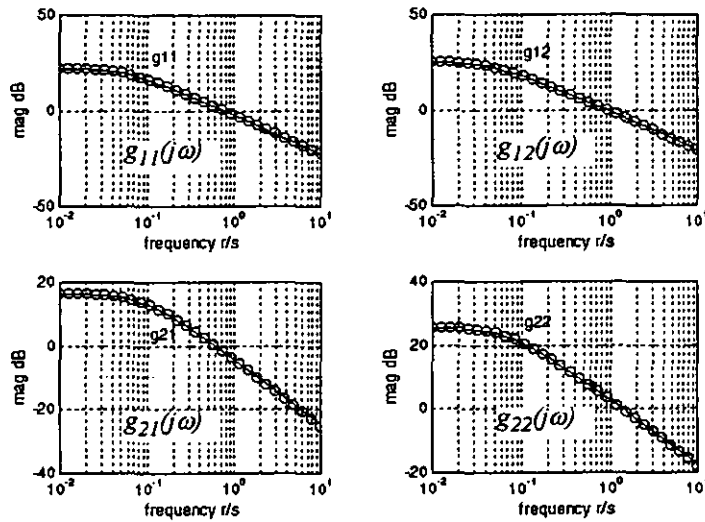
feedback scheme of Figure 7.4 ( $k(s)$  is replaced by  $K(s)$  and  $g(s)$  is replaced by  $G(s)$ ), the controller settings are taken from Wood and Berry.

$$G(s) = \begin{bmatrix} \frac{12.8e^{-s}}{16.7s+1} & \frac{-18.9e^{-3s}}{21s+1} \\ \frac{6.6e^{-7s}}{10.9s+1} & \frac{-19.4e^{-3s}}{14.4s+1} \end{bmatrix} \quad (7.27)$$

$$K(s) = \begin{bmatrix} 0.2 \left( 1 + \frac{1}{4.44s} \right) & 0 \\ 0 & -0.04 \left( 1 + \frac{1}{2.67s} \right) \end{bmatrix}$$

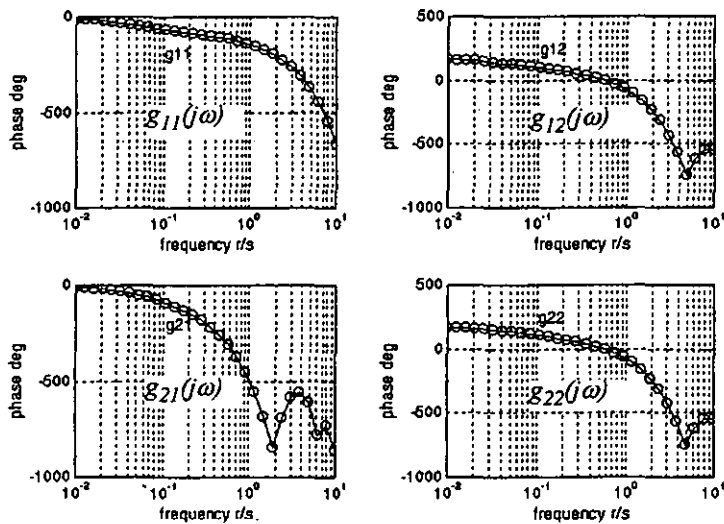
The closed-loop system and the correlation of Figure 7.3 were constructed in SIMULINK [55], the ensuing measurement simulations returning  $I_c(K)$  and  $I_s(K)$ , equations (7.24). Forty cycles of excitation per measurement under ideal conditions, i.e. zero noise and disturbance, were sufficient to determine the open-loop frequency response using equations (7.25) and (7.26) for a number of frequencies in the range 0.01 to 10 rad/s. The results are presented as circles in the plots of Figures 7.6 and 7.7, the continuous lines in Figures 7.6 and 7.7 are the true frequency response. The results indicate a very good match from the correlation method.

To investigate the response of the method to an unanticipated disturbance, step inputs were introduced into both plant outputs at each measurement. The step disturbances were introduced approximately 100 seconds into the measurement simulation, at which point the transient response of the plant due to the sinusoidal excitation had decayed to an insignificant level. Again, 40 cycles of excitation per measurement were sufficient and the frequency response was measured over a number of frequencies in the range 0.01 to 10 rad/s. The results are presented as circles in the plots of Figure 7.8 and 7.9 where it can be seen that, apart from a small band of frequencies near 1 rad/s, the impact of the step disturbances is negligible.



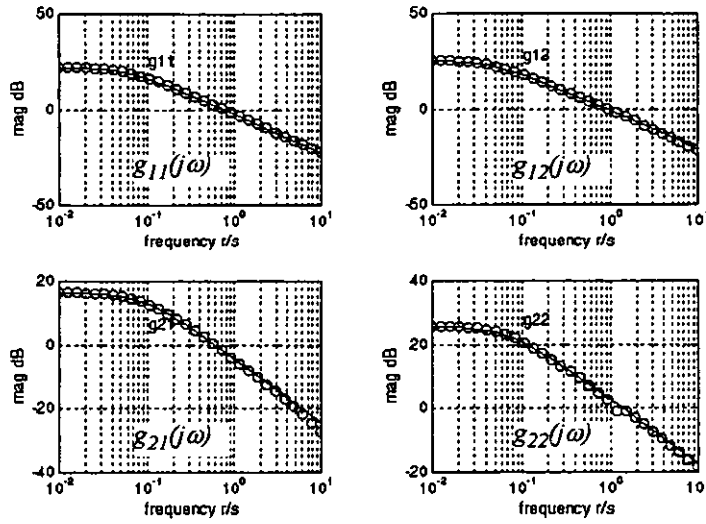
Solid line is true frequency response, circles are measured frequency response

**Figure 7.6** Frequency response of the magnitude of the multivariable plant in example 7.5.1. Ideal measurement conditions



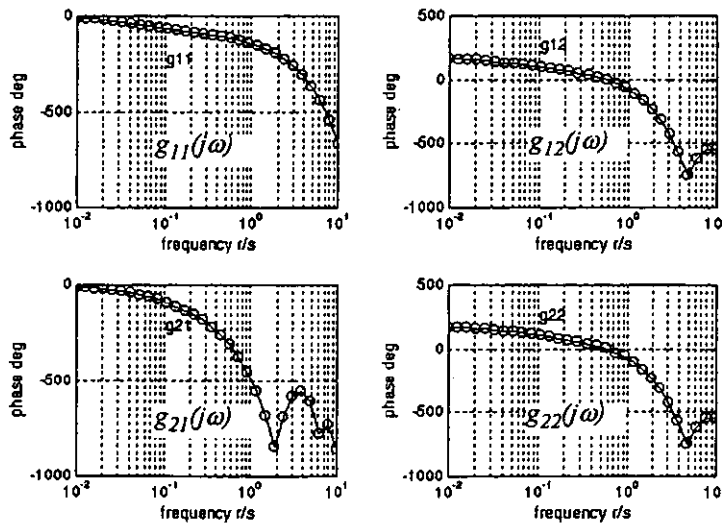
Solid line is true frequency response, circles are measured frequency response

**Figure 7.7** Frequency response of the phase of the multivariable plant in example 7.5.1. Ideal measurement conditions



Solid line is true frequency response, circles are measured frequency response

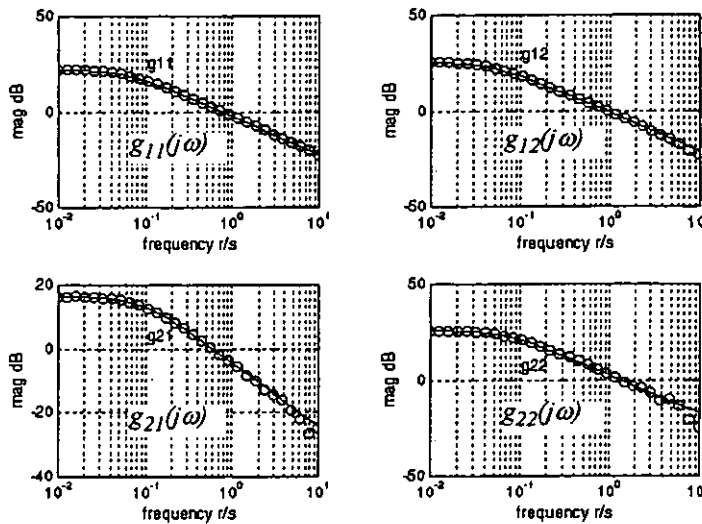
**Figure 7.8** Frequency response of the magnitude of the multivariable plant in example 7.5.1. Measurement with disturbance



Solid line is true frequency response, circles are measured frequency response

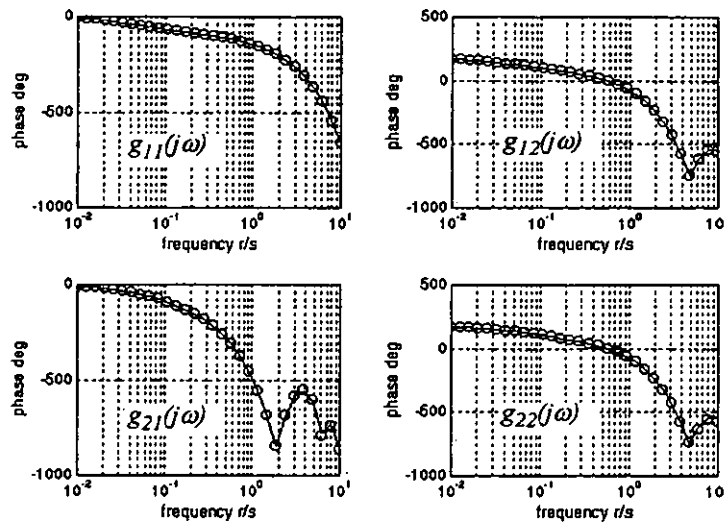
**Figure 7.9** Frequency response of the phase of the multivariable plant in example 7.5.1. Measurement with disturbance

Any practical identification method must perform satisfactorily in a noisy environment. To this end, independent white noise sources with zero mean, unity standard deviation and whose amplitudes were multiplied by 0.2 were introduced into both plant outputs (inside the feedback loop as in Figure 7.4). Again, 40 cycles of excitation were sufficient to identify the plant frequency response using equations (7.25) and (7.26) over a number of frequencies in the range 0.01 to 10 rad/s. The results are presented in the plots of Figure 7.10 and 7.11 where the simulated measurements are indicated by circles and the true frequency response is shown by the solid lines. It can be seen that the noise has little effect on the identification, other than at high frequencies where the signal to noise ratio at the plant outputs will be low. The effect of the noise can be clearly observed by contrasting the time traces of the plant outputs given in Figures 7.12 and 7.13 - the former is without noise and the latter is with noise.



Solid line is true frequency response, circles are measured frequency response

**Figure 7.10** Frequency response of the magnitude of the multivariable plant in example 7.5.1. Noisy measurement



Solid line is true frequency response, circles are measured frequency response

**Figure 7.11** Frequency response of the phase of the multivariable plant in example 7.5.1. Noisy measurement

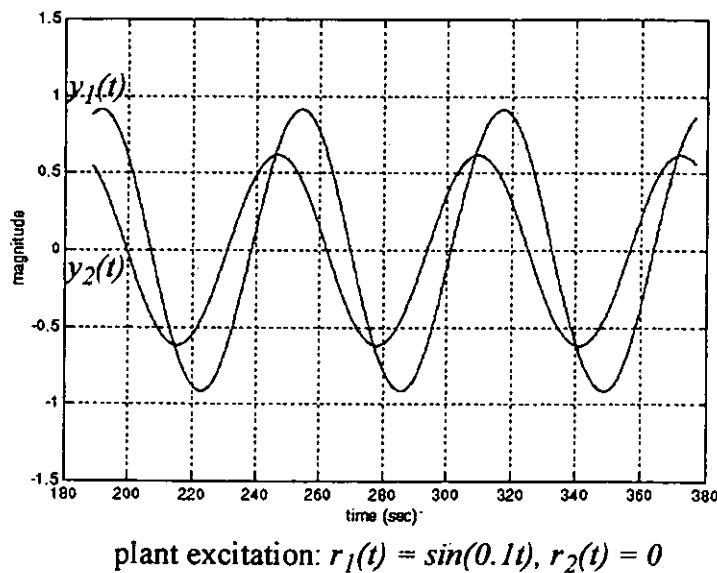


**Figure 7.12** Time trace of output signals without measurement noise

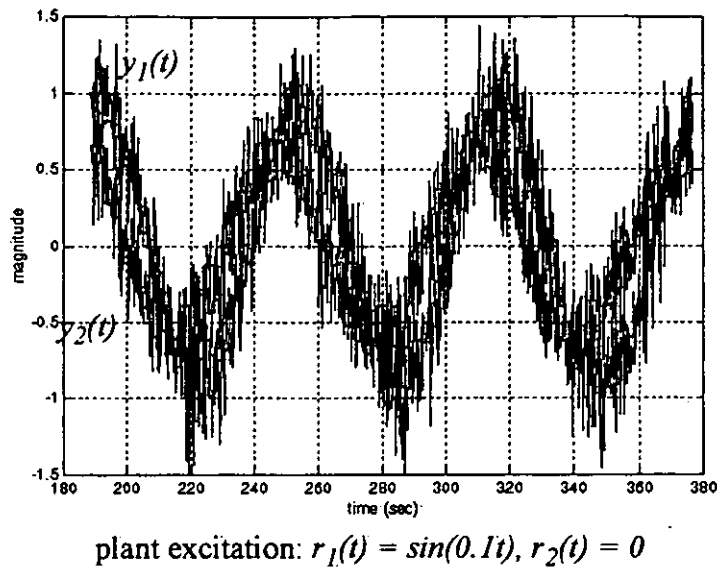


**Figure 7.13** Time trace of output signals with measurement noise

Melo and Friedly [53] have also simulated the closed-loop frequency response identification of this plant using fast fourier techniques, with step changes in the reference inputs providing the necessary plant excitation. The results presented in Figures 7.6 to 7.11 are an improvement upon the results of Melo and Friedly and if sinusoidal excitation is permissible, the author proposes that the correlation technique is preferable.

### 7.5.2 Experimental identification of the Torsion rig

The very real problem of identifying the frequency response of the Torsion rig described in chapter 4 motivated the closed-loop identification technique described in this chapter. Obviously, if the Torsion-rig could be operated open-loop then the identification would be simplified as the correlation technique could be applied directly to the open-loop system. Therefore, the rig was initially operated open-loop and several attempts were made to excite the rig sinusoidally. However, the outputs (the forces applied by the hydraulic actuators) drifted up to their maximum values. In an attempt to cancel out the drift, compensating offsets were manually applied to the excitation signals as illustrated in Figure 7.14. Unfortunately, the drift proved to be too problematic and open-loop operation was simply not feasible. Additionally, allowing the applied forces to drift to their maximum values will stress the rig in an uncontrolled manner. Whilst the actuators were rated so as not to damage the rig in this event, in

general such extreme loading could invalidate a dynamic structural test or even damage a specimen. It was this very real problem that motivated the closed-loop identification method discussed in this chapter

Therefore we now return to the Torsion rig and put the identification method to the test in a practical experiment.

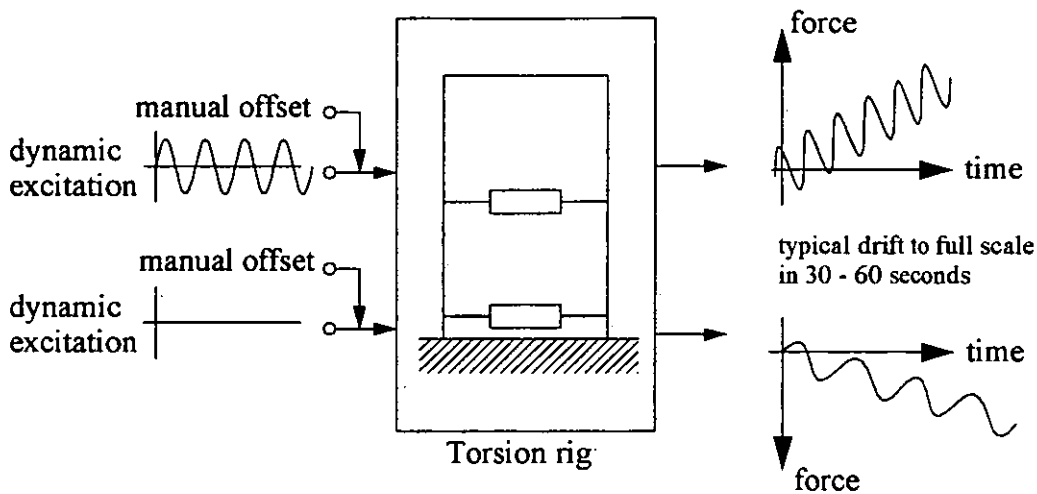


**Figure 7.14 Excitation of Torsion rig under open-loop operation**

The frequency response of the Torsion rig was identified using the closed-loop technique described, providing the necessary *a priori* model for the controller design discussed in chapter 8. The frequency response is shown in Figure 7.15 and Figure 7.16, the type '1' behaviour of the open-loop system can be clearly observed at low frequencies and can be thought of as multivariable integrator action (The dynamics of the test rig have been altered since reference [46] to their current form described in chapter 3 of this thesis).

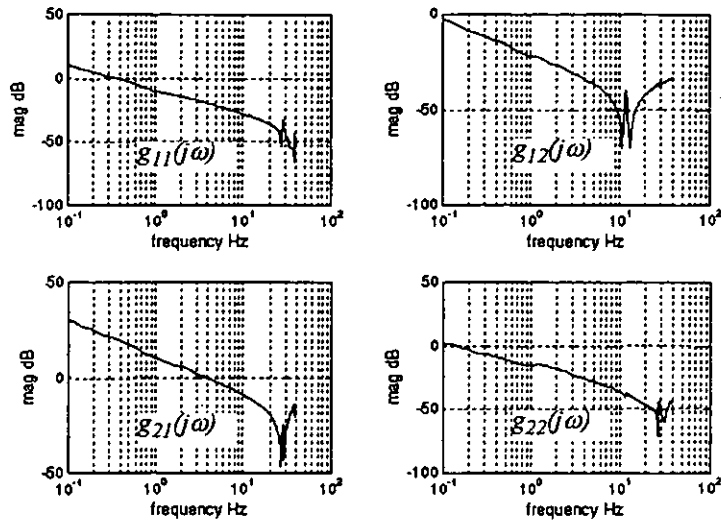


Figure 7.15 Frequency response of the magnitude of the Torsion rig

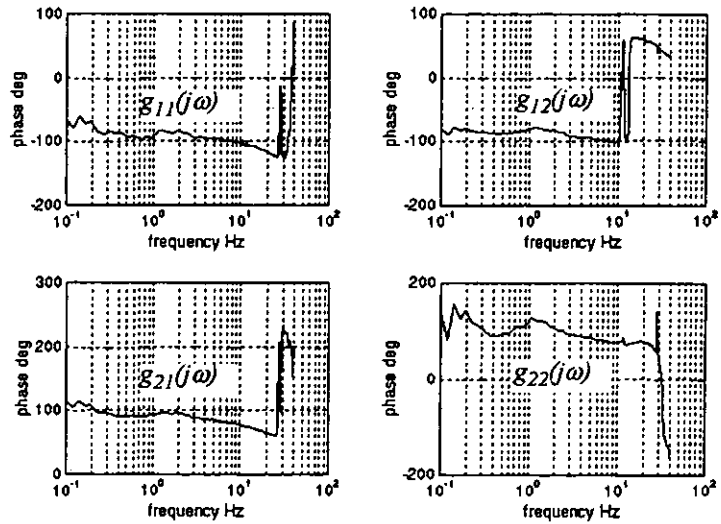


Figure 7.16 Frequency response of the phase of the Torsion rig



## 7.6 Conclusions

Some plants cannot be operated open-loop for stability, economic or safety reasons. The necessary imposition of closed-loop operation creates a problem in identifying the open-loop plant frequency response, a problem which is hardly addressed in the relevant literature. A robust and practical method has been presented which successfully addresses this identification problem for a MIMO plant. A correlation technique is used to perform the frequency response measurements and a systematic procedure has been derived to obtain the desired open-loop frequency response from a set of closed-loop measurements. The method has been shown to perform well in the simulated identification of a multivariable plant and the experimental identification of the Torsion rig.

## **Chapter 8**

### **Controller Design and Implementation**

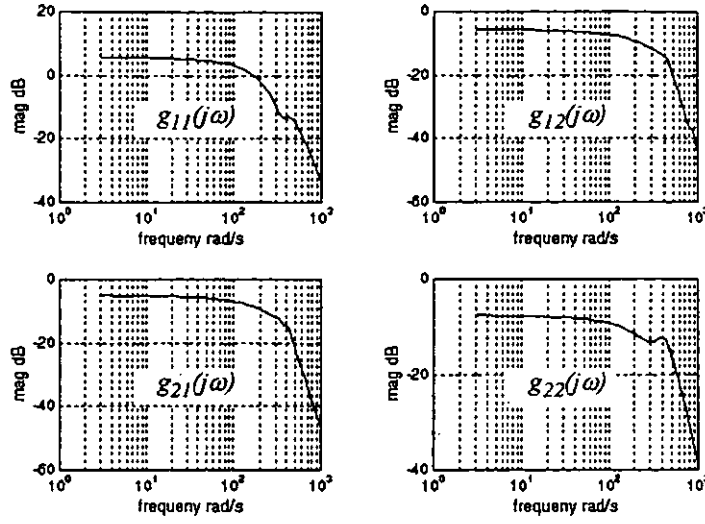
#### **8.1 Introduction**

In this chapter the design and implementation of several controllers are presented for the two test rigs described in chapter 3 - the Beam and Vibrator rig and the Torsion rig. In section 8.2 the Beam and Vibrator rig is considered with controllers designed according to a Sequential Loop Closure (SLC) method and the Characteristic Locus (CL) method. Additionally, recent extensions to the CL method are incorporated. In section 8.3 the Torsion rig is considered and, again, controllers are designed and implemented according to a Sequential Loop Closure (SLC) method and the Characteristic Locus (CL) method. Control system performance is summarised in section 8.4.

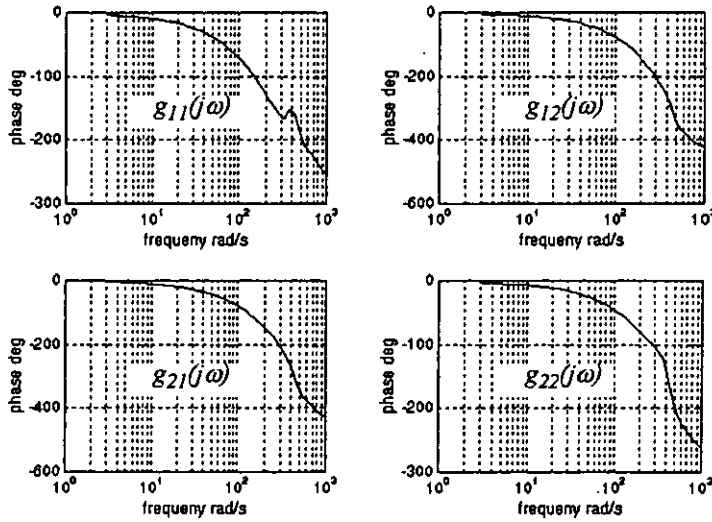
A 386 DX 33 MHz personal computer with a Metrabyte DAS1600 data acquisition card was used in the implementation of all control schemes with control algorithms written in QuickBASIC.

#### **8.2 Beam and Vibrator test rig**

In the following section three controllers are presented, based on the design principles of Sequential Loop Closure, Characteristic Locus and recent discrete approaches to the Characteristic Locus method. The first two controller designs, SLC and CL, are based upon the experimental open-loop frequency response of the test rig, presented in Figure 8.1. The discrete CL controller design is based upon a state space model of the rig [4]. The test rig has two inputs and two outputs.



(a) Magnitude



(b) Phase

Figure 8.1 Open-loop frequency response of the Beam and Vibrator rig

### 8.2.1 Sequential Loop Closure (SLC) design

A schematic of the SLC scheme is illustrated in Figure 5.1, PI action is used in the loop controllers  $k_i(s)$  :

$$\begin{aligned} k_1(s) &= K_1 \left( 1 + \frac{1}{sT_{i_1}} \right) \\ k_2(s) &= K_2 \left( 1 + \frac{1}{sT_{i_2}} \right) \end{aligned} \quad (8.1)$$

Tuning of the controller parameters can be performed based on experience of the dynamics of the rig or by using empirical rules. The latter approach is used, based on the tuning rules for PID controllers due to Ziegler Nichols [56].

Ziegler Nichols (ZN) tuning rules were developed for SISO systems and require either open-loop step tests to be carried out on the plant or the closed-loop system to be brought to the limit of stability. The latter is appropriate since the vibrator coils can be burned out due to current surges resulting from a step input. Hence, the closed-loop system is brought to the limit of stability under proportional control only; the value of the proportional gain ( $k(s) = K$ ) is known as the ultimate gain,  $K_u$ , and the period of the corresponding continuous cycling is known as the ultimate period  $P_u$ . The tuning rules are given in equation (8.2)

$$K = 0.6K_u \quad T_i = 0.5P_u \quad (8.2)$$

In the case of a SISO system, there will be a unique value for the ultimate gain and the ultimate period. However, in the case of a multiple-input, multiple-output system with interaction, there will not be a unique set of ultimate gains. Consequently, for the Beam and Vibrator rig any pair of ultimate gains  $(K_{u_1}, K_{u_2})$  will be a coordinate on the stability boundary of the test rig in the two dimensional space formed by  $k_1(s) = K_{u_1}$  and  $k_2(s) = K_{u_2}$ , known as gain-space. The gain-space of the test rig was determined from consideration of the stability of the characteristic loci of  $G(j\omega)$  diag  $(k_1, k_2)$  and is illustrated below, from which the stability boundary is

$$\begin{aligned} K_{u_1} &= 1.95, 0 \leq K_{u_2} \leq 4.3 \\ K_{u_2} &= 4.3, 0 \leq K_{u_1} \leq 1.95 \end{aligned} \quad (8.3)$$

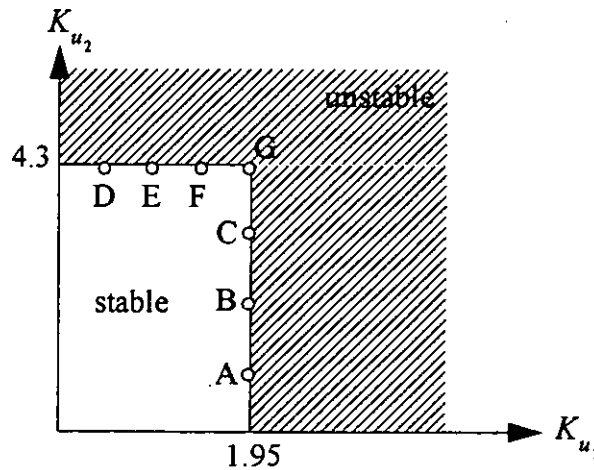


Figure 8.2 Gain-space of the Beam and Vibrator test rig

To use ZN then,  $(K_{u_1}, K_{u_2})$  coordinates must be chosen from the stability boundary, these will be the ultimate gains, and the corresponding ultimate periods are then required. Seven equally spaced coordinates  $(K_{u_1}, K_{u_2})$  were selected, these are marked on Figure 8.2 as A to G inclusive, and the following table of data generated. The ultimate period for all the systems was found to be in the range 0.01 to 0.02 seconds.  $T_i$  was derived from the lower value of  $P_u = 0.01$  to provide large integral gain for reducing steady-state error and reducing interaction at low frequencies.

**TABLE 8.1** Loop controller parameters determined from ZN tuning rules

system	$K_{u_1}$	$K_{u_2}$	$P_u$	$K_1$	$K_2$	$T_{i_1}$	$T_{i_2}$
A	1.95	1.08	0.01	1.17	0.65	0.005	0.005
B	1.95	2.15	0.01	1.17	1.29	0.005	0.005
C	1.95	3.23	0.01	1.17	1.94	0.005	0.005
D	0.49	4.3	0.01	0.29	2.58	0.005	0.005
E	0.98	4.3	0.01	0.59	2.58	0.005	0.005
F	1.46	4.3	0.01	0.88	2.58	0.005	0.005
G	1.95	4.3	0.01	1.17	2.58	0.005	0.005

The simulated closed-loop frequency responses with these controller settings are illustrated in Figure 8.3 (a) through to Figure 8.3(g). The figures show that the interaction has been reduced at frequencies below 100 rad/s. However, all the responses exhibit large resonant peaks in the region 200 to 400 rad/s where the interaction is also severe. The nature of these responses serve to illustrate that the use of high gain to reduce interaction can reduce stability margins, a disadvantage of the SLC approach. The closed-loop performance in all cases was considered to be poor and implementation was not carried out.

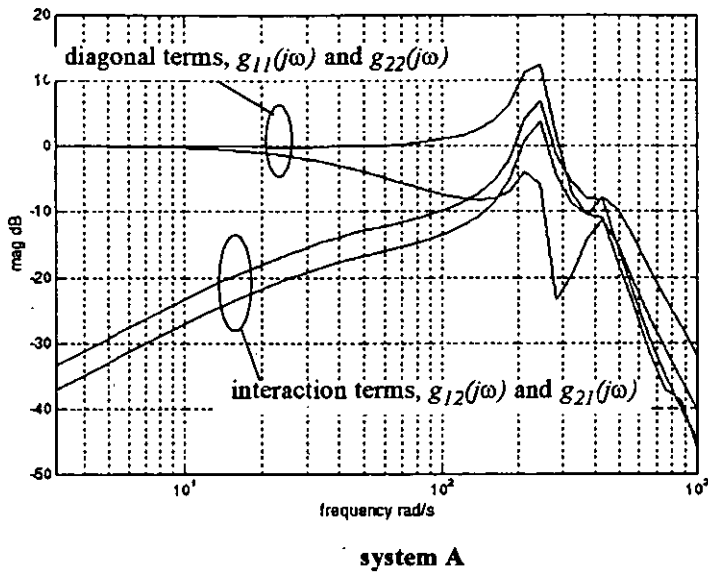


**Figure 8.3(a) Closed-loop frequency response of the magnitude of the Beam and Vibrator rig, simulated SLC scheme**

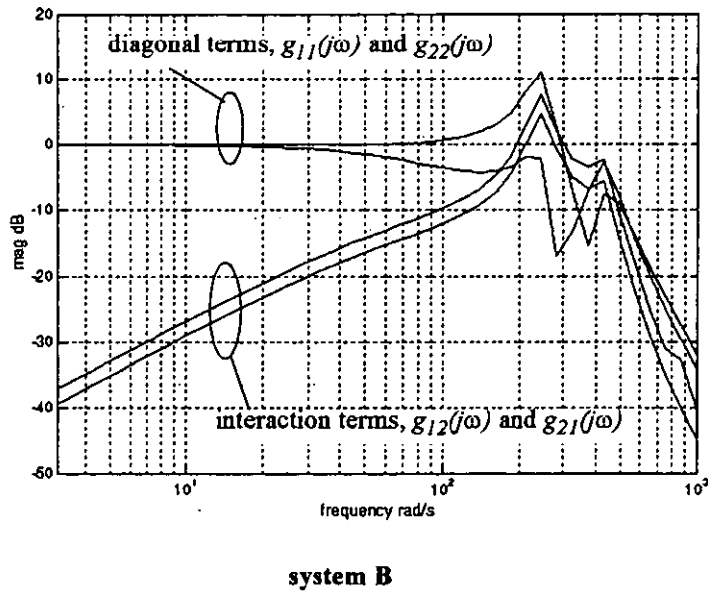


**Figure 8.3(b) Closed-loop frequency response of the magnitude of the Beam and Vibrator rig, simulated SLC scheme**

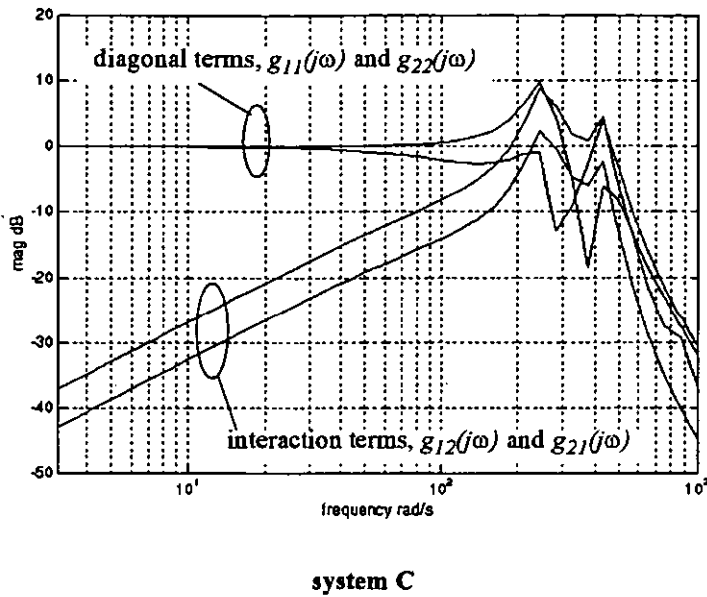


**Figure 8.3(c)** Closed-loop frequency response of the magnitude of the Beam and Vibrator rig, simulated SLC scheme

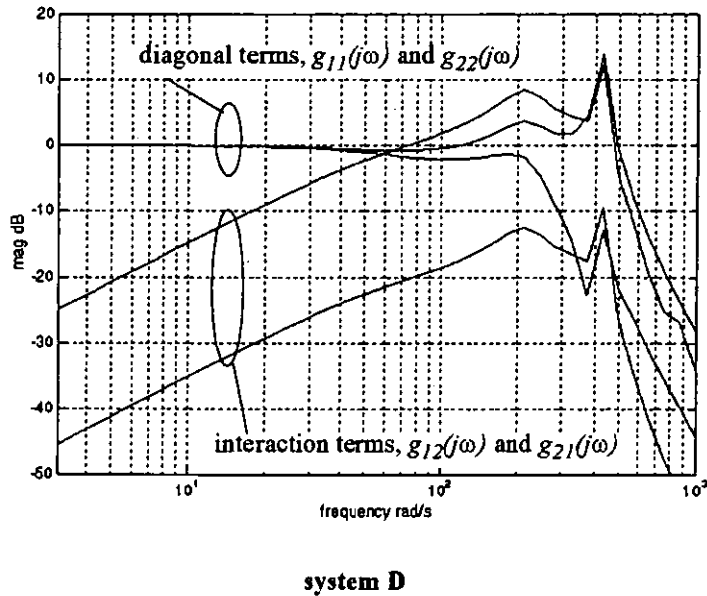


**Figure 8.3(d)** Closed-loop frequency response of the magnitude of the Beam and Vibrator rig, simulated SLC scheme

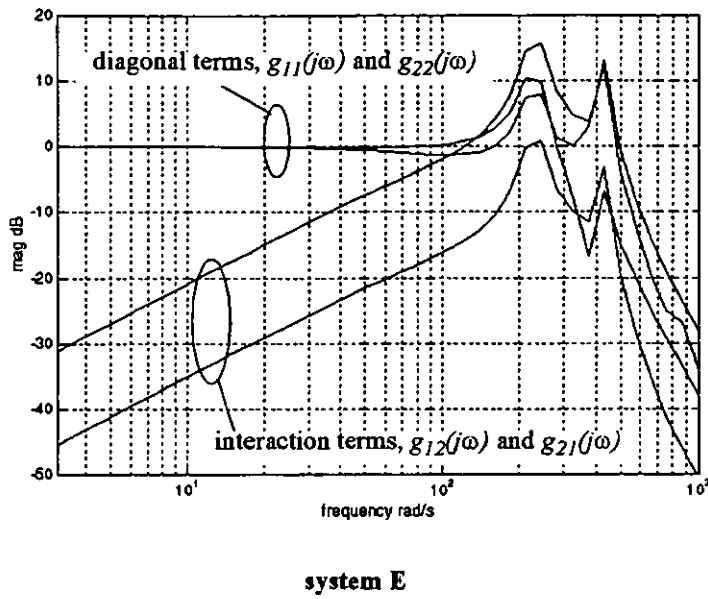


**Figure 8.3(e)** Closed-loop frequency response of the magnitude of the Beam and Vibrator rig, simulated SLC scheme

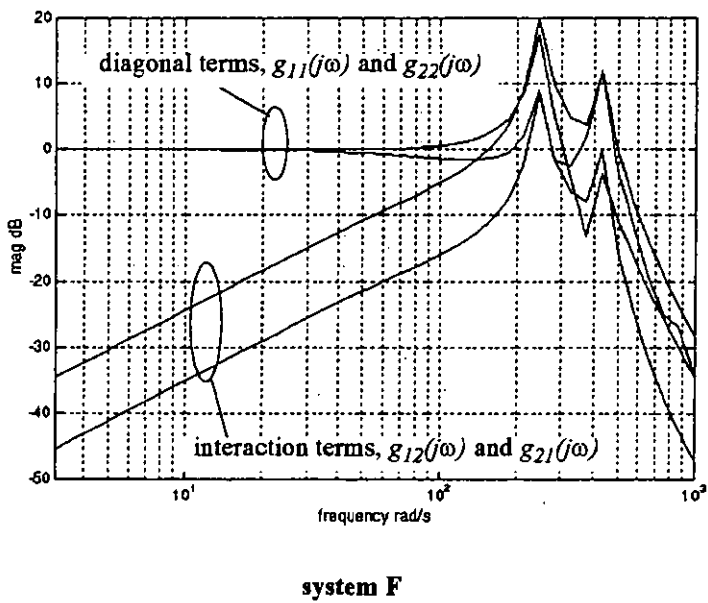
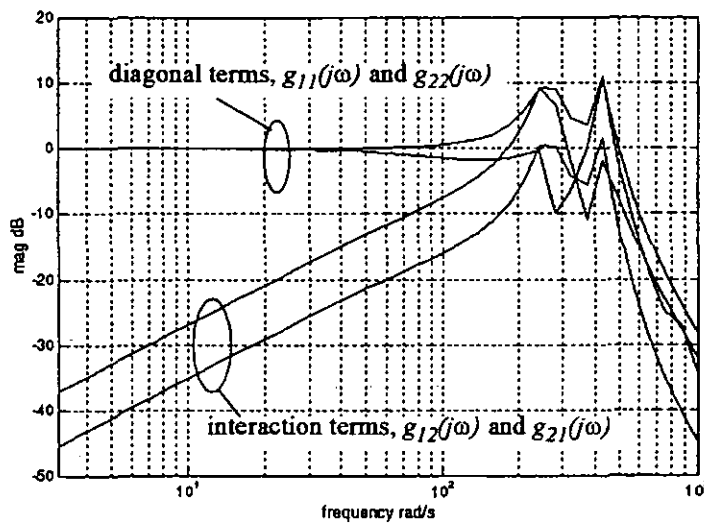


**Figure 8.3(f)** Closed-loop frequency response of the magnitude of the Beam and Vibrator rig, simulated SLC scheme





system G

**Figure 8.3(g) Closed-loop frequency response of the magnitude of the Beam and Vibrator rig, simulated SLC scheme**

## 8.2.2 Characteristic Locus

The Beam and Vibrator test rig has been described in chapter 3. Previous research [4 - Tsavdaras] had lead to an encouraging Characteristic Locus controller design for the rig, although this had not been implemented at that time. The design [4] is summarised below, the reader is referred to Tsavdaras for details. The implementation was carried out during the course of this work [57].

### Design

The Beam and Vibrator rig has two characteristic loci since it has two inputs and two outputs. The characteristic loci of the open-loop plant are the eigenvalues of its frequency response and are shown in Figure 8.4 overleaf. The aim of the design process is to shape the loci to achieve desirable performance of the closed-loop system. Herein lies the attraction of the method: the loci are shaped independently in a very similar manner to classical SISO controller design in the frequency domain. In fact, the gain and phase margins of the loci effect the stability and performance of the closed-loop system in an analogous manner to the gain and phase margins of the open-loop frequency response of a SISO system.

It can be seen that there is a large imbalance in the magnitudes of the loci. Tsavdaras found, through trial and error, that balancing the loci prior to controller design simplified the latter stages of controller design; it is noted that this is not part of the standard procedure for designing a characteristic locus controller. The scaling compensator that balanced the loci is

$$K_s = \begin{bmatrix} 0.53 & -1 \\ 0 & 3.8 \end{bmatrix} \quad (8.4)$$

The resulting loci of  $G(s)K_s$  are shown in Figure 8.5.

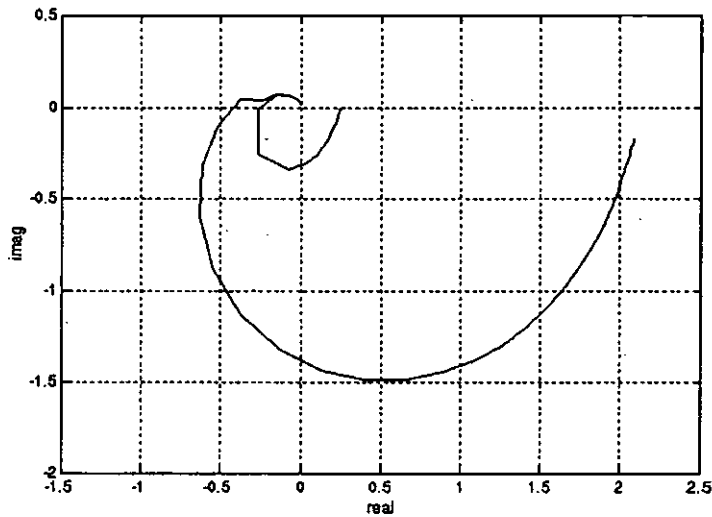


**Figure 8.4** Characteristic loci of open-loop system  $G(j\omega)$ , Beam and Vibrator rig

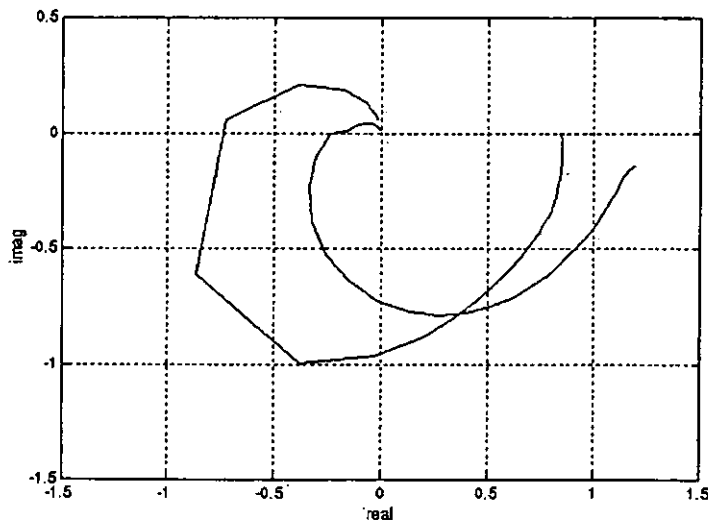


**Figure 8.5** Characteristic loci of  $G(j\omega)K_s$ , Beam and Vibrator rig

### High-frequency compensation $K_h$

The objective of the control system design was to improve upon the open-loop bandwidth of the rig (in the region 100 rad/s to 200 rad/s) and significantly reduce interaction over the chosen bandwidth. A target closed-loop bandwidth of approximately 300 rad/s was selected, this being the frequency near which all the elements of the open-loop frequency response have similar magnitudes and hence represents severe interaction. However,  $K_h$  was obtained at a higher frequency of 850 rad/s to help minimise the interference that would result from the medium-frequency compensator  $K_m(s)$ . The high-frequency compensator was calculated using the ALIGN algorithm [58, 59] available in MATLAB [38] to approximate  $G^{-1}(j850)$ .

$$K_h = \begin{bmatrix} 1.397 & 1.428 \\ 0.0699 & 0.308 \end{bmatrix} \quad (8.5)$$

The resulting characteristic loci of  $G(s)K_sK_h$  are shown in Figure 8.6.

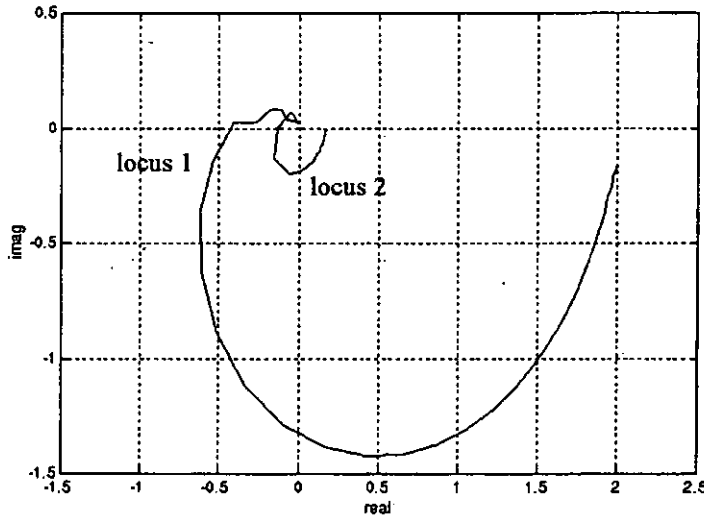


Figure 8.6 Characteristic loci of  $G(j\omega)K_sK_h$ , Beam and Vibrator rig

### Medium-frequency compensation $K_m(s)$

Recall from chapter 5 that the medium-frequency compensator has the form given below

$$K_m(s) = A_m \text{diag}(k_i(s)) B_m \quad (8.6)$$

where  $A_m$  and  $B_m$  are the constant approximations to the eigenvectors and dual eigenvectors of  $G(s)K_sK_h$  at a chosen frequency  $s = j\omega_m$ . The diagonal controllers

$k_i(s)$  are designed to shape the characteristic loci of  $G(s)K_sK_h$  to meet stability and performance requirements in a similar fashion to SISO frequency response shaping. The gain and phase margins of the loci of  $G(s)K_sK_h$  are summarised in Table 8.2.

TABLE 8.2 Gain and Phase margins of loci (medium-frequency compensation)

locus	gain margin	phase margin
1	2.5	57
2	6.7	$\infty$

Locus 1 has satisfactory margins and does not require compensation. Locus 2, however, has excessively large margins which are compensated by the following lag compensator

$$k_2(s) = 12 \frac{(1 + 0.0003s)}{(1 + 0.155s)} \quad (8.7)$$

giving the diagonal controller

$$\text{diag}(k_i(s)) = \begin{bmatrix} 1 & 0 \\ 0 & 12 \frac{(1 + 0.0003s)}{(1 + 0.155s)} \end{bmatrix} \quad (8.8)$$

However, when pre-multiplied and post-multiplied by  $A_m$  and  $B_m$  respectively, numerical difficulties were encountered in the resulting medium frequency compensator  $K_m(s)$  in the way of large condition numbers. Consequently,  $\text{diag}(k_i(s))$  was modified to

$$\text{diag}(k_i(s)) = \begin{bmatrix} \frac{(1 + 0.01s)}{(1 + 0.01s)} & 0 \\ 0 & 12 \frac{(1 + 0.0003s)}{(1 + 0.155s)} \end{bmatrix} \quad (8.9)$$

which solved the numerical problems. With  $A_m$  and  $B_m$  calculated using the ALIGN algorithm, the medium frequency compensator is

$$K_m(s) = \frac{1}{d(s)} \begin{bmatrix} 0.0007s^2 + 3.65s + 29.2 & 0.0006s^2 - 0.505s - 56.8 \\ 0.0002s^2 - 0.170s - 19.1 & 0.0005s^2 + 0.585s + 53.9 \end{bmatrix} \quad (8.10)$$

$$d(s) = 0.001s^2 + 0.1645s + 6.451$$

The resulting characteristic loci of  $G(s)K_sK_hK_m(s)$  are given in Figure 8.7.

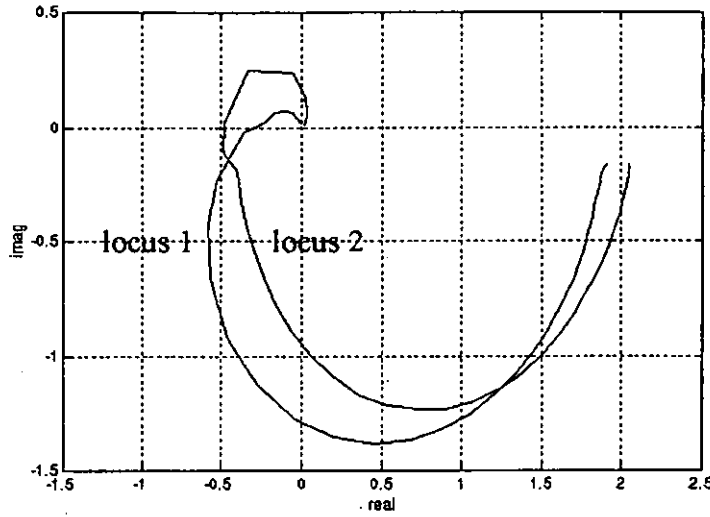


**Figure 8.7** Characteristic loci of  $G(s)K_sK_hK_m(s)$ , Beam and Vibrator rig

#### Low-frequency compensation $K_l(s)$

The structure of the compensator is given in equation (5.17) and is repeated below

$$K_l(s) = A_l \text{diag} \left( \frac{k_i}{s} \right) B_l + I \quad (8.11)$$

The diagonal gains  $k_i$  were taken to be the reciprocals of the respective characteristic loci at a suitable low frequency  $\omega_l$ .  $A_l$  and  $B_l$  were again calculated using the ALIGN algorithm and the low frequency compensator is

$$K_l(s) = \frac{1}{s} \begin{bmatrix} s + 50.855 & 8.219 \\ -0.6328 & s + 54.5 \end{bmatrix} \quad (8.12)$$

The complete controller is then  $K(s) = K_sK_hK_m(s)K_l(s)$  which gives

$$K(s) = \frac{1}{d(s)} \begin{bmatrix} k_{11}(s) & k_{12}(s) \\ k_{21}(s) & k_{22}(s) \end{bmatrix} \quad (8.13)$$

where

$$\begin{aligned}
 k_{11}(s) &= 0.5591s^3 + 196.62s^2 + 19646s + 569450 \\
 k_{12}(s) &= 0.6265s^3 - 37.32s^2 - 16691s - 668660 \\
 k_{21}(s) &= 0.4204s^3 - 81.20s^2 - 20195s - 775610 \\
 k_{22}(s) &= 0.7455s^3 + 596.13s^2 + 77315s + 2499300 \\
 d(s) &= s^3 + 164.5s^2 + 6451s
 \end{aligned} \tag{8.14}$$

and the characteristic loci of the compensated plant  $G(s)K_sK_hK_m(s)K_l(s)$  are shown in Figure 8.8.

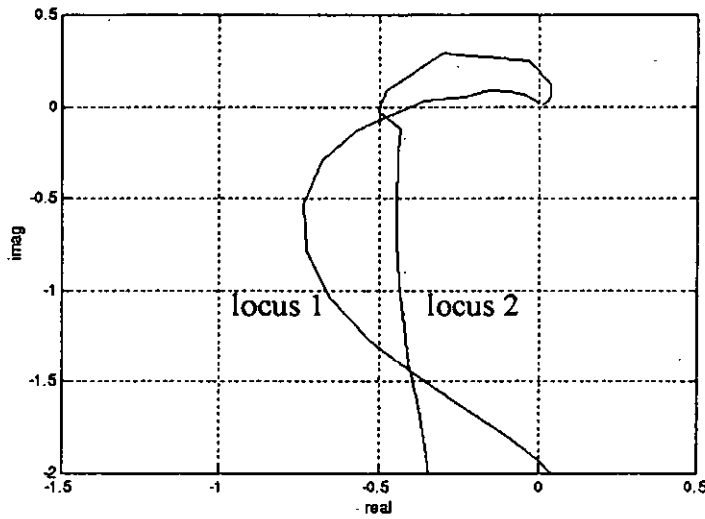


**Figure 8.8** Characteristic loci of compensated Beam and Vibrator rig

The fully compensated characteristic loci have desirable gain and phase margins: locus 1 has a gain margin of 2.5 and a phase margin of  $43^\circ$ , locus 2 has a gain margin of 2 and a phase margin of  $64^\circ$ . The simulated closed-loop frequency response is presented in Figure 8.9. This is an improvement upon all of the SLC schemes shown in Figures 8.3(a) through to Figure 8.3(g) and the bandwidth is approximately 300 rad/s. Additionally, interaction from the element [2,1] has been effectively reduced over the entire frequency range. However, beyond 200 rad/s the element [1,2] causes severe interaction and there are small peaks in the response of the diagonal elements close to 200 rad/s.

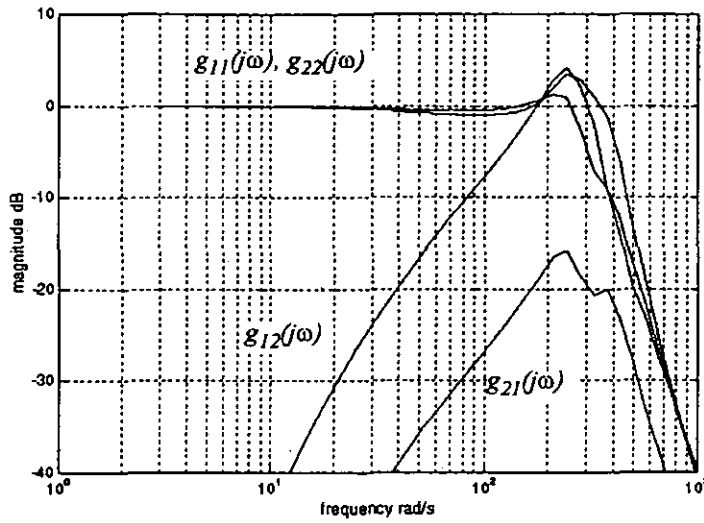


**Figure 8.9** Closed-loop frequency response of Beam and Vibrator rig, simulated CL control

### Implementation

An important decision to be made in discretising the controller is selecting an appropriate sampling frequency. Several empirical rules exist for determining the sampling frequency, which generally recommend a figure of five to ten times the desired closed-loop bandwidth. The upper figure was chosen and with a bandwidth of 300 rad/s this gives a sampling frequency of approximately 500 Hz, i.e. a sampling period of 2ms. The continuous-time controller in equation (8.14) was discretised using Tustin's approximation with a 2ms sampling period, giving

$$K(z) = \frac{1}{d(z)} \begin{bmatrix} k_{11}(z) & k_{12}(z) \\ k_{21}(z) & k_{22}(z) \end{bmatrix} \quad (8.15)$$

where

$$\begin{aligned} k_{11}(z) &= 0.5591 - 1.3016z^{-1} + 0.9965z^{-2} - 0.2502z^{-3} \\ k_{12}(z) &= 0.6267 - 1.9669z^{-1} + 1.9923z^{-2} - 0.6567z^{-3} \\ k_{21}(z) &= 0.42 - 1.4299z^{-1} + 1.5259z^{-2} - 0.5213z^{-3} \\ k_{22}(z) &= 0.7446 - 1.0746z^{-1} + 0.1954z^{-2} + 0.1516z^{-3} \\ d(z) &= 1 - 2.6977z^{-1} + 2.4173z^{-2} - 0.7196z^{-3} \end{aligned} \quad (8.16)$$

In writing the controller algorithm, the coefficients of the TFM elements are formed into the following vectors:  $c_{11} = [0.5591, -1.3016, 0.9965, -0.2502]$ ,  $c_{12} = [0.6267, -1.9669, 1.9923, -0.6567]$ ,  $c_{21} = [0.42, -1.4299, 1.5259, -0.5213]$ ,  $c_{22} = [0.7446, -1.0746, 0.1954, 0.1516]$  and  $d = [1, -2.6977, 2.4173, -0.7196]$ . Interpreting  $z^{-1}$  as the delay operator, the controller outputs at the  $k^{th}$  sample instant can be written as below.

$$\begin{aligned} u_{1k} &= \sum_{i=0}^3 (c_{11}^{(i)} e_{1_{k-i}} + c_{12}^{(i)} e_{2_{k-i}}) + \sum_{i=1}^3 d^{(i-1)} u_{1_{k-i}} \\ u_{2k} &= \sum_{i=0}^3 (c_{21}^{(i)} e_{1_{k-i}} + c_{22}^{(i)} e_{2_{k-i}}) + \sum_{i=1}^3 d^{(i-1)} u_{2_{k-i}} \end{aligned} \quad (8.17)$$

The notation  $u_{1k}$  refers to the value of  $u_1$  at the  $k^{th}$  sample instant and the notation  $c_{11}^{(i)}$  refers to the  $i^{th}$  element in  $c_{11}$ . Clearly, it is necessary to retain the past three values of the controller outputs and controller inputs. This is achieved by defining arrays which contain the required values. The arrays are updated every sampling instant. The control algorithm was written in QuickBASIC for ease of programming and is summarised below.

#### set-up sequence

- step 1: initialise data acquisition board and load controller parameters
- step 2: initialise arrays of previous controller outputs and inputs
- step 3: set control outputs to zero

#### control algorithm

- step 4: sample error signals and convert to binary voltages (A/D)
- step 5: convert binary voltages to decimal voltages  $e_{1k}, e_{2k}$
- step 6: compute  $u_{1k}, u_{2k}$ , equations (8.17)
- step 7: if either  $u_{1k}$  or  $u_{2k}$  is out of limits, reset controller output to zero and STOP
- step 8: convert  $u_{1k}, u_{2k}$  to binary voltage
- step 9: write binary voltage to controller output and convert (D/A)
- step 10: update arrays of previous controller inputs and outputs
- step 11: return to step 4 until STOP is requested.



The closed-loop frequency response obtained with the implemented controller is presented in Figure 8.10.

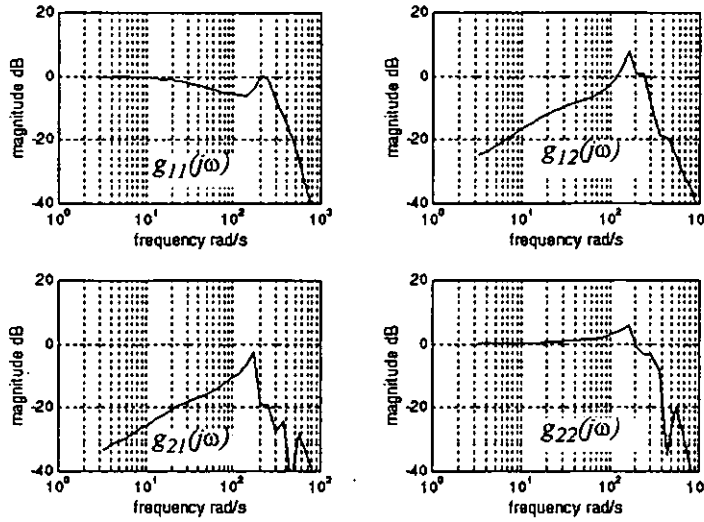


**Figure 8.10** Closed-loop frequency response of Beam and Vibrator rig, implemented CL controller

There is a significant degradation from the simulated analog response, this is due to the effect of the discretisation and the computational delay (which was a whole sampling period).

### 8.2.3 Discrete Characteristic Locus Design

This time, since there is no medium-frequency compensator with which to interfere, the high-frequency controller  $K_h$  was calculated using the ALIGN algorithm at a frequency in the region of the desired closed-loop bandwidth. The high-frequency controller was obtained at 200 rad/s and is given in equation (8.18)

$$K_h = \begin{bmatrix} -1.295 & 0.366 \\ -0.757 & 0.931 \end{bmatrix} \quad (8.18)$$

The  $W_a(z)$  and  $V_a(z)$  sequences were calculated using the algorithm described in [60]. Since the branch points of the compensated plant  $G(z)K_h$  were all stable and fast, only 5 terms were required in each sequence to decouple the system very accurately. The appropriate sequences were

$$\begin{aligned}
 W_a(z) &= \begin{bmatrix} -0.9757 & -0.1098 \\ -0.1912 & -1.0019 \end{bmatrix} + \begin{bmatrix} -0.0307 & -0.0879 \\ -0.2842 & -0.0431 \end{bmatrix} z^{-1} + \begin{bmatrix} -0.0369 & -0.1337 \\ -0.2181 & -0.0395 \end{bmatrix} z^{-2} \\
 &\quad + \begin{bmatrix} -0.0120 & 0.0110 \\ -0.1756 & 0.0083 \end{bmatrix} z^{-3} + \begin{bmatrix} -0.0033 & 0.0235 \\ 0.0255 & 0.0269 \end{bmatrix} z^{-4} \\
 V_a(z) &= \begin{bmatrix} -1.0365 & 0.0594 \\ 0.2332 & -1.0236 \end{bmatrix} + \begin{bmatrix} -0.0162 & 0.1678 \\ 0.2300 & -0.0000 \end{bmatrix} z^{-1} + \begin{bmatrix} -0.0323 & 0.0553 \\ 0.3258 & -0.0457 \end{bmatrix} z^{-2} \\
 &\quad + \begin{bmatrix} -0.0571 & 0.0369 \\ 0.0985 & -0.0743 \end{bmatrix} z^{-3} + \begin{bmatrix} -0.0434 & -0.0092 \\ 0.0797 & -0.0761 \end{bmatrix} z^{-4}
 \end{aligned} \tag{8.19}$$

The nominal characteristic loci of  $G(z)K_h$  are given in Figure 8.11. Note that the implementation introduced a 4ms pure delay into the controller output. This was accounted for in the design and is included in the loci plotted in Figure 8.11, hence the very poor phase margins. Moreover, one of the loci is on the negative real axis at steady-state and so a change of sign is required. There is also a mismatch in gain.

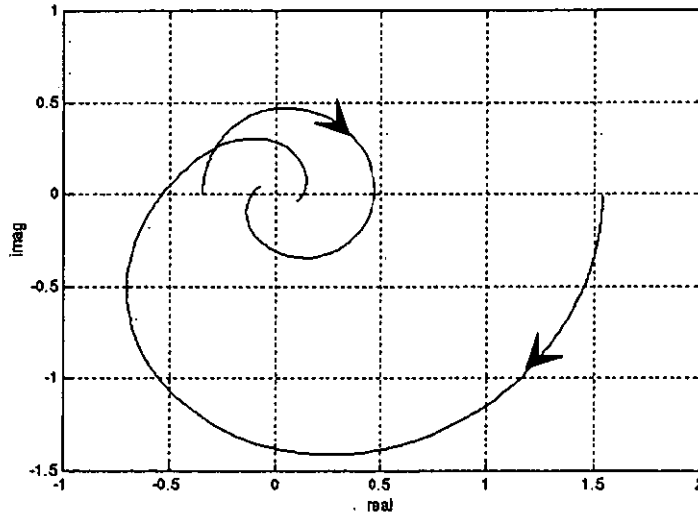


**Figure 8.11** Characteristic loci of  $G(z)K_h$  with sample delay, Beam and Vibrator rig

A simple PID controller was designed to compensate each locus, giving the diagonal controller

$$\Lambda_K(z) = \text{diag} \left( \frac{-0.511 + 0.049z^{-1}}{1 - z^{-1}}, \frac{0.166 - 0.0156z^{-1}}{1 - z^{-1}} \right) \tag{8.20}$$

The overall controller is then

$$K(z) = K_h W_a \Lambda_K(z) V_a(z) \quad (8.21)$$

The characteristic loci of the compensated plant and the simulated frequency response of the closed-loop system are given in [61, 62], where it is shown that the bandwidth is much reduced from the calculated frequency response of the original analog design. This is the expected penalty incurred in discretisation and the introduction of a dead time into the system.

At this point, it is pertinent to examine how well the dynamic matrices  $W_a(z)$  and  $V_a(z)$  have approximated the eigenvectors of  $G(z)K_h$ . Ideally, the characteristic loci of the compensated plant  $G(z)K(z)$  should be equal to  $\Lambda_K(z) \text{ eig}(G(z)K_h)$ . In [61, 62] it is shown that the error between these two quantities is less than 1% over the whole frequency range. Thus, the dynamic approximations have successfully decoupled the plant, giving confidence in the design of the simple SISO compensation of the characteristic loci.

### Implementation

Choice of sampling period is an important criterion in any digital control system, affecting both control system performance and the hardware cost of the project. Long sampling periods are undesirable since aliasing will occur at reduced frequencies (i.e., the sampling theory of Shanon), thereby degrading performance and disturbance rejection. Also, long sampling periods will obviously have a detrimental effect upon stability. However, long sample periods will reduce the computational load and the speed of A/D, D/A conversion, thus reducing the cost of the hardware. Not surprisingly, therefore, choice of the sampling period is a compromise between performance and hardware cost.

To promote the use of the direct digital design of the characteristic locus controller it was felt essential that good results should be achievable with the modest computational facility described in the introduction to this chapter. Several empirical rules exist for determining the sampling frequency, for example [63], which generally recommend a figure of five to ten times the desired closed-loop bandwidth. Close inspection of the frequency response of the simulated analog system (Figure 8.10) reveals a bandwidth of approx. 300 rad/s (50 Hz), indicating a sampling frequency of 250 to 500 Hz. With the previously described computational facility, the maximum obtainable sampling frequency was 250 Hz per channel (4ms sampling period), achievable only at the cost of reducing the entire sampling period to the computational delay. This has the destabilising effect of introducing a whole sample delay into the controller outputs but was accounted for in the design.

The implementation is shown schematically in Figure 8.12. The elements of the controller are shown explicitly and indeed were treated explicitly in the control algorithm by introducing the internal variables  $p(z)$  and  $q(z)$ . This greatly reduced time spent debugging the control algorithm software and promoted quick development of the software. Importantly, this approach makes future modification to the algorithm simple.

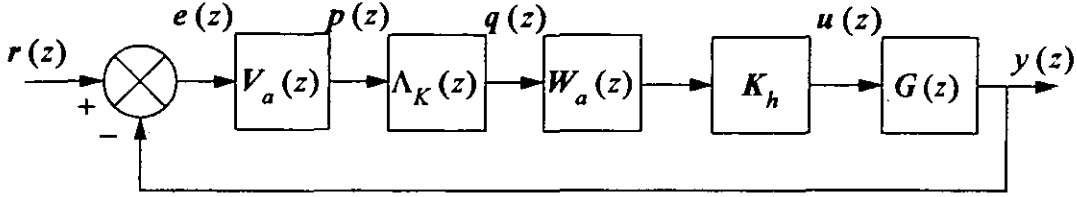


**Figure 8.12** Block diagram for implementation of the discrete CL controller

Referring to Figure 8.12,  $e(z)$  is the output of the feedback comparator,  $p(z)$  is the output of the  $V_a(z)$  block,  $q(z)$  is the output of the diagonal controller block  $\Lambda_K(z)$  and the external controller output is  $u(z)$ . These vector-valued variables will be referred to in the discrete time domain as  $e_k$ ,  $p_k$ ,  $q_k$  and  $u_k$  respectively, where the subscript  $k$  refers to their value at the  $k^{th}$  sample period.

Now from equation (8.19),  $W_a(z)$  and  $V_a(z)$  may be written

$$\begin{aligned} W_a(z) &= W_0 + W_1 z^{-1} + W_2 z^{-2} + W_3 z^{-3} + W_4 z^{-4} \\ V_a(z) &= V_0 + V_1 z^{-1} + V_2 z^{-2} + V_3 z^{-3} + V_4 z^{-4} \end{aligned} \quad (8.22)$$

Similarly,  $\Lambda_K(z)$  may be written  $\Lambda_K(z) = (\Lambda_{K_0} + \Lambda_{K_1} z^{-1}) / (1 - z^{-1})$ . Consequently, the controller variables at the  $k^{th}$  sample may be written in terms of their values at current and previous sample points as in equations (8.23)

$$\begin{aligned} u_k &= K_h \sum_{i=0}^4 W_i q_{k-i} \\ q_k &= q_{k-1} + \Lambda_{K_0} p_k + \Lambda_{K_1} p_{k-1} \\ p_k &= \sum_{i=0}^4 V_i e_{k-i} \end{aligned} \quad (8.23)$$

The control algorithm requires at any sampling instant the necessary previous values of  $e_k$ ,  $p_k$  and  $q_k$ . These are stored in arrays of four, one and four elements

respectively. The algorithm is summarised below and comprises of an initial set-up sequence, followed by the control algorithm proper.

**set-up sequence**

- step 1: initialise data acquisition board
- step 2: load controller parameters
- step 3: initialise arrays of previous values of  $e_k$ ,  $p_k$  and  $q_k$
- step 4: set control outputs to zero

**control algorithm**

- step 5: sample error signals and convert to binary voltages (A/D)
- step 6: convert binary voltages to decimal voltages  $e_k$
- step 7: determine  $p_k$ , equation (8.23)
- step 8: determine  $q_k$ , equation (8.23)
- step 9: determine  $u_k$ , equation (8.23)
- step 10: if  $u_k$  is out of limits, reset controller output (D/A) to zero and STOP
- step 11: convert  $u_k$  to binary voltage
- step 12: write binary voltage to controller output and convert (D/A)
- step 13: update arrays of previous values of  $e_k$ ,  $p_k$  and  $q_k$
- step 14: return to step 5 until STOP is requested.

The closed-loop frequency response with the implemented controller is shown in Figure 8.13. The bandwidth is approximately 200 rad/s and interaction from the element [2,1] has been effectively reduced over the entire frequency range. Also, the magnitude response of the diagonal elements are desirably flat, rolling off as 200 rad/s is approached. However, beyond approximately 80 rad/s, the element [1,2] causes severe interaction.

Comparing the frequency response with that obtained from the implementation of the continuous-time controller, Figure 8.10, the improvement is significant and is derived from two differences in the design of the controller. Firstly, the discrete design uses a dynamic approximation to the eigenvectors of the plant and so decouples the plant over the entire frequency range, whereas the continuous-time design only decouples the plant at three separate frequencies (those used in the design of the high-,

medium- and low-frequency compensators). Secondly, the discrete design accounts for the computational delay that will be present in the implementation.

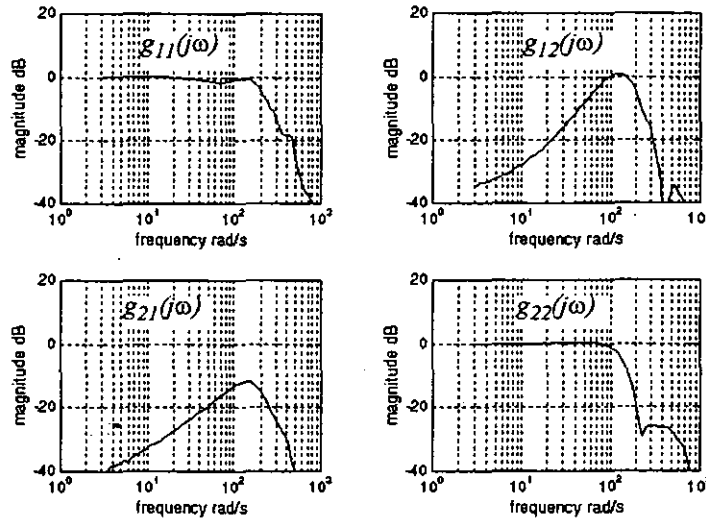
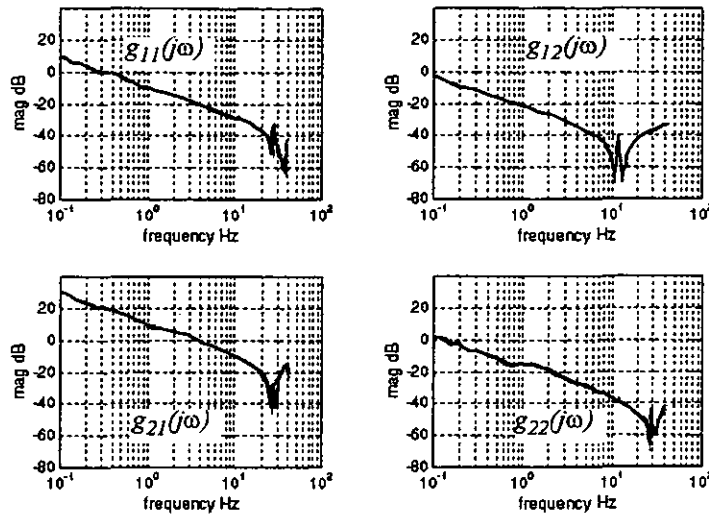


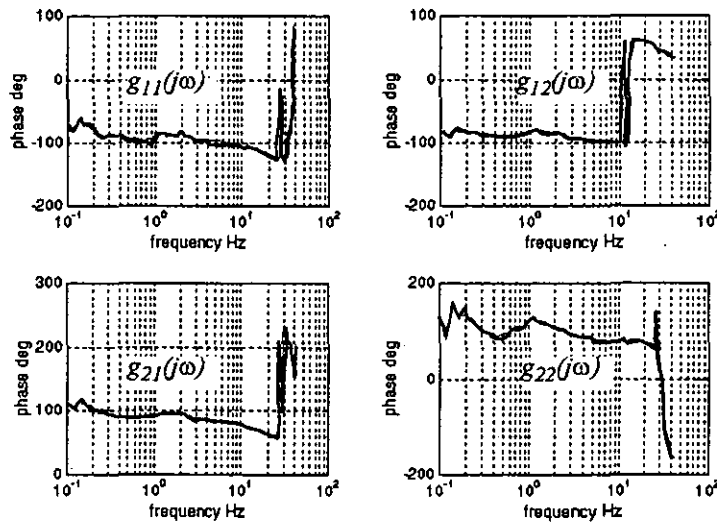
**Figure 8.13** Closed-loop frequency response of Beam and Vibrator rig, implemented discrete CL controller

### 8.3 Torsion Rig

The frequency response of the Torsion rig has been presented in chapter 3 and the magnitude response is repeated below in Figure 8.14; the simulated SLC control schemes and the design of the CL controller were based on this experimental data.



(a) Magnitude



(b) Phase

Figure 8.14 Frequency response of the magnitude of the Torsion rig

### 8.3.1 Sequential Loop closure

The block diagram for the SLC scheme is shown in Figure 5.1. It is common practice in industry to use PID control action in the individual loop controllers,  $k_i(s)$ , either in analog or digital form. The latter form lends itself well to the inclusion of fault monitoring/test shutdown, gain scheduling and data logging. PID action was employed on this test rig with the transfer function of the loop controller given in equation (8.24). The constant  $\alpha$  restricts the bandwidth of derivative action, typically  $\alpha = 10$ .

$$k(s) = K \left( 1 + \frac{1}{sT_i} + \frac{sT_d}{1 + s\alpha T_d} \right) \quad (8.24)$$

Following common practice, the parameters of each loop controller ( $K$ ,  $T_i$ ,  $T_d$ ) were adjusted experimentally from experience of the dynamics of the Test rig. Preliminary tuning with square wave excitation revealed serious closed-loop interaction with highly oscillatory step responses. Obviously, this is very undesirable as the unrecorded fatigue loading on the structure should be minimised during the tuning of the loop controllers. Consequently, tuning proceeded with sinusoidal excitation at 0.1 Hz. The PID parameters of each loop controller were manually adjusted, in turn, to achieve the best tracking with minimum steady state error for that loop. However, tuning of the second loop controller degraded the performance achieved with the first loop controller and *vica versa*, owing to interaction in the rig. Hence, the entire process became a lengthy iterative procedure until a satisfactory response was achieved.

The loop controllers were implemented as in Figure 5.1, the PID parameters are given in Table 8.3 below and the closed-loop frequency response with the implemented controller is shown in Figure 8.15. The bandwidth of the closed-loop system is approximately 2Hz with peaks in the magnitude response of the diagonal elements at approximately 1.3Hz. Also, the excitation applied to the bottom actuator interacts severely with the force applied by the top actuator, this is the element [1,2]. This performance is unacceptably poor.

**TABLE 8.3 PID parameters for SLC control**

controller	$K$	$T_i$ (ms)	$T_d$ (ms)
channel 1	9.71	13.33	13.33
channel 2	2.81	13.33	13.33

The closed-loop system was also excited by a small amplitude square wave to observe its transient response and the presence of interaction. Figure 8.16 shows the force applied by each actuator in response to a square wave demand in the force applied by the bottom actuator. The bottom actuator tracks the demand in force, although the response is undesirably oscillatory. However, the interaction with the top actuator is severe with a peak amplitude approximately five times greater than the peak response of the bottom actuator. Figure 8.17 shows the force applied by each actuator in response to a square wave demand in the force applied by the top actuator. Figure



8.17(b) clearly shows that the interaction with the bottom actuator is substantially less than that observed in the top actuator, Figure 8.16(c). The top actuator tracks the demand in force but the response is again undesirably oscillatory.

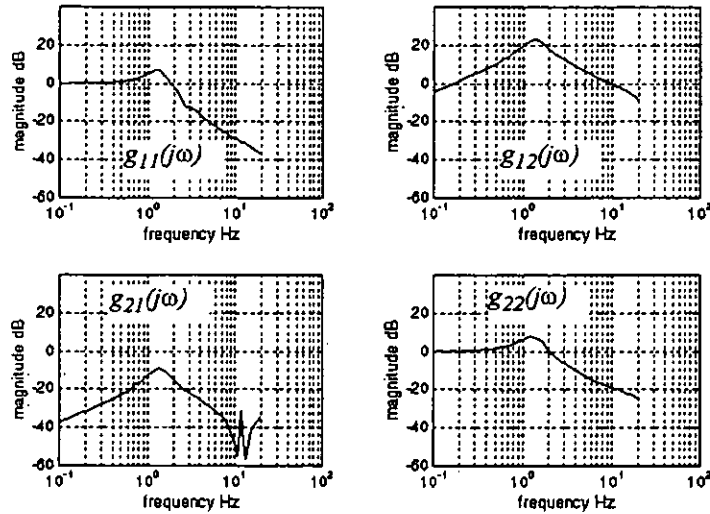


**Figure 8.15** Closed-loop frequency response of the magnitude of the Torsion rig, implemented SLC scheme

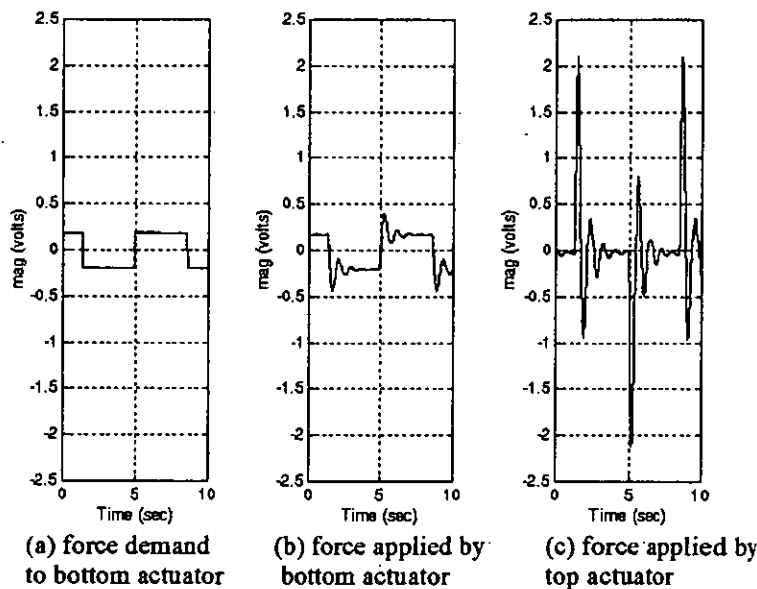


**Figure 8.16** Response of Torsion rig to a square wave demand in bottom actuator force, implemented SLC scheme

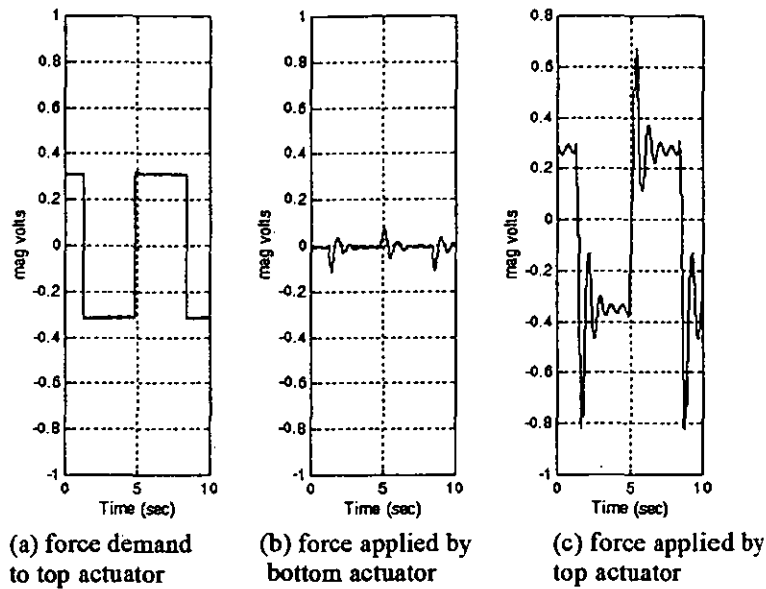


**Figure 8.17 Response of Torsion rig to a square wave demand in top actuator force, implemented SLC scheme**

In addition to the experimental tuning, Ziegler Nichols rules were used to derive the loop controller parameters. Since the test rig must be operated in the closed-loop at all times, the parameters of the control action are most appropriately determined from closed-loop continuous cycling of the plant (with proportional action only) at it's limit of stability. The standard tuning rules with derivative action are given in equation (8.25).

$$K = 0.6K_u \quad T_i = 0.5P_u \quad T_d = 0.125P_u \quad (8.25)$$

The non-unique nature of the resulting parameters has been explained in section 8.2.1, controller settings derived from two experimental continuous cycling tests are presented in Table 8.4.

**TABLE 8.4 PID parameters for simulated SLC control**

	$K_u$	$P_u$ (ms)	$K$	$T_i$ (ms)	$T_d$ (ms)
Design #1					
channel 1	16.19	26.67	9.71	13.33	13.33
channel 2	4.69	26.67	2.81	13.33	13.33
Design #2					
channel 1	5.39	24.00	3.23	12.00	3.00
channel 2	7.48	24.00	4.49	12.00	3.00

Simulated closed-loop frequency responses are shown in Figures 8.18(a) and 8.18(b). Comparing with the performance of Figure 8.15 it can be seen that the bandwidth has been improved and onset of interaction has been delayed but the performance is still poor. Thus, sequential loop closure cannot control the rig to an acceptable level of performance and implementation was not carried out.

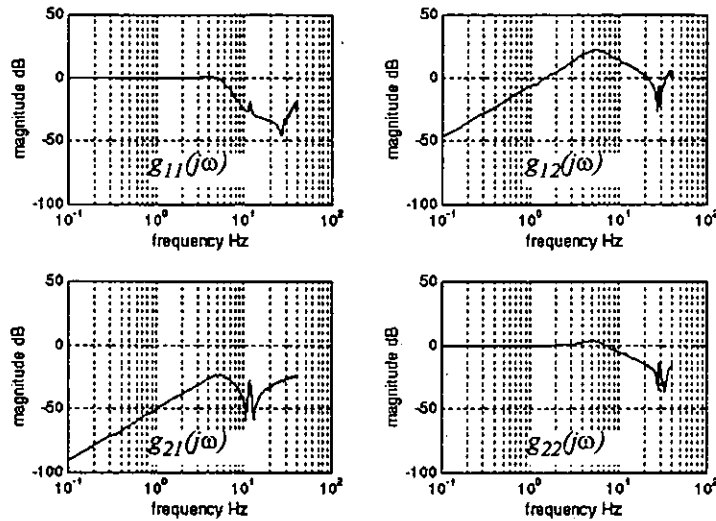


**Figure 8.18(a)** Closed-loop frequency response of the magnitude of the Torsion rig, simulated SLC scheme #1

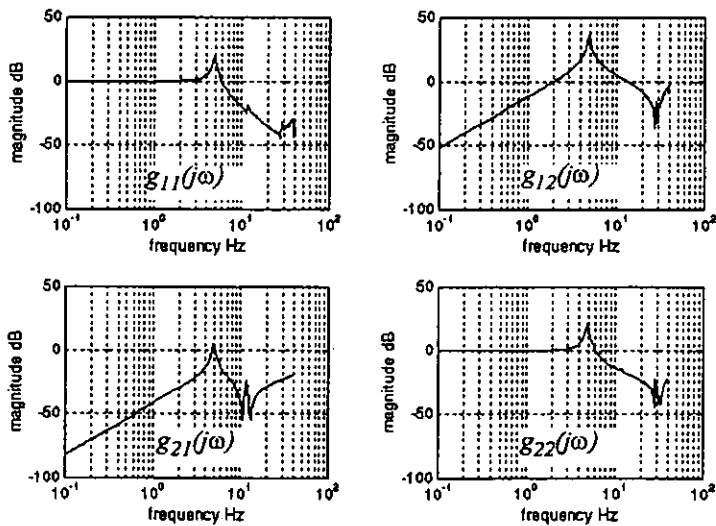


**Figure 8.18(b)** Closed-loop frequency response of the magnitude of the Torsion rig, simulated SLC scheme #2

### 8.3.2 Characteristic Locus Design [14]

The desired bandwidth of the closed-loop system was 10 Hz. To lessen the effect of interaction with the ensuing mid-frequency compensator,  $K_h$  was determined at 20 Hz. The ALIGN algorithm in MATLAB was used to calculate  $K_h \approx G^{-1}(j40\pi)$  and resulted in one of the loci of  $G(s)K_h$  lying on the negative real axis at steady state. This is undesirable since that locus will have poor gain and phase margins. The problem was resolved by negating the elements in the second column of  $K_h$ , resulting in both loci then lying on the real positive axis at steady state. The modified  $K_h$  is given in equation (8.26)

$$K_h = \begin{bmatrix} -5.2399 & -8.9309 \\ 114.0641 & -18.0609 \end{bmatrix} \quad (8.26)$$

The characteristic loci of  $G(s)K_h$  are plotted in Figure 8.19 and their gain and phase margins are given in Table 8.5. The loci approach the origin of the complex plane in a relatively smooth manner, but beyond the origin they appear noisy. This is because of a diminishing signal to noise ratio in the measured data and the highly resonant nature of the frequency response of the Torsion rig beyond 10 Hz, Figure 8.14. These 'noisy' regions have been included for completeness and it will be seen in the following pages that they have no bearing upon the controller design owing to the small magnitude of the loci at higher frequencies.

TABLE 8.5 Gain and phase margins of the characteristic loci of

	gain margin	phase margin
locus 1	$\infty$	$85.6^\circ$ (5.3Hz)
locus 2	$\infty$	$66.0^\circ$ (19.5Hz)

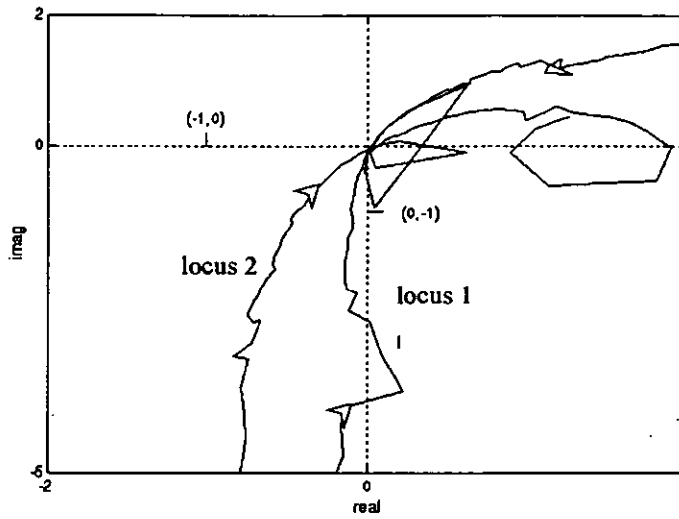


**Figure 8.19** Characteristic loci of  $G(s)K_h$ , Torsion rig

Although both loci have large gain margins these were considered acceptable in view of the likely degradation in stability and performance that would follow with discretisation and the phase lag introduced by ant-alias filtering. Likewise, the phase margin of locus 2 was considered acceptable and it was decided to compensate locus 1 with 20 degrees of phase lag at 5.3 Hz. A suitable compensator is

$$k_1(s) = \frac{s + 50.2655}{s + 25.1924} \quad (8.27)$$

The eigenvector approximations  $A_m$  and  $B_m$  were computed at  $\omega_m = 10.6\pi$  rad/s and the overall medium frequency compensator  $K_m(s) = A_m \text{diag}(k_i(s)) B_m$  is given in equation (8.28). The characteristic loci of  $G(s)K_h K_m(s)$  are shown in Figure 8.20

$$K_m(s) = \frac{1}{s + 25.19} \begin{bmatrix} s + 50.01 & 3.91 \\ 1.62 & s + 25.45 \end{bmatrix} \quad (8.28)$$

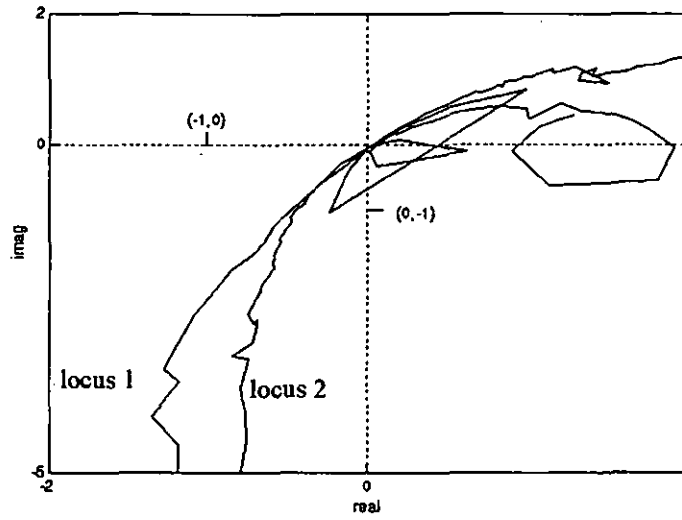


**Figure 8.20** Characteristic loci of  $G(s)K_h K_m(s)$ , Torsion rig

Low frequency compensation was designed to inject gain into the controller at low frequencies, thereby reducing steady-state error and also reducing interaction at low frequencies. The form of the compensation is that given in equation (5.17) with the diagonal gain constants chosen to be unity and the approximation matrices  $A_l$  and  $B_l$  computed at 0.1 Hz. The resulting compensator is

$$K_l(s) = \frac{1}{s} \begin{bmatrix} s + 0.61 & -0.03 \\ 0.08 & s + 1.04 \end{bmatrix} \quad (8.29)$$

The final CL controller is given by

$$K(s) = \frac{1}{d(s)} \begin{bmatrix} k_{11}(s) & k_{12}(s) \\ k_{21}(s) & k_{22}(s) \end{bmatrix} \quad (8.30)$$

where

$$\begin{aligned} k_{11}(s) &= -5.24s^2 - 280.45s - 188.21 \\ k_{12}(s) &= -8.93s^2 - 256.95s - 251.59 \\ k_{21}(s) &= 114.06s^2 + 5742.80s + 3454.30 \\ k_{22}(s) &= -18.06s^2 - 35.52s - 159.07 \\ d(s) &= s(s + 25.19) \end{aligned} \quad (8.31)$$

The characteristic loci of the compensated plant are given in Figure 8.21 where it can be seen that the loci possess adequate gain and phase margins. The simulated closed-loop frequency response is shown in Figure 8.22 and it can be seen immediately that the closed-loop performance is much improved compared to any of the SLC schemes (Figure 8.15 and Figures 8.18).

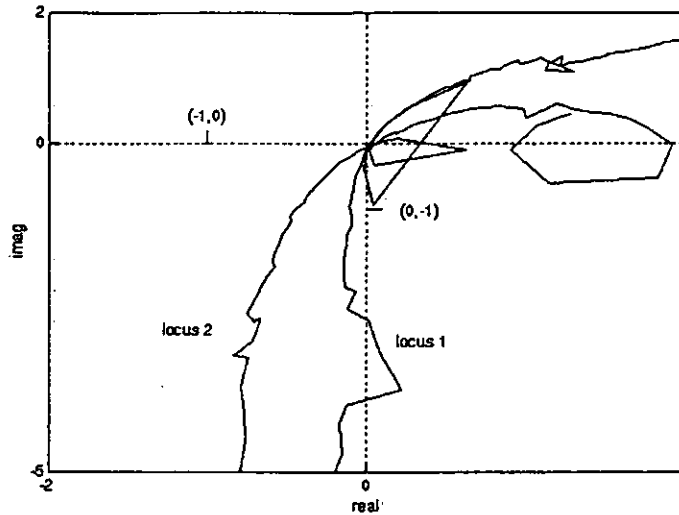


**Figure 8.21** Characteristic loci of compensated Torsion rig

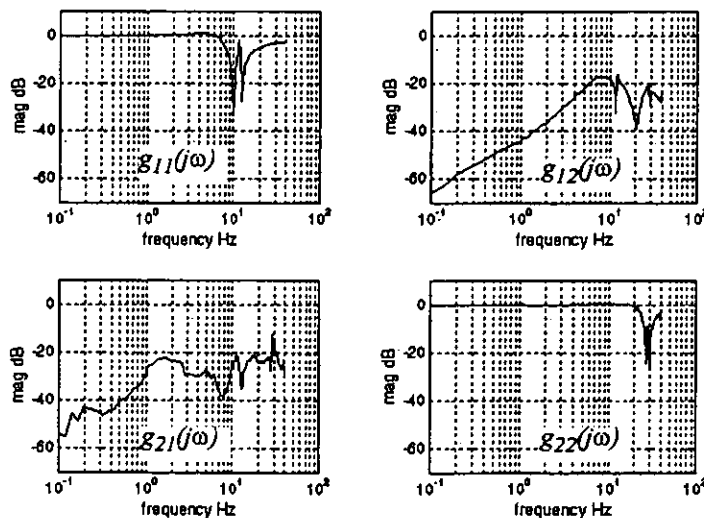


**Figure 8.22(a)** Closed-loop frequency response of the magnitude of the Torsion rig, simulated CL controller

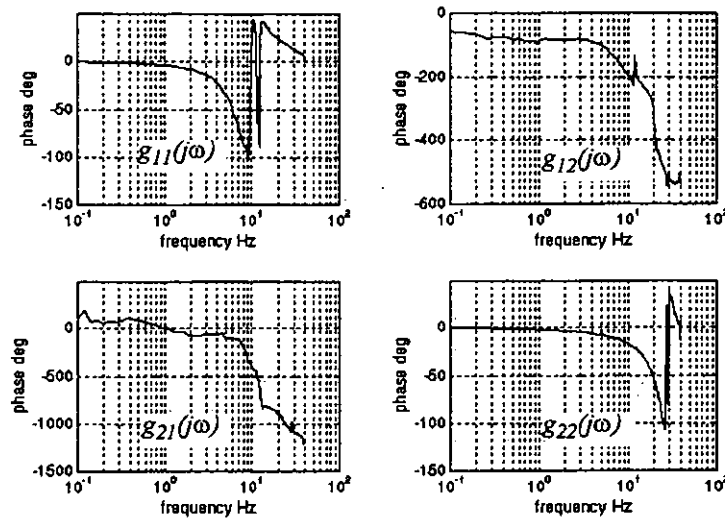


**Figure 8.22(b) Closed-loop frequency response of the phase of the Torsion rig, simulated CL controller**

### Implementation

Recall from chapter 4 that the open-loop test rig can be regarded as a type '1' system and will therefore exhibit, in the closed-loop, almost no interaction at steady-state. Therefore, the low-frequency stage of compensation was omitted from the design procedure and the CL controller is obtained from the product of equation (8.26) and equation (8.28), given below in equation (8.32)

$$K(s) = K_h K_m(s) = \frac{\begin{bmatrix} -(5.2399s + 276.5403) & -(8.9309s + 247.7576) \\ (114.0641s + 5674.86) & -(18.0609 + 13.7522) \end{bmatrix}}{s + 25.1924} \quad (8.32)$$

The sampling period for the discretisation of the controller was based on the frequency up to which the dynamics of the rig were identified - 40Hz. A sampling frequency of five to ten times this figure gives a sampling period between 2.5ms and 5 ms. The minimum sampling period that could be achieved with the computational facility available was 3ms, hence the controller was discretised using Tustin's approximation with a sampling period of 3ms. The computational facility has been previously described and the implementation is illustrated in Figure 8.23. However, the closed-loop system suffered from limit cycling. The bandwidths of the anti-alias filters and the smoothing filters were varied in an attempt to stop the limit cycling but this had no affect. The gain of the controller was systematically reduced, this reduced



the limit cycling and eventually solved the problem when the elements of the compensator  $K_h$  were reduced by a factor of 1.5.

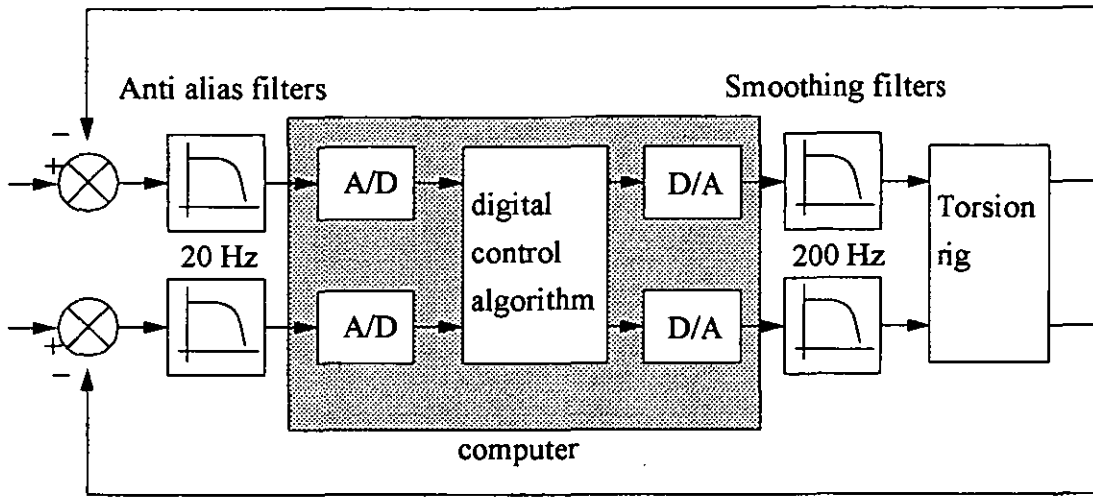


**Figure 8.23 Schematic of digital controller implementation**

The experimental closed-loop frequency response achieved with the reduced-gain controller is presented in Figure 8.24. It can be seen that the controller performs well with the exception of a resonant peak in the response of the controlled top actuator (element [1,1]). The bandwidths are similar to those of the ideal, Figure 8.22, (approximately 6 Hz for the bottom actuator, element [2,2], and approximately 16 Hz for the top actuator, element [1,1]) and interaction has been suppressed effectively up to 6 Hz.

The test rig was excited by a sinusoidal demand in force and the its response captured by a digital oscilloscope. Figure 8.25(a) shows the response of the rig to a 1Hz sinusoidal demand in the force applied by the bottom actuator. The actual force applied by the bottom actuator tracks the demand very closely, with only a small phase lag (approximately 10 degrees). Notice how the top actuator applies hardly any force - the interaction between the actuators has been effectively minimised by the multivariable controller. Similarly, Figure 8.25(b) shows the response of the rig to a 1Hz sinusoidal demand in the force applied by the top actuator. The actual force applied by the top actuator again tracks the demand very closely, with only a small phase lag (less than 10 degrees). This time, notice how the bottom actuator applies hardly any force - as before, the interaction between the actuators has been effectively minimised by the multivariable controller.

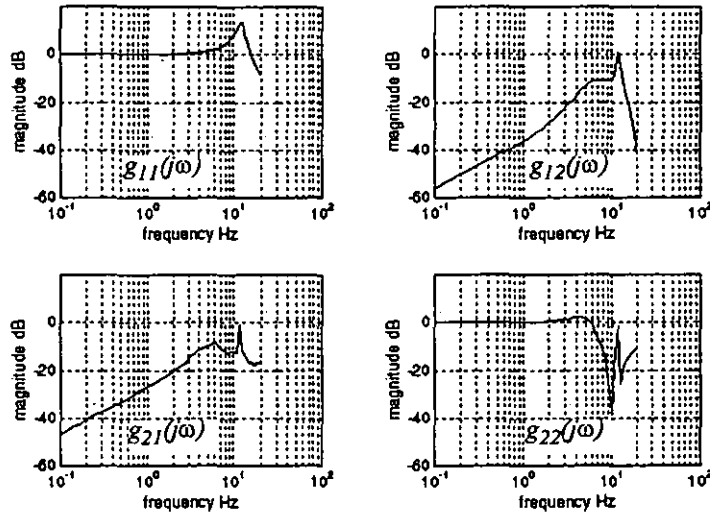


**Figure 8.24(a)** Closed-loop frequency response of the magnitude of the Torsion rig, implemented CL controller

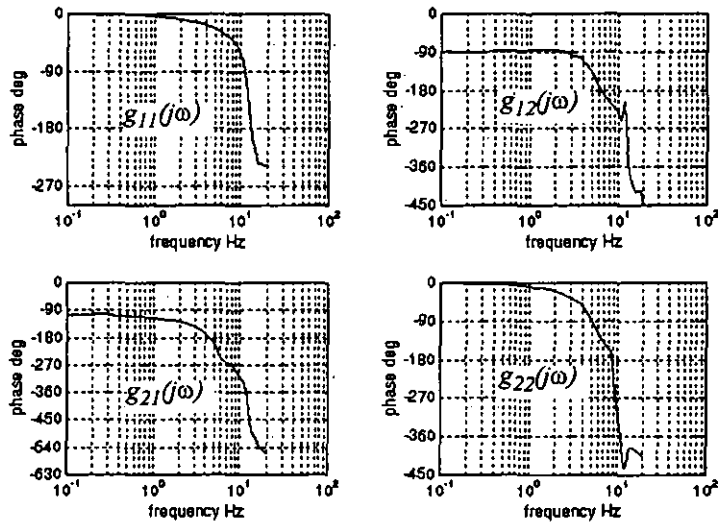


**Figure 8.24(b)** Closed-loop frequency response of the phase of the Torsion rig, implemented CL controller

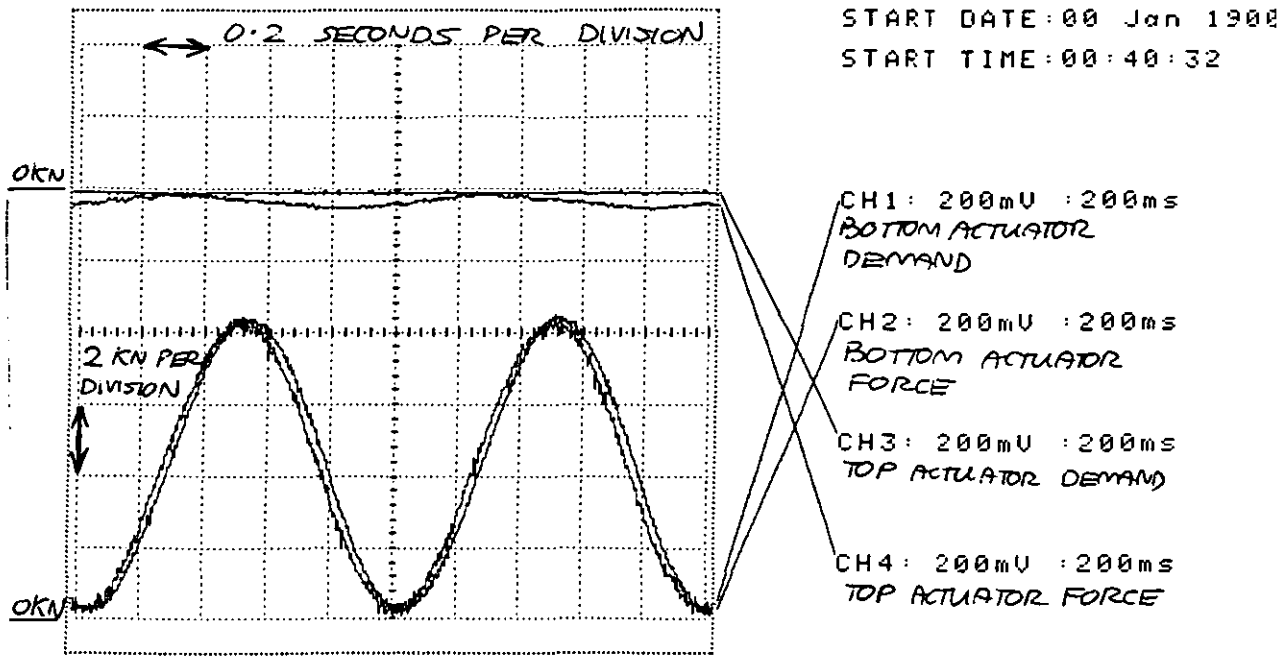


Figure 8.25(a) Sinusoidal response of Torsion rig, implemented CL controller

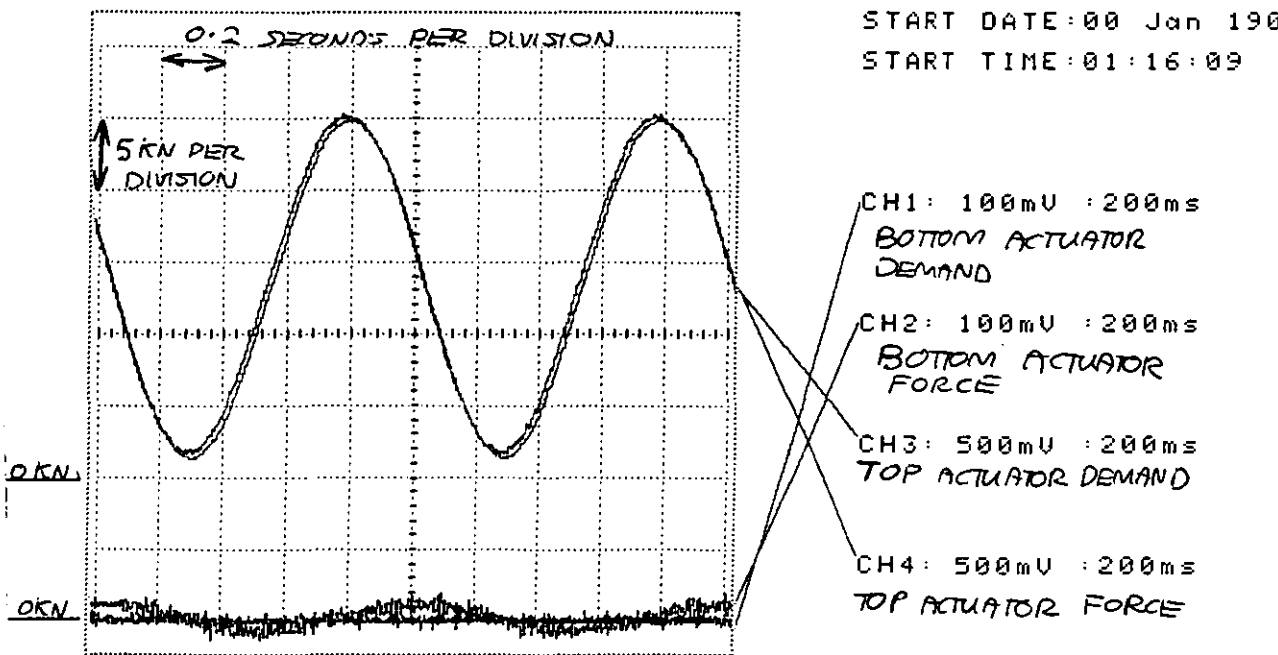


Figure 8.25(b) Sinusoidal response of Torsion rig, implemented CL controller

## 8.4 Conclusions

Controller design and implementation has been presented for two different multiple-input, multiple-output test rigs. In both cases the test rig posed a significant control problem, with major open-loop interaction, and the performance of a Sequential Loop Closure scheme has been shown to be unsatisfactory. By contrast, a Characteristic Locus controller has delivered superior performance, the greatest improvement being achieved on the Torsion rig. The controller design, for both rigs, was based upon experimental frequency response data and a mathematical model of the rig was not required. Finally, a new discrete approach to the Characteristic Locus design method, which allows dynamic approximation to the eigenvectors of the plant, has been demonstrated to provide further improvement upon the traditional Characteristic Locus method.

## Chapter 9

### Conclusions

Current control schemes for multi-channel dynamic structural tests have been reviewed and ideal specifications for control systems have been examined, with loads ranging from quasi-static to service-recorded load histories. It has been shown that for accurate dynamic testing, interaction between different inputs and outputs should be minimised. Furthermore, the frequency response of the controlled system must have unity magnitude with zero phase over the bandwidth of the test input signals. Fundamentally, a multivariable approach to controller design has been shown to directly tackle the problem of interaction whilst the use of an array of single loop controllers is limited in this respect.

In many applications the dynamic structural test is controlled with an array of single-loop controllers. This approach can lead to poor performance when loop gains are limited by stability requirements and has motivated an investigation into the conditions under which this situation is likely to occur. It is in these situations that multivariable control can offer the greatest potential for improved performance. When displacement is the controlled variable, multivariable control has been shown to more appropriate as the mass of the specimen increases and/or the stiffness of the specimen reduces. When load (force) is the controlled variable, relative stability has been shown to be very dependent upon the mass of the specimen, undergoing a local and significant minimum value as the mass increases from zero. Thus, multivariable control is appropriate in the region of this worst-case stability. By contrast, the stiffness of the specimen has little effect on stability.

Two very different test rigs have been used for the design and implementation of multivariable controllers. The first consists of a laboratory scale cantilever beam excited by two electro-dynamic vibrators, with the controlled variable being the displacement measured at the points where the beam is excited. The second rig is an industrial-scale test rig in which a steel frame is excited by two hydraulic actuators, the controlled variable being the measured force applied by the actuators. Both rigs exhibit

significant interaction, in the case of the second rig this is severe, and pose challenging control problems.

Experimental identification of the frequency response of both rigs has provided data for multivariable controller design. Identification of the industrial-scale rig was made more difficult by the imposition of closed-loop control during the identification experiment. A robust and practical method has been presented which successfully addresses this identification problem, using a correlation technique to perform closed-loop frequency response measurements and a systematic procedure to derive the open-loop frequency response from these measurements.

The Characteristic Locus method has been used to design multivariable controllers for both rigs, based upon experimental frequency response data. In the case of the laboratory rig, an existing design [4] was implemented in digital form successfully in this project. However, the design did not anticipate the effects of discretisation, leading to poor performance when compared to the analog simulation. This led naturally to the design of a new controller using a recent discrete formulation of the Characteristic Locus method, where such problems will not arise. The design was based upon a state space model of the rig. When implemented, the performance of the control system was far superior to the previous discretised analog design.

In the case of the industrial-scale test rig, the standard approach of using an array of single-loop controllers was carried out to obtain a performance bench-mark. The performance achieved with the single-loop controllers was very poor and significant interaction was experienced, even in the closed-loop. Using the standard Characteristic Locus method, a multivariable controller was designed and implemented on the rig. Performance of the control system was far superior to the bench-mark. This result is extremely important as it has demonstrated, on an industrial-scale test rig, that the performance achieved with a multivariable control system can be significantly better than that achieved with the standard array of single loop controllers.

The discrete formulation of the Characteristic Locus method requires a state space model of the plant. Future work should develop the formulation to design controllers based on frequency response data identified experimentally. Also, robust techniques should be pursued for identifying the state-space model of a plant from closed-loop experiments. This will make available many more multivariable control methods, for instance LQG,  $H_\infty$ .

---

## References

1. 'Full Scale Fatigue Testing of Components and Structures', ed. K.J. Marsh, Butterworths, Cambridge, England, 1988.
2. DeSilva, C.W., 'Optimal input design for the dynamic testing of mechanical systems', ASME Journal of Dynamic Systems, Measurement and Control, volume 109, number 2, June 1989, pp. 111-119.
3. Dodds, C.J., 'A computer system for multichannel remote parameter control of a test specimen', MTS Systems Corporation, vehicle systems division, 1978.
4. Tsavdaras, S., 'An investigation into the use of multivariable control theory in multi-channel structural testing', PhD Thesis, Loughborough University of Technology, 1990.
5. Tsavdaras, S. and Pratt, R.W., 'Developments in the design of multivariable controllers for the structural testing of systems with unknown dynamics', Proc. American Control Conference, San Diego, USA, pp. 2025-2030, 1990.
6. Pratt, R.W. and Tsavdaras, S., 'Multivariable control problems in dynamic structural testing', Trans. Inst. MC, Vol. 13, No. 2, pp. 186-189, 1991.
7. Pratt, R.W., Smith, K.J. and Tsavdaras, S., 'Using the Characteristic Locus method to design robust controllers for multichannel structural test systems', Proc. 34th AIAA Structures, Structural Dynamics and Materials conference, La Jolla, CA, pp. 2163-2173, 1993.
8. Pratt, R.W., 'The role of multivariable control in multi-channel fatigue and vibration tests', Proc. 64th SAVIAC Shock and Vibration Symposium, Fort Walton Beach, FL, USA, 1993, pp. 359-367.
9. Rossiter, J.A., Pratt, R.W. and Smith, K.J., 'A direct digital design for a multichannel structural test system using the Characteristic Locus method', Proc. Control '94, University of Warwick, UK, pp. 1548 - 1553, March 1994.
10. Pratt, R.W. and Smith, K.J., , 'Stability issues and the relevance of multivariable control in multi-channel fatigue and vibration tests', 5th



- 
- International conference on Recent Advances in Structural Dynamics, University of Southampton, UK, 18th - 21st July 1994, pp. 993-1002.
11. Pratt, R.W., Smith, K.J. and Tsavdaras, S., 'Using the Characteristic Locus method to design robust controllers for multichannel structural test systems', 34th AIAA Structures, Structural Dynamics and Materials conference, La Jolla, CA, USA, 1993, pp. 2163-2173.
  12. Smith, K.J. and Pratt, R.W., 'Obtaining open loop frequency response data from a multi-input, multi-output closed loop system for use in multivariable controller design', Proc. 10th International conference on Systems Engineering, Coventry, UK, pp. 1159-1166.
  13. Rossiter, J.A., Pratt, R.W. and Smith, K.J., 'A discrete Characteristic Locus design for a multichannel structural test system', Trans. IMC, 1995.
  14. Smith, K.J., Pratt, R.W. et. al., 'A comparison of multivariable control and sequential loop closure control in a dynamic structural test system - design and implementation', American Control Conference, Seattle, USA, 1995.
  15. Smith, K.J., Pratt, R.W. et. al., 'Stability issues and the relevance of multivariable load control in multichannel dynamic structural tests', 36th AIAA Structures, Structural Dynamics and Materials conference, New Orleans, USA, 1995.
  16. Boggs, B.C., Mondol, N.K., McQuown, R.E. and Anderson, J.G., 'Digital and analogue computer equipment and it's application to in-house testing', Use of Computers in the Fatigue Laboratory, ASTM STP 613, American Society for Testing and Materials, Philadelphia, Pa., 1976, pp 2-6.
  17. Anonymous, 'Suspension springs for motor vehicles', Engineering, 31<sup>st</sup> August, 1928, p. 273.
  18. Troughton, A.J., '33 years of aircraft fatigue', Proceedings of the 10<sup>th</sup> ICAF Symposium, Brussels, May, 1979, paper 1.1.
  19. Palmgren, A., 'Die lebensdauer von kugellagern', Zeitschrift VDI, volume 68, part 14, 1924, pp. 339-341.
  20. Miner, M.A., 'Cumulative damage in fatigue', Journal of Applied Mechanics, volume 12, part 3, 1945, pp A159-164.
-

21. Gassner, E., 'Effect of variable load and cumulative damage on fatigue in vehicle and airplane structures', Proceedings of the International Conference on Fatigue of Metals, London, September 1956, pp. 304-309.
22. Moreau, R.A. and Peterson, L., 'Field testing of diesel locomotive axles', Proceedings SESA, volume XIII, part 2, 1955, pp. 27-38.
23. Haas, T. and Kreiskorte, H., 'Critical comparison of modern fatigue testing machines with regard to requirements and design', Proceedings of the Institution of Mechanical Engineers, volume 180, part 3A, 1965-1966, pp. 31-45.
24. Ripley, E.L., 'The philosophy of structural testing a supersonic transport aircraft with particular reference to the influence of the thermal cycle', Proceedings of the 6<sup>th</sup> ICAF Symposium, Miami Beach, 1971, NASA publication SP-309.
25. Potter, J.M. and Watanabe, R.T., 'Development of fatigue loading spectra', American Society for Testing and Materials, publication ASTM STP 1006, ed.'s J. M. Potter and R.T. Watanabe, 1989, p.1, pp. 3-16.
26. Dodds, C.J. and Robson, J. D., 'The description of road surface roughness', Journal of Sound and Vibration, volume 31, part 2, 1973, pp. 175-183.
27. 'FALSTAFF, Description of a fighter aircraft loading standard for fatigue evaluation', Laboratorium fur Betriebsfestigkeit (LBF), Germany; National Aerospace Laboratory (NLR), The Netherlands; Industrie-Anlagen-Betriebsgesellschaft mbH (IABG), West Germany, 1976.
28. De Jonge, J.B. *et al.*, 'A standardised load sequence for flight simulation tests on aircraft wing structures', LBF-Bericht TB-106, NLR TR73029 U, National Aerospace Laboratory, Amsterdam, The Netherlands, 1973.
29. Lowak, H. *et al.*, 'miniTWIST, a shortened version of TWIST', LBF-Bericht TB-146, NLR MP79018 U, National Aerospace Laboratory, Amsterdam, The Netherlands, 1976.
30. Edwards, P.R. and Darts, J., 'Standardised fatigue loading sequences for helicopter rotors (Helix and Felix). Part 1: background and fatigue evaluation', RAE TR84084, Royal Aircraft Establishment, Farnborough, U.K., 1982.

31. Edwards, P.R. and Darts, J., 'Standardised fatigue loading sequences for helicopter rotors (Helix and Felix). Part 2: Final definition of Helix and Felix', RAE TR84085, Royal Aircraft Establishment, Farnborough, U.K., 1982.
32. Maciejowski, J.M., 'Multivariable feedback design', Addison-Wesley, New York, 1989.
33. Merritt, H.E., 'Hydraulic Control Systems', John Wiley & Sons, New York, 1967.
34. Shinskey, F. G., 'Process Control Systems', McGraw-Hill, New York, 1979.
35. Shinskey, F. G., 'Controlling Multivariable Processes', Instrument Society of America, Research Triangle Park NC, 1981.
36. McAvoy, T. J., 'Interaction Analysis', Instrument Society of America, Research Triangle Park NC, 1983.
37. MacFarlane, A. G. J. and Kouvaritakis, B., 'A design technique for linear multivariable feedback systems', International Journal of Control, 25, pp. 837 - 874, 1977.
38. Ford, M. P. et. al., 'Multivariable frequency domain toolbox for use with MATLAB: User guide', Cambridge Control, Cambridge, England, April 1988.
39. MacFarlane, A. G. J. and Postlethwaite, I., 'The generalized Nyquist stability criterion and multivariable root loci', International Journal of Control, 25, pp. 81 - 127, 1977.
40. Kouvaritakis, B., 'A geometric approach to the inversion of multivariable systems', International Journal of Control, 24, pp. 593 - 622, 1976.
41. Edwards, J. and Kouvaritakis, B., 'Extensions of the frame alignment technique and their use in the Characteristic Locus design method', International Journal of Control, 29, pp.787 - 796, 1979.
42. Cloud, D. J. and Kouvaritakis, B., 1987, 'Commutative controllers revisited: parallel computation a new lease of life', International Journal of Control, pp. 1335 - 1370, 1987.
43. Kouvaritakis, B. and Rossiter, J. A., 'Multivariable Nyquist self-tuning: a general approach', Proc. IEE Pt. D., 136, pp. 189 - 202, 1989.

- 44. Kouvaritakis, B. and Rossiter, J. A., 'Branch point placement', *Linear Algebra and its Applications*, 140, pp. 217-249, 1990.
- 45. same as reference [13].
- 46. Smith, K.J. and Pratt, R.W., 'Obtaining open-loop frequency response data from a multi-input, multi-output closed-loop system for use in multivariable controller design', *Proc. 10th Int. conf. on Systems Engineering*, Coventry University, UK, pp 1159-1166, 1994.
- 47. Ljung, L., 'System identification: theory for the user', Prentice-Hall Inc., New Jersey, 1987
- 48. Soderstrom, T. and Stoica, P., 'System identification', Prentice-Hall Inc., New Jersey, 1987
- 49. Godfrey, K.R., 'Correlation Methods', *Automatica*, 16, 527-534, 1980
- 50. Ljung, L. and Glover, K., 'Frequency domain versus time domain methods in system identification', *Automatica*, 17, pp 71-86, 1981
- 51. Wellstead, P. E., 'Nonparametric methods of system identification', *Automatica*, 17, pp 55-69, 1981
- 52. Unbehauen, H. and Rao, G. P., 'Continuous-time approaches to system identification - a survey', *Automatica*, 26, pp 23-35, 1990
- 53. Melo, D. L. and Friedly, J. C., 'On-line, closed-loop identification of multivariable systems', *Ind. Eng. Chem. Res.*, 31, pp 274-281, 1992
- 54. Wood, R. K. and Berry, M. W., 'Terminal composition control of a binary distillation column', *Chem. Eng. Sci.*, 28, pp 1707-1717, 1973
- 55. SIMULINK User's Guide, The MathWorks Inc., Natick, Massachusetts, 1993
- 56. Ziegler, J.G. and Nichols, N.B., 'Optimum settings for automatic controllers', *Trans. ASME*, vol.64, pp. 759 - 768.
- 57. Pratt, R.W., Smith, K.J. and Tsavdaras, S., 'Using the Characteristic Locus method to design robust controllers for multichannel structural test systems', *Proc. 34th AIAA Structures, Structural Dynamics and Materials conference*, La Jolla, CA, pp. 2163-2173, 1993.

- 58. Kouvaritakis, B., 'A geometric approach to the inversion of multivariable systems', *International Journal of Control*, 24, pp. 593 - 622, 1976.
- 59. Edwards, J. and Kouvaritakis, B., 'Extensions of the frame alignment technique and their use in the Characteristic Locus design method', *International Journal of Control*, 29, pp.787 - 796, 1979.
- 60. Kouvaritakis, B. and Rossiter, J. A., 'Multivariable Nyquist self-tuning: a general approach', *Proc. IEE Pt. D.*, 136, pp. 189 - 202, 1989.
- 61. Rossiter, J.A. et. al., 'A direct digital design for a multichannel structural test system using the Characteristic Locus method', *Proc. Control '94*, University of Warwick, UK, pp. 1548 - 1553, March 1994.
- 62. same as reference [13].
- 63. Astrom, K. J. and Wittenmark, B., 'Computer controlled systems: theory and design', Prentice-Hall International Inc., 1984, p. 31.

## Appendix 1

### Flow-Pressure Characteristic of a Two-Stage Force Feedback Servo-Valve

At the heart of a servo-valve is a four-way valve known as a spool-valve, illustrated in Figure A1.1. The relationship between the pressure at the ports and the flow of fluid through the ports defines the hydraulic characteristic of the valve. This characteristic is known as the flow-pressure characteristic of the valve and is derived below.

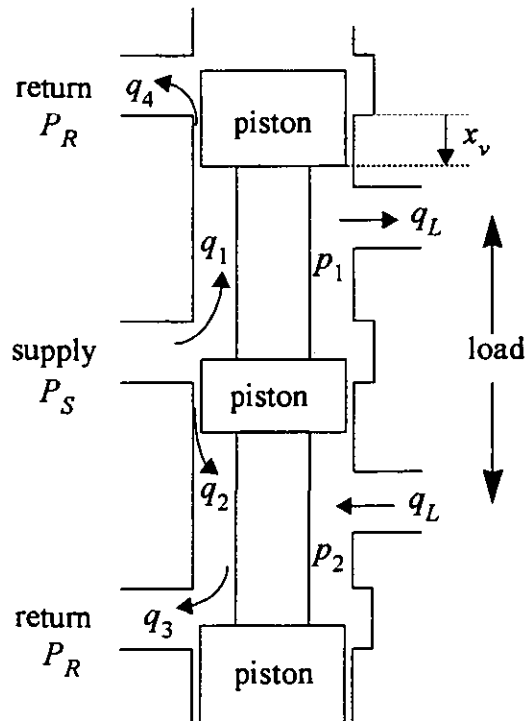


Figure A1.1 Four-way valve

In the following analysis it is assumed that (1) the valve ports are matched and symmetrical, (2) the fluid in the valve is incompressible, (3) the supply pressure  $P_s$  is

constant, (4) the return pressure  $P_R$  is zero, and (5) that there is no leakage across the pistons.

The pressure drop across the load  $p_L$  is defined below. For the remainder of this analysis  $p_L$  will be referred to as the load pressure.

$$p_L = p_1 - p_2 \quad (\text{A1.1})$$

The flow of fluid from the hydraulic supply and to the hydraulic return is indicated by  $q_1, q_2$  and  $q_3, q_4$  respectively in Figure A1.1. Applying the fundamental orifice flow equation to the spool valve gives

$$\begin{aligned} q_1 &= C_d A_1(x_v) \sqrt{\frac{2}{\rho} (P_s - p_1)} \\ q_2 &= C_d A_2(x_v) \sqrt{\frac{2}{\rho} (P_s - p_2)} \\ q_3 &= C_d A_3(x_v) \sqrt{\frac{2}{\rho} p_2} \\ q_4 &= C_d A_4(x_v) \sqrt{\frac{2}{\rho} p_1} \end{aligned} \quad (\text{A1.2})$$

Since the valve orifices are matched and symmetrical

$$\begin{aligned} A_1(x_v) &= A_3(x_v) = A_2(-x_v) \\ A_2(x_v) &= A_4(x_v) = A_1(-x_v) \end{aligned} \quad (\text{A1.3})$$

Also, since zero leakage is assumed

$$\begin{aligned} A_1(x_v < 0) &= A_2(x_v > 0) = 0 \\ A_3(x_v < 0) &= A_4(x_v > 0) = 0 \end{aligned} \quad (\text{A1.4})$$

Furthermore, since the oil is assumed to be incompressible

$$q_L = q_1 - q_4 = q_3 - q_2 \quad (\text{A1.5})$$

Also

$$\begin{aligned} q_1 &= q_3 \\ q_2 &= q_4 \end{aligned} \quad (\text{A1.6})$$

Substituting for  $q_1$  and  $q_3$  from equation (A1.2) into equation (A1.6), noting that  $A_1(x_v) = A_3(x_v)$  from equation (A1.3), the following is obtained

$$P_s = p_1 + p_2 \quad (\text{A1.7})$$

Equation (A1.1) and equation (A1.7) are a simultaneous pair which describe the pressure at each load port as a function of the supply pressure and the load pressure, thus

$$\begin{aligned} p_1 &= \frac{P_s + p_L}{2} \\ p_2 &= \frac{P_s - p_L}{2} \end{aligned} \quad (\text{A1.8})$$

Hence, at zero load pressure, the pressure at each load port is exactly one half of the supply pressure. It is desirable to express the load flow as a function of the supply pressure and the load pressure: Substituting for  $q_1$  and  $q_4$  from equation (A1.2) into equation (A1.5) gives the following, where equation (A1.8) has been used to express the pressure at each load port in terms of  $P_s$  and  $p_L$

$$q_L = C_d A_1(x_v) \sqrt{\frac{P_s - p_L}{\rho}} - C_d A_4(x_v) \sqrt{\frac{P_s + p_L}{\rho}} \quad (\text{A1.9})$$

However, for  $x_v > 0$  the orifice area  $A_4(x_v)$  is zero and

$$q_L|_{x_v > 0} = C_d A_1(x_v) \sqrt{\frac{P_s - p_L}{\rho}} \quad (\text{A1.10})$$

In a similar fashion

$$q_L|_{x_v < 0} = -C_d A_4(x_v) \sqrt{\frac{P_s + p_L}{\rho}} \quad (\text{A1.11})$$

From equation (A1.3)  $A_1(x_v) = A_4(-x_v)$  and so equations (A1.10) and (A2.11) can be combined into the following

$$q_L = \text{sgn}(x_v) C_d A_1(|x_v|) \sqrt{\frac{P_s - \text{sgn}(x_v) p_L}{\rho}} \quad (\text{A1.12})$$

Furthermore, since the spool valve has rectangular orifices width a width  $w$ , then  $A_1(x_v) = w x_v$ . Thus, equation (A1.12) can be written



$$q_L = x_v (C_d w \sqrt{P_s / \rho}) \sqrt{1 - \operatorname{sgn}(x_v) \frac{p_L}{P_s}} \quad (\text{A1.13})$$

## Appendix 2

### Decoupling a Damped System

#### A2.1 Introduction

In this appendix it is shown how to determine a viscous damping matrix  $C$  for a mechanical system such that all of the modes of the system have the same damping ratio and the system is decoupled under a linear transformation. The mechanical system is described by the matrix equation

$$f(t) = M\ddot{x}(t) + C\dot{x}(t) + Kx(t) \quad (\text{A2.1})$$

where  $f(t)$  is a vector of forces,  $x(t)$  is a vector of displacements,  $M$  is a diagonal matrix of mass elements,  $C$  is a matrix of viscous damping elements and  $K$  is a symmetric matrix of stiffness elements.

#### A2.2 General result

First of all consider the original system without damping, i.e.

$$f(t) = M\ddot{x}(t) + Kx(t) \quad (\text{A2.2})$$

A generalised transformation  $x = Vq$  can be derived from the mass-stiffness eigenvalue problem, equation (A2.3), that will decouple the system.  $\Lambda$  is a diagonal matrix whose diagonal elements are the eigenvalues of  $M^{-1}K$  and  $V$  is a matrix of eigenvectors of  $M^{-1}K$

$$M^{-1}K = V\Lambda V^{-1} \quad (\text{A2.3})$$

Applying the transformation to the undamped system of differential equations, equation (A2.2), leads to the system of equations given in equation (A2.4), where the transformed mass and stiffness matrices are diagonal. Thus the system is decoupled.

$$V^T f(t) = V^T M V \ddot{q}(t) + V^T K V q(t) \quad (\text{A2.4})$$

The objective is to introduce damping into the system of equations in such a way that the system remains decoupled under the transformation. The transformed system with damping becomes

$$V^T f(t) = V^T M V \ddot{q}(t) + V^T C V \dot{q}(t) + V^T K V q(t) \quad (\text{A2.5})$$

Firstly some preliminaries. The generalised transformation matrix can be written as the product

$$V = M^{-1/2} \Phi \quad (\text{A2.6})$$

noting that the eigenvectors constituting the columns of  $V$  are normalised such that  $V^T M V = I$ , giving

$$\Phi^T \Phi = I \quad (\text{A2.7})$$

From equation (A2.6) and equation (A2.7), the transformed system can be written as

$$V^T f(t) = I \ddot{q}(t) + \Phi^T A \Phi \dot{q}(t) + \Phi^T B \Phi q(t) \quad (\text{A2.8})$$

where

$$\begin{aligned} A &= M^{-\frac{1}{2}} C M^{-\frac{1}{2}} \\ B &= M^{-\frac{1}{2}} K M^{-\frac{1}{2}} \end{aligned} \quad (\text{A2.9})$$

Now  $V^T K V$  is diagonal, and from equations (A2.5) and (A2.8)

$$\begin{aligned} \Phi^T B \Phi &= V^T K V = \text{diag}(b) \\ \therefore B &= \Phi \text{diag}(b) \Phi^{-1} \end{aligned} \quad (\text{A2.10})$$

Comparing equation (A2.10) with equation (A2.3) it is clear that  $\Phi$  is a matrix of eigenvectors of  $B$  and  $\text{diag}(b)$  is the matrix of eigenvalues of  $B$ . Consequently, powers of  $B$  (integer or fractional) are easily determined thus

$$B^{\frac{p}{q}} = \Phi \text{diag} \left( b^{\frac{p}{q}} \right) \Phi^{-1} \quad (\text{A2.11})$$

Hence from equation (A2.7) and equation (A2.11)

$$\Phi^T B^{\frac{p}{q}} \Phi = \text{diag} \left( b^{\frac{p}{q}} \right) \quad (\text{A2.12})$$

which is diagonal. This leads to a general rule for decoupling viscously damped systems:

### General rule

Provided that  $A$  is any linear combination of powers (integer or fractional) of  $B$

$$A = \alpha_1 B^{\frac{p_1}{q_1}} + \alpha_2 B^{\frac{p_2}{q_2}} + \dots \quad (\text{A2.13})$$

Then  $\Phi^T A \Phi$  will be diagonal and the system will be decoupled, since from equations (A2.12) and (A3.13)

$$\Phi^T A \Phi = \alpha_1 \text{diag} \left( b^{\frac{p_1}{q_1}} \right) + \alpha_2 \text{diag} \left( b^{\frac{p_2}{q_2}} \right) + \dots \quad (\text{A2.14})$$

## A2.3 Global Damping ratio

It is not uncommon in modelling lightly damped structures to specify a global damping ratio to be applied to all vibrational modes of the structure. Assuming that equation (A2.8) is decoupled then it can be written in the following standard second

order form, where  $\zeta$  is the global damping ratio applied to all modes and  $W$  is the diagonal matrix of natural (modal) frequencies.

$$V^T f(t) = I\ddot{q}(t) + 2\zeta W\dot{q}(t) + W^2 q(t) \quad (\text{A2.15})$$

Comparing equation (A2.8) and equation (A2.15) yields

$$\begin{aligned} A &= \Phi (2\zeta W) \Phi^T \\ W &= \Phi^T B^{1/2} \Phi \end{aligned} \quad (\text{A2.16})$$

from which

$$A = 2\zeta B^{\frac{1}{2}} \quad (\text{A2.17})$$

and equation (A2.13) is satisfied. Finally, substituting for  $A$  and  $B$  from equations (A2.9) into equation (A2.17) and rearranging gives

$$C = 2\zeta M (M^{-1} K)^{\frac{1}{2}} \quad (\text{A2.18})$$

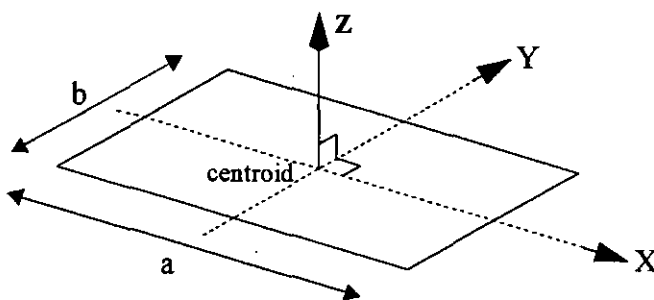
## Appendix 3

### Mass Moment of Inertia Calculations for the Torsion Rig

#### A3.1 Introduction

For the Torsion rig described in chapter 3 and modelled in chapter 4, the mass moment of inertia is required for both the top and bottom lever arms. The inertias are determined from the appropriate application of the formulae in section A3.2 to the geometry of the lever arms thus: bottom lever arms - section A3.3, top lever arms - section A3.4. The calculated inertias are summarised in section A3.5

#### A3.2 Formulae



Second moment  
of area of a rectangle

$$I_X = \frac{ab^3}{12} \quad (\text{A3.1})$$

$$I_Y = \frac{ba^3}{12} \quad (\text{A3.2})$$

Figure A3.1 Second moment of area of a rectangle

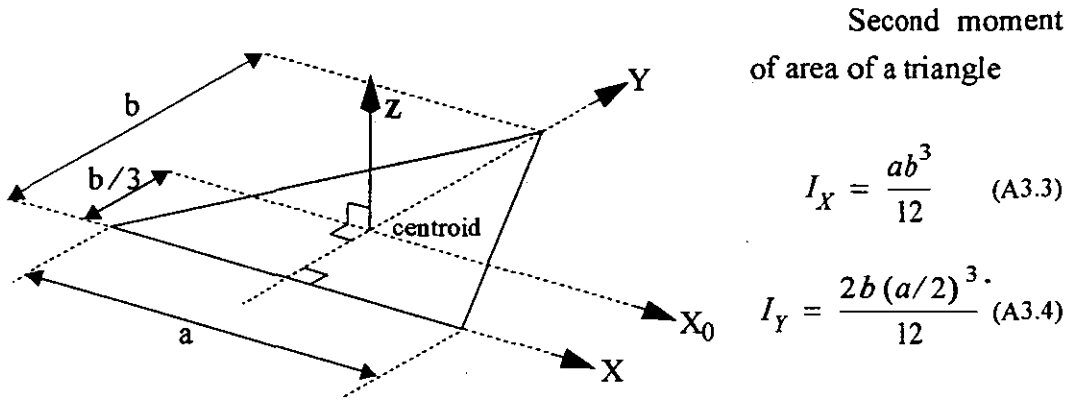


**Figure A3.2 Second moment of area of a triangle**

Perpendicular axes theorem:

$$I_Z = I_X + I_Y \quad (\text{A3.5})$$

Parallel axes theorem ( $A$  = area,  $d$  = distance between axes):

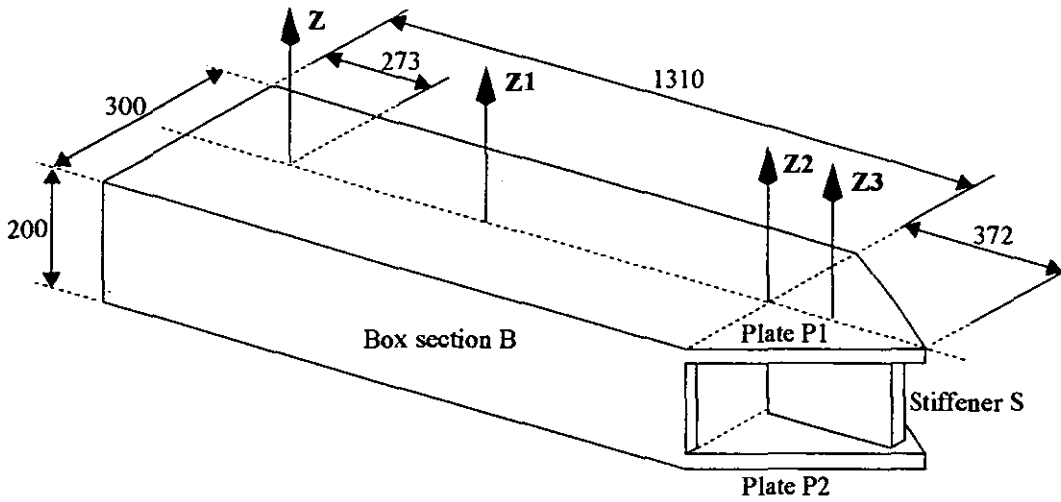
$$I_{Z1} = I_Z + Ad^2 \quad (\text{A3.6})$$

Mass moment of inertia - rectangular cross section ( $I_Z$  = second moment of area,  $\rho$  = density of material,  $t$  = thickness of material):

$$I_{Z_{mass}} = \rho t I_Z \quad (\text{A3.7})$$

### A3.3 Bottom lever arms

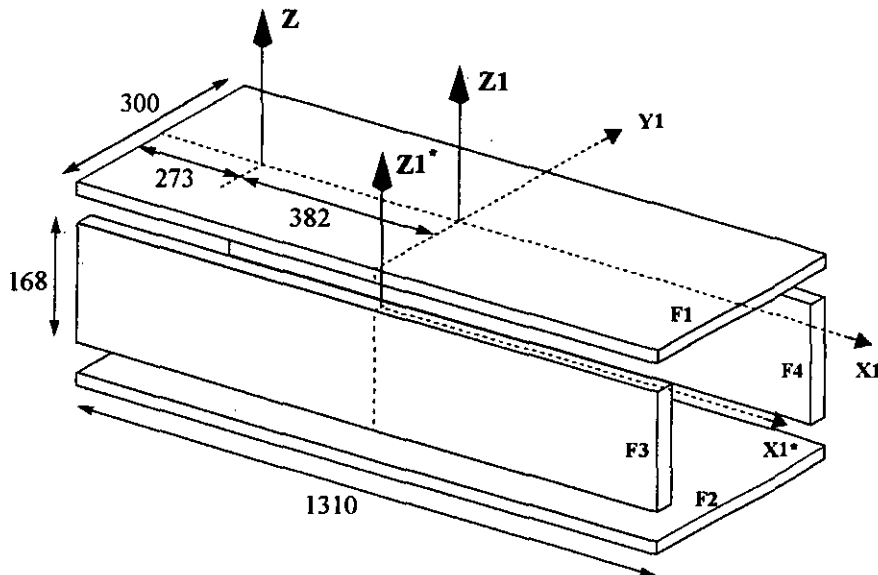
The two bottom lever arms are identical with the geometry illustrated in Figure A3.3. The lever arm is decomposed into three distinct sections for the purpose of calculating the mass moment of inertia: the box section B, the triangular plates P1 and P2, and the stiffener S. The inertia is calculated for each of these sections and summarised in tables A3.1 through to A3.3 respectively. The total inertia of the lever arm is then given by the sum of these component values, plus the inertia of the discrete mass located toward the tip of the lever arm, table A3.4.



Z is polar axis of upright beam  
 S: thickness of material 29 mm  
 B, P1 and P2: thickness of material 16 mm

NOTE: (1) Discrete mass M rests on plate P1, centred on Z3  
 (not illustrated)  
 (2) All dimensions in mm

**Figure A3.3 Schematic of bottom lever arm**



Thickness of all plates 16 mm

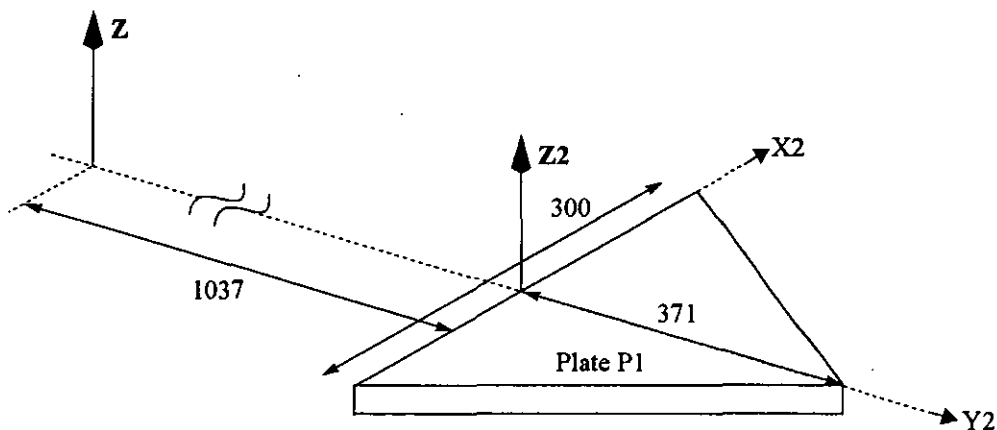
NOTE: All dimensions in mm

**Figure A3.4 Exploded view of box section**



TABLE A3.1 Moment of inertia of box section

Face F1			Face F2 (same as F1)	Face F3			Face F4 (same as F3)
$a$	1.31 m	Fig. A3.4	0.117 m <sup>4</sup>	$a$	1.31 m	Fig. A3.4	0.007 m <sup>4</sup>
$b$	0.3 m	Fig. A3.4		$b$	0.016 m	Fig. A3.4	
$A$	0.393 m <sup>2</sup>	$a \times b$		$A$	0.021 m <sup>2</sup>	$a \times b$	
$d$	0.382 m	Fig. A3.4		$d$	0.41m	Fig. A3.4	
$I_{X1}$	0.00295 m <sup>4</sup>	Eq. A3.1		$I_{X1}^*$	$0.447 \times 10^{-6} \text{ m}^4$	Eq. A3.1	
$I_{Y1}$	0.0562 m <sup>4</sup>	Eq. A3.2		$I_{Y1}$	0.003 m <sup>4</sup>	Eq. A3.2	
$I_{Z1}$	0.0592 m <sup>4</sup>	Eq. A3.5		$I_{Z1}^*$	0.003 m <sup>4</sup>	Eq. A3.5	
$I_Z$	0.117 m <sup>4</sup>	Eq. A3.6		$I_Z$	0.007 m <sup>4</sup>	Eq. A3.6	
$t$	0.016 m	Fig. A3.4		$t$	0.168 m	Fig. A3.4	
$\rho$	7800 Kg/m <sup>3</sup>			$\rho$	7800 Kg/m <sup>3</sup>		
$I_{Z_{mass}}$	14.601 Kg m <sup>2</sup>	Eq. A3.7	14.601 Kg m <sup>2</sup>	$I_{Z_{mass}}$	9.173 Kg m <sup>2</sup>	Eq. A3.7	9.173 Kg m <sup>2</sup>
Total mass moment of inertia of box section: $\sum I_{Z_{mass}} = 47.548 \text{ Kg m}^2$							



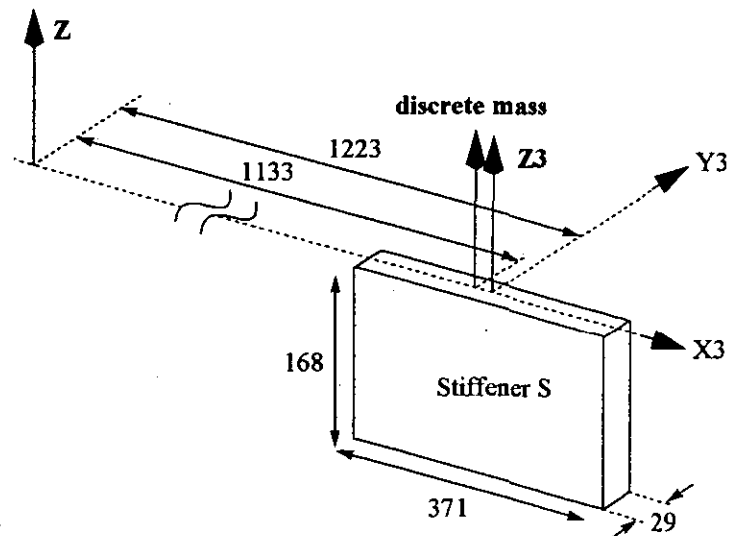
Thickness of all plates 16 mm

NOTE: All dimensions in mm

Figure A3.5 Triangular plate

**TABLE A3.2 Moment of inertia of triangular plates**

Plate P1			Plate P2 (same as P1)
$a$	0.3 m	Fig. A3.5	0.062 m <sup>4</sup>
$b$	0.371 m	Fig. A3.5	
$A$	0.056 m <sup>2</sup>	$(a \times b) / 2$	
$d$	1.037 m	Fig. A3.5	
$I_{x2}$	$1.277 \times 10^{-3}$ m <sup>4</sup>	Eq. A3.3	
$I_{y2}$	$2.089 \times 10^{-4}$ m <sup>4</sup>	Eq. A3.4	
$I_{z2}$	$1.486 \times 10^{-3}$ m <sup>4</sup>	Eq. A3.5	
$I_z$	0.062 m <sup>4</sup>	Eq. A3.6	
$t$	0.016 m	Fig. A3.5	7.701 Kgm <sup>2</sup>
$\rho$	7800 Kg/m <sup>3</sup>		
$I_{z_{mass}}$	7.701 Kgm <sup>2</sup>	Eq. A3.7	
Total mass moment of inertia of triangular plates:			
$\sum I_{z_{mass}} = 15.402$ Kgm <sup>2</sup>			



NOTE: All dimensions in mm

**Figure A3.6 Stiffener (bottom lever arm)**

**TABLE A3.3 Moment of inertia of stiffener**

Stiffener S		
$a$	0.371 m	Fig. A3.6
$b$	0.029 m	Fig. A3.6
$A$	$1.706 \times 10^{-2} \text{ m}^2$	$(a \times b)$
$d$	1.223 m	Fig. A3.6
$I_{X3}$	$7.540 \times 10^{-7} \text{ m}^4$	Eq. A3.1
$I_{Y3}$	$1.234 \times 10^{-4} \text{ m}^4$	Eq. A3.2
$I_{Z3}$	$1.242 \times 10^{-4} \text{ m}^4$	Eq. A3.5
$I_Z$	$1.622 \times 10^{-2} \text{ m}^4$	Eq. A3.6
$t$	0.168 m	Fig. A3.6
$\rho$	7800 Kg/m <sup>3</sup>	
$I_{Z_{mass}}$	21.25 Kg m <sup>2</sup>	Eq. A3.7

**TABLE A3.4 Moment of inertia of discrete mass**

Discrete mass M		
$M$	100 Kg	
$r$	1.133 m	Fig. A3.6
$I_{Z_{mass}}$	128.369 Kg m <sup>2</sup>	$(M \times r^2)$

The mass moment of inertia of the lever arm is then given by the sum of the  $I_{Z_{mass}}$  values in tables A3.1 to A3.4 thus:

$$I_{Z_{mass}} = 47.548 + 15.402 + 21.250 + 128.369 = 212.6 \quad \text{Kg m}^2 \quad (\text{A3.8})$$

## A3.4 Top lever arms

The two top lever arms are identical with the outline geometry illustrated in Figure A3.7 (not to scale). The lever arm is decomposed into three distinct sections for the purpose of calculating the mass moment of inertia: the plates P1 and P2, the stiffener S and the section of upright beam running through the lever arm, B. The inertia is calculated for each of these sections and summarised in tables A3.5 through

to A3.7 respectively. The total inertia of the lever arm is then given by the sum of these component values.

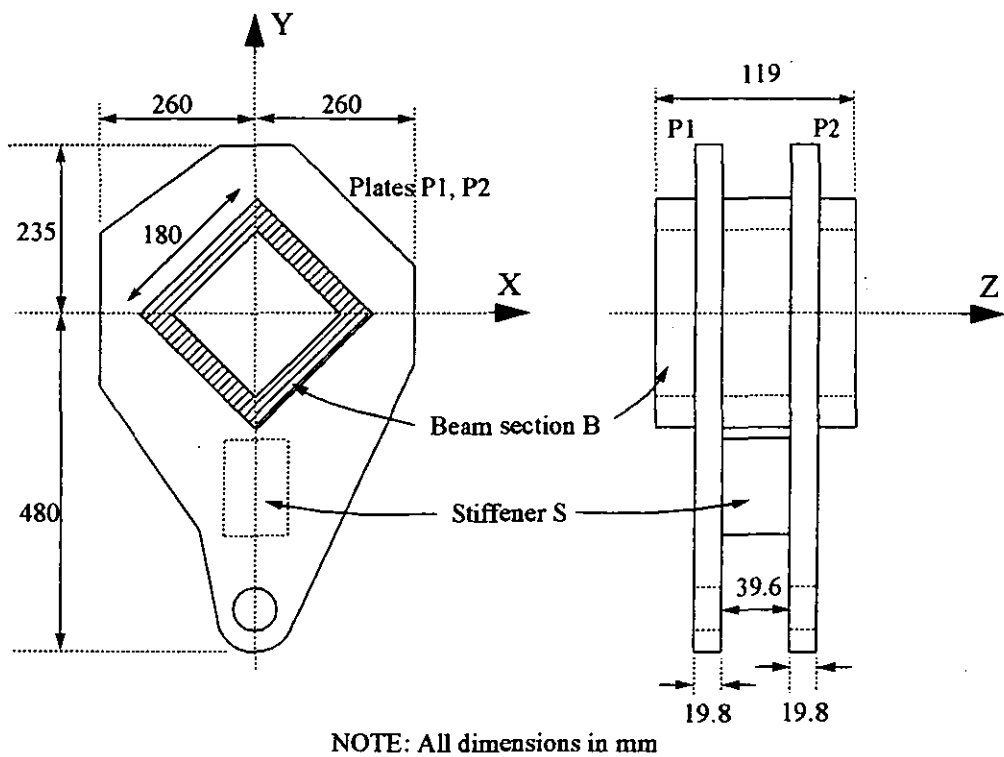


Figure A3.7 Schematic of top lever arm

To calculate the mass moment of inertia of the plates P1 and P2, their geometry is simplified to the diamond shape illustrated in Figure A3.8, the diamond is then split into four triangles for the calculations summarised in table A3.5. The area occupied by the upright beam is taken into account in table A3.5.

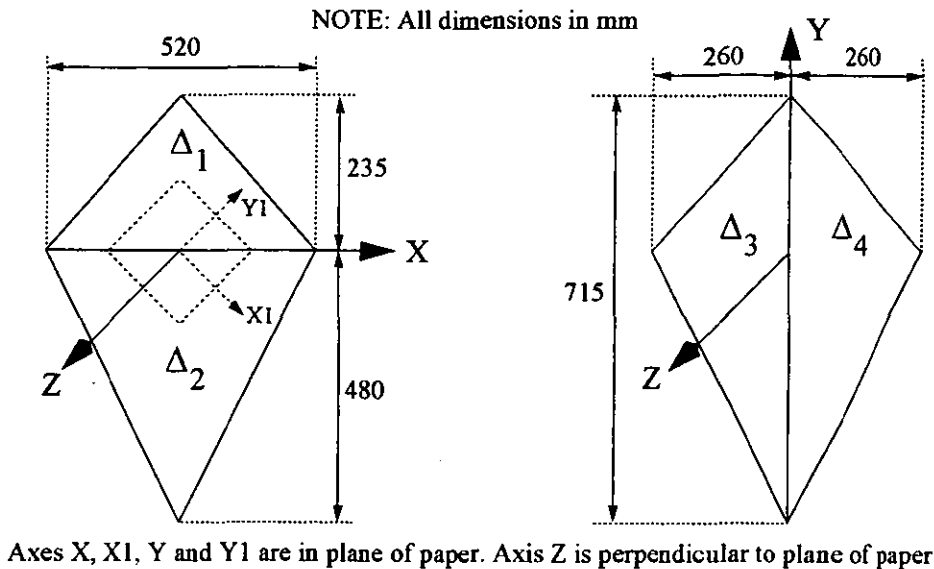
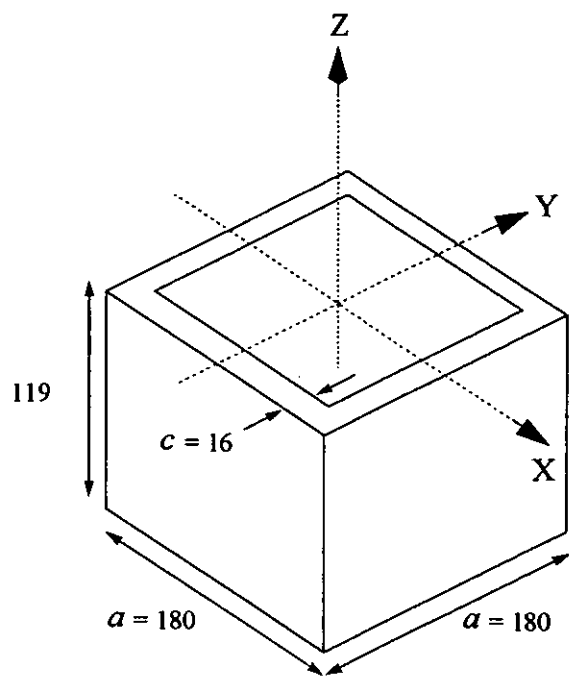


Figure A3.8 Simplified geometry of plates (top lever arm)

TABLE A3.5 Moment of inertia of triangular plates

Plate P1			Plate P2 (same as P1)
Second moment of area about X ( $\Delta_1$ ):			1.123 Kgm <sup>2</sup>
$a$	0.52 m	Fig. A3.8	
$b$	0.235 m	Fig. A3.8	
$I_X(\Delta_1)$	$5.624 \times 10^{-4} \text{ m}^4$	Eq. A3.3	
Second moment of area about X ( $\Delta_2$ ):			
$a$	0.52 m	Fig. A3.8	
$b$	0.48 m	Fig. A3.8	
$I_X(\Delta_2)$	$4.792 \times 10^{-3} \text{ m}^4$	Eq. A3.3	
Second moment of area about Y ( $\Delta_3, \Delta_4$ ):			
$a$	0.715 m	Fig. A3.8	
$b$	0.26 m	Fig. A3.8	
$I_Y(\Delta_3)$	$1.047 \times 10^{-3} \text{ m}^4$	Eq. A3.3	
$I_Y(\Delta_4)$	$1.047 \times 10^{-3} \text{ m}^4$	Eq. A3.3	
Total second moment of area about Z axis:			
$I_Z = I_X(\Delta_1) + I_X(\Delta_2) + I_Y(\Delta_3) + I_Y(\Delta_4)$			
$I_Z = 7.448 \times 10^{-3} \text{ m}^4$			
Second moment of area of square cut-out:			
$a$	0.180 m	Fig. A3.8	
$b$	0.180 m	Fig. A3.8	
$I_{X1}$	$8.748 \times 10^{-5} \text{ m}^4$	Eq. A3.1	
$I_{Y1}$	$8.748 \times 10^{-5} \text{ m}^4$	Eq. A3.2	
$I_Z$	$1.750 \times 10^{-4} \text{ m}^4$	Eq. A3.5	
Net second moment of area of plate			
$I_Z = 7.448 \times 10^{-3} - 1.750 \times 10^{-4} = 7.273 \times 10^{-3} \text{ m}^4$			
Moment of inertia:			
$t$	0.0198 m	Fig. A3.7	
$\rho$	7800 Kg/m <sup>3</sup>		
$I_{Z_{mass}}$	1.123 Kgm <sup>2</sup>	Eq. A3.7	
Combined mass moment of inertia of plates P1 and P2:			
$\sum I_{Z_{mass}} = 2.247 \text{ Kgm}^2$			



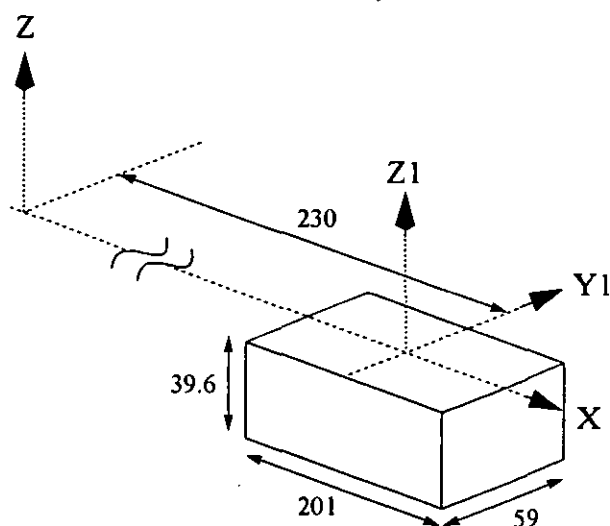
$$I_z = \frac{1}{6} [a^4 - (a - 2c)^4] \tag{A3.9}$$

NOTE: All dimensions in mm

Figure A3.9 Beam section

TABLE A3.6 Moment of inertia of beam section

Beam section		
$a$	0.18 m	Fig. A3.9
$c$	0.016 m	Fig. A3.9
$I_z$	$9.500 \times 10^{-5} \text{ m}^4$	Eq. A3.9
$t$	0.119 m	Fig. A3.9
$\rho$	7800 Kg/m <sup>3</sup>	
$I_{z_{mass}}$	0.088 Kg m <sup>2</sup>	Eq. A3.7



NOTE: All dimensions in mm

Figure A3.10 Stiffener (top lever arm)

TABLE A3.7 Moment of inertia of stiffener (top lever arm)

Stiffener S		
$a$	0.201 m	Fig. A3.10
$b$	0.059 m	Fig. A3.10
$A$	$0.012 \text{ m}^2$	$(a \times b)$
$d$	0.230 m	Fig. A3.10
$I_X$	$3.440 \times 10^{-6} \text{ m}^4$	Eq. A3.1
$I_{Y1}$	$3.993 \times 10^{-5} \text{ m}^4$	Eq. A3.2
$I_{Z1}$	$4.337 \times 10^{-5} \text{ m}^4$	Eq. A3.5
$I_Z$	$6.782 \times 10^{-4} \text{ m}^4$	Eq. A3.6
$t$	0.0396 m	Fig. A3.10
$\rho$	$7800 \text{ Kg/m}^3$	
$I_{Z_{mass}}$	$0.209 \text{ Kg m}^2$	Eq. A3.7

The moment of inertia of the top lever arm is then given by the sum of the  $I_{Z_{mass}}$  values in tables A3.5 to A3.7 thus:

$$I_{Z_{mass}} = 2.247 + 0.088 + 0.209 = 2.54 \quad \text{Kg m}^2 \quad (\text{A3.10})$$

### A3.5 Summary of calculated moment of inertias

**TABLE A3.8 Summary of calculated moments of inertia**

lever arm	$I_{Z_{mass}}$ Kgm <sup>2</sup>	calculation
bottom	212.6	(Eq. A3.8)
top	2.54	(Eq. A3.10)



## Appendix 4

### Model Data for SISO Stability Investigation

**TABLE A4.1 Hydraulic parameters**

Parameter	Description	Value	Units
$K_{ce} = K_l + K_p$	Combined pressure coefficient of the servo-valve and actuator	$1 \times 10^{-13}$	$\text{m}^5 \text{N}^{-1} \text{s}^{-1}$
$K_B = 4\beta_e$	Bulk modulus of the oil	$4 \times 1.8616 \times 10^9$	$\text{Nm}^{-2}$
$A$	Effective area of the actuator piston	0.008107	$\text{m}^2$
$V_t$	Volume of oil in the actuator	0.002469	$\text{m}^3$
$\omega_T$	Natural frequency in the frequency response of the servo-valve	880	$\text{rads}^{-1}$
$\zeta_T$	Damping in the frequency response of the servo-valve	0.9	none
$K_i K_q$	Gain of the servo-valve	0.042	$\text{m}^3 \text{s}^{-1} \text{A}^{-1}$

**TABLE A4.2 Nominal specimen**

parameter	description	value	units
$K_s$	Stiffness of the specimen	3.178	$\text{MNm}^{-1}$
$M_s$	Mass of the specimen	392.3457	Kg

**TABLE A4.3 Variation in the mass of the specimen**

system number	Mass (Kg)	system number	Mass (Kg)
1	0.32	11	32.94
2	0.51	12	52.35
3	0.81	13	83.21
4	1.29	14	132.27
5	2.04	15	210.23
6	3.25	16	334.16
7	5.16	17	531.14
8	8.20	18	844.23
9	13.04	19	1341.9
10	20.72	20	2132.9

**TABLE A4.4 Variation in the stiffness of the specimen**

system number	Stiffness (MNm <sup>-1</sup> )	system number	Stiffness (MNm <sup>-1</sup> )
1	0.0032	9	0.62
2	0.0062	10	1.19
3	0.012	11	2.30
4	0.023	12	4.45
5	0.044	13	8.58
6	0.086	14	16.57
7	0.17	15	32.00
8	0.32		

## Appendix 5

### Model Data for MIMO Stability Investigation

TABLE A5.1 Hydraulic parameters

Parameter	Description	Value	Units
$K_{ce} = K_l + K_p$	Combined pressure coefficient of the servo-valve and actuator	$1 \times 10^{-13}$	$\text{m}^5 \text{N}^{-1} \text{s}^{-1}$
$K_B = 4\beta_e$	Bulk modulus of the oil	$4 \times 1.8616 \times 10^9$	$\text{Nm}^{-2}$
$A$	Effective area of the actuator piston	0.008107	$\text{m}^2$
$V_l$	Volume of oil in the actuator	0.002469	$\text{m}^3$
$\omega_T$	Natural frequency in the frequency response of the servo-valve	880	$\text{rads}^{-1}$
$\zeta_T$	Damping in the frequency response of the servo-valve	0.9	none
$K_i K_q$	Gain of the servo-valve	0.042	$\text{m}^3 \text{s}^{-1} \text{A}^{-1}$

TABLE A5.2 Nominal specimen

parameter	description	value	units
$K_1$	Stiffness of the specimen	3.178	$\text{MNm}^{-1}$
$K_2$	Stiffness of the specimen	3.178	$\text{MNm}^{-1}$
$M_1$	Mass of the specimen	140.68	Kg
$M_2$	Mass of the specimen	140.68	Kg
	Damping ratio of vibrational modes	0.01	none

**TABLE A5.3 Variation in mass  $m$** 

system number	Mass (Kg)	system number	Mass (Kg)
1	7.03	11	85.39
2	9.03	12	109.60
3	11.59	13	140.68
4	14.88	14	180.57
5	19.09	15	231.78
6	24.51	16	297.50
7	31.46	17	381.86
8	40.38	18	490.15
9	51.83	19	629.14
10	66.52	20	807.54
		21	1036.5

**TABLE A5.4 Variation in stiffness  $k$** 

system number	Stiffness (MN/m)	system number	Stiffness (MN/m)
1	0.16	11	1.93
2	0.20	12	2.48
3	0.26	13	3.18
4	0.34	14	4.08
5	0.43	15	5.24
6	0.55	16	6.72
7	0.71	17	8.63
8	0.91	18	11.07
9	1.17	19	14.21
10	1.50	20	18.24
		21	23.42

**TABLE A5.5 Variation in  $\beta$  or  $\gamma$** 

system number	$\beta$ or $\gamma$	system number	$\beta$ or $\gamma$
1	0.010	12	0.681
2	0.015	13	1.000
3	0.022	14	1.468
4	0.032	15	2.154
5	0.046	16	3.162
6	0.068	17	4.642
7	0.100	18	6.813
8	0.147	19	10.000
9	0.215	20	14.678
10	0.316	21	21.544
11	0.464		

